Enzyme-material composites for solar-driven reactions

Bhavin Siritanaratkul

New College

Hilary Term 2017

A thesis submitted for the degree of

Doctor of Philosophy, University of Oxford

Enzyme-material composites for solar-driven reactions

Bhavin Siritanaratkul, New College, University of Oxford

A thesis submitted for the degree of Doctor of Philosophy, Hilary Term 2017

Abstract

Using sunlight to drive chemical reactions has long been one of the goals in developing sustainable processes. Previous research has focused on solar fuel production in the form of H_2, but this thesis demonstrates that solar-to-chemicals processes can be constructed to produce more complex compounds, using hybrid systems composed of enzymes and inorganic materials.

Tetrachloroethene reductive dehalogenase (PceA), an enzyme that catalyzes the conversion of tetrachloroethene (PCE) to trichloroethene (TCE) and subsequently to *cis*-dichloroethene (*c*DCE), was shown to accept electrons from both graphite and TiO_2 electrodes. Irradiation by UV light onto PceA-adsorbed TiO_2 particles led to the selective production of TCE and *c*DCE, which was not possible without PceA as a catalyst.

Ferredoxin-$NADP^+$ reductase (FNR) is a key enzyme in photosynthesis, as it receives energetic electrons from Photosystem I and produces NADPH as an energy carrier for downstream 'Dark' reactions involving CO_2 assimilation. This thesis presents the discovery of FNR activity on indium tin oxide (ITO) electrodes which led to direct electrochemical investigation of the properties of FNR, both in the absence and presence of its substrate, $NADP^+$. The FNR-adsorbed electrode, termed 'the electrochemical leaf', rapidly interconverts $NADP^+$/NADPH, and this was coupled to a downstream NADPH-dependent enzyme, thus demonstrating a new approach to cofactor regeneration for enzyme-catalyzed organic synthesis. The $NADP^+$ reduction by FNR was also driven by light using a photoanode made of visible-light responsive semiconductors.

Dedicated to my parents

Collaborations and contributions

The tetrachloroethene reductive dehalogenase PceA from *Sulfurospirillum multivorans* was provided by Professor Gabriele Diekert's group at Friedrich-Schiller-Universität Jena. Dr. James Wickens kindly gave advice and assistance on GC-MS measurements. Plasmids encoding genes for ferredoxin-$NADP^+$ reductase (FNR) and initial batches of FNR were provided by Dr. Martin Winkler (Professor Thomas Happe's group, Bochum). Some experiments on FNR@ITO electrodes in Chapter 3 were carried out by Thomas Roberts, a Part II student under my supervision. Dr. Clare F. Megarity generously assisted with purification of FNR as well as some overnight experiments in Chapter 4. Experiments with FNR and particulate TiO_2 in Chapter 5 were carried out by Nicholas Kossoff, a Part II student under my supervision. Thomas O.M. Samuels (Professor Jamie Warner's group, Materials, Oxford) carried out scanning electron microscopy (SEM).

Acknowledgements

First of all, I thank my parents for providing me with every kind of support, from financial to emotional. You made sure that I can achieve whatever I dream of, and I would not have come this far without your love.

I would like to thank Fraser for his unwavering support at all stages of my DPhil. Even when things seemed bleak, he gave me numerous chances and spurred me on, knowing that in the end I would be able to make something work. In this lab, I learned not only about electrochemistry and enzymes, but also perseverance and problem-solving.

Special thanks go to three people in the group, without which I would not have crossed the finish line. Andreas was a tremendous help at the start of my DPhil, and he led by example. Tania provided the spark that led to the dehalogenase project, the first time that anything had worked for me in this lab. Clare generously accepted me into the FNR team, made sure I was no longer sitting in a corner on my own, and comforted me after breakdowns during thesis writing.

This thesis was much improved by the proofreading efforts of Clare and Non, who both stressed the importance of adding more explanations and making the graphs bigger.

Everyone in the group has been a joy to work with. In rough order of appearance: Non, Elena, Vincent, Bonnie, Phillip, Suzannah, Wang, Claudia, Thomas, Emily, Matthew, Zhijiang, Kavita, Liyun, Kourosh, Stephen, Giorgio, Lei. Working with Part II students was both enjoyable and educational. I hope Deborah, Tom, and Nicky have learned as much as I have from taking care of them. I thank James for help at the GC-MS, Thomas for the SEM, my collaborators at Jena and Bochum who provided PceA and FNR, and the ICL support staff.

Publications

1. B. Siritanaratkul, C.F. Megarity, T.G. Roberts, T.O.M. Samuels, M. Winkler, J.H. Warner, T. Happe, F.A. Armstrong, "Transfer of photosynthetic $NADP^+$/NADPH recycling activity to a porous metal oxide for highly specific, electrochemically-driven organic synthesis", *Chemical Science*, **2017**, 8, 4579-4586

2. B. Siritanaratkul, S.T.A. Islam, T. Schubert, C. Kunze, T. Goris, G. Diekert, F.A. Armstrong, "Selective, light-driven enzymatic dehalogenations of organic compounds", *RSC Advances*, **2016**, 6, 84882-84886

3. A. Bachmeier, B. Siritanaratkul, F.A. Armstrong, "Enzymes as exploratory catalysts in artificial photosynthesis", in *From Molecules to Materials, Pathways to Artificial Photosynthesis*, **2015**, 99-123

Contents

Chapter 1

Introduction

1.1 Natural and artificial photosynthesis

1.1.1 Natural photosynthesis

Energy conversion is central to all life, since the primary source of all energetic processes on Earth is the sun. Solar energy in the form of photons must therefore be converted to chemical energy for it to be of use in biological systems. This process, namely photosynthesis, is composed of two parts (Figure 1.1): first, light absorption by chlorophyll pigment molecules and generation of energy carriers (ATP and NADPH), and second, usage of these energy carriers by CO_2-assimilation enzymes in the Calvin cycle to produce precursors of sugars and more complex carbohydrates.[1]

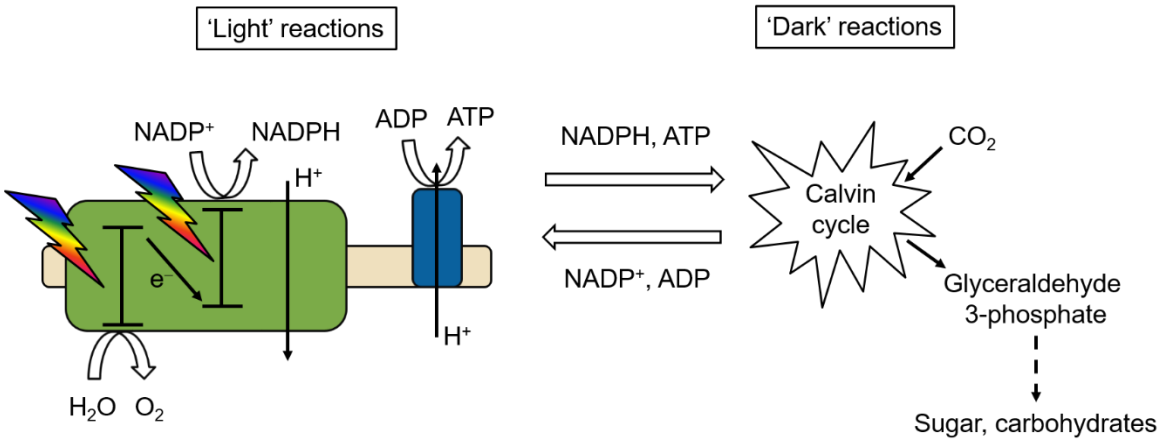

Figure 1.1 Diagram of the photosynthetic processes

In the 'Light' reactions, excited electrons are generated from light absorption by chlorophylls in Photosystems I and II, and these electrons transfer efficiently to nearby acceptors, resulting in charge separation. The electrons are replenished by water oxidation at the oxygen-evolving complex (OEC) in Photosystem II. The excited electrons are transferred successively to plastoquinone, cytochrome b_6f, and plastocyanin, and in the process protons are taken up from the stroma and released in the lumen, creating a proton gradient. This proton gradient is then used to drive ATP production by ATP synthase.

Electrons are transferred from plastocyanin to Photosystem I, after which it undergoes another excitation step. The energy carrier NADPH is generated from excited electrons from Photosystem I, via an electron carrier, ferredoxin, and an enzyme, ferredoxin-$NADP^+$ reductase (FNR).

In the 'Dark' reactions, CO_2 fixation and reduction are driven by the consumption of ATP and NADPH, which are regenerated in the 'Light' reactions. In the first step, CO_2 fixation is catalysed by the enzyme RuBisCO, converting ribulose-1,5-bisphosphate (5 carbons) into 2 molecules of 3-phosphoglycerate (3 carbons). Next, 3-phosphoglycerate is reduced to glyceraldehyde 3-phosphate (3 carbons), consuming 1 ATP and 1 NADPH per molecule. Finally, 3 molecules of ribulose-1,5-bisphosphate are regenerated from 5 molecules of glyceraldehyde 3-phosphate, again consuming ATP. One excess glyceraldehyde 3-phosphate is produced per 3 turns of the cycle, i.e. one carbon atom is fixed per cycle. One hexose can be formed from 2 molecules of glyceraldehyde 3-phosphate, and thus 6 cycles is required to produce one sugar molecule. The overall reaction of photosynthesis is the reduction of CO_2 and oxidation of water, driven by photons.

1.1.2 Artificial photosynthesis

Scientists have long sought to replicate the natural phenomena of photosynthesis, and the field of artificial photosynthesis has focused mostly on solar water splitting[2,3] since the first demonstration by Honda and Fujishima in 1972,[4] where a single crystal of n-type rutile TiO_2 was used as a photoanode for oxygen evolution under UV irradiation. The water splitting reaction is an uphill reaction, with ΔG^0 of 237 kJ/mol, which is equivalent to 1.23 V, and this can be considered storage of solar energy in the form of molecular hydrogen. Hydrogen gas, although potentially explosive, is thought to be a good 'energy

carrier' because it only forms water upon release of energy, either through combustion or in a fuel cell.

Artificial photosynthesis can be broken down into 3 processes: Light absorption, charge transfer, and catalytic reactions.[5-7] Semiconductors can be used as light absorbers, as they generate electron-hole pairs when irradiated with light that has energy at least equal to their band gap (see also Chapter 6). The electrons can subsequently be used in a reduction reaction if the conduction band level is more negative than the reduction potential of the reduction half-reaction, and the hole can be used in oxidation if the valence band is more positive than the reduction potential of the oxidation half-reaction (Figure 1.2). In other words, the band gap dictates the range of light that a semiconductor can absorb, and the band positions dictate the redox reactions it can perform.

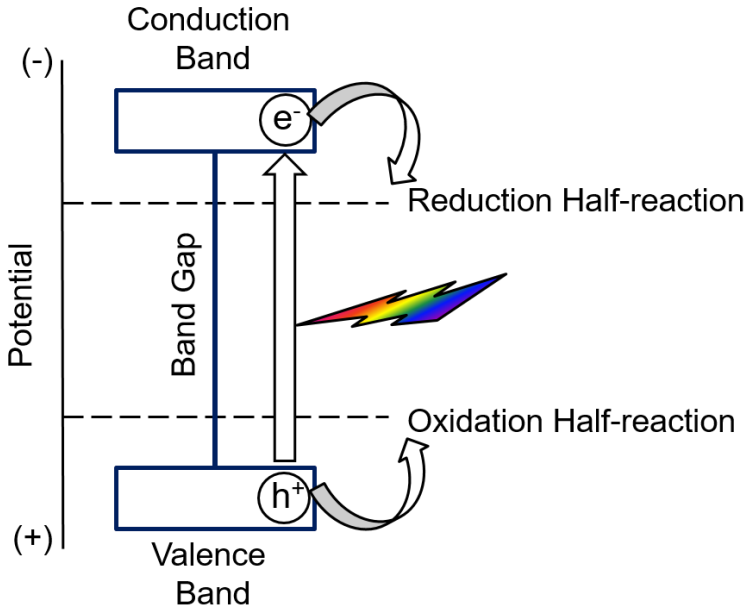

Figure 1.2 Diagram of light-driven redox reactions using a semiconductor (i.e. artificial photosynthesis). Electron-hole pairs are generated by light excitation, and they can carry out reduction and oxidation half-reactions provided that the band positions are favourable.

Taking water splitting as an example, the associated processes including the redox half-reactions are as follows:

Light absorption: $h\nu \rightarrow e^- + h^+$

Reduction half reaction: $4H^+ + 4e^- \rightarrow 2H_2$ $E^0 = -0.41$ V *vs* SHE at pH 7

Oxidation half reaction: $2H_2O + 4h^+ \rightarrow O_2 + 4H^+$ $E^0 = 0.82$ V

Overall reaction: $2H_2O \rightarrow 2H_2 + O_2$

Once the electron-hole pairs are photogenerated, they need to separate and be transported to the semiconductor surface to carry out redox reactions. Although the desired reactions (hydrogen and oxygen evolution, for example) can proceed on the bare semiconductor surface in some cases, the rate is slow and therefore surface catalysts are required. A variety of inorganic materials have been studied as catalysts for hydrogen[8] and oxygen evolution[9] , and noble metals such as Pt, Rh, Ir, and their oxides are typically good catalysts.

1.1.3 Aspects of artificial photosynthetic systems

Semiconductor materials that were studied at the beginning of the artificial photosynthesis field were typically wide band gap semiconductors such as TiO_2 and $SrTiO_3$, which can only absorb light in the UV region. Since UV light comprises less than 4 % of the solar spectrum,[10] materials that respond to visible light are required for a practical system. There are several strategies to engineer visible-light absorption, with the schemes shown in Figure 1.3.

1. Dye sensitization – A sensitizer such as an organic dye could be used for light absorption, after which, the photogenerated electron can be injected into the conduction band of the semiconductor. This usually necessitates the use of a sacrificial electron donor, since the rate of water oxidation by dyes are usually slow.

2. Native narrow band gap materials – Non-oxide materials such as chalcogenides, oxynitrides, and nitrides possess a narrower band gap than oxides, mostly due to the contribution of S, Se, or N to the valence band.[11]

3. Band gap engineering – An electron donor level can be created in a wide band gap material, usually by doping with other metal ions (*e.g.* Rh-doped $SrTiO_3$).[12]

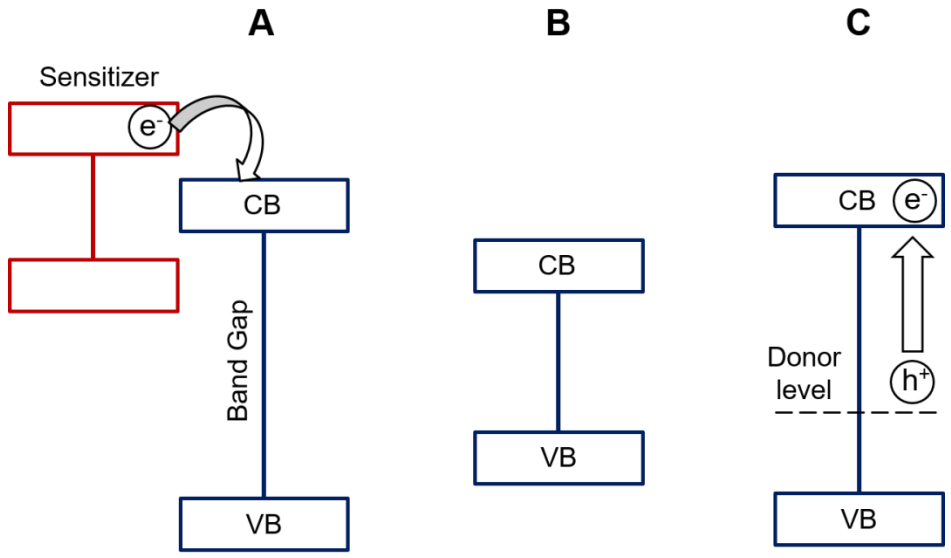

Figure 1.3 Strategies for visible light absorption. **A)** Sensitization by a dye, **B)** Native narrow band gap materials, **C)** Band gap engineering by doping.

Artificial photosynthetic systems can be configured in two ways: a particulate system (also known as photochemical or colloidal) and a photoelectrochemical system.[13] First, in a particulate system (Figure 1.4A), semiconductors particles are suspended in aqueous solution, and electron-hole pairs are generated within these particles under light

irradiation. The charges then migrate to the surface of the particles to drive redox reactions. Catalysts can be loaded onto the particles to carry out either or both of the half-reactions.

In a photoelectrochemical system[14,15], the reduction and oxidation reactions occur on two separate electrodes, as shown in Figure 1.4B using an n-type semiconductor as an example. When an n-type semiconductor electrode comes into contact with the solution, it transfers electrons to the solution until equilibrium is reached, resulting in 'band-bending' (see Chapter 6 for a detailed explanation). When it receives light irradiation, the photogenerated electrons can travel to the back contact, and across the circuit to the cathode where they can drive the reduction half-reaction. The photogenerated holes travel to the electrode surface, where they drive the oxidation half-reaction, thus resulting in a photo-oxidation current. Without light irradiation, the population of holes is too low for oxidation to occur. Thus, the photocurrent is generated from photoproduction of the minority carrier, which are holes in the case of n-type semiconductors. For p-type semiconductors, the reverse is true, and it can be expected to generate a photo-reduction current and therefore act as a photocathode.

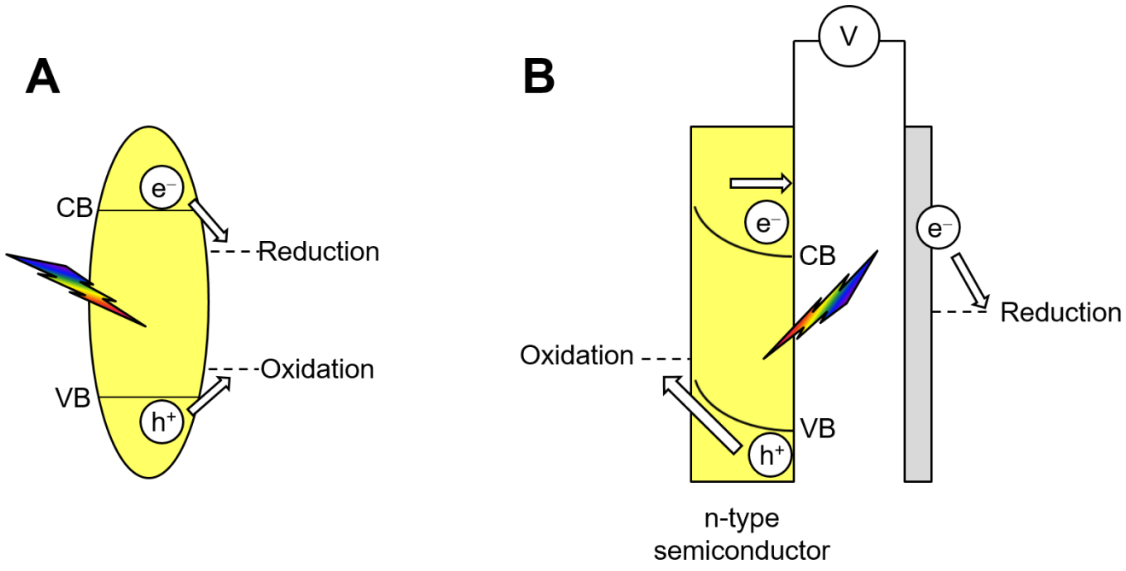

Figure 1.4 Two configurations for artificial photosynthesis systems. **A)** Particulate system. **B)** Photoelectrochemical system with a n-type semiconductor.

Even when the band potentials of some semiconductors are not suitable for a half-reaction, they can still be used in conjunction with a different material in what is called a 'Z-scheme' (Figure 1.5),[16] similar to the configuration of Photosystem II and Photosystem I. One semiconductor material carries out the reduction reaction, while another carries out oxidation, with electrons transferred from one to the other via a mediator such as I^-/IO_3^-. One drawback of Z-scheme systems is that they require twice the number of photons required in a single band gap system, and therefore the quantum yield is halved. However, this does not mean that the energy conversion efficiency of a dual band gap system is necessarily lower than that of a single band gap system. One cause of low energy conversion efficiency in a single band gap system is the energy loss per photon. This energy loss can be lessened by using two materials with different band gaps, chosen such that they absorb complementary parts of the solar spectrum.[6,17,18]

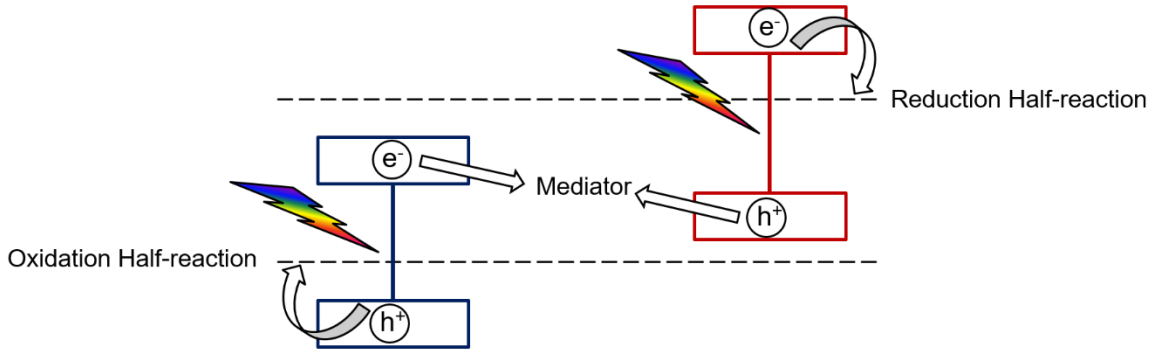

Figure 1.5 Diagram of Z-scheme configuration, where electrons are transferred from one light-absorbing material to another via an electron mediator.

Although most of the work on artificial photosynthesis has focused on water splitting, partly due to the relative simplicity in producing hydrogen, other fuels such as formate can also be made in a light-driven CO_2-assimilation process.[19-21] To increase the selectivity of the reaction towards a specific product, molecular catalysts are usually employed,[22] as solid state materials such as copper give a mixture of products (ranging from

H_2, CO, HCOOH, to CH_4).[23,24] This illustrates the importance of using a catalyst to tailor the process towards making a specific product. To go further, producing even more complex chemicals from sunlight should be possible, given the appropriate catalysts for the reaction. Indeed, natural photosynthesis produces a multitude of complex chemicals by harnessing a vast array of components, from light-harvesting complexes to enzymes for CO_2 fixation. This division of labour, utilising separate components tailored for light absorption and catalytic reaction, is the key to creating solar-to-chemicals processes, and it would be unreasonable to expect a single material to possess all the required properties.

1.2 Enzymes as catalysts

Enzymes have been designed by evolution to be excellent catalysts, in terms of rates, selectivity of the substrate, and stereo- and regio-specificity of the product.[25,26] Catalysts accelerate the rate of a chemical reaction by lowering the activation energy through stabilization of the transition state. While catalysis occurs at the enzyme active site, the entire protein structure works in concert to ensure that the active site geometry is aligned for substrate binding, chemical reaction, and subsequent release of product. The resulting catalytic rate is enhanced compared to the uncatalyzed case because the substrate is held in close proximity to the active site, in effect becoming an intramolecular reaction. The enzymes used in this thesis are from two families: cobalt-containing enzymes and flavoenzymes. A more detailed introduction to the each of the specific enzymes is given in Chapters 2 and 3.

1.2.1 Cobalt-containing enzymes

In order to function, some enzymes require additional components that are not part of the protein chain, and these are called cofactors. These cofactors are either metal ions or small organic molecules (the latter are also called coenzymes). One of the enzymes studied in this thesis, tetrachloroethene reductive dehalogenase (PceA, Chapter 2), uses a cobalt-containing cofactor (also known as a cobalamin, see Figure 1.6).

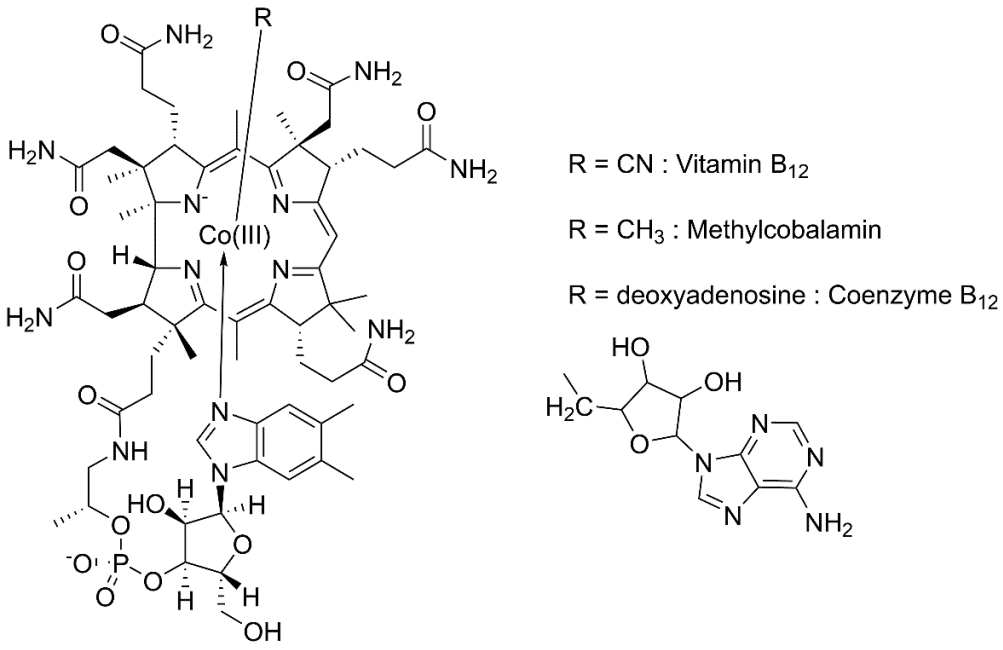

Figure 1.6 Structures of some cobalamins: vitamin B_{12} (or cyanocobalamin), methylcobalamin, and coenzyme B_{12}.

The majority of studied cobalt-containing enzymes are either isomerases or methyltransferases.[27,28] For isomerases, the coenzyme B_{12} (also denoted as adenosylcobalamin or AdoCbl) acts as a ready source of radicals as shown in Figure 1.7. The Co-carbon bond undergoes homolysis, and the generated radical on the deoxyadenosine can abstract H from the substrate. The substrate radical rearranges and abstracts H from the deoxyadenosine, regenerating the radical on the coenzyme. For methyltransferases, one of the substrates donates a methyl group to the cobalamin, creating a Co-methyl bond, which is then broken when the methyl group is transferred to a second substrate. Reductive dehalogenases work by a different mechanism, and this will be discussed in more detail in Chapter 2.

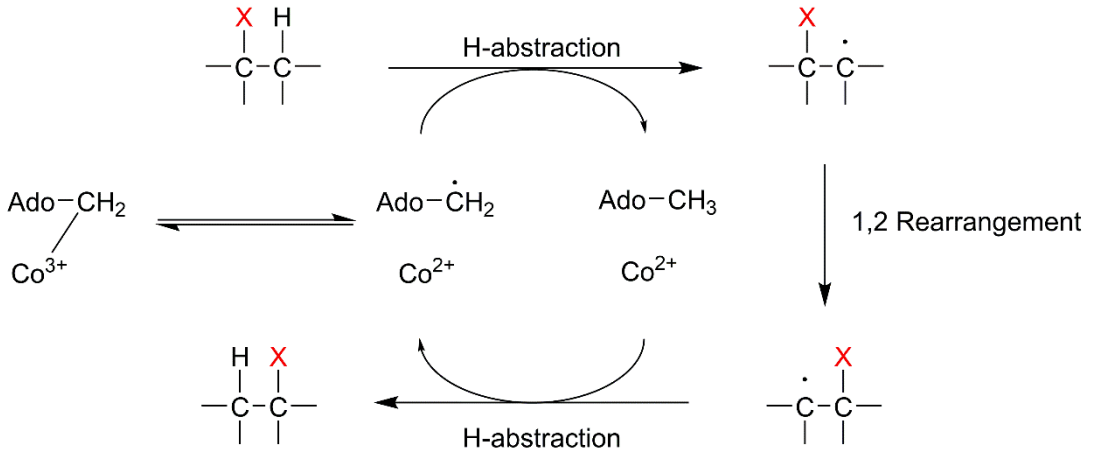

Figure 1.7 Mechanism of coenzyme B_{12}-dependent isomerases, adapted from ref[27]. Ado denotes the deoxyadenosine group.

1.2.2 Flavoenzymes

One important property of enzymes is their ability to store multiple electrons that are required for a complete reaction. For example, one class of enzymes called flavoenzymes, which usually contain an FMN (Flavin mononucleotide) or an FAD (Flavin adenine dinucleotide) cofactor, can mediate between one-electron and two-electron reactions.[29] This is because the flavin cofactor can exist in three redox states: fully oxidized, one-electron reduced (semiquinone), and fully reduced (hydroquinone) as shown in Figure 1.8 below.

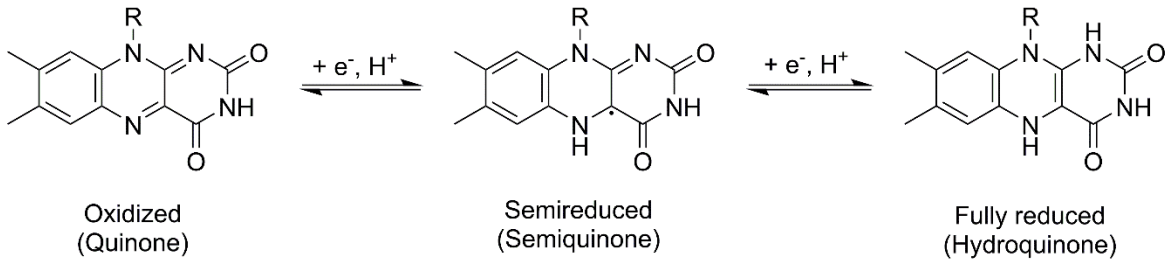

Figure 1.8 Redox states of a flavin group

One of the enzymes investigated in this thesis (Chapters 3 – 5) is a flavoenzyme called ferredoxin-$NADP^+$ reductase (FNR) which catalyses the two-electron reduction of $NADP^+$ to NADPH, by receiving electrons from ferredoxin which can only transfer one electron at a time. Without enzymes, the reduction of NAD^+ and oxidation of NADH can proceed at bare metal electrodes such as mercury, but this requires large overpotentials and can lead to physiologically undesirable side-products (*i.e.* the unusable 1,6 NADH instead of the usable 1,4 NADH).[30-32] The first step is the one-electron reduction of NAD^+ to $NAD^\bullet$, which occurs at ca. -1.1 V *vs* SCE at pH 7. This $NAD^\bullet$ can be further reduced at more negative potentials, yielding both 1,4 NADH and 1,6 NADH, however, the $NAD^\bullet$ can also dimerize to form $(NAD)_2$. Oxidation of NADH at bare electrodes occurs at ca. +0.5 V *vs* SCE, where the first step is a one-electron oxidation of NADH to $NADH^{\bullet+}$ which deprotonates to $NAD^\bullet$ then finally oxidized to NAD^+.[33] The results of this thesis show that, in contrast to bare metals, enzymatic $NADP^+$/NADPH interconversion by FNR can proceed with almost no overpotential, and this will be discussed in detail in Chapter 3.

1.3 Enzyme-material composites

In the study of enzyme activity in conjunction with an inorganic material, a distinction can be made based on the level of involvement of the material in the enzymatic reaction. For many cases, the material plays no role in catalysis, and acts only as a passive anchor for enzymes. In other cases, usually involving oxidoreductases, the inorganic material is involved in electron transfer with the enzyme.

Enzymes can be immobilized onto passive supports *(i.e.* without electron transfer) to facilitate handling as well as removal and recovery of the enzyme after the reaction is completed and to eliminate the need for product separation.[34-36] These properties are relevant for biocatalysis,[37] especially on an industrial scale. Enzymes can be attached to the surface of solids (usually inorganic materials or polymers), entrapped inside a gel or polymer, or crosslinked with other enzyme molecules to create crystals or aggregates.

For the interests of this thesis, emphasis is placed on enzyme-material composites involving electron transfer. This can be divided into two broad classes, similar to the types of artificial photosynthesis systems covered in the previous section: an electrochemical system and a particulate (or colloidal) system, both of which can be made up of conducting or semi-conducting materials.

If an enzyme can be immobilized onto an electrode in an electroactive configuration, then the enzyme can be studied under direct potential control. Various approaches have been investigated for enzyme immobilization on electrodes.[38,39] For example, the surface of metals (Au, Ag, etc.) can be modified with self-assembled monolayers (SAM), which possess one end (such as a thiol group) to interact with the metal surface, and the other end (-COOH, -OH, -NH_2, etc.) to interact with the enzyme.[40-42] Graphite is another common electrode material,[43,44] especially a freshly abraded edge plane

of pyrolytic graphite which is rough and possesses -COOH and -OH groups[45] allowing the adsorption of enzymes. Conducting and semiconducting metal oxides can also be used as electrode materials, as will be discussed later in this section, as well as in other chapters of this thesis.

One example of practical usage of an enzymatic electrochemical system is glucose oxidase (GOx), which is a component in glucose biosensors (Figure 1.9A).[46] In earlier-generation systems, these sensors worked by amperometric detection of H_2O_2 produced by GOx when consuming glucose, i.e. H_2O_2 acted as an electron mediator between GOx and the working electrode. In this setup, there is no direct electron transfer between GOx and the working electrode (due to the buried nature of the FAD active site), thus interference was possible by other redox components present in the solution such as ascorbic acid or uric acid. Later work has tried to replace H_2O_2 with other electron mediators, such as ferrocene or a redox polymer which also acted to immobilize GOx on the working electrode. Carbon nanotubes have been used to covalently link an FAD cofactor to a working electrode,[47] after which apo-GOx (GOx without an FAD group) could be bound, thereby creating a direct electronic contact between GOx and the working electrode.

The electrode in an enzymatic electrochemical system could also be a light-absorbing material. For example, a p-type InP photoelectrode was used to drive CO_2 reduction by a formate dehydrogenase (Figure 1.9B).[48] The enzyme was not directly attached to the electrode, but instead the photogenerated electrons reduced methyl viologen (MV^{2+}) in the solution, which in turn reduced the enzyme, driving the conversion of CO_2 to formate.

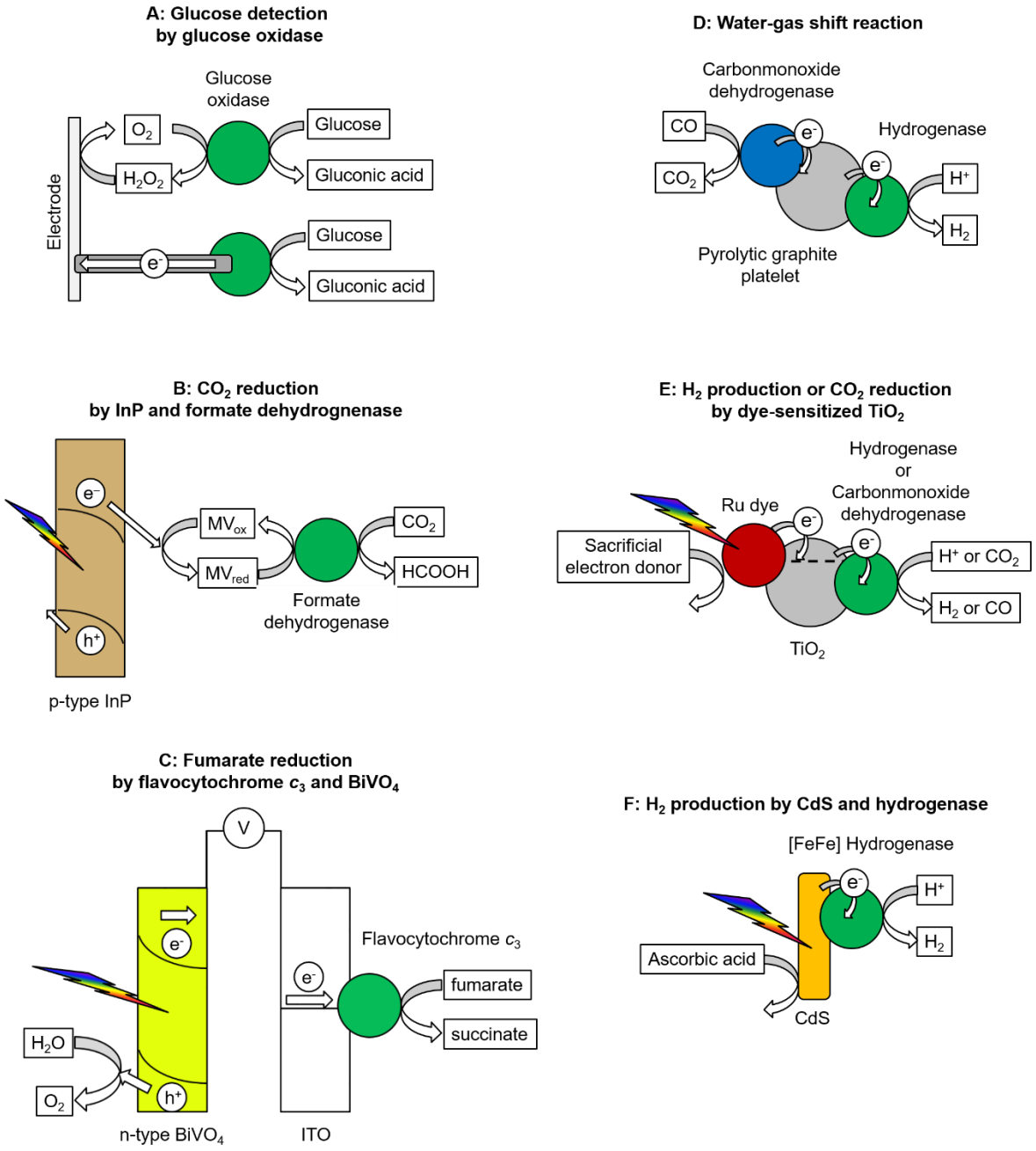

Figure 1.9 Examples of enzyme-material composite systems. **A)** Glucose oxidation by glucose oxidase, in either indirect contact with an electrode via H_2O_2 formation, or with its FAD group covalently linked to an electrode surface. **B)** CO_2 reduction by formate dehydrogenase receiving electrons indirectly from a InP photocathode. **C)** Fumarate reduction by flavocytochrome c_3 on an ITO cathode and light absorption and water oxidation at a $BiVO_4$ photoanode. **D)** Water-gas shift reaction by carbon monoxide dehydrogenase (CODH) and hydrogenase connected by conductive graphite particles. **E)** H_2 production or CO_2 reduction by hydrogenase or CODH, respectively, adsorbed onto dye-sensitized TiO_2 particles. **F)** H_2 production by hydrogenase adsorbed onto visible-light active CdS particles.

In particulate systems, the conducting or semiconducting material is not connected to a power source like in the case of an electrode system, and therefore electrons must be supplied from a different source. One example is the water-gas shift reaction demonstrated by Lazarus *et al*.,[49] where two different enzymes were co-adsorbed onto conducting graphite platelets (Figure 1.9D). The water-gas shift reaction is the conversion of CO to CO_2, coupled to H_2 production, utilizing the difference in reduction potentials of CO oxidation and H^+ reduction. A carbon dioxide dehydrogenase enzyme (CODH) is used to transform CO to CO_2, releasing electrons that can travel through the conducting particle to a hydrogenase enzyme, which can use these electrons to drive H^+ reduction to H_2.

Electrons can also be supplied by light, as described in the previous section on artificial photosynthesis by semiconductors. Work in the Armstrong group on light-driven enzymatic reactions began with Reisner in 2009, in which various hydrogenases were connected to dye-sensitized TiO_2 particles to produce H_2 under visible light irradiation (Figure 1.9E).[50] The dye was a Ru-based complex, with ligands possessing phosphonate groups for attachment to the TiO_2 surface. The TiO_2 particles, though not directly involved in light absorption, act as both a scaffold to hold both the dye and enzyme, and also participate in electron transport from dye to enzyme. The best-performing hydrogenase was a NiFeSe-hydrogenase from *Desulfomicrobium baculatum*, with a turnover of 50 moles of H_2 per enzyme molecule per second. Interestingly, the hydrogenase Hyd2 from *Escherichia coli*, a good H_2 producer and relatively tolerant to O_2, only produced negligible amounts of H_2 when attached to TiO_2 particles even though it was able to adsorb on to the particles from solution. This implies that the enzyme has to be adsorbed in an electroactive orientation, *i.e.* to allow for direct electron transfer from TiO_2 to the electron entry point in the enzyme. Other hydrogenases including typically good H_2-producing FeFe-hydrogenases such as HydA1 from *Chlamydomonas reinhartii*, performed poorly, possibly due to O_2-inactivation

or photodamage. This work showcased a particular configuration of a solar-to-H_2 system: organic dye as visible-light absorber, TiO_2 as electronic bridge and support, and a hydrogenase as the H_2 evolving catalyst. Limitations of this system include the use of noble metals in the organic dye (Ru in this case) and the need for a sacrificial electron donor to replenish the electrons in the dye HOMO. In any system using dye-sensitized TiO_2 particles, the HOMO of the dye is typically not positive enough for water oxidation, therefore the system needs a substance more easily oxidized than water, i.e. sacrificial reagents such as triethanolamine (TEOA) and 2-(N-morpholino)ethanesulfonic acid (MES).

Woolerton *et al* used the same light-absorbing system in conjuction with carbonmonoxide dehydrogenase (CODH) from *Carboxydothermus hydrogenoformans* to catalyse the reduction of CO_2 to CO.[51,52] The adsorption of CODH onto TiO_2 was expected to be mainly determined by electrostatic interactions, with CODH adsorbing favourably on positively charged surfaces. In an attempt to modify the surface with o-phosphorylethanol amine which has a phosphonate group for attachment to the TiO_2 surface and a protruding amine group to provide a positive surface charge, the CO_2 reduction activity was lowered, contrary to expectations, which suggests that electrostatic interactions cannot be the whole story. The photoreduction of CO_2 was also accomplished in a photoelectrochemical system, where CODH was immobilized on a dye-sensitized p-type NiO electrode.[53] In this case, the production of CO was too small to be measured directly, and inhibition experiments with KOCN were used to confirm that the photocurrent was due to CO_2 reduction by CODH.

The scope of solar-driven enzymatic reactions was extended beyond H_2 production and CO_2 reduction, for example to conversion of fumarate to succinate by flavocytochrome c_3 (fcc_3).[54] The reaction was driven by light in two configurations: a particulate system (on dye-sensitized TiO_2) and a photoelectrochemical system (fcc_3 on ITO electrode coupled to a $BiVO_4$ photoanode, Figure 1.9C). Because the reduction potential of fumarate was more

positive than H^+ reduction, the reaction proceeded even without applied bias, which is not possible in the case of water splitting on $BiVO_4$ electrodes due to its conduction band level.

The groups of Dukovic and King have studied H_2 production by hydrogenases in complex with CdS nanorods (Figure 1.9F).[55,56] The FeFe-hydrogenase from *Clostridium acetobutylicum* adsorbed onto CdS which were capped with 3-mercaptopropionic acid which provided a surface negative charge via a carboxylic acid group. Ascorbic acid was used as the sacrificial electron donor for CdS. It was shown that the binding of the hydrogenase to CdS was stronger than to ferredoxin, its biological redox partner, probably due to the larger contact area and more negatively charged surface. The electron transfer from CdS to hydrogenases was fast, but the system is limited by the self-oxidation of CdS under light, and therefore a sacrificial electron donor is always necessary.

A related system is a composite made of a molecular catalyst immobilized onto a conductive support. For example, Maeda and co-workers have used a composite of C_3N_4 (a visible-light absorbing semiconductor) and noble metal complexes of Ru and Re for CO_2 reduction to either formate or CO.[57] Other workers have attached Dubois-type Ni complex catalysts for H_2 evolution onto semiconductors.[58,59] A clear analogy can be observed between these systems and enzyme-material composites; both are light-absorbing materials connected electrically to a catalyst for a specific reaction. An enzyme is a macromolecule and as such takes up more space on the support surface, thus the limit for coverage is lower than that for molecular catalysts. In addition, enzymes also possess specific regions as electron entry/exit points, and therefore they have a preferred orientation on a surface, with the electron entry/exit point positioned closest to the surface. However, the structure of molecular catalysts can be distorted, or even completely lost, when immobilized on a surface, whereas the backbone of an enzyme maintains it in an active configuration.

In summary, enzyme-materials composites have been used for a variety of reactions, both with and without electron transfer between the inorganic material and the enzyme. This thesis focuses on materials that participate in electron transfers to and from an enzyme. The inorganic material is either an electrochemical or a particulate configuration, and the source of high-energy electrons is either a potentiostat, light excitation (in the case of semiconductors) or electron donors such as hydrogen.

1.4 Scope of this thesis

This thesis explores solar-to-chemical reactions using enzyme-material composites, extending beyond H_2 production and CO_2 reduction. In Chapter 2, I demonstrate regiospecific dehalogenation catalysed by tetrachloroethene reductive dehalogenase (PceA), both on TiO_2 electrodes and TiO_2 particles. This work serves as a demonstration of light-driven production of a specific compound, *cis*-dichloroethene, which could not be achieved in other non-enzymatic systems.

Chapters 3 to 5 focus on the production of a valuable product, NADPH, by ferredoxin-$NADP^+$ reductase (FNR) immobilized on ITO electrodes. Chapter 3 lays the groundwork of basic electrochemistry of FNR and investigates its reduction potential and catalytic activity. Having established electroactive FNR on an electrode, in Chapter 4 it was used as an $NADP^+$/NADPH recycling system which could be coupled to downstream enzyme-catalysed organic syntheses. This was termed 'The electrochemical leaf', as it mimicked NADPH recycling in the biological leaf. In Chapter 5, light-driven NADPH production was achieved by connecting the FNR-adsorbed electrode to a photoelectrode.

Finally, Chapter 6 covers background electrochemical theory and details of experimental methods.

For convenience, Table 1.1 below lists the reduction potentials of all redox reactions discussed in this thesis.

Table 1.1 Reduction potentials of relevant reactions

Reduction potential (V *vs* SHE at pH 7)	Reaction
-0.53	CO_2/CO
-0.41	H^+/H_2
-0.32	$NAD(P)^+$/NAD(P)H
0.54	TCE/*c*DCE
0.58	PCE/TCE
0.82	O_2/H_2O

1.5 References

(1) Berg, J. M.; Tymoczko, J. L.; Stryer, L. *Biochemistry. 5th edition*; W. H. Freeman: New York, 2002.

(2) Bard, A. J.; Fox, M. A. *Accounts of Chemical Research* **1995**, *28*, 141.

(3) Lewis, N. S.; Nocera, D. G. *Proceedings of the National Academy of Sciences* **2006**, *103*, 15729.

(4) Fujishima, A.; Honda, K. *Nature* **1972**, *238*, 37.

(5) Maeda, K. *Journal of Photochemistry and Photobiology C: Photochemistry Reviews* **2011**, *12*, 237.

(6) Walter, M. G.; Warren, E. L.; McKone, J. R.; Boettcher, S. W.; Mi, Q.; Santori, E. A.; Lewis, N. S. *Chemical Reviews* **2010**, *110*, 6446.

(7) Kudo, A.; Miseki, Y. *Chemical Society Reviews* **2009**, *38*, 253.

(8) Conway, B. E.; Bockris, J. O. M. *The Journal of Chemical Physics* **1957**, *26*, 532.

(9) Harriman, A.; Pickering, I. J.; Thomas, J. M.; Christensen, P. A. *Journal of the Chemical Society, Faraday Transactions 1: Physical Chemistry in Condensed Phases* **1988**, *84*, 2795.

(10) Reference Solar Spectral Irradiance: Air Mass 1.5, The National Renewable Energy Laboratory (NREL), US Department of Energy, http://rredc.nrel.gov/solar/spectra/am1.5/

(11) Maeda, K.; Domen, K. *The Journal of Physical Chemistry C* **2007**, *111*, 7851.

(12) Kawasaki, S.; Akagi, K.; Nakatsuji, K.; Yamamoto, S.; Matsuda, I.; Harada, Y.; Yoshinobu, J.; Komori, F.; Takahashi, R.; Lippmaa, M.; Sakai, C.; Niwa, H.; Oshima, M.; Iwashina, K.; Kudo, A. *The Journal of Physical Chemistry C* **2012**, *116*, 24445.

(13) Hisatomi, T.; Kubota, J.; Domen, K. *Chemical Society Reviews* **2014**, *43*, 7520.

(14) Nozik, A. J.; Memming, R. *The Journal of Physical Chemistry* **1996**, *100*, 13061.

(15) Gratzel, M. *Nature* **2001**, *414*, 338.

(16) Maeda, K. *ACS Catalysis* **2013**, *3*, 1486.

(17) Bolton, J. R.; Strickler, S. J.; Connolly, J. S. *Nature* **1985**, *316*, 495.

(18) Weber, M. F.; Dignam, M. J. *Journal of The Electrochemical Society* **1984**, *131*, 1258.

(19) Windle, C. D.; Perutz, R. N. *Coordination Chemistry Reviews* **2012**, *256*, 2562.

(20) Morris, A. J.; Meyer, G. J.; Fujita, E. *Accounts of Chemical Research* **2009**, *42*, 1983.

(21) Bachmeier, A.; Armstrong, F. *Current Opinion in Chemical Biology* **2015**, *25*, 141.

(22) Takeda, H.; Cometto, C.; Ishitani, O.; Robert, M. *ACS Catalysis* **2017**, *7*, 70.

(23) Gattrell, M.; Gupta, N.; Co, A. *Journal of Electroanalytical Chemistry* **2006**, *594*, 1.

(24) Qiao, J.; Liu, Y.; Hong, F.; Zhang, J. *Chemical Society Reviews* **2014**, *43*, 631.

(25) Bugg, T. *Introduction to Enzyme and Coenzyme Chemistry* 2nd ed.; Blackwell, 2004.

(26) Fersht, A. *Enzyme Structure and Mechanism*; 2nd ed.; W.H. Freeman and Company, 1985.

(27) Banerjee, R.; Ragsdale, S. W. *Annual Review of Biochemistry* **2003**, *72*, 209.

(28) Kräutler, B. In *Encyclopedia of Inorganic and Bioinorganic Chemistry*; John Wiley & Sons, Ltd: 2011.

(29) Miura, R. *The Chemical Record* **2001**, *1*, 183.

(30) Gorton, L.; Domínguez, E. In *Encyclopedia of Electrochemistry*; Wiley-VCH Verlag GmbH & Co. KGaA: 2007.

(31) Elving, P. J.; Schmakel, C. O.; Santhanam, K. S. V.; Zuman, P. *C R C Critical Reviews in Analytical Chemistry* **1976**, *6*, 1.

(32) Schmakel, C. O.; Santhanam, K. S. V.; Elving, P. J. *Journal of the American Chemical Society* **1975**, *97*, 5083.

(33) Moiroux, J.; Elving, P. J. *Journal of the American Chemical Society* **1980**, *102*, 6533.

(34) Sheldon, R. A. *Advanced Synthesis & Catalysis* **2007**, *349*, 1289.

(35) Sheldon, R. A.; van Pelt, S. *Chem. Soc. Rev.* **2013**, *42*, 6223.

(36) Kim, J.; Grate, J. W.; Wang, P. *Chemical Engineering Science* **2006**, *61*, 1017.

(37) Schmid, A.; Dordick, J. S.; Hauer, B.; Kiener, A.; Wubbolts, M.; Witholt, B. *Nature* **2001**, *409*, 258.

(38) Armstrong, F. A.; Wilson, G. S. *Electrochimica Acta* **2000**, *45*, 2623.

(39) Walcarius, A.; Minteer, S. D.; Wang, J.; Lin, Y.; Merkoçi, A. *Journal of Materials Chemistry B* **2013**, *1*, 4878.

(40) Chen, D.; Wang, G.; Li, J. *The Journal of Physical Chemistry C* **2007**, *111*, 2351.

(41) Chaki, N. K.; Vijayamohanan, K. *Biosensors and Bioelectronics* **2002**, *17*, 1.

(42) Samanta, D.; Sarkar, A. *Chemical Society Reviews* **2011**, *40*, 2567.

(43) Blanford, C. F.; Armstrong, F. A. *Journal of Solid State Electrochemistry* **2006**, *10*, 826.

(44) Hirst, J.; Armstrong, F. A. *Analytical Chemistry* **1998**, *70*, 5062.

(45) Takahagi, T.; Ishitani, A. *Carbon* **1984**, *22*, 43.

(46) Wang, J. *Chemical Reviews* **2008**, *108*, 814.

(47) Xiao, Y.; Patolsky, F.; Katz, E.; Hainfeld, J. F.; Willner, I. *Science* **2003**, *299*, 1877.

(48) Parkinson, B. A.; Weaver, P. F. *Nature* **1984**, *309*, 148.

(49) Lazarus, O.; Woolerton, T. W.; Parkin, A.; Lukey, M. J.; Reisner, E.; Seravalli, J.; Pierce, E.; Ragsdale, S. W.; Sargent, F.; Armstrong, F. A. *Journal of the American Chemical Society* **2009**, *131*, 14154.

(50) Reisner, E.; Powell, D. J.; Cavazza, C.; Fontecilla-Camps, J. C.; Armstrong, F. A. *Journal of the American Chemical Society* **2009**, *131*, 18457.

(51) Woolerton, T. W.; Sheard, S.; Reisner, E.; Pierce, E.; Ragsdale, S. W.; Armstrong, F. A. *Journal of the American Chemical Society* **2010**, *132*, 2132.

(52) Woolerton, T. W.; Sheard, S.; Pierce, E.; Ragsdale, S. W.; Armstrong, F. A. *Energy & Environmental Science* **2011**, *4*, 2393.

(53) Bachmeier, A.; Hall, S.; Ragsdale, S. W.; Armstrong, F. A. *Journal of the American Chemical Society* **2014**, *136*, 13518.

(54) Bachmeier, A.; Murphy, B. J.; Armstrong, F. A. *Journal of the American Chemical Society* **2014**, *136*, 12876.

(55) Brown, K. A.; Wilker, M. B.; Boehm, M.; Dukovic, G.; King, P. W. *Journal of the American Chemical Society* **2012**, *134*, 5627.

(56) Wilker, M. B.; Shinopoulos, K. E.; Brown, K. A.; Mulder, D. W.; King, P. W.; Dukovic, G. *Journal of the American Chemical Society* **2014**, *136*, 4316.

(57) Kuriki, R.; Maeda, K. *Physical Chemistry Chemical Physics* **2017**.

(58) Moore, G. F.; Sharp, I. D. *The Journal of Physical Chemistry Letters* **2013**, *4*, 568.

(59) Seo, J.; Pekarek, R. T.; Rose, M. J. *Chemical Communications* **2015**, *51*, 13264.

Chapter 2

Solar-driven reductive dehalogenation of organic compounds

Chapter 2

Solar-driven reductive dehalogenation of organic compounds

Abstract

The tetrachloroethene reductive dehalogenase (PceA) from *Sulfurospirillum multivorans* catalyzes the sequential reduction of tetrachloroethene (also known as perchloroethylene, PCE) to trichloroethene (TCE) then regiospecifically to *cis*-1,2-dichloroethene (*c*DCE). This chapter investigates the use of a semiconductor as a light absorber, generating and transfering electrons to PceA and thereby exemplifying a light-driven enzymatic system for reductive dehalogenation. Direct electron transfer from an electrode to PceA showed that PceA was active on both pyrolytic graphite edge (PGE) and TiO_2 electrodes. When PceA-loaded TiO_2 particles received UV irradiation, the photogenerated electrons were able to transfer from TiO_2 to PceA, and the sequential reductive dehalogenation of PCE to TCE and then *c*DCE was confirmed by GC-MS. This result contributes to the library of solar-to-chemical processes, and the system could potentially be adapted to use with other dehalogenases that utilizes a different range of substrates.

Results from this chapter were published:

Bhavin Siritanaratkul, Shams T. A. Islam, Torsten Schubert, Cindy Kunze, Tobias Goris, Gabriele Diekert and Fraser A. Armstrong, **"Selective, light-driven enzymatic dehalogenations of organic compounds"**, RSC Advances, 2016, 6, 84882-84886

2.1 Introduction

2.1.1 Reductive dehalogenation by organohalide-respiring bacteria

Organohalides have many industrial uses, for example trichloroethene (TCE, C_2HCl_3) was first used as an anesthetic then as an organic solvent and metal degreaser, despite its toxicity and carcinogenicity.[1] Organohalides that are found in soil and water can be generated from naturally occurring processes[2,3] as well as industrial processes.[4] A large variety of marine plant, fungi, and bacteria can synthesize halogenated compounds, possibly as a self-defence mechanism. Therefore, it is not surprising that some organisms have evolved the ability for organohalide respiration using organohalides as the final electron acceptor.[5,6]

Reductive dehalogenation of organohalides are exergonic reactions, providing a driving force for the final goal of ATP synthesis.[7] Simple models of the electron transport chain in organohalide respiration are shown in Figure 2.1. For illustrative purposes, H_2 is assumed to be the electron donor, but other donors are possible including formate, pyruvate, and lactate. A hydrogenase oxidises H_2 to produce two protons and two electrons, of which the latter is transported via a mediator in the membrane to a reductive dehalogenase. Again, a variety of substrates are possible for dehalogenation, and in this case we use the example of tetrachloroethene (PCE, C_2Cl_4, also known as perchloroethene), which is reduced to trichloroethene (TCE) releasing a chloride ion. The reductive dehalogenase (RDase) could either be located on the cytoplasmic side (‘inside’, Figure 2.1A) or the periplasmic side (‘outside’, Figure 2.1B) of the cytoplasmic membrane. It was only recently that some evidence had been gathered for the latter case.[8,9] The mediator delivering electrons to reductive dehalogenases has not been identified, and it may differ between species, though some studies implicate menaquinone, which also functions as a proton translocator.[10]

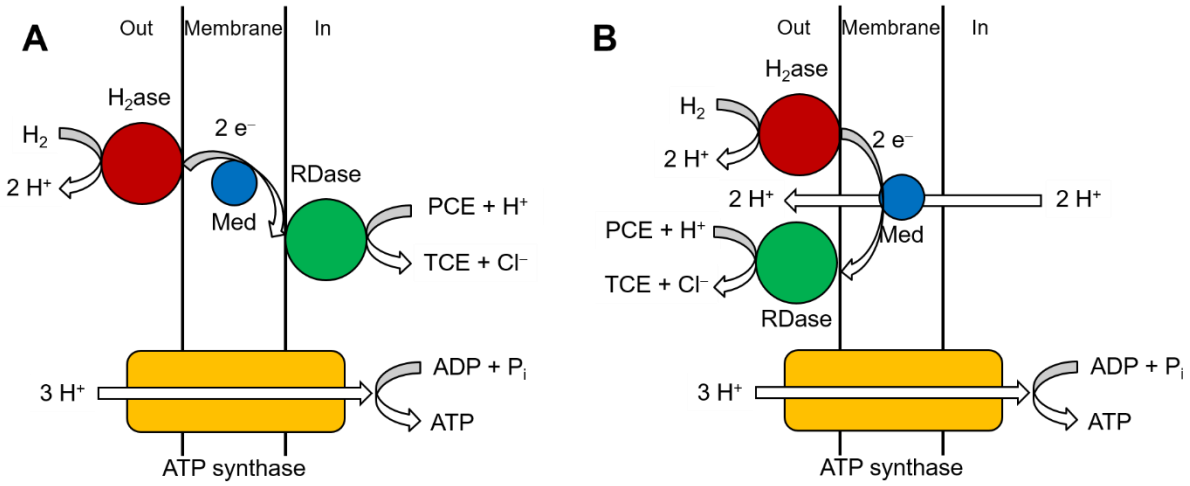

Figure 2.1 Models of organohalide respiration with H_2 as electron donor and PCE as electron acceptor, with the RDase on the **A)** inside and **B)** outside of the cytoplasmic membrane. H_2ase, hydrogenase; Med, electron mediator; RDase, reductive dehalogenase; PCE, tetrachloroethene (perchloroethene); TCE, trichloroethene.

In general, organohalide-respiring bacteria are anaerobes, with the first example (*Desulfomonile tiedjei*) isolated from sewage sludge containing 3-chlorobenzoate.[11] These bacteria usually show a preference for either chlorinated aromatic compounds or chlorinated ethenes.

There have been studies using electrochemistry with whole-cell organohalide-respiring bacteria.[12,13] A mixed culture including *Desulfitobacterium* sp. and *Dehalococcoides* sp. was grown in an electrochemical cell with a carbon paper electrode. When a potential of -0.45 V *vs* SHE was applied and no other source of reducing equivalents (such as H_2) were present, the cells were able to reduce TCE (C_2HCl_3) to cis-1 2-dichloroethene (*c*DCE, $C_2H_2Cl_2$), vinyl chloride (C_2H_3Cl), and ethene (C_2H_4). No additional electron mediators were added to the electrochemical cell, but the results indicated a mediator species, still unidentified, was produced by the bacteria as a response to applied potential.

2.1.2 Reductive dehalogenase PceA from *Sulfurospirillum multivorans*

The enzyme used in this study is the tetrachloroethene reductive dehalogenase PceA (EC 1.97.1.8) from *Sulfurospirillum multivorans* (also previously known as *Dehalospirillum multivorans*), provided by the Diekert research group at Friedrich-Schiller-Universität Jena. The crystal structure of PceA is shown in Figure 2.2A. The enzyme has a Co-containing norpseudo-B_{12} cofactor (Figure 2.2B) as the active site, as well as two [4Fe-4S] clusters. The distance between Co and the proximal [4Fe-4S], and between the proximal and distal [4Fe-4S] are 8.4 and 9.5 Å, respectively.[9] This suggests an electron transfer chain from the [4Fe-4S] clusters to the buried norpseudo-B_{12} active site, since the distances are within the limit (14 Å) for intramolecular electron transfer.[14]

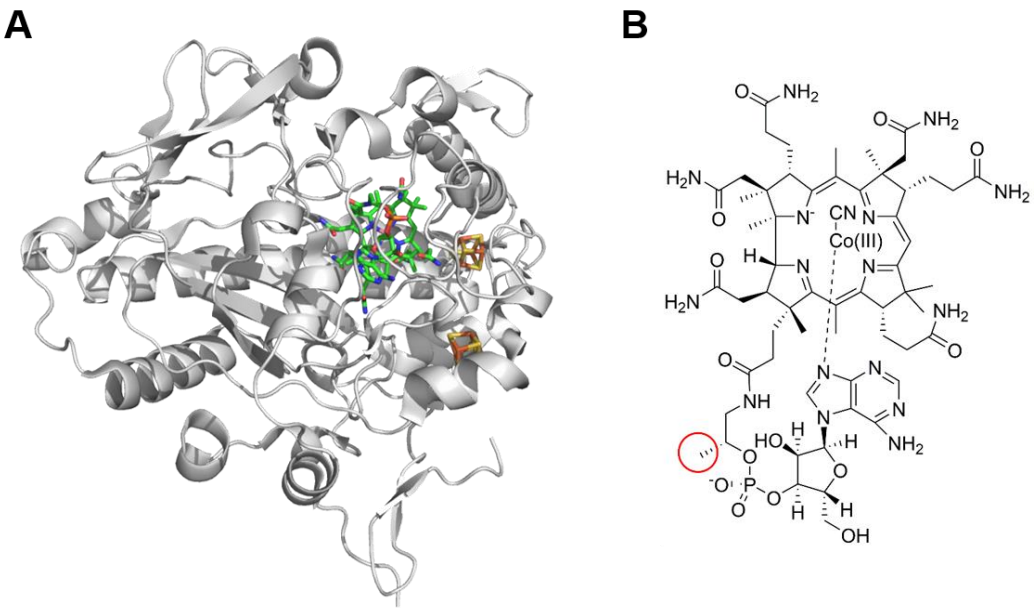

Figure 2.2 A) Crystal structure of PceA, with norpseudo-B12 (green) and two [4Fe-4S] clusters (yellow and orange) shown.[9] (PDB code 4UQU) **B)** Structure of pseudovitamin B_{12}. For norspeudo-B_{12}, the methyl group in the red circle is replaced by a hydrogen.

Extensive characterization of PceA identified the reductive dechlorination activity of *Sulfurospirillum multivorans*,[15] followed by isolation of PceA.[16] Activity assays are

reported using a variety of electron donors,[16] including methyl viologen (MV^{2+}/MV^{+}, E = -446 mV *vs* SHE), benzyl viologen ($BV^{2+/}BV^{+}$, E = -359 mV), methylene blue, pyridine nucleotides, flavins, cytochrome *c*, and ferredoxin, but only reduced methyl viologen was able to act as the electron donor. Methyl viologen was reduced chemically by titanium(III) citrate, and the extent of reaction of PceA with PCE or TCE was monitored by the change in absorbance at 578 nm; PceA catalyzed the reduction of tetrachloroethene (PCE) to trichloroethene (TCE) and the reduction of TCE to *cis*-1,2-dichloroethene (*c*DCE), equations (1) and (2), respectively. Both reactions are exergonic, with reduction potentials of 0.58 and 0.54 V vs SHE at pH 7.[17] Alternatively, the change in Gibbs free energy of the reaction can also be estimated from the Gibbs energy of formation of the compounds, which results in -138 and -128 kJ/mol for equations (1) and (2), respectively.

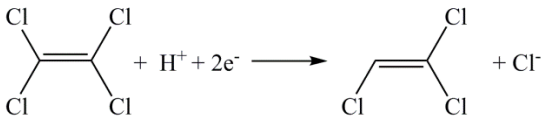

Eq.1

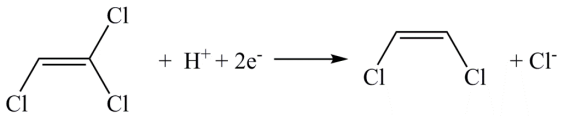

Eq.2

The involvement of a corrinoid cofactor (norpseudo-B_{12} in this case) was first shown by inhibition experiments with propyl iodide which binds to cobalt in the reduced state.[16] This binding is reversible, and the cobalt-carbon bond can be broken by light irradiation, restoring the original activity. The norpseudo-B_{12} cofactor was isolated,[18] and the reduction potential of Co(II)/Co(I) for the enzyme-bound cofactor was -0.38 V *vs* SHE, while the free form was at -0.48 V.

The first step in the catalytic cycle is the reaction of Co(I) in the norpseudo-B_{12} with the substrate (PCE for example),[19] with two different pathways postulated, (Figure 2.3). In pathway A, the Co(I) is a reductant in an electron transfer mechanism, creating a

trichlorovinyl radical, which is then converted to TCE after protonation and a further reduction step. In pathway B, the Co(I) acts as nucleophile attacking one of the carbons and forms a cobalt-tetrachloroethyl complex, which then releases a chloride, then the complex is protonated to release TCE.

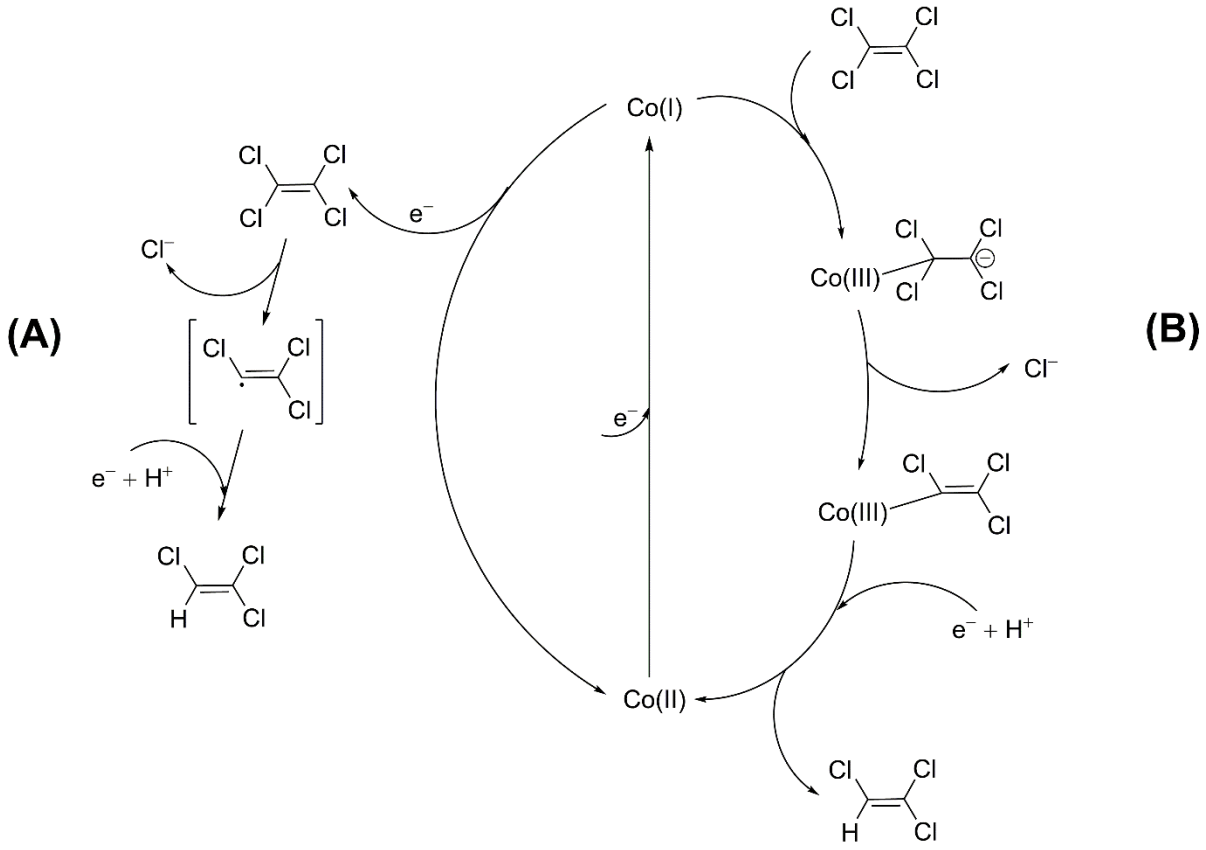

Figure 2.3 Catalytic cycle of PceA in reduction of PCE to TCE. **A)** electron transfer mechanism, **B)** nucleophilic alkylation mechanism. Adapted from Schubert and Diekert.[6]

The enzyme PceA has also been previously studied by indirect electrochemistry,[20] using a graphite working electrode and methyl viologen as an electron mediator. The work also identified other electron mediators that could drive dehalogenation by PceA: cobaltocene (Cc^+/Cc^0, E = -0.93 V vs SHE), and doubly reduced benzyl viologen (BV^+/BV^0, E = -0.62 V). Note that singly reduced benzyl viologen was unable to reduce PceA in solution assays. Almost all of the contribution to the current was from PceA adsorbed onto

the electrode rather than the free enzyme in solution, although direct electron transfer was not observed.

The isolated Co-containing cofactor and its derivatives also has catalytic properties.[21] Cyanocobalamin, as well as the heat-inactivated PceA, showed some activity for conversion of other halogenated organic molecules, but not PCE or TCE. Other workers have adsorbed a cobalamin derivative onto TiO_2, and used that system for light-driven dehalogenation, such as for conversion of benzotrichloride to methyl benzoate,[22] phenethyl bromide to ethyl benzene,[23] and radical 1,2 migration of the phenyl group in diethyl 2-bromomethyl-2-phenylmalonate.[24]

2.1.3 Aims of this chapter

In this chapter, light-driven electrocatalysis by PceA is investigated, using TiO_2 as a light absorber as shown in Figure 2.4, for the conversion of PCE to TCE then *c*DCE. Since the reaction is exergonic, as mentioned in Section 2.1.1, solar energy is not stored, but instead used to overcome the activation barrier.[25] This process can be convoluted by the fact that PCE and TCE can undergo photooxidative decomposition on the bare TiO_2 surface. Trichloroethene (TCE) has been used as a model compound to study photocatalytic oxidation on TiO_2.[26-28] In the presence of molecular oxygen, the photogenerated electrons and holes in TiO_2 can generate reactive oxygen species such as hydroxyl radical and atomic oxygen on the TiO_2 surface. These reactive oxygen species can then oxidize TCE that is adsorbed on TiO_2 through a complicated series of pathways, producing a mixture of products including $COCl_2$ (phosgene), CO, CO_2, HCl, and $CHCl_3$.

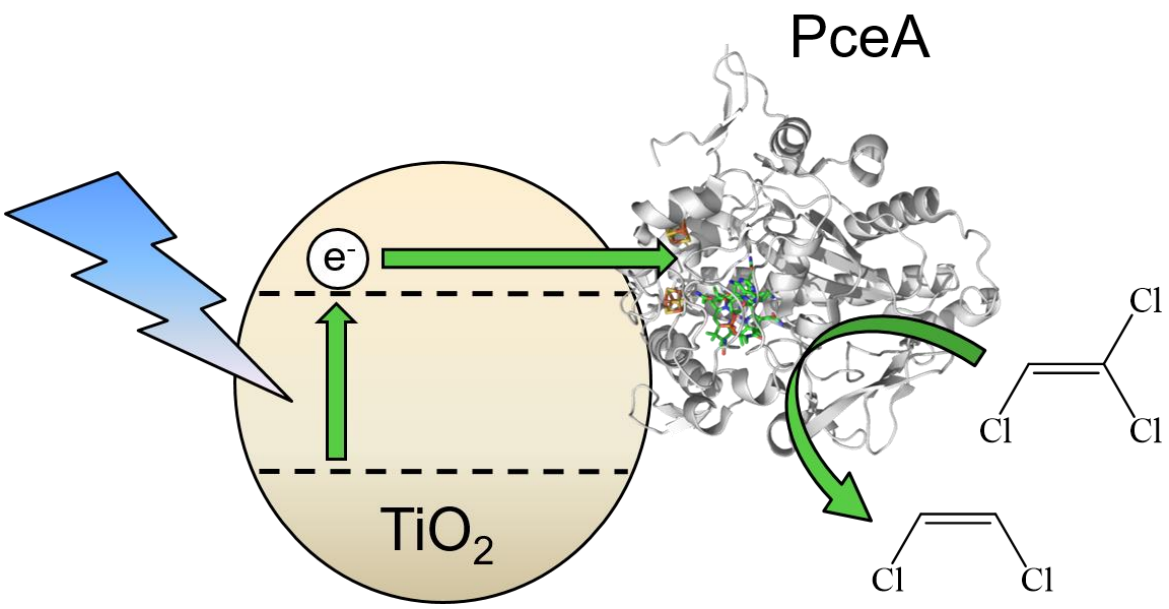

Figure 2.4. Scheme of light-driven enzymatic dehalogenation by PceA adsorbed onto TiO_2 particles. Band gap excitation of TiO_2 generates electrons in its conduction band, which is then directly injected into PceA enabling reduction of PCE and TCE. The holes in the valence band of TiO_2 oxidize a sacrificial electron donor (Tris buffer in this case).

By carrying out all experiments under anaerobic conditions, the PCE and TCE conversion pathways should be *via* the enzyme alone, and not from reactive oxygen species produced on the TiO_2 surface. The TiO_2 particles generate electron-hole pairs under UV illumination, and the electrons can be transferred to PceA adsorbed onto the TiO_2 surface. The holes are then consumed by a sacrificial electron donor in the solution, for example Tris buffer or ethanol that was used to dissolve the substrates. For electron transfer to occur from TiO_2 to PceA, the conduction band potential of TiO_2 (-0.60 V vs SHE at pH 7 for anatase TiO_2)[29,30] must be more negative than the entry points of electrons into PceA, which are the [4Fe-4S] centres.[31]

Towards this goal, the feasibility of direct electron transfer from an electrode (both pyrolytic graphite edge, PGE, and TiO_2) to PceA was first established. Furthermore, a colloidal system with PceA adsorbed onto TiO_2 particles was then examined under UV light

irradiation, and the light-driven conversion of PCE to TCE and *c*DCE quantified by GC-MS. Note that the enzymatic reaction(s) can be easily distinguished from the photodecomposition process on bare TiO_2, as PceA will give specific dehalogenated products (only TCE and *c*DCE), whereas decomposition of PCE by TiO_2 will give a complex mixture of products (see above), none of which are TCE or *c*DCE.

2.2 Results and discussion

2.2.1 Electrochemistry of PceA

The activity of PceA was examined on a PGE electrode (Figure 2.5); the electrode was abraded with sandpaper, then 1 µL of PceA solution (21 µM) was dropped onto the electrode surface, and left to adsorb for approximately 1 min. Cyclic voltammograms were measured, before and after injection of the substrate (TCE, 0.8 mM final concentration) into the cell. All electrochemical experiments were performed inside an anaerobic glovebox with a N_2 atmosphere (O_2 < 5 ppm). Due to their low solubility in water, all chlorinated compounds (PCE, TCE, *c*DCE) were first dissolved in a small amount of EtOH (typically 100 µL), before injection into the electrochemical cell at 0.11 V (See Chapter 6 Section 6.2.4 for more experimental details). All buffer solutions (Tris, pH 6.0 – 8.0) contained a small amount of $(NH_4)_2SO_4$ (4 mM) as it was shown to increase the activity of PceA although the reason remains unclear.[32]

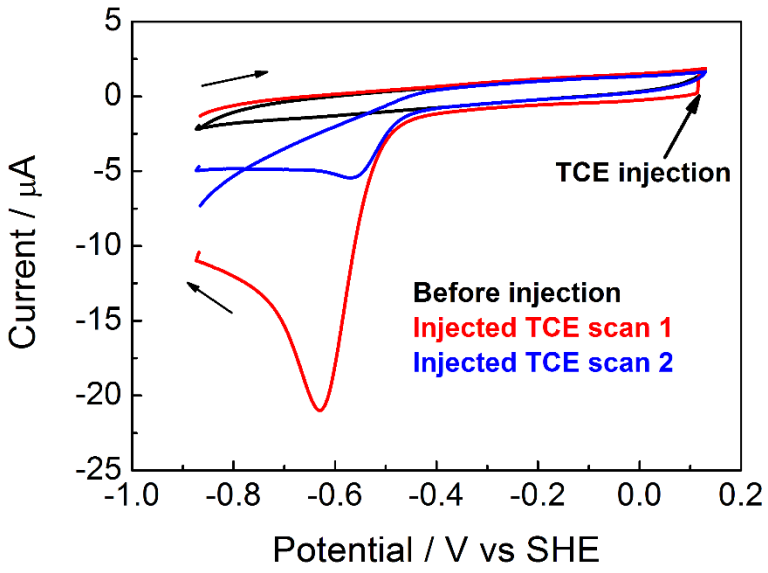

Figure 2.5 Cyclic voltammograms of PceA on a pyrolytic graphite 'edge' (PGE) electrode, before (black) and after injection (red and blue) of trichloroethene (TCE) to 0.8 mM final concentration. Reaction conditions: Tris buffer 0.1 M, pH 7.0, 25 °C, scan rate 20 mV/s, stationary electrode.

In the presence of TCE (0.8 mM), the PceA-loaded electrode showed a strong reductive current with an onset potential of *ca*. -0.42 V *vs.* SHE (pH 7, Figure 2.5). On a blank PGE electrode control experiment with no PceA no reductive current could be observed with the injection of either PCE, TCE nor *c*DCE under the same conditions as those shown in Figure 2.5, indicating that these organohalides are not reduced by bare PGE in the potential range -0.9 – 0.1 V *vs* SHE (data not shown). These results confirm that the reductive current observed in Figure 2.5 is due to enzymatic dehalogenation of TCE by PceA. On the second scan, the reduction current is significantly reduced, which is attributed to the volatile nature of the substrate and to a lesser extent, loss of the enzyme film. The decrease in current cannot be due to consumption of the substrate, as the amount of charge passed during the reductive scan is insignificant compared to the starting amount of substrate. The dehalogenation of TCE to cDCE by PceA was irreversible, as there were no oxidation currents observed, neither from oxidation of *c*DCE produced during the reductive scan, or from direct injection of *c*DCE into the cell.

The catalytic reduction current onset potential was approximately -0.42 V vs SHE at pH 7, slightly more negative than the spectrocopically-derived reduction potential of the cofactor Co(II)/Co(I) (-0.38 V vs SHE at pH 7.5).[18] This suggests that the [4Fe-4S] that is the initial electron entry point possesses a more negative reduction potential than the norspeudo-B_{12} active site, leading to a lack of activity for the reverse reaction. This result agrees with the results from solution assays with an electron mediator, where the mediators that could reduce PceA were reduced methyl viologen (MV^{2+}/MV^{+}, E = -0.44 V vs SHE), cobaltocene (Cc^{+}/Cc^{0}, E = -0.93 V), and doubly reduced benzyl viologen (BV^{+}/BV^{0}, E = -0.62 V). A mediator with a higher potential, singly reduced benzyl viologen ($BV^{2+/}BV^{+}$, E = -0.36 V), was unable to reduce PceA.[16]

No non-turnover peaks were observed in the absence of substrate. However, the TOF of the enzyme can be estimated from the amount of enzyme drop-casted onto the electrode, and the catalytic current: a TOF of 5 per enzyme molecule per second was achieved. As not all enzyme molecules would be adsorbed onto the electrode in an electroactive configuration, this TOF is an underestimate. For comparison, the TOF from solution assays using reduced methyl viologen[9] was ca. 90 s^{-1}.

The dehalogenation of TCE terminates at *c*DCE, as measured by solution assays,[32] and can now be confirmed by electrochemistry (Figure 2.6). After injection of *c*DCE into the cell, no reductive current was observed, indicating that *c*DCE is not a substrate for PceA.

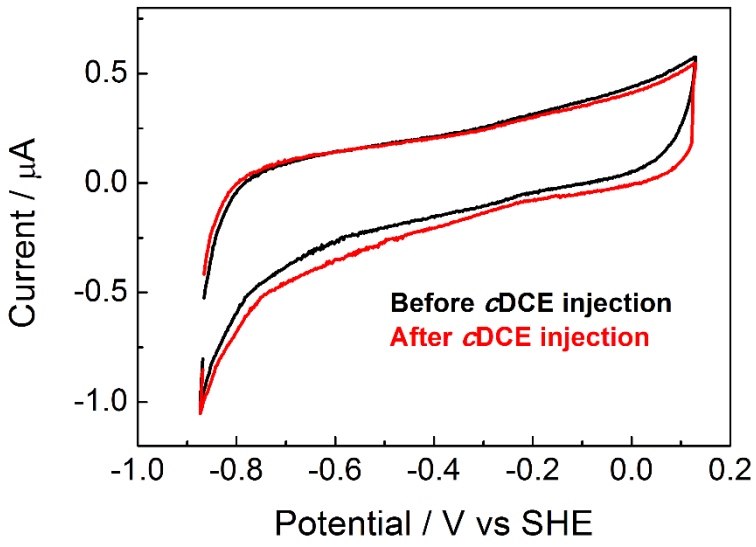

Figure 2.6 Cyclic voltammograms of PceA on a PGE electrode, before and after injection of *c*DCE to 0.8 mM final concentration. Reaction conditions: Tris buffer 0.1 M, pH 7.0, 25 °C, scan rate 20 mV/s, stationary electrode.

The activity of the isolated norspeudo-B_{12} cofactor was also tested on PGE electrodes (work carried out by Shams T. A. Islam, DPhil candidate, University of Oxford, Department of Chemistry, data not shown), but the cofactor alone did not reduce either PCE or TCE. This agrees with results from solution assays,[21] in which heat-inactivated PceA lost the

ability to reduce PCE or TCE, but gained the ability to reduce a variety of other alkyl halides. This was interpreted as the effect of the protein scaffold in restricting access to the norpseudo-B_{12} active site as compared to the heat-inactivated samples where the norspseudo-B_{12} was released from the protein.

The activity of PceA was next measured on TiO_2 electrodes. The TiO_2 electrodes were fabricated by loading TiO_2 particles onto conductive glass slides using the doctor's blade method (see Chapter 6 Section 6.2.3 for more experimental details), and PceA was drop-casted onto the electrodes in a similar manner to PGE electrodes. Figure 2.7 shows cyclic voltammograms of PceA-adsorbed TiO_2 electrodes. The blank TiO_2 electrode shows a distinctive "trumpet-like" shape,[29] due to the reduction and oxidation of Ti^{3+} in the lattice. After adsorption of PceA, the voltammogram remains unchanged, hence no non-turnover peaks were observed.

After injection of TCE (0.8 mM final concentration) into the cell, a catalytic reduction current was observed in the pH range 6.0 – 8.0 in all cases (Figure 2.7A-C). To observe the current from TCE reduction alone, the measured current was subtracted by the current of the blank TiO_2 electrode (Figure 2.7D). One feature that is immediately clear is the difference in the onset potential of the reduction current between the cases of TiO_2 and PGE electrodes (compare Figures 2.5 and 2.7). In the case of TiO_2 electrodes, the onset potential is not only a function of the reduction potential of the electron entry point in PceA, but also of the flat-band potential of TiO_2. This can be seen in the negative shift of the onset potential with increasing pH (Figure 2.7D), which is the expected behavior of the flat-band potential of TiO_2. For an ideal n-type semiconductor electrode in the dark, when the potential is taken below its flat-band potential, the electrode behaves like a conductive material. This also means that at potentials higher than the flat-band potential, the electron density is low and TiO_2 behaves more like an insulator, and therefore no electron transfer occurrs to PceA.

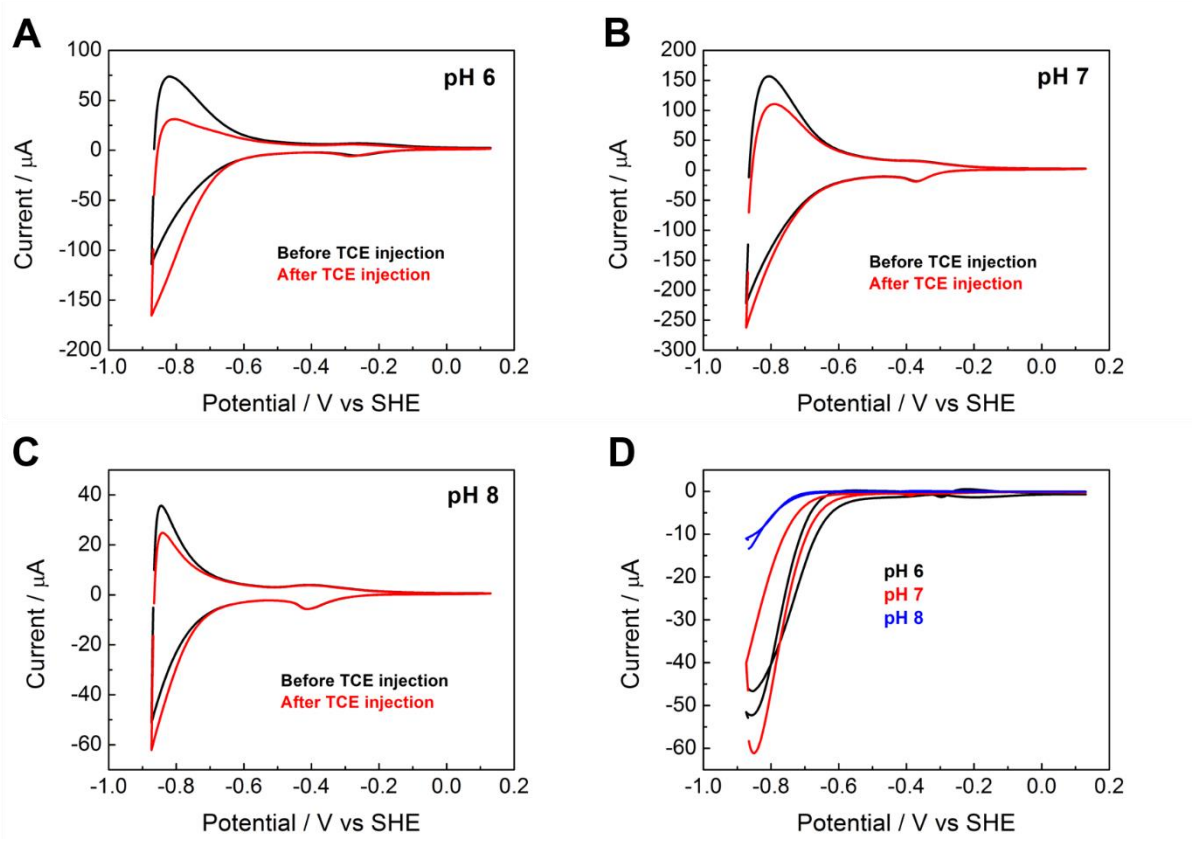

Figure 2.7 Cyclic voltammograms of PceA adsorbed on a TiO_2 electrode, at pH **A)** 6.0, **B)** 7.0 and **C)** 8.0 with the current before (black line) and after (red line) injection of TCE (final concentration 0.8 mM). **D)** The blank-subtracted voltammograms at pH 6.0 – 8.0. Reaction conditions: Tris buffer 0.1 M, 25 °C, scan rate 20 mV/s, stationary electrode, no gas flow.

In similar experiments, using PCE (0.8 mM) as the substrate instead of TCE (Figure 2.8), catalytic reduction currents were also observed. In this case, the reduction current has contributions from both PCE reduction as well as further reduction of the TCE product that still remain near the electrode surface due to mass transport limitation at the stationary electrode. As in the case of PGE electrodes, control experiments with no enzyme confirmed that neither PCE or TCE were reduced on TiO_2 electrodes (data not shown); the observed reduction current is therefore due to the enzyme catalysis of PceA. Taken together, the data described show that PceA can receive electrons directly from TiO_2 and use the electrons in the reductive dehalogenation of TCE and PCE.

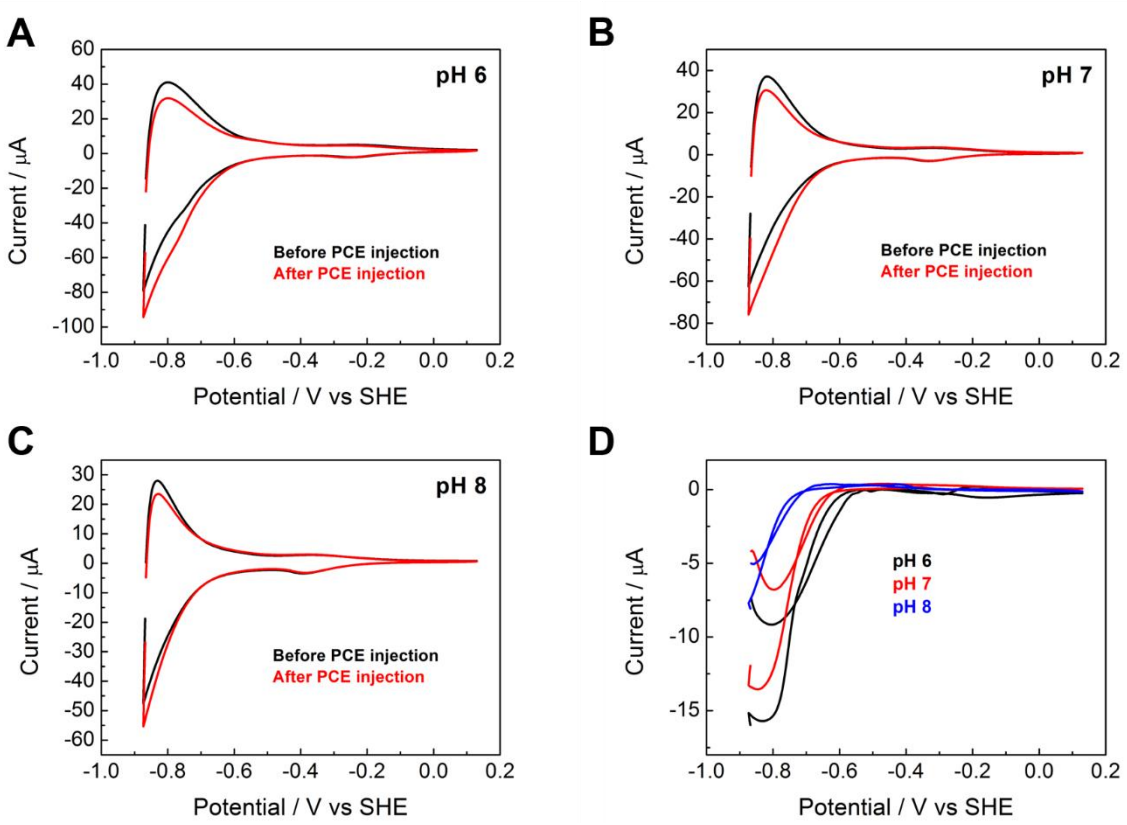

Figure 2.8 Cyclic voltammograms of PceA adsorbed on a TiO_2 electrode, at pH **A)** 6.0, **B)** 7.0 and **C)** 8.0, with the current before (black line) and after (red line) injection of PCE (final concentration 0.8 mM). **D)** The blank-subtracted voltammograms at pH 6.0 – 8.0. Reaction conditions: Tris buffer 0.1 M, 25 °C, scan rate 20 mV/s, stationary electrode, no gas flow.

2.2.2 Light-driven reduction of tetrachloroethylene (PCE) and trichloroethylene (TCE) by PceA adsorbed on TiO_2 particles

Having established direct electron transfer from a TiO_2 electrode to PceA (in Section 2.2.1), this principle was utilised in the assembly of a PceA-TiO_2 particulate system in order to allow for the investigation of light-driven dehalogenation. The extent of PceA adsorption onto TiO_2 particles was measured indirectly by UV-vis spectroscopy (Figure 2.9): The absorbance of PceA solution was first measured (0.1 μM was used here because at lower concentrations the PceA absorbance was too low to be observed clearly by UV-spectrometry) then stirred with TiO_2 particles (P25, 1 mg/mL) for 20 mins, followed by centrifugation to remove the TiO_2 particles. The absorbance of the supernatant solution was then measured for direct comparison to the solution before stirring with TiO_2. The absorbance at around 280 nm attributed to the enzyme's peptide bonds and aromatic residues almost completely disappeared after stirring with TiO_2, confirming that PceA had been adsorbed onto TiO_2 particles. In all subsequent photochemical reactions the PceA concentration used for adsorption on TiO_2, maintaining all other conditions constant, was lower (at 0.02 μM), and it could therefore be assumed that PceA adsorption on TiO_2 particles was complete.

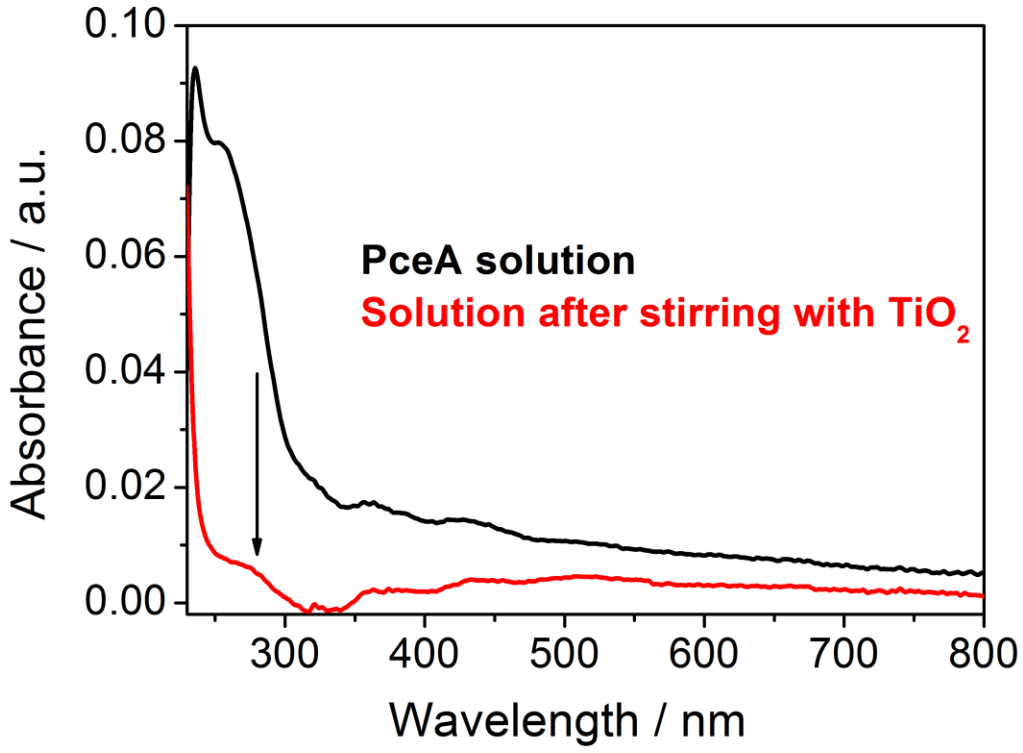

Figure 2.9 UV-vis absorbance of PceA (0.1 μM) in Tris buffer pH 7, before and after stirring with TiO_2 particles (1 mg/mL) for 20 min.

Light-driven reductive dehalogenation was demonstrated in the particulate system. PceA was adsorbed onto TiO_2 particles by simply stirring in buffer solution, as demonstrated previously. Under UV irradiation, TiO_2 can generate electron-hole pairs. The electrons can be transferred to PceA to drive reductive dehalogenation while the holes can be consumed by a sacrificial reagent (Tris buffer). Initial experiments used a rubber septum to seal the reaction vial, which led to inconsistent results since the rubber septa absorbed the substrates PCE and TCE. All subsequent experiments therefore used a Teflon cap to seal the reaction vial.

In a typical experiment, a solution of PceA (0.17 nmol) in 8 mL of Tris buffer (Tris 100 mM, pH 7.0), was mixed with TiO_2 particles (P25, 8 mg) and the suspension was placed

in a vial and sealed tightly with a Teflon cap. A solution of the substrate, (either PCE or trichloroethene TCE dissolved in ethanol), was injected into the suspension before sealing the vial and commencing irradiation with a UV lamp (365 nm, 8 W, 1.5 cm distance). Small aliquots (0.5 mL) of the solution were sampled periodically by syringe extraction through the Teflon seal then transferred to a sample vial, and the product was detected and quantified by GC-MS headspace analysis, where the sample vial was heated to increase the vapor pressure of the chlorinated compounds, then a sample of the headspace was injected into the GC (see details in Chapter 6 Section 6.2.7). The temperature of the suspension increased by 5-6 ºC (typical values being 24 ºC to 30 ºC) over 4 h of irradiation.

A typical chromatogram of a GC-MS headspace sample is shown in Appendix 1, as well as the obtained mass spectrum of each compound (PCE, TCE, and *c*DCE) compared to mass spectra from a database. The program Agilent MassHunter Qualitative Analysis (ver. B.06.00) was used to analyze the GC-MS data, and the mass spectra database was NIST Mass Spectral Search Program (ver. 2.0). The retention times for PCE, TCE, and *c*DCE were 6.6, 4.4, and 2.9 minutes, respectively. In the mass spectra, the isotope effect from the mass of chlorine can be observed. The two main isotopes of chlorine are ^{35}Cl and ^{37}Cl, with natural abundances of 75.77 % and 24.23 %, respectively.[33] As an example, *c*DCE has 2 Cl atoms, both of which could be either ^{35}Cl or ^{37}Cl, and therefore we would expect to observe masses of 96 (for 2 ^{35}Cl), 98 (for a ^{35}Cl and a ^{37}Cl), and 100 (for 2 ^{37}Cl). The ratio of these different masses is expected to be 1 : 0.64 : 0.10, calculated from the natural abundances of Cl, and the experimentally measured ratio was approximately 1 : 0.62 : 0.09.

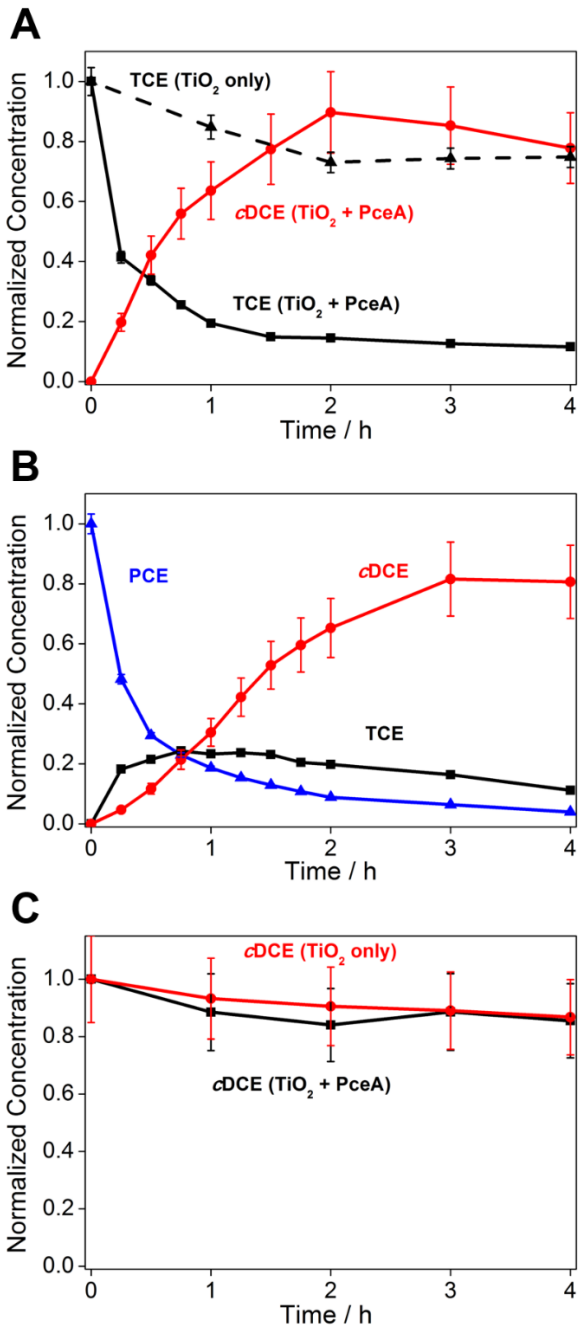

Figure 2.10 Enzymatic reductive dechlorination by UV irradiation of TiO_2-PceA. **A)** Time courses of the change in concentrations of trichloroethene (TCE, initial concentration 0.55 mM, solid black line) and cis-1,2-dichloroethene (*c*DCE, red line) in sealed, aqueous TiO2-PceA suspensions under UV irradiation. The control reaction (TiO_2 particles in the absence of PceA) is shown in dashed black line; no *c*DCE was detected in the control. **B)** A similar set up, but starting with tetrachloroethene (PCE, blue line) in solution at 0.26 mM. Normalized concentrations of TCE and cDCE are shown as black and red lines, respectively. In the control reaction without enzyme (not shown), neither TCE nor cDCE could be detected. **C)** A similar setup, but starting with cDCE (0.8 mM), with PceA (black line) and without (red line). The error bars are estimations of systematic errors involving sampling and GC-MS calibrations. Reaction vial was closed and continuously stirred inside an anaerobic glovebox at room temperature.

Figure 2.10A shows the consumption of TCE and concurrent production of *c*DCE by PceA-TiO_2 under UV illumination. The decrease in activity after approximately 2 hours varied in extent from one experiment to another but is likely due to slow enzyme deactivation caused by oxidative damage from the valence-band holes. Control experiments with TiO_2 but no PceA (dashed line in Figure 2.10A) showed a much smaller decrease in TCE concentration after 4 h and no *c*DCE was detected. This slow decrease is due to decomposition of TCE on TiO_2 as well as possible losses during sampling. Photocatalysis of TCE on bare TiO_2 does not produce *c*DCE,[26] and PceA is required for the specific reduction of TCE to *c*DCE to occur. A similar PceA-TiO_2 experiment was carried out with PCE as substrate (Figure 2.10B): Production of both TCE and *c*DCE was observed after irradiation, with the TCE concentration reaching a maximum value after approximately 0.75 h, before decreasing due to conversion to *c*DCE.

From the electrochemical measurements discussed in Section 2.2.1, *c*DCE is not expected to be converted further by PceA - as confirmed by particulate experiments shown in Figure 2.10C. The concentration of *c*DCE decreased slightly over time, but there was no difference in the cases with and without PceA. This slow decrease is probably due to decomposition of *c*DCE on the bare TiO_2 surface or losses through sampling. Together, this set of results demonstrates light-driven sequential conversion of PCE to TCE and then *c*DCE by PceA.

From the molecular mass of PceA based on crystallography (52.3 kDa calculated for a monomer)[9] and the maximum product concentration obtained, the turnover number (TON) is estimated at 18,000 per enzyme active site for *c*DCE production after 4 h, and an average turnover frequency (TOF) of 2.4 s^{-1} (per enzyme active site). Both TON and TOF are underestimates of their true values, because not all enzyme molecules are likely to be adsorbed onto TiO_2 in an electroactive configuration, and the product *c*DCE is slowly

decomposed on bare TiO_2. The TOF from the photochemical experiments is an order of magnitude lower than the TOF value (ca. 90 s^{-1}) measured by a chemical assay using reduced methyl viologen.[9] This result could be due to the relative lack of access of electrons to the electron entry point as compared to soluble electron mediators, as well as the small driving force which is determined by the conduction band level of TiO_2.

Due to the limitation of using UV light irradiation with TiO_2, owing to its large bandgap of 3.0 eV, an attempt was made to see if visible light could be utilized in a light-driven dehalogenation system; the TiO_2 nanoparticles were modified with a Ru-based dye [$(Ru(bpy)_2(4,4\text{-}(PO_3H_2)_2bpy))Br_2$ (bpy = 2,2-bipyridine)] as used in previous systems with CODH or flavocytochrome c_3.[34,35] Upon visible light irradiation (λ >420 nm), the dye-TiO_2-PceA system was able to convert TCE to *c*DCE as shown in Figure 2.11, although at a much lower rate. This is probably due to the lower amount of available electrons in TiO_2, possibly from the Tris buffer being a less effective sacrificial electron donor compared to MES or triethanolamine (TEOA) used in previous studies.[35,36]

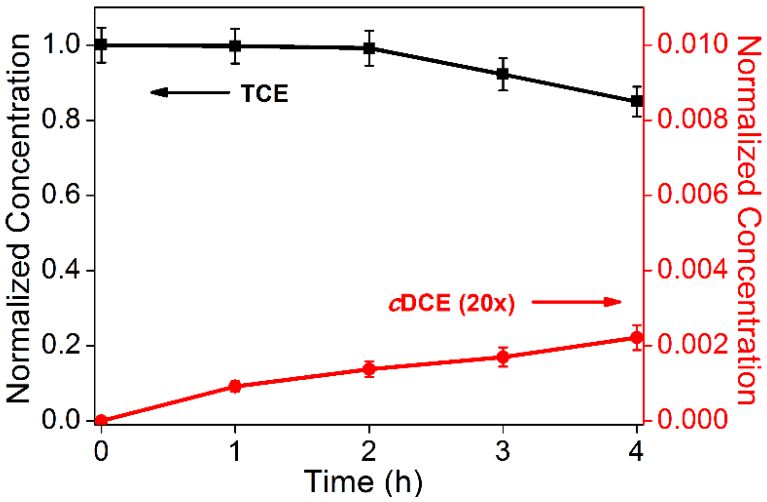

Figure 2.11 Time course of concentrations of TCE (black line, left axis) and *c*DCE (red line, magnified 20 times, right axis) for a Ru dye-TiO_2-PceA system under visible light irradiation (λ > 420 nm) with a starting TCE concentration of 0.55 mM.

2.3 Conclusions and perspectives

Previous studies have extensively characterized the activity of PceA by conventional solution assays, and this work is the first demonstration of the direct electrochemistry of PceA. Protein film electrochemistry provides a facile method to assess possible substrates and inhibitors of an enzyme. In this chapter, the data presented provide electrochemical confirmation that PCE and TCE are substrates of PceA, and that the reaction(s) terminate at *c*DCE. The onset of reduction current (-0.42 V *vs* SHE) was in agreement with the range of electron mediators that were able to reduce PceA in solution assays.

Furthermore, it has been shown that PceA is able to receive electrons directly from a TiO_2 electrode and is active in the pH range 6.0–8.0. This result, in conjunction with quantification of PceA adsorption onto TiO_2 by UV-vis spectroscopy, indicates the feasibility of a PceA-TiO_2 particulate system. Previous work with TiO_2 were accomplished with hydrogenases,[37] carbonmonoxide dehydrogenase,[35] and flavocytochrome c_3,[34] and the work presented herein extends the field into reductive dehalogenases and further demonstrates the versatility of TiO_2 in acting as an electron donor for a large variety of enzymes.

Reductive dehalogenation by PceA was achieved using TiO_2 particles as electron donors under UV light irradiation. Although it is possible to photo-oxidize PCE and TCE on bare TiO_2, this non-enzymatic pathway was minimized by carrying out all experiments in an anaerobic glovebox, thus avoiding creation of reactive oxygen species. No TCE nor *c*DCE were detected in control runs without PceA, and even though the substrates and products slowly decreased over time, mainly due to their volatility, the activity of PceA was clear.

Although practical environmental remediation using this TiO_2-PceA system may be limited, as the enzyme only works under strictly anaerobic conditions, it serves to demonstrate a new solar-to-chemicals route. More specifically, it showed that electron transfer from an inorganic material to an enzyme is not just an isolated phenomenon limited to a few enzymes, and that production of specific chemicals from solar energy is possible given the appropriate light absorber and catalyst.

2.4 References

(1) *Toxicological Review of Trichloroethylene*, U.S. Environmental Protection Agency, 2011.

(2) Gribble, G. W. *Chemosphere* **2003**, *52*, 289.

(3) Wagner, C.; El Omari, M.; König, G. M. *Journal of Natural Products* **2009**, *72*, 540.

(4) Breivik, K.; Alcock, R.; Li, Y.-F.; Bailey, R. E.; Fiedler, H.; Pacyna, J. M. *Environmental Pollution* **2004**, *128*, 3.

(5) Holliger, C.; Wohlfarth, G.; Diekert, G. *Fems Microbiology Reviews* **1998**, *22*, 383.

(6) Schubert, T.; Diekert, G. In *Organohalide-Respiring Bacteria*; Adrian, L., Löffler, F. E., Eds.; Springer Berlin Heidelberg: Berlin, Heidelberg, 2016, p 397.

(7) Jugder, B.-E.; Ertan, H.; Bohl, S.; Lee, M.; Marquis, C. P.; Manefield, M. *Frontiers in Microbiology* **2016**, *7*.

(8) John, M.; Schmitz, R. P.; Westermann, M.; Richter, W.; Diekert, G. *Arch Microbiol* **2006**, *186*, 99.

(9) Bommer, M.; Kunze, C.; Fesseler, J.; Schubert, T.; Diekert, G.; Dobbek, H. *Science* **2014**.

(10) Schumacher, W.; Holliger, C. *Journal of Bacteriology* **1996**, *178*, 2328.

(11) DeWeerd, K. A.; Mandelco, L.; Tanner, R. S.; Woese, C. R.; Suflita, J. M. *Archives of Microbiology* **1990**, *154*, 23.

(12) Aulenta, F.; Canosa, A.; Reale, P.; Rossetti, S.; Panero, S.; Majone, M. *Biotechnology and Bioengineering* **2009**, *103*, 85.

(13) Aulenta, F.; Tocca, L.; Verdini, R.; Reale, P.; Majone, M. *Environmental Science & Technology* **2011**, *45*, 8444.

(14) Page, C. C.; Moser, C. C.; Chen, X.; Dutton, P. L. *Nature* **1999**, *402*, 47.

(15) Neumann, A.; Scholz-Muramatsu, H.; Diekert, G. *Arch Microbiol* **1994**, *162*, 295.

(16) Neumann, A.; Wohlfarth, G.; Diekert, G. *Archives of Microbiology* **1995**, *163*, 276.

(17) Vogel, T. M.; Criddle, C. S.; McCarty, P. L. *Environmental Science & Technology* **1987**, *21*, 722.

(18) Kräutler, B.; Fieber, W.; Ostermann, S.; Fasching, M.; Ongania, K.-H.; Gruber, K.; Kratky, C.; Mikl, C.; Siebert, A.; Diekert, G. *Helvetica Chimica Acta* **2003**, *86*, 3698.

(19) Schumacher, W.; Holliger, C.; Zehnder, A. J. B.; Hagen, W. R. *FEBS Letters* **1997**, *409*, 421.

(20) Diekert, G.; Gugova, D.; Limoges, B.; Robert, M.; Saveant, J. M. *J Am Chem Soc* **2005**, *127*, 13583.

(21) Neumann, A.; Siebert, A.; Trescher, T.; Reinhardt, S.; Wohlfarth, G.; Diekert, G. *Archives of Microbiology* **2002**, *177*, 420.

(22) Shimakoshi, H.; Hisaeda, Y. *Angewandte Chemie International Edition* **2015**, *54*, 15439.

(23) Hisashi, S.; Emiko, S.; Kenji, K.; Yoshio, H. *Chemistry Letters* **2009**, *38*, 468.

(24) Shimakoshi, H.; Abiru, M.; Izumi, S.-i.; Hisaeda, Y. *Chemical Communications* **2009**, 6427.

(25) Osterloh, F. E. *ACS Energy Letters* **2017**, *2*, 445.

(26) Fan, J.; Yates, J. T. *Journal of the American Chemical Society* **1996**, *118*, 4686.

(27) Driessen, M. D.; Goodman, A. L.; Miller, T. M.; Zaharias, G. A.; Grassian, V. H. *The Journal of Physical Chemistry B* **1998**, *102*, 549.

(28) Joung, S.-K.; Amemiya, T.; Murabayashi, M.; Itoh, K. *Chemistry - A European Journal* **2006**, *12*, 5526.

(29) Kavan, L.; Grätzel, M.; Gilbert, S. E.; Klemenz, C.; Scheel, H. J. *Journal of the American Chemical Society* **1996**, *118*, 6716.

(30) Burnside, S.; Moser, J.-E.; Brooks, K.; Grätzel, M.; Cahen, D. *The Journal of Physical Chemistry B* **1999**, *103*, 9328.

(31) Hexter, S. V.; Esterle, T. F.; Armstrong, F. A. *Physical Chemistry Chemical Physics* **2014**, *16*, 11822.

(32) Neumann, A.; Wohlfarth, G.; Diekert, G. *Journal of Biological Chemistry* **1996**, *271*, 16515.

(33) Lide, D. R. *CRC Handbook of Chemistry and Physics*; 77th ed.; CRC Press, 1996.

(34) Bachmeier, A.; Armstrong, F. *Current Opinion in Chemical Biology* **2015**, *25*, 141.

(35) Woolerton, T. W.; Sheard, S.; Reisner, E.; Pierce, E.; Ragsdale, S. W.; Armstrong, F. A. *Journal of the American Chemical Society* **2010**, *132*, 2132.

(36) Reisner, E.; Powell, D. J.; Cavazza, C.; Fontecilla-Camps, J. C.; Armstrong, F. A. *Journal of the American Chemical Society* **2009**, *131*, 18457.

(37) Armstrong, F. A.; Belsey, N. A.; Cracknell, J. A.; Goldet, G.; Parkin, A.; Reisner, E.; Vincent, K. A.; Wait, A. F. *Chemical Society Reviews* **2009**, *38*, 36.

Chapter 3

Electrochemistry of

ferredoxin-$NADP^+$ reductase (FNR)

Chapter 3

Electrochemistry of ferredoxin-$NADP^+$ reductase (FNR)

Abstract

Ferredoxin-$NADP^+$ reductase (FNR) is an enzyme that catalyses the reduction of $NADP^+$ to NADPH, using electrons supplied by ferredoxin. On a graphite electrode, FNR was inactive, possibly due to dissociation of the FAD group. However, on a conductive oxide surface such as indium tin oxide (ITO), FNR was able to bind in an electroactive configuration with coverage of over 500 pmol cm^{-2} (or 100 monolayer equivalents). This ability to construct an FNR@ITO electrode has allowed, for the first time, detailed investigation of the properties of FNR by direct electrochemistry *i.e.* without a requirement for mediators. Under non-turnover conditions, FNR coverage and potential, and their pH dependence were measured. In the presence of its substrate, $NADP^+$, FNR catalysed the reversible interconversion of $NADP^+$ and NADPH, and kinetic properties such as K_M and turnover frequency were determined. The ITO electrode could also be fabricated on a rotatable pyrolytic graphite edge (PGE) support, thus enabling an electrochemical investigation of FNR under hydrodynamic conditions. This direct and controllable electrochemistry of FNR can be exploited, for potential use as a cofactor regeneration system coupled to enzyme-catalyzed organic synthesis.

3.1 Introduction

3.1.1 Ferredoxin-NADP$^+$ Reductase (FNR): Function

Ferredoxin-NADP$^+$ reductase (FNR, EC 1.18.1.2) is an FAD-containing enzyme found in chloroplasts.[1-3] Its role is to receive electrons from ferredoxin (Fd), which is at the end of the electron transport chain composed of two light harvesting units (Figure 3.1), and reduce NADP$^+$ to NADPH. The produced NADPH is then used in the Calvin cycle as reducing equivalents to drive CO_2 assimilation.

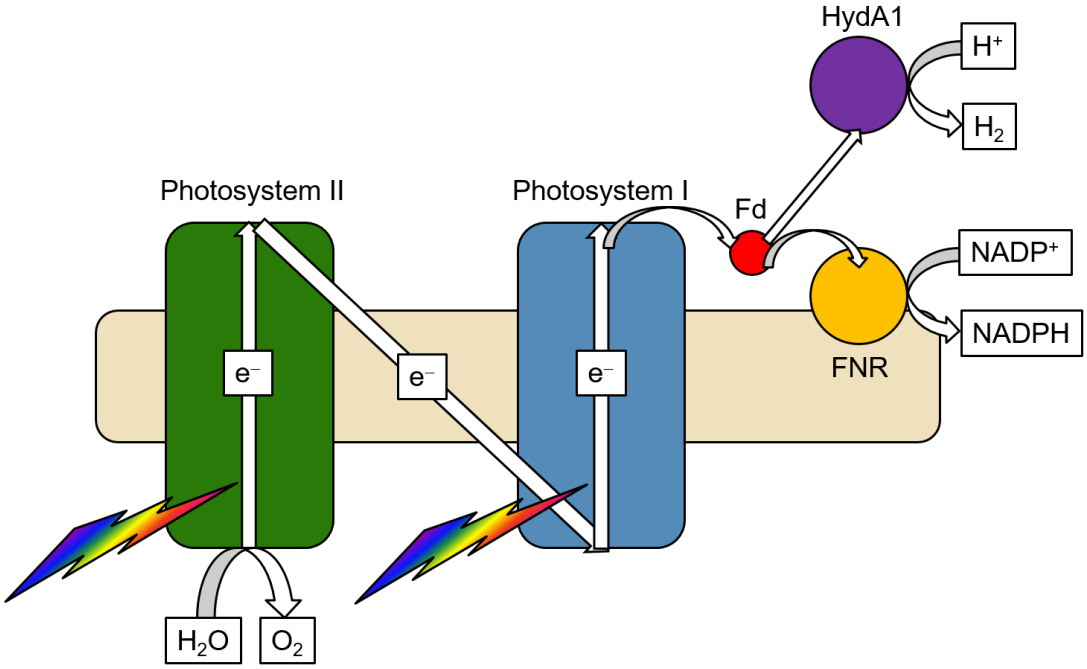

Figure 3.1 Diagram of the photosynthetic process, showing the role of FNR. Energetic electrons are generated in Photosystems I and II, and the electrons are transferred to ferredoxin (Fd), then subsequently to FNR. The electrons are replenished by water oxidation at Photosystem II. Ferredoxin can also supply electrons to other enzymes such as a hydrogenase (HydA1 in *Chlamydomonas reinhardtii*).

Reduction of NADP$^+$ is a 2-electron reaction, but ferredoxin is a 1-electron carrier. The reaction is possible because the FAD group can exist in 3 redox states: oxidized, semiquinone (1-electron reduced) and hydroquinone (2-electron reduced), therefore it can

act as an electron store, and the two ferredoxins must donate electrons in two separate events. The overall reaction is shown in Equation 1 below.

$$2\ Fd_{red} + NADP^+ + H^+ \overset{FNR}{\rightleftharpoons} 2\ Fd_{ox} + NADPH \qquad \text{(Eq. 1)}$$

The FNR used throughout this thesis was from C*hlamydomonas reinhardtii*, a single-cell green alga. (The recombinant enzyme was over-expressed in *Escherichia coli*, see details in Chapter 6 Section 6.2.2) In general, FNR found in chloroplasts and cyanobacteria (also called plastidic class) has a higher turnover rate for NADPH production compared to so-called bacterial class FNR.[4] These bacterial FNR usually operate in the reverse direction, providing reduced ferredoxin from NADPH, which is involved in processes such as nitrogen fixation and anaerobic metabolism. The electron flows of these processes are much slower than in photosynthesis, and this less demanding pathway may be the reason for the difference in rates.

Although it is not the focus of this thesis, the reduced ferredoxin generated by Photosystem I in *Chlamydomonas reinhardtii* can also deliver electrons to other enzymes, one of which is HydA1, an FeFe-hydrogenase (also shown in Figure 3.1). This pathway can be induced by sulfur deprivation,[5-7] which inhibits photosynthetic activity and induces expression of HydA1. Electrons are supplied to HydA1 from metabolism of starch, and also from ferredoxin reduced by Photosystem I. This is currently being studied as a method to produce renewable solar hydrogen.[8,9]

3.1.2 FNR: Structure and mechanism

Figure 3.2 shows the structure of FNR (from *Nostok sp.*, PDB 1GJR),[10] with FAD and $NADP^+$ also shown. Although the FNR used throughout this thesis was from

C*hlamydomonas reinhardtii*, its structure has not been published, but it can be expected that the structure from *Nostok sp.* would be similar due to its similar gene sequence.

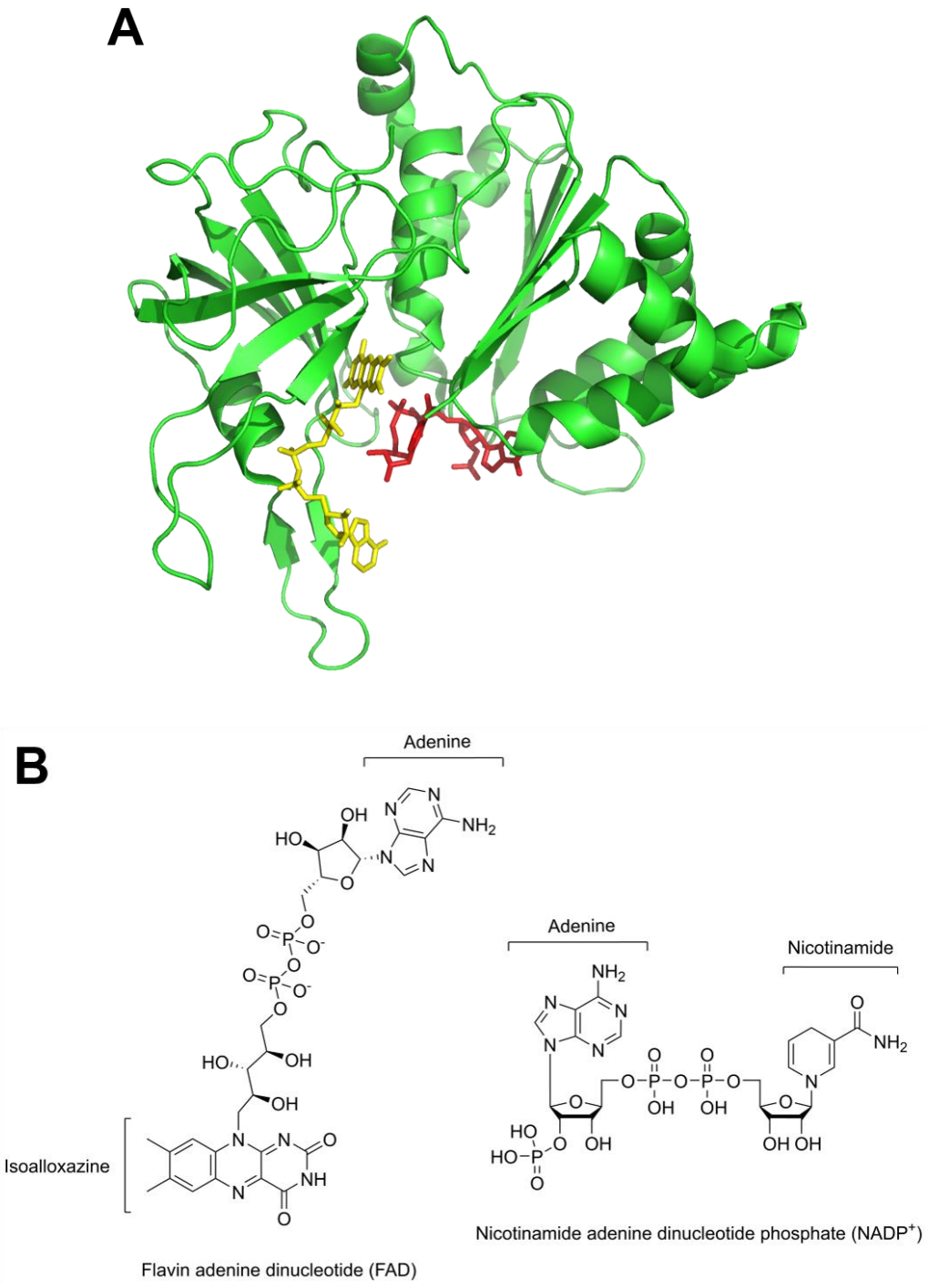

Figure 3.2 Structure of FNR (from *Nostok sp.*, PDB 1GJR), with the FAD group (yellow) and $NADP^+$ (red). The chemical structures of FAD and $NADP^+$ are shown below.

Although the difference between $NADP^+$ and NAD^+ is only a phosphate group on the ribose connected to the adenine, FNR is very specific for $NADP^+$ and not for NAD^+, in some cases with over 30,000-fold difference in specificity.[11] The binding of $NADP^+$ to FNR can be considered to involve two parts:[12] the nicotinamide part and the adenine part, each with its own corresponding binding cleft in FNR responsible for recognition. Positively charged residues (Arg, Lys) interact electrostatically to the negatively charged 2'-phosphate group on the ribose. For the nicotinamide moiety, however, the presence of a conserved C-terminal aromatic residue (Tyr) destabilizes its interaction with the isoalloxazine ring. The 2'-phosphate group interactions are sufficient to overcome the barrier in displacing the Tyr residue, therefore NAD^+ which lacks the phosphate group does not bind to FNR. Mutants in which the Tyr residue was replaced by site-directed mutagenesis with another aromatic group (Phe, Trp) still favoured $NADP^+$, while mutants with non-aromatic and small residues (Gly, Ser) showed enhanced activity for NAD^+.[11]

Figure 3.3 shows the structure of FNR in complex with both ferredoxin (Fd) and $NADP^+$, in which $NADP^+$ has been modeled into the Fd:FNR structure (PDB 1GAQ) using data obtained from another structure of FNR containing bound $NADP^+$ (PDB 1GJR), thus forming a ternary complex as implied by kinetic studies.[13] The interaction between FNR and ferredoxin arises mainly from electrostatic attractions:[14] ferredoxin is a negatively charged protein with a large excess of amino acids with acidic side chains and the contact surface of FNR is dominated by amino acids with basic side chains. The shortest distance between the [2Fe-2S] cluster of ferredoxin and the FAD group of FNR is approximately 6 Å, which allows rapid, direct electron transfer.[15] Besides ferredoxin, FNR can also conduct electron transfers with flavodoxin, as well as nonbiological electron mediators such as viologen or ferricyanide,[2] all of which are distinctly different in shape and structure from ferredoxin. This indicates that the FAD group in FNR is relatively accessible, thus making FNR

compatible with a wide range of redox partners, and the prospect of direct electron transfer from FNR to an electrode seems promising.

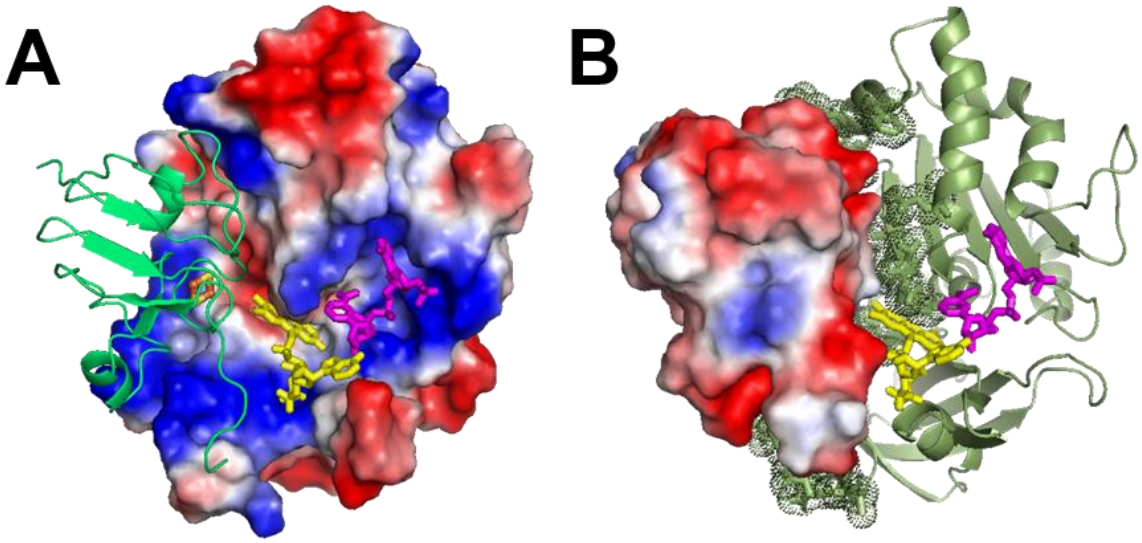

Figure 3.3 Structure of ferredoxin-$NADP^+$ reductase (FNR) complexed with ferredoxin (PDB 1GAQ). The position of bound $NADP^+$ was included within the same structure (Pymol) by aligning the ferredoxin:FNR complex (PDB 1GAQ) with the structure of FNR in complex with $NADP^+$ (PDB 1GJR); the protein structure from PDB 1GJR was then deleted to leave only the $NADP^+$ molecule in position within the ferredoxin:FNR complex. **A)** Projection in which FNR is shown as a charge-smoothed surface (red and blue represent positive and negative charges, respectively) and bound ferredoxin is shown in green, as cartoon main chain. **B)** Projection in which ferredoxin is shown as a charge-smoothed surface and FNR is shown as a cartoon main chain in green. In both projections, FAD is represented as yellow sticks, and $NADP^+$ is represented as mauve sticks.

The mechanism of FNR was investigated by Batie and Kamin[13,16-18] using rapid mixing and spectrophotometric assays. They proposed a mechanism involving a ternary complex as shown in Figure 3.4. First $NADP^+$ binds to FNR, then FNR is sequentially reduced by electrons from two molecules of reduced ferredoxin (Fd_{red}), one at a time. The reduced FNR then catalyses the two-electron reduction of $NADP^+$ to NADPH which is subsequently released. In the absence of $NADP^+$, the rate of electron transfer from Fd_{red} to FNR was slower than the overall rate, thus the ternary complex is implicated. Measurements

of the dissociation constants (K_d) showed that the binding of $NADP^+$ decreases the association of FNR and ferredoxin, and ferredoxin decreases the association of FNR and $NADP^+$, *i.e.* the binding of the two substrates show negative cooperativity. Although this may seem contradictory, it can be interpreted as product inhibition, *i.e.* the release of oxidized ferredoxin (Fd_{ox}) being the rate limiting step, and binding of $NADP^+$ facilitates the release of Fd_{ox} thus increasing the overall rate.

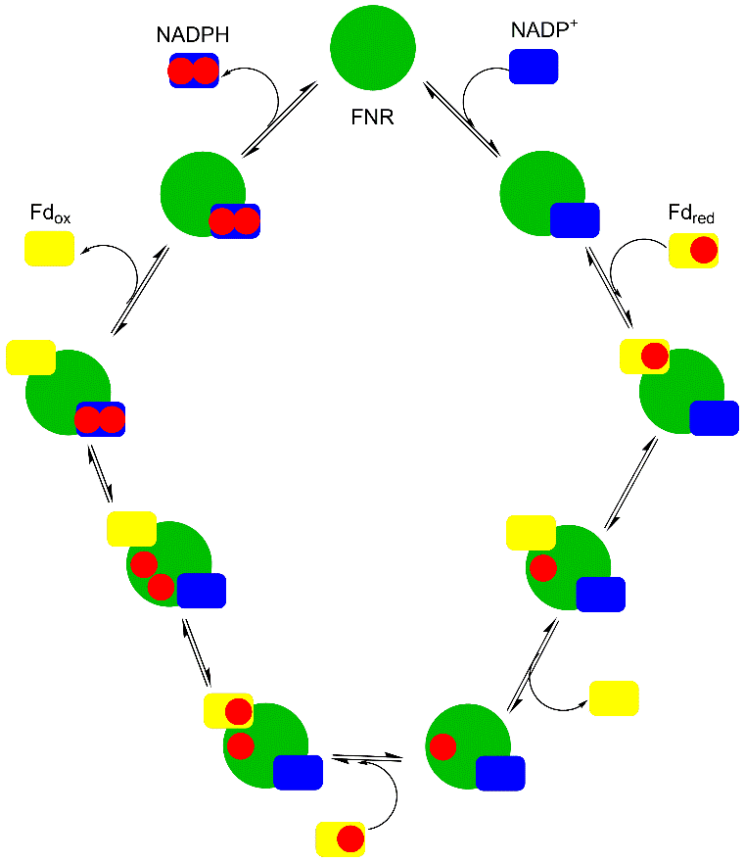

Figure 3.4 Catalytic cycle of FNR, adapted from Batie and Kamin,[13] with FNR (green), Fd (yellow), $NADP^+$ (blue) and electrons (red).

There are only a few reports of electrochemical investigation of FNR in literature, all of which involved indirect electrochemistry (*i.e.* using an electron mediator between the electrode and FNR). Madoz *et al*. used a gold electrode with ferrocenemethanol as the electron mediator[19] and observed an enhanced oxidation current when NADPH was added

to the cell solution (already containing FNR and ferrocenemethanol), thus demonstrating mediated NADPH oxidation by FNR. A similar experiment by de Lacey *et al*. used amino viologen derivatives as mediators,[20] but in this case the mediator was co-immobilized with FNR onto glassy carbon electrodes with cross-linked bovine serum albumin, and mediated $NADP^+$ reduction was observed. In later work, an Au electrode was used after modification with a self-assembled monolayer in which electron mediators were covalently attached.[21] The photosynthetic electron transport chain involving cytochrome c_6, Photosystem I, ferredoxin, and FNR was studied by cyclic voltammetry.[22] The working Au electrode was modified by a self-assembled monolayer of 3-mercapto-1-propanol which provided hydroxyl groups for favourable interaction with cytochrome c_6, and the chain of electron transfers culminating in $NADP^+$ reduction was observed under light irradiation. Incidentally, glutamate dehydrogenase was also put into the solution to consume the produced NADPH, in order to suppress the reverse reaction. Note that in the absence of any mediator, FNR was unable to receive electrons from the electrode.

3.1.3 Aims of this chapter

The aim of this work was to characterize FNR using, for the first time, direct electrochemical methods. This was made possible by the construction of a porous indium tin oxide (ITO) electrode, onto which FNR could be adsorbed, achieving direct electron transfer with the electrode. This allowed measurement of the reduction potential of FNR, as well as the extent of its binding to ITO as reflected in its electroactive coverage. Upon addition of $NADP^+$, the kinetic properties of FNR could also be measured.

3.2 Results and discussion

3.2.1 Electrochemical activity of FNR

First, the electrochemical activity of FNR was examined on a pyrolytic graphite edge (PGE) electrode, which is a typical electrode material used for protein film electrochemistry in the Armstrong group. A solution of FNR (1 µL, 200 µM) was drop-casted onto the surface of a freshly abraded PGE electrode, then the enzyme drop was left to adsorb (30 s – 3 min) taking care to ensure that the electrode did not completely dry out. Excess enzyme was removed by rinsing with milliQ water before putting the electrode into the cell solution. Electrochemical measurements were taken after purging the cell with Ar for at least 5 min to remove any dissolved O_2. The FNR itself is stable in air, but dissolved O_2 would give rise to a reduction current and interfere with the signal from FNR.

As shown in Figure 3.5A, the cyclic voltammogram of an FNR-loaded PGE electrode was indistinguishable from a blank PGE electrode. After injection of the substrate ($NADP^+$, 100 µM), no reduction current was observed. This result suggested that either FNR did not adsorb onto the PGE electrode, or it was adsorbed in an inactive configuration. This is probably due to the FAD group having an affinity for the graphite surface because of π-stacking, which could lead to dissociation of FAD from the enzyme, or the enzyme being adsorbed with the FAD group facing the graphite surface, thus limiting access to the substrate. A previous study on an FAD-containing flavohemoglobin[23] also reported that the enzyme was inactive on a graphite electrode.

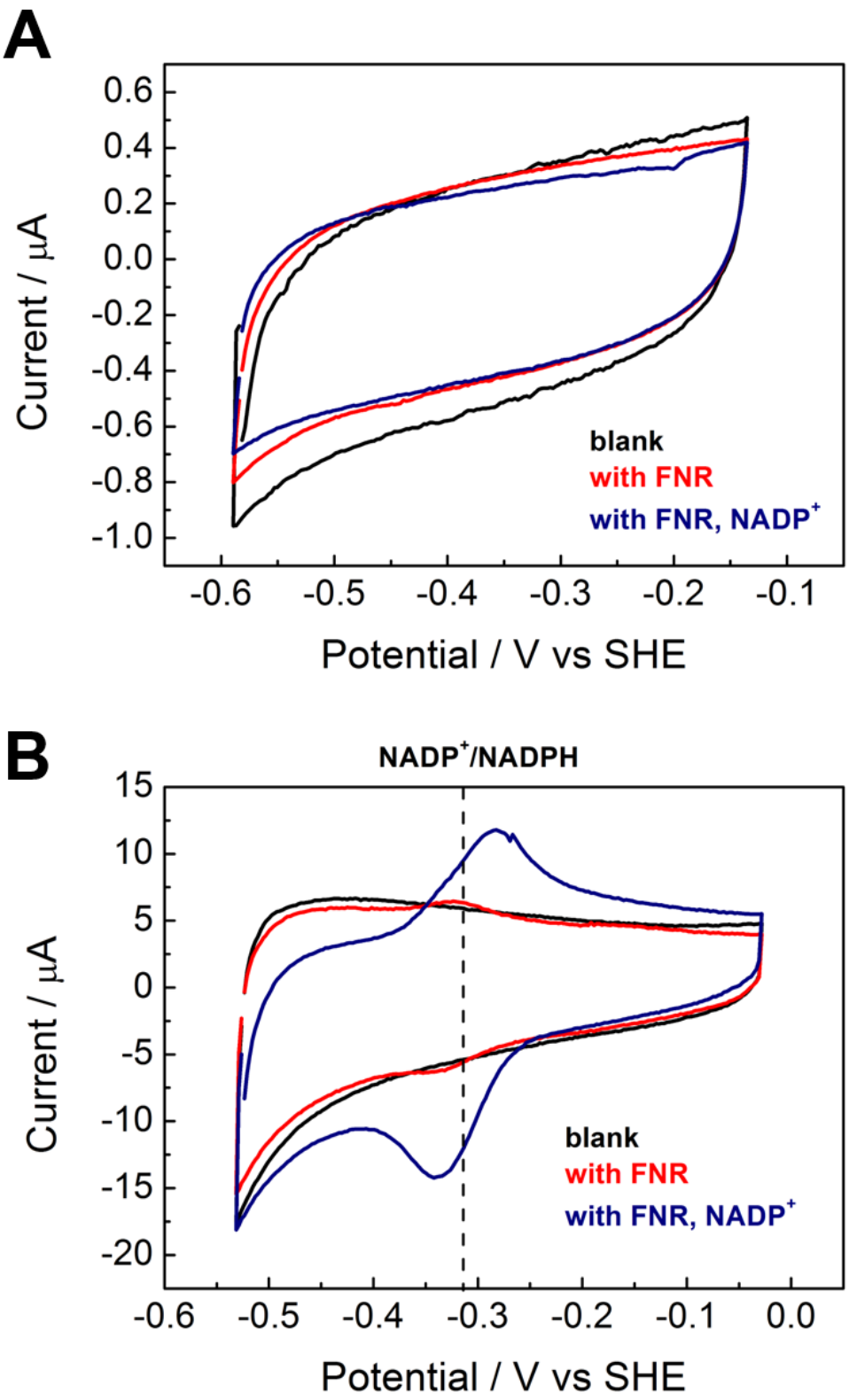

Figure 3.5 Cyclic voltammograms of FNR loaded on **A)** PGE electrode and **B)** ITO/ITO glass electrode, with the dotted line indicating the $NADP^+$/NADPH reduction potential. The traces for blank electrode (black), FNR-loaded electrode (red), and after addition of 100 μM $NADP^+$ (blue) are shown. Other conditions: MES 25 mM and TAPS 25 mM buffer pH 7.0, 20 °C, scan rate 5 mV/s, stationary electrode.

It was reasonable to assume that a more hydrophilic surface would be better for FNR adsorption, therefore FNR was loaded onto electrodes made of indium tin oxide (ITO). The ITO electrodes were made from ITO particles coated onto a conductive support, either by the doctor's blade method or by electrophoretic deposition (see Chapter 6 Section 6.2.3 for experimental details). Because the isoelectric point of ITO is *ca.* pH 6,[24] at a higher pH, the ITO surface would be negatively charged. This is similar to ferredoxin, the biological redox partner of FNR, which is also negatively charged. In addition, a metal oxide surface lacks the aromaticity of graphite, thus being less likely create undesirable interactions with the FAD group of FNR.

Figure 3.5B shows the activity of FNR on an ITO electrode. After drop-casting FNR, a pair of redox peaks was observed at *ca.* -0.35 V *vs* SHE, which were attributed to the reduction and oxidation of the FAD group in FNR, hereafter these are termed non-turnover signals of FNR. The area under these peaks, after baseline subtraction, correspond to the amount of redox-active FNR on the electrode surface, considering 2 electrons per FAD and 1 FAD per FNR molecule, as shown in the equation below:

$$\int I \, dE = nFA\Gamma_{total}\nu$$

where n is the number of electrons, F is the Faraday constant, A is the electrode area, Γ_{total} is the coverage of FNR and ν is the scan rate (see details of electrochemistry of adsorbed redox species in Chapter 6 Section 6.1.4).

Preliminary measurements showed the amount of FNR was *ca.* 100 – 200 pmol cm^{-2}, which is higher than an ideal planar monolayer coverage (5 pmol cm^{-2}, estimated from a close-packed layer of spheres with diameter of FNR as 6 nm). This is due to the porous

nature of the ITO electrode which allows more enzyme molecules to be loaded than a flat surface.

The activity of FNR was confirmed by addition of its substrate ($NADP^+$), which resulted in a reduction current. The oxidation current on the return scan is the oxidation of NADPH produced by FNR which remains near the electrode surface because the electrode was stationary. These results show that FNR is electroactive on an ITO electrode, unlike the case for PGE, and that FNR catalyzes the interconversion of $NADP^+$/NADPH in either direction. The immobilization of FNR on an ITO electrode enabled direct electrochemical investigation of the properties and kinetic parameters of FNR, which are described in detail in the following sections.

3.2.2 The ITO electrode

The ITO electrodes constructed from both the doctor's blade method and electrophoretic deposition (EPD) yielded similar results. Since electrophoretic deposition allowed for construction of the ITO layer on different conductive supports (Figure 3.6, either pyrolytic graphite edge (PGE), ITO glass, or Ti foil in this thesis), hereafter the ITO electrode will be termed ITO/support to denote the conductive support, and an FNR-adsorbed ITO electrode termed FNR@ITO/support. The PGE support was useful in experiments involving rotation, and Ti foil support was used where a higher electrode area was desired (see also Chapter 4 Section 4.2.1) as it can be shaped, as well as loaded with ITO on both sides. No electroactive FNR was observed on any of the bare conductive supports (*i.e.* without loading ITO particles).

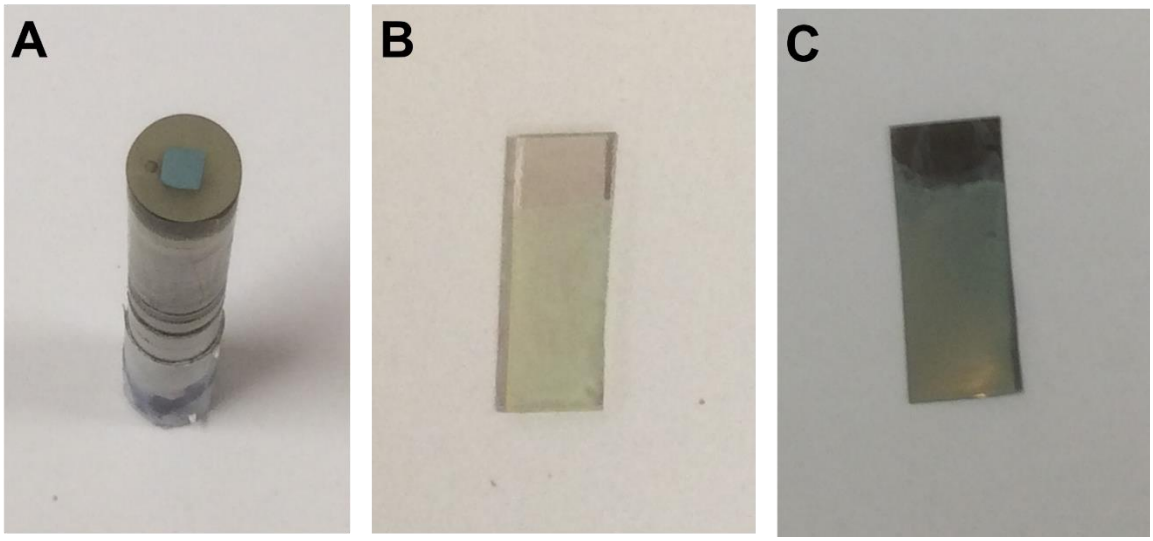

Figure 3.6 Photos of electrodes made by loading ITO onto various conductive supports. **A)** ITO/PGE (Pyrolytic graphite edge electrode in a rotatable casing) **B)** ITO/ITO glass (Glass slide with a thin layer of ITO on one side) **C)** ITO/Ti foil (Ti foil with thickness 0.127 mm, loaded with ITO on both front and back sides).

Figure 3.7 shows a scanning electron microscope (SEM) image of an ITO electrode, constructed by electrophoretic deposition of ITO nanoparticles onto an ITO glass slide. The individual ITO particle sizes were estimated to be 50 nm, the pore apertures are in the order of 100 nm in diameter, and the ITO layer thickness is 1 – 3 µm.

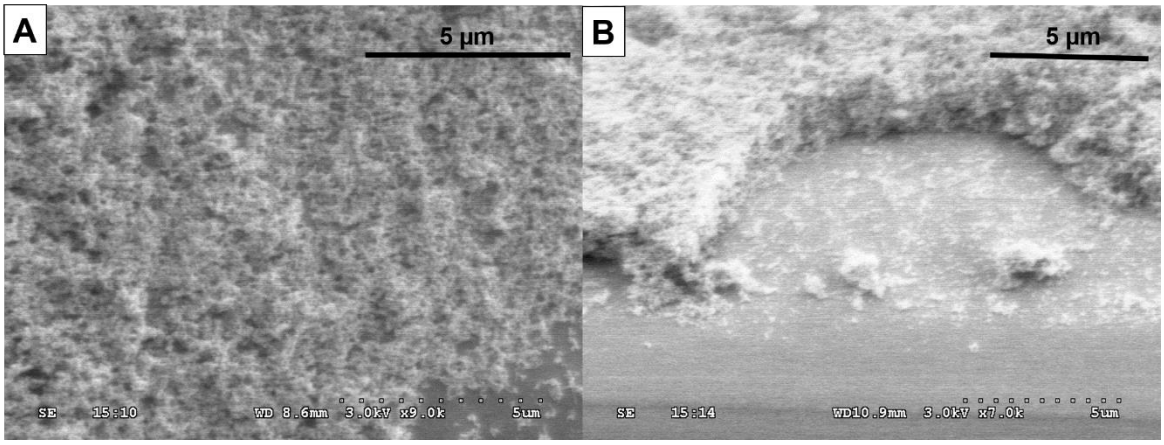

Figure 3.7 SEM images of an ITO electrode made by coating ITO particles on conductive glass. **A)** Top view **B)** Viewed at a 50 degree angle, focusing on a scratch to determine ITO layer thickness. Scale bars are located top right.

3.2.3 FNR on ITO under non-turnover conditions

Electrochemical measurements in the absence of the substrate, *i.e.* non-turnover signals,[25] can give information on the reduction potentials of the FAD group in FNR and the electroactive coverage of FNR on the electrode. Figure 3.8A shows a cyclic voltammogram of FNR on an ITO electrode at pH 8.0, with the background-subtracted trace (FNR non-turnover signal) also shown, and Figure 3.8B shows FNR non-turnover peaks in the pH range 5.0 – 9.0.

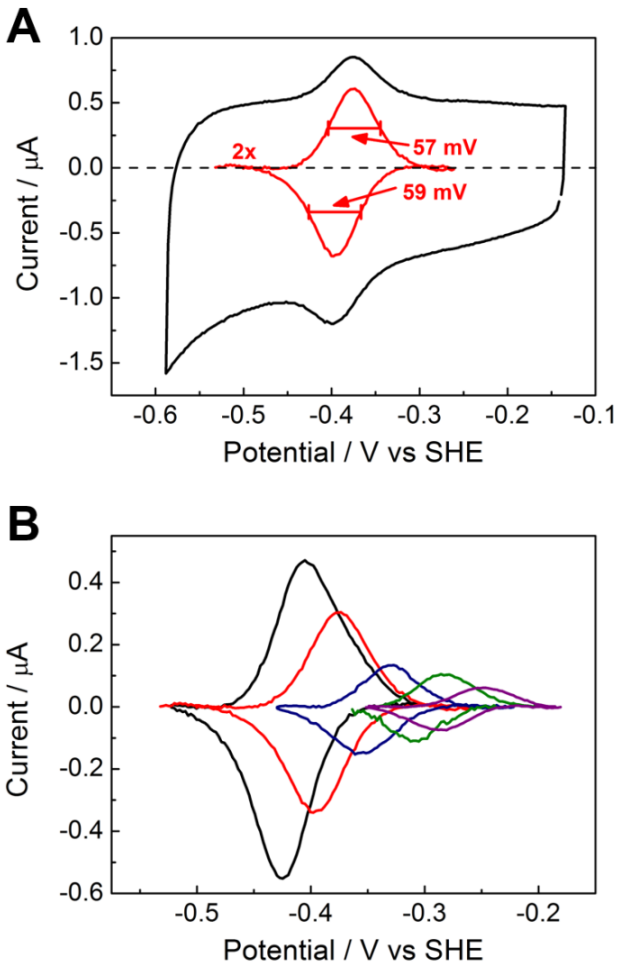

Figure 3.8 Non-turnover signals of FNR immobilized on an ITO electrode. **A)** Cyclic voltammogram of FNR (black line) and background-subtracted trace (red line, magnified X2) at pH 8.0. The label indicates the peak width at half maximum height. **B)** Background-subtracted signals from pH 5.0 (right) to 6.0, 7.0, 8.0, and 9.0 (left). Other conditions: MES 25 mM, TAPS 25 mM, 20 °C, scan rate 5 mV s^{-1}, stationary electrode, solution purged with Ar before measurement.

The ideal peak width at half maximum height (δ) for a redox species adsorbed onto an electrode (also known as a thin layer) is given as

$$\delta = \frac{89}{n}\ mV \text{ at } 20\ ^{\circ}\text{C},$$

where n is a coefficient corresponding to the number of electrons transferred cooperatively.[26] The derivation is explained in Chapter 6 Section 6.1.4. A fully-cooperative two-electron reaction, *i.e.* with the intermediate radical having no stability, should have a peak width of 45 mV. In a detailed study of FNR using potentiometry, it was shown[18] that a semiquinone species forms during titrations indicating partial cooperativity, but the level was never more than 10% of the total flavin content at pH 8.0. Therefore, the peak shape of FNR is not expected to be the ideal n = 2 case, and the reduction of the FAD group in FNR can be considered as two sequential one-electron transfers as in the following Latimer scheme.

$$\mathrm{FAD} \overset{E_1}{\rightleftharpoons} \mathrm{FADH^{\cdot}} \overset{E_2}{\rightleftharpoons} \mathrm{FADH_2}$$

The overall two-electron reduction potential is the average of the two one-electron potentials E_1 (oxidized/semiquinone) and E_2 (semiquinone/hydroquinone). If the first step is much more favorable than the second step, *i.e.* ΔE ($E_1 - E_2$) is more than 200 mV,[26] the radical can form with some stability and there should be two distinct peaks, one centered on each step. At the other extreme, a ΔE value less than -200 mV indicates that the second step is much more favorable than the first (*i.e.* the two steps are fully cooperative and the two-electron reaction completes rapidly after the first electron has been transferred) and the signal should be a single peak corresponding to n = 2. In the intermediate case, a broader single peak is expected.

From Figure 3.8, the peak widths are 57 – 59 mV in each direction at pH 8.0, and 59 ± 3 mV in the pH range 5.0 – 9.0 with no significant pH dependence. The data are

summarized in Table 3.1 below. The fact that the peak widths are much smaller than 89 mV indicates that the reaction involves two electrons transferring with considerable cooperativity. Based on the relationship between ΔE and the peak width at half-maximum,[27] the difference in E_1 and E_2 was estimated to be -14 mV on average (with the range being -6 to -24 mV), *i.e.* the reduction potential of the first step is slightly more negative than for the second step, thus the two electrons transfer cooperatively.

Table 3.1 The potential, peak width at half maximum height, and coverage of FNR on an ITO electrode in the pH range 5.0 – 9.0. The average values from 6 repeats are shown, ± 1 standard deviation.

pH	FNR potential (mV vs SHE)	Half-height peak width (mV)		Coverage (pmol cm^{-2})
		Anodic	Cathodic	
5.0	-265 ± 3	56 ± 3	61 ± 3	100 ± 50
6.0	-298 ± 1	57 ± 1	64 ± 3	170 ± 85
7.0	-344 ± 2	57 ± 1	61 ± 3	240 ± 120
8.0	-383 ± 3	57 ± 1	59 ± 2	480 ± 280
9.0	-413 ± 4	61 ± 6	57 ± 1	900 ± 590

Previous studies (see Table 3.2) have measured the reduction potential of FNR by potentiometric titration, using electron mediators such as methylviologen or benzylviologen. Studies that measured the concentration of the semiquinone form of FNR were also able to define the separate one-electron steps (E_1:oxidized/semiquinone, E_2:semiquinone/hydroquinone), and almost all of them observed that E_1 and E_2 were close, indicating partial cooperativity and a relatively unstable semiquinone form. My value for the overall reduction potential of FNR agrees well with that obtained by potentiometric

titration (-0.376 V vs SHE at pH 8 from Batie and Kamin,[18] and also other literature values which are listed in Table 3.2 below).

Table 3.2 Literature values for the two-electron reduction potential of FNR ($E_{overall}$:oxidized/hydroquinone) and the separate one-electron steps (E_1:oxidized/semiquinone, E_2:semiquinone/hydroquinone) in the pH range 7 – 8.

Species	pH	$E_{overall}$ (mV)	E_1 (mV)	E_2 (mV)	$E_1 - E_2$ (mV)	Reference
Spinach	7	-320	-	-	-	Keirns 1972[28]
Spinach	8	-340	-	-	-	Keirns 1972[28]
Spinach	7.3	-372	-	-	-	Smith 1981[29]
Spinach	8	-376	-	-	-	Batie 1986[18]
Anabaena	7	-344	-	-	-	Pueyo 1991[30]
Anabaena	8	-376	-	-	-	Pueyo 1991[30]
Spinach	7	-342	-350	-335	-15	Corrado 1996[31]
Spinach	8	-380	-402	-358	-44	Corrado 1996[31]
Anabaena	8	-325	-338	-312	-26	Faro 2002[32]
Anabaena	7	-296	-280	-312	32	Anusevicius 2005[33]
Pea	8	-342	-373	-311	-62	Sanchez-Azqueta 2012[34]
Anabaena	8	-370	-384	-357	-27	Sanchez-Azqueta 2014[35]
C*hlamydomonas reinhardtii*	7	-344	-349	-339	-14	This work
C*hlamydomonas reinhardtii*	8	-383	-388	-378	-14	This work

These values for the reduction potential of FNR describe an almost perfect condition for NADPH reduction. The reduction potential of FNR should be more negative than that of $NADP^+$ so that it can donate electrons to reduce it, but more positive than that of ferredoxin to be able to receive electrons from it. For a fully cooperative two-electron reduction, E_1 must be much more negative than E_2, this, together with the constraint for the average reduction potential in place, means that E_1 would be too negative for efficient electron

transfer from ferredoxin. The reaction being only partially cooperative, helps to satisfy the constraints for the reduction potential while retaining a cooperative nature between the two steps of electron transfer.

Figure 3.9 shows the average peak positions of FNR in the pH range 5.0 – 9.0, compared to the pH dependence of the $NADP^+$/NADPH couple. The reduction potential of $NADP^+$ is -0.32 V vs SHE at pH 7.0, with a slope of -30 mV per pH unit.[36]

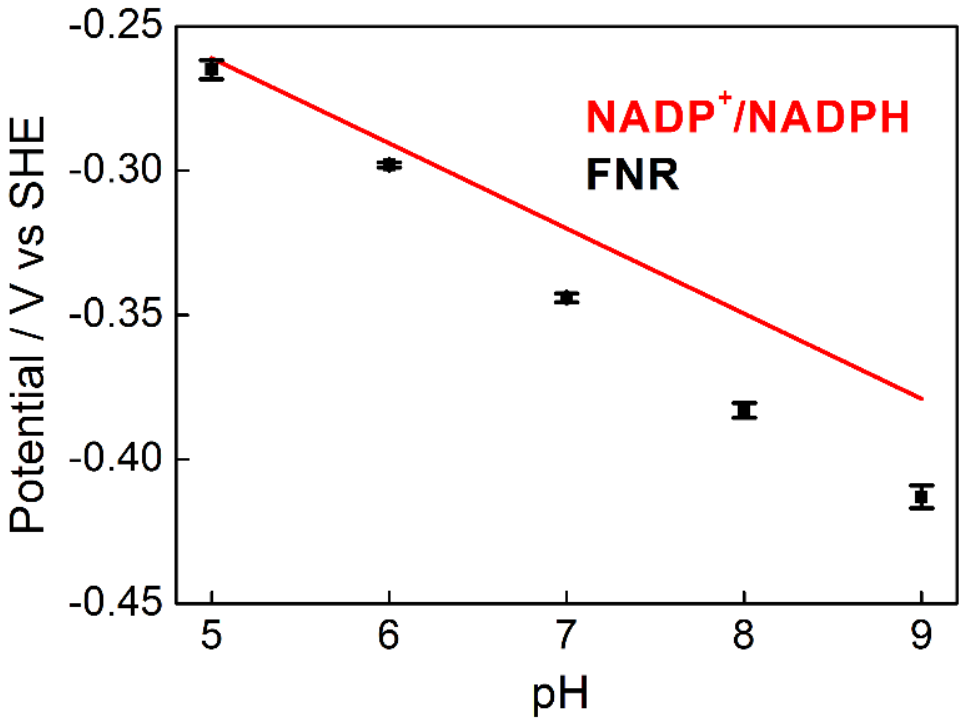

Figure 3.9 pH dependence of the reduction potential of FNR (black) compared to the $NADP^+$/NADPH couple (red). The FNR potential is calculated from the average peak positions at each pH value. The $NADP^+$/NADPH potential is -0.32 V vs SHE at pH 7, with a -30 mV slope per pH.[36] Other conditions: MES 25 mM, TAPS 25 mM, 20 °C, scan rate 5 mV s^{-1}, stationary electrode, solution purged with Ar before measurement.

The relationship between FNR reduction potential and pH can be analyzed by constructing an extended square scheme, assuming the FAD group has 2 possible protonation sites, as follows:

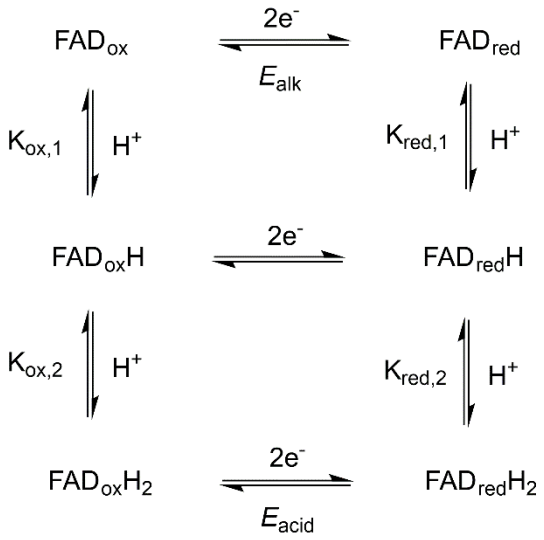

Scheme 3.1 Extended square scheme of FNR-bound FAD. E_{alk} and E_{acid} are the reduction potentials at the alkaline and acid limits, respectively. K is the acid dissociation constant.

At the alkaline limit, the FAD group will always be fully deprotonated, and the reduction potential is denoted as E_{alk}, and at the acid limit the FAD group will be doubly protonated, and the reduction potential is denoted as E_{acid}. The acid dissociation constants are denoted as K, with the subscripts referring to the redox state of the FAD group and the order of the step. The FNR reduction potential at a given pH can be written as a function of $[H^+]$ as follows:

$$E^0_{pH} = E^0_{alk} + \frac{RT}{2F}\ln\frac{(1+\frac{[H^+]}{K_{red,1}}+\frac{[H^+]^2}{K_{red,1}K_{red,2}})}{(1+\frac{[H^+]}{K_{ox,1}}+\frac{[H^+]^2}{K_{ox,1}K_{ox,2}})}$$

The measured FNR reduction potential in Figure 3.9 was fitted to this equation using non-linear curve fitting by the Solver function in Excel, and the result is shown in Figure 3.10 and Table 3.3.

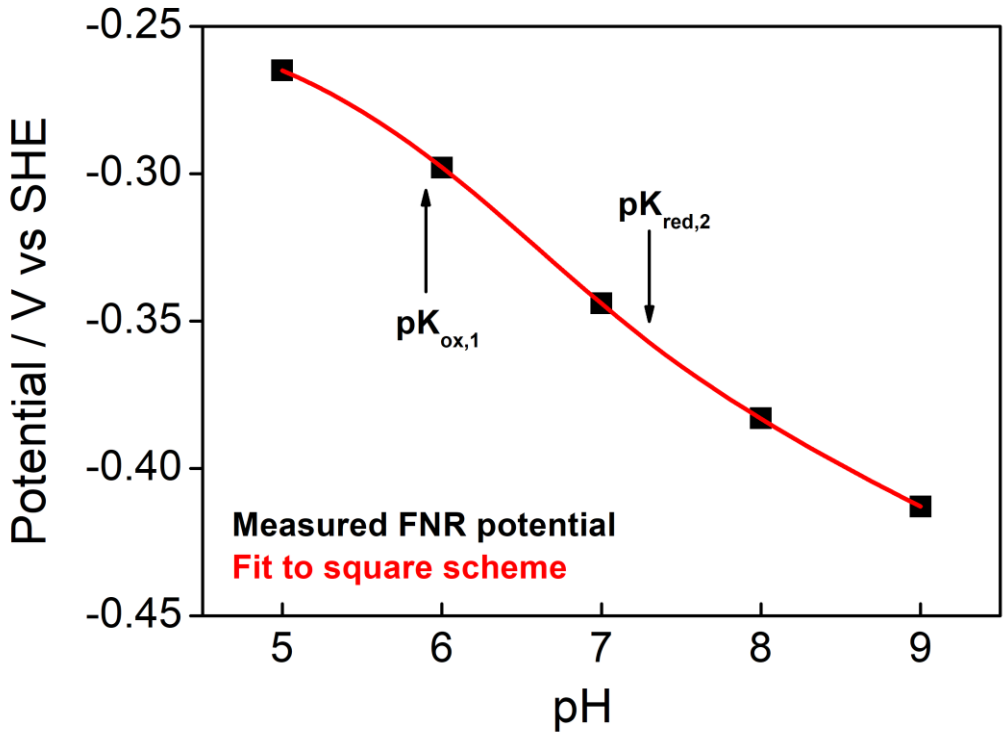

Figure 3.10 The measured FNR reduction potential (black dot) and the values obtained from fitting to the extended square scheme (red line).

Table 3.3 The FNR reduction potential at the alkaline limit and acid dissociation constants obtained from fitting measured FNR reduction potential to the extended square scheme

Parameter	Value
E_{alk}	-0.44 V
$pK_{ox,1}$	5.9
$pK_{ox,2}$	4.7
$pK_{red,1}$	10.0
$pK_{red,2}$	7.3

From the obtained values of pK, we can expect that the FAD_{red} and $FAD_{ox}H_2$ states would not be significantly present in the experimental pH range of 5 to 9. In the low pH

region, the reaction is mainly $FAD_{ox}H$ to $FAD_{red}H_2$ ($2e^-$, $1H^+$) and in the high pH region the reaction is mainly FAD_{ox} to $FAD_{red}H$ (also $2e^-$, $1H^+$). Therefore, the slopes of potential *vs* pH in those regions are close to the theoretical 30 mV/pH unit. However, in the intermediate pH values, the reaction path from FAD_{ox} to $FAD_{red}H_2$ ($2e^-$, $2H^+$) is also possible, thus the slope is slightly higher in that region than would be predicted for a simple $2e^-$, $1H^+$ reaction.

In this pH range, the potential of FNR is always more negative than that of $NADP^+$, the difference increasing with pH. The data show that FNR is biased slightly to favor $NADP^+$ reduction especially at higher pH values, this is especially relevant since in the chloroplast, the pH is approximately 8. The two-electron reduction potential of FAD in its free state (i.e. not enzyme-bound) is -0.22 V vs SHE at pH 7.0,[37] and assuming a -30 mV slope per pH unit, at pH 8.0 the reduction potential of FNR-bound FAD (-0.38 V) is ca. 130 mV more negative than that of free FAD. The protein environment causes the reduction potential of the FNR-bound FAD group to shift to a much more negative value, thus allowing the reduction of $NADP^+$. The reduction potentials of the free and FNR-bound FAD can be related to the dissociation constants K_d of the reduced and oxidized forms of FAD, as shown in Scheme 3.2 below.

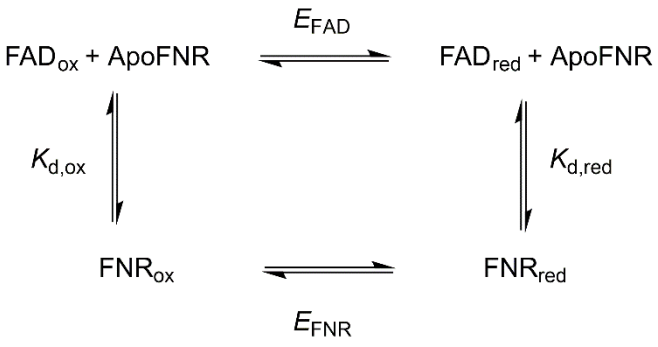

Scheme 3.2 Thermodynamic cycle of free and FNR-bound FAD.

The relationship between the dissociation constants, reduction potentials and concentrations are as follows:

$$K_{d,ox} = \frac{[FAD_{ox}][ApoFNR]}{[FNR_{ox}]}, \quad K_{d,red} = \frac{[FAD_{red}][ApoFNR]}{[FNR_{red}]}$$

$$E_{FAD} = \frac{RT}{nF} ln \frac{[FAD_{red}]}{[FAD_{ox}]}, \qquad E_{FNR} = \frac{RT}{nF} ln \frac{[FNR_{red}]}{[FNR_{ox}]}$$

$$E_{FNR} - E_{FAD} = \frac{RT}{nF} ln \frac{K_{d,ox}}{K_{d,red}}$$

With $n = 2$ and the difference between E_{FAD} and E_{FNR} as 130 mV, we obtain $\frac{K_{d,ox}}{K_{d,red}} = 3 \times 10^{-5}$, *i.e.* the oxidized form of FAD is much less likely to dissociate from FNR than the reduced form. This means that the reduced FAD is much less stable within FNR, therefore holding FNR at a very negative potential for longer periods may lead to dissociation of FAD, especially in the absence of $NADP^+$ to accept electrons. However, non-turnover peaks from FNR are typically very stable, both in terms of potential and coverage, with at least 50 % of the coverage remaining after 24 h at 20 °C (see Chapter 4 Section 4.2.3 for experiments on stability).

The electroactive coverage of FNR was calculated from non-turnover peaks at each pH in the range 5.0 – 9.0 as in Figure 3.8B, and repeated measurements were made with a fresh film of FNR each time. The data is summarized in Table 3.1 above. Although the variation in coverage is considerable, a clear trend of higher coverage with increasing pH is evident. This is in line with our reasoning that at higher pH the ITO surface becomes more negative (due to the surface hydroxyl groups becoming deprotonated) therefore allowing FNR to bind more tightly (as its biological redox partner, ferredoxin, is negatively charged). The high variation in coverage is mainly due to the nature of ITO electrode construction

(leading to variation in ITO layer thickness) and the process of loading FNR, as well as possible errors from baseline subtraction.

The relationship between FNR coverage and pH was also investigated using a single film of FNR and a series of buffer exchanges as shown in Figure 3.11. A single film of FNR on ITO/PGE was made and voltammograms were recorded to measure the coverage at pH 9.0. Then, with the same FNR film in place, a buffer exchange was conducted to change the cell solution to pH 8.0, and the coverage was again measured before another buffer exchange restored the pH to 9. This was repeated successively with lower pH values until pH 5.0. The FNR coverage decreased when the film was taken to a lower pH, but partial recovery was observed when returning the film to higher pH.

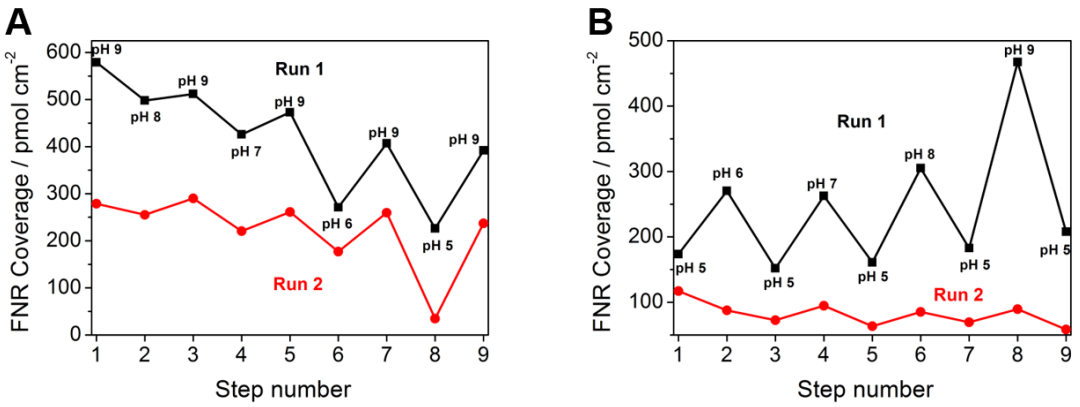

Figure 3.11 Changes in FNR coverage with pH. **A)** Starting at pH 9.**B)** Starting at pH 5. Other conditions: MES 25 mM, TAPS 25 mM buffer solution, 20 °C, solution purged with Ar before measurement.

This indicates that while the FNR binding to ITO is weaker at low pH, the FNR molecules are not totally desorbed from the ITO layer. The recovery in the coverage at pH 9.0 can be interpreted as FNR molecules that became loosely bound or bound in an inactive configuration at low pH (thus not contributing to the non-turnover peak signal) which then returned to an active bound state when the ITO surface became more negative. The same experiment was conducted with the initial buffer at pH 5.0, then exchanged with a higher

pH before returning to pH 5.0 (Figure 3.11B). In this case, the extent of recovery is much lower than when starting at pH 9.0. In any case, the trend of higher coverage at higher pH holds.

From the results of the pH-step experiment, it can be concluded that binding of FNR within the pores involves: (i) general permeation that is more favourable at high pH, (ii) localized binding in an electroactive configuration that is also stronger at high pH. Lowering the pH therefore causes some enzyme molecules to become more loosely bound, but most remain deeply buried in the pores, so that restoring the high pH condition causes the still-entrapped enzyme molecules to re-bind.

The scan rate dependence of the FNR non-turnover signals was investigated (Figure 3.12). A film of FNR on ITO/PGE was made as described previously, and cyclic voltammograms were taken at a scan rate of 3 – 200 mV s^{-1} (only a subset is shown for clarity in Figure 3.11A). Figure 3.11B shows a plot of the peak current, after baseline subtraction, against the scan rate. For an ideal adsorbed redox species, the peak current is given as

$$I_{peak} = \frac{n^2 F^2 A \Gamma_{total} \nu}{4RT}$$

where n is the number of electrons, F is Faraday's constant, A is the electrode area, Γ_{total} is the total coverage of the redox species, ν is the scan rate, R is the gas constant, and T is the temperature (see also details in Chapter 6 Section 6.1.4). The peak current should vary linearly with the scan rate, and this is observed up to *ca.* 30 mV s^{-1}, and at faster scan rates the current deviates to lower values than expected. This is explained by the peak broadening (Figure 3.12C) and increasing peak separation (Figure 3.12D) at faster scan rates due to the interfacial electron transfer rate being too low to sustain a Nernstian equilibrium at each potential.

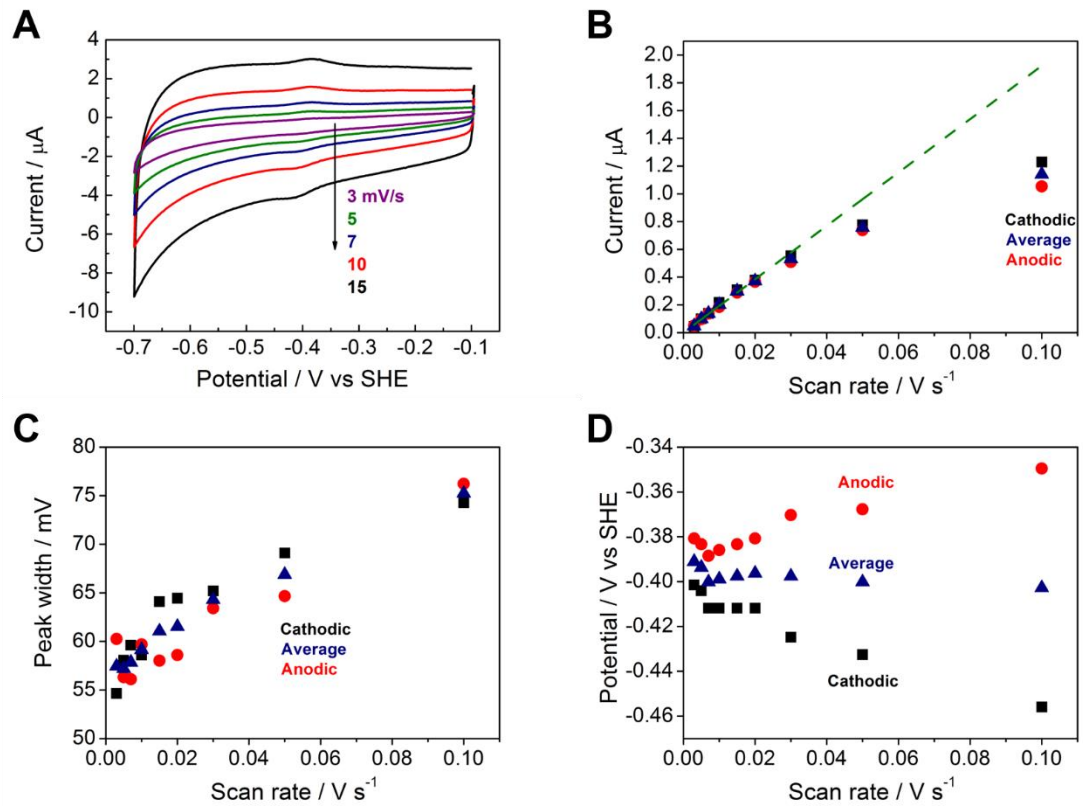

Figure 3.12 Scan rate dependence of FNR non-turnover signals on ITO. **A)** Cyclic voltammograms of an FNR@ITO electrode at scan rates of 3 – 15 mVs^{-1}. **B)** Background-subtracted peak current with the scan rate. The dashed line shows the linear fit up to a scan rate of 0.02 Vs^{-1}. **C)** Peak width at half maximum with the scan rate. **D)** Peak potential with the scan rate. Other conditions: buffer: MES 25 mM, TAPS 25 mM, pH 8.0, 20 °C, purged with Ar before measurement.

3.2.4 FNR on ITO under catalytic conditions

The previous section dealt with FNR on ITO electrodes in the absence of $NADP^+$, *i.e.* non-turnover conditions, and this section investigates FNR in the presence of $NADP^+$, *i.e.* turnover or catalytic conditions.

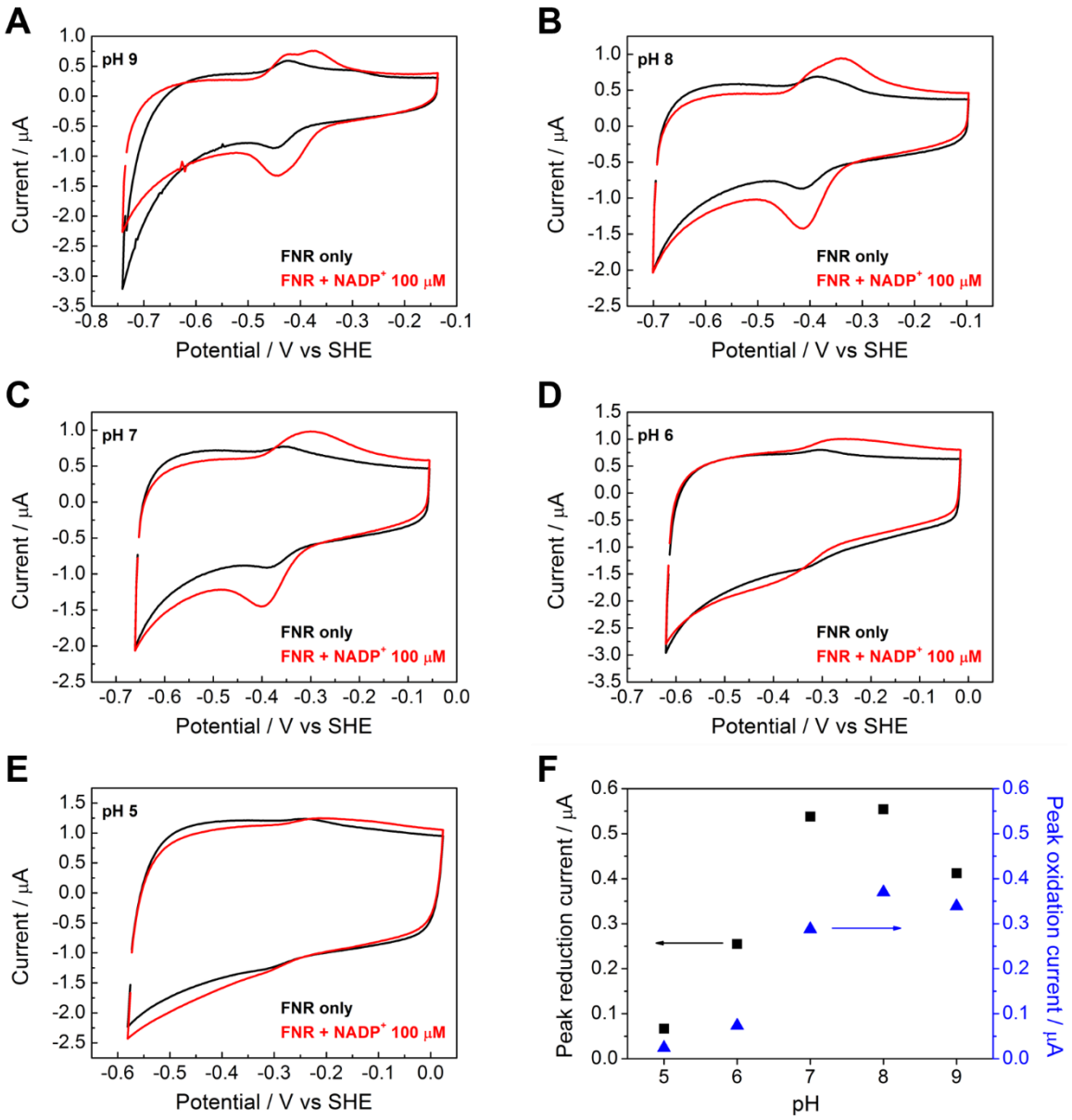

Figure 3.13 Cyclic voltammograms of FNR@ITO/PGE in the absence of $NADP^+$ (black) and presence of $NADP^+$ 100 µM (red). **A)** pH 9.0, **B)** pH 8.0, **C)** pH 7.0, **D)** pH 6.0, **E)** pH 5.0. **F)** Peak reduction and oxidation currents at each pH. Other conditions: scan rate 5 mVs^{-1}, buffer MES 25 mM, TAPS 25 mM, 20 °C, stationary electrode, purged with Ar before measurement.

An ITO/PGE electrode was made by electrophoretic deposition and FNR was dropped and left to adsorb, as described previously. Then the FNR@ITO/PGE was put into pH 9.0 buffer, and cyclic voltammograms were measured before and after adding $NADP^+$ (100 μM final concentration) to the cell (Figure 3.13). The FNR@ITO/PGE electrode was kept and rinsed with MQ water, then put into pH 8.0 buffer, similar measurements were taken and this was repeated in buffers with pH 7.0, 6.0, and 5.0. In this pH range of 5.0 to 9.0, $NADP^+$ reduction and NADPH oxidation currents were observed, but these currents were peak-like (*i.e.* diffusion limited) at only pH 7.0 – 9.0, while at pH 5.0 and 6.0 the currents were broadened and less reversible. This indicates that the rate of catalysis by FNR is slower at pH 5.0 and 6.0.

At pH 9.0 (Figure 3.13A), and to a lesser extent at pH 8.0 (Figure 3.13B), a shoulder or double peak is visible on the oxidative scan, located negative of the oxidation peak for NADPH. From its position, the shoulder coincides with the FNR oxidative non-turnover peak, and it may be assigned to FNR molecules that are buried and thus redundant in regard to catalytic activity. This was verified by varying the scan rate (Figure 3.14 below), as the shoulder diminishes in comparison to the main peak as the scan rate is decreased (since slow conditions favor oxidation of diffusing NADPH) and is not visible on the reductive scan because its position is more negative than the $NADP^+$ reduction potential, thus it is masked by the $NADP^+$ reduction peak. The shoulder is more visible at higher pH due to the larger difference between the reduction potential of FNR and $NADP^+$/NADPH (see also Figure 3.9). This agrees with the overall picture of the system, where the ITO layer is porous and suffused throughout with FNR. The outermost FNR molecules catalyze the redox reaction, thus consuming the substrate before it can reach the inner-lying FNR molecules. Therefore, the intensity of the shoulder varies with ITO layer thickness and FNR loading. For the first cyclic voltammogram after $NADP^+$ injection, there would be $NADP^+$ present inside the

pores of the ITO electrode, but this amount is too small to detect a change in current. The catalytic voltammograms in Figure 3.13 (red lines) were first scans after $NADP^+$ injection, and no significant differences were observed between the first and subsequent catalytic scans.

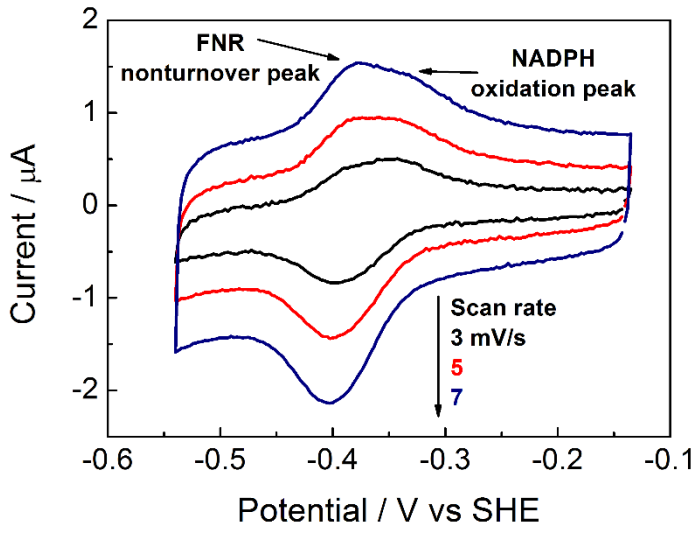

Figure 3.14 Cyclic voltammograms of FNR@ITO/PGE with $NADP^+$ 50 μM at a scan rate of v = 3 (black), 5 (red) and 7 (blue) mV s^{-1}. Non-turnover peak of FNR is observed on the left in the oxidative scan, and it increases more with higher scan rate compared to the NADPH oxidation peak on the right. Other conditions: MES 25 mM, TAPS 25 mM buffer solution pH 8.0, 20 °C, solution purged with Ar before measurement.

The turnover frequency (TOF) of FNR, defined as moles of NADPH produced per mole of total electroactive FNR per second, is obtainable from the steady-state catalytic reduction current if the number of active enzyme molecules is known. Using the total electroactive coverage obtained from the area of a non-turnover peak, the TOF with 50 μM $NADP^+$ was typically 0.4 s^{-1} at pH = 8.0, which is three orders of magnitude lower than expected from steady state experiments.[3,13] Since the electrochemical reduction of $NADP^+$ is controlled by diffusion through aqueous solution, only those FNR molecules bound closest to the bulk solution interface will contribute to catalysis, and buried FNR molecules

could be completely redundant. This means that calculating the TOF from total FNR coverage would lead to an underestimate. Assuming, instead, that the amount of accessible FNR is equivalent to one monolayer (although the actual amount could be higher), this leads to a revised TOF of at least 40 s^{-1}.

The scan rate dependence of $NADP^+$ reduction current at an FNR@ITO/PGE was further investigated in the range 3 – 200 mVs^{-1} (Figure 3.15). Since experiments in Figure 3.13 showed that a large proportion of the FNR loaded onto the ITO electrode was redundant, the FNR coverage was reduced by diluting the FNR solution (to approximately 20 μM, which is 10 times less concentrated than in previous experiments) before dropping onto the electrode, in order to minimize the contribution of FNR to the current. The non-turnover signal from FNR was still visible (Figure 3.15C), but lowering the FNR coverage further also made the $NADP^+$ reduction current less clear (data not shown), therefore this level of FNR coverage was used in the experiments.

The peak $NADP^+$ reduction current was obtained by subtracting an extrapolated baseline from the capacitive current in the region immediately positive of the start of reduction current, and this was plotted against the square root of scan rate (Figure 3.15D, black trace). This value was also corrected (Figure 3.15D, red trace) by subtracting the current assigned to FNR, obtained from cyclic voltammograms in the absence of $NADP^+$. At slower scan rates (up to approximately 20 mVs^{-1}) the $NADP^+$ reduction behaved reversibly, as evidenced from the linear relationship with the square root of scan rate as well as the peak position being constant. At faster scan rates the behaviour moved into the quasi-reversible regime, and at scan rates of 200 mVs^{-1} or above the reduction current became difficult to observe.

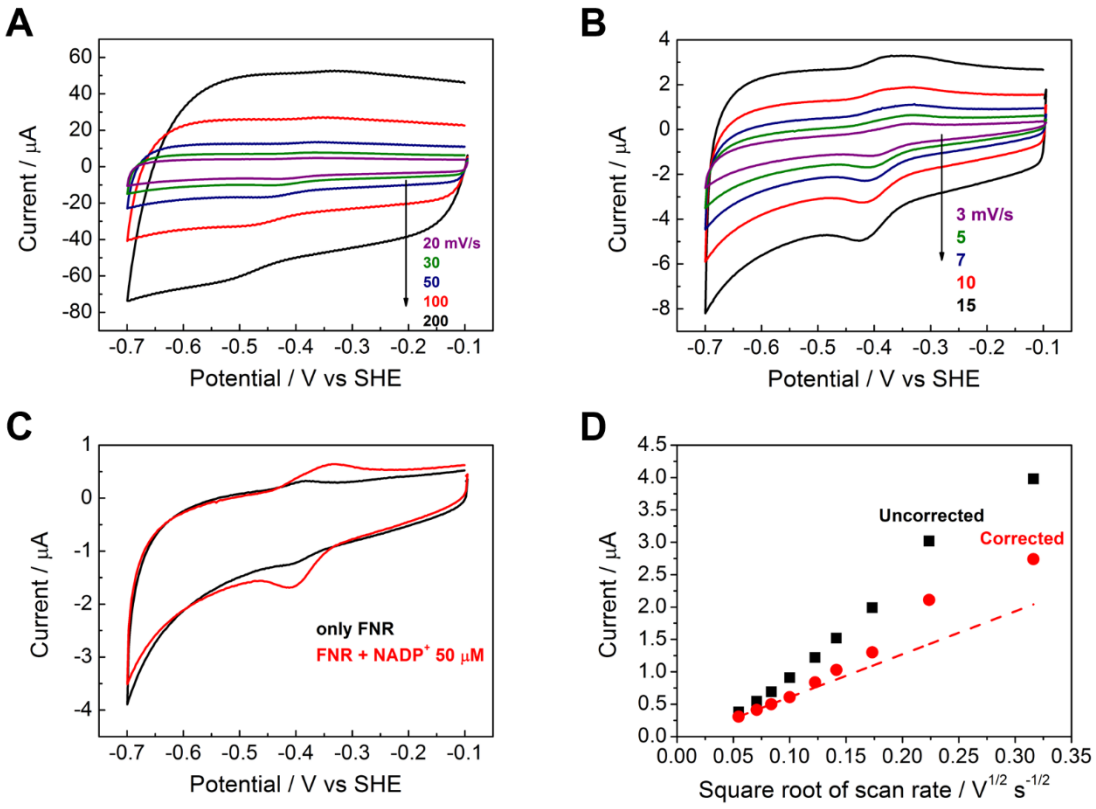

Figure 3.15 Scan rate dependence of FNR@ITO with $NADP^+$ 50 μM. **A)** Scan rates 20 – 200 mVs^{-1}. **B)** Scan rates 3 – 15 mVs^{-1}. **C)** Comparison of the FNR@ITO electrode without $NADP^+$ (black) and with $NADP^+$ 50 μM (red) at a scan rate of 5 mVs^{-1}. **D)** Peak reduction current with the square root of scan rate, showing uncorrected values (black) and values corrected for the FNR signal (red). Other conditions: buffer: MES 25 mM, TAPS 25 mM, pH 8.0, 20 °C, purged with Ar before measurement.

The Randles-Sevcik equation, which describes a stationary reversible system, gives the peak current[38] as:

$$I_{peak} = 0.4463\left(\frac{F^3}{RT}\right)^{1/2} n^{3/2} A D^{1/2} C \nu^{1/2}$$

where F is the Faraday constant, R is the gas constant, T is the temperature, n is the number of electrons in the reaction, A is the electrode area, D is the diffusion coefficient, C is the bulk concentration of the redox species, and ν is the scan rate. Using the slope of the corrected current against the square root of scan rate (Figure 3.14D) in the slow scan rate region, a diffusion coefficient of $NADP^+$ was determined to be 6.2×10^{-6} cm^2s^{-1}. This agrees

with the diffusion coefficient for NADP(H) in literature,[39-42] which is in the range of 2.0 – 6.7 × 10^{-6} cm^2s^{-1} (and the diffusion coefficients for $NADP^+$ and NADPH should be similar).

Using the current as a measure of $NADP^+$ reduction, the Michaelis-Menten constant (K_M) of FNR can be obtained. A FNR@ITO/PGE electrode was prepared as described previously, and cyclic voltammograms were measured with increasing concentrations of $NADP^+$ in the range 0 – 600 µM (Figure 3.16A).

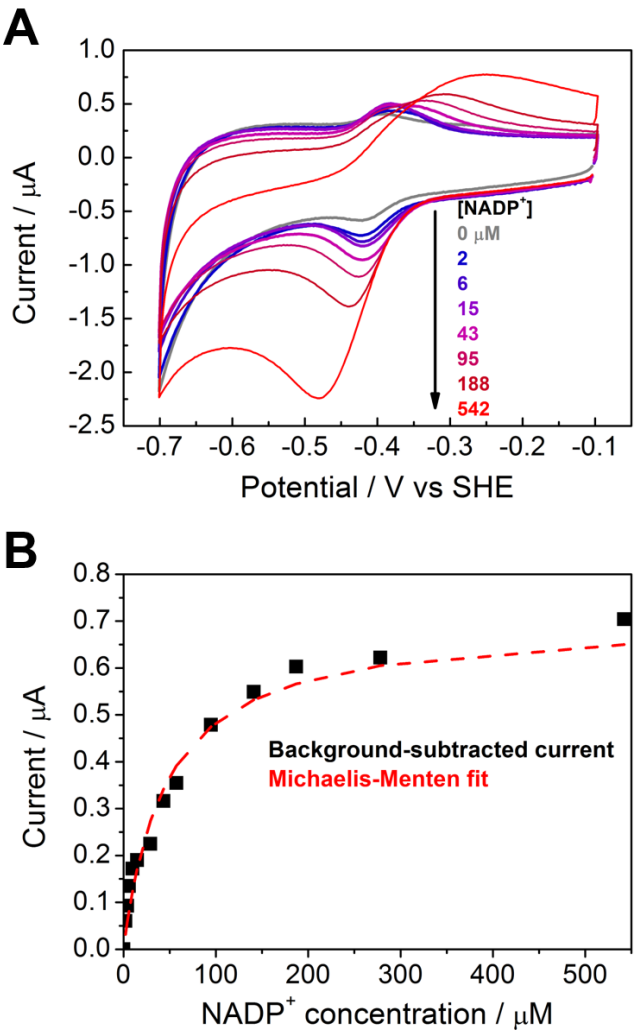

Figure 3.16 Activity of FNR@ITO for $NADP^+$ reduction. **A)** Cyclic voltammograms of FNR@ITO/PGE with increasing concentrations of $NADP^+$. Scan rate 5 mV s^{-1}. **B)** Background subtracted NADP+ reduction current at -0.41 V vs SHE (black) and the fitted curve from the Michaelis-Menten equation. Other conditions: buffer: MES 25 mM, TAPS 25 mM, pH 8.0, 20 °C, purged with Ar before measurement.

The Michaelis-Menten model describes the following scheme:

$$E + S \underset{k_b}{\overset{k_f}{\rightleftharpoons}} ES \xrightarrow{k_{cat}} E + P$$

where E is the enzyme, S is the substrate, ES is the enzyme-substrate complex, and P is the product.[43,44] The enzyme and substrate binds reversibly, with the k_f and k_b the forward and backward rate constants, respectively, and the enzyme-substrate complex produces the product with a rate constant k_{cat}. Using the steady state approximation where the concentration of ES is constant, the rate is described as

$$V = \frac{V_{max}[S]}{K_M + [S]}$$

where V is the rate, V_{max} is the maximum rate, [S] is the substrate concentration, and K_M is the Michaelis-Menten constant.

The background subtracted $NADP^+$ reduction current at -0.41 V vs SHE was plotted against the concentration of $NADP^+$ (Figure 3.16B), and the data points were fitted to the Michaelis-Menten rate equation by nonlinear curve fitting (minimization of the square of errors using the Solver function in Microsoft Excel). The K_M of FNR for $NADP^+$ was 39 ± 15 μM (the average from 3 separate measurements ± 1 standard deviation). Possible contributions to the error are from the baseline subtraction process as well as the deviation of the current from the ideal reversible case.

One benefit of constructing an ITO electrode by electrophoretic deposition onto a PGE is that this made measurements under hydrodynamic conditions possible. In Figure 3.17A, a sigmoidal curve for the reduction of 50 μM $NADP^+$ was obtained at a high rotation rate (3000 rpm) and a slow scan rate (1 mV s^{-1}). At slower rotation and/or faster scan rates, $NADP^+$ reduction appeared to show a small depletion peak, but this could be convoluted

from the signal of FNR. Likewise, if the cell solution contained only NADPH (also 50 μM), a sigmoidal oxidation wave was observed. With both $NADP^+$ and NADPH in solution (50 μM each, Figure 3.17B), a sigmoidal shape could be observed for both $NADP^+$ and NADPH oxidation.

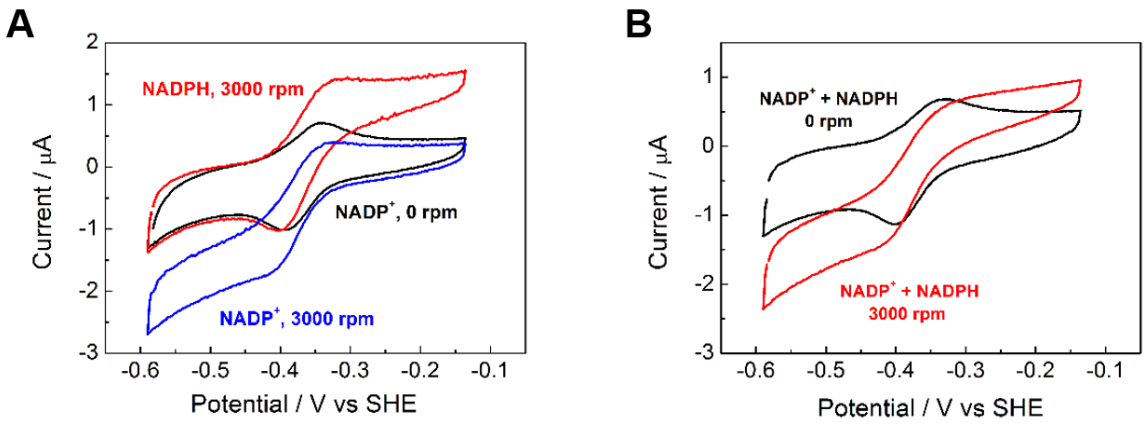

Figure 3.17 Effect of electrode rotation on FNR@ITO/PGE. **A)** stationary electrode with 50 μM $NADP^+$ (black) and rotated at 3000 rpm with 50 μM $NADP^+$ (blue) or 50 μM NADPH (red). **B)** 50 μM $NADP^+$ and 50 μM NADPH at 0 rpm (black) and 3000 rpm (red). Other conditions: scan rate 1 mV s^{-1}, buffer solution:25 mM MES 25 mM TAPS, pH 8.0, 20 °C, and purged with Ar before measurement.

Rotation rate dependence measurements were conducted with FNR@ITO/PGE electrodes prepared as described previously, using rotation in the range 400 – 3000 rpm (Figure 3.18A). The background subtracted signal, shown in Figure 3.18B, contains distortions in the low potential region due to effect of the shape of the background cyclic voltammogram.

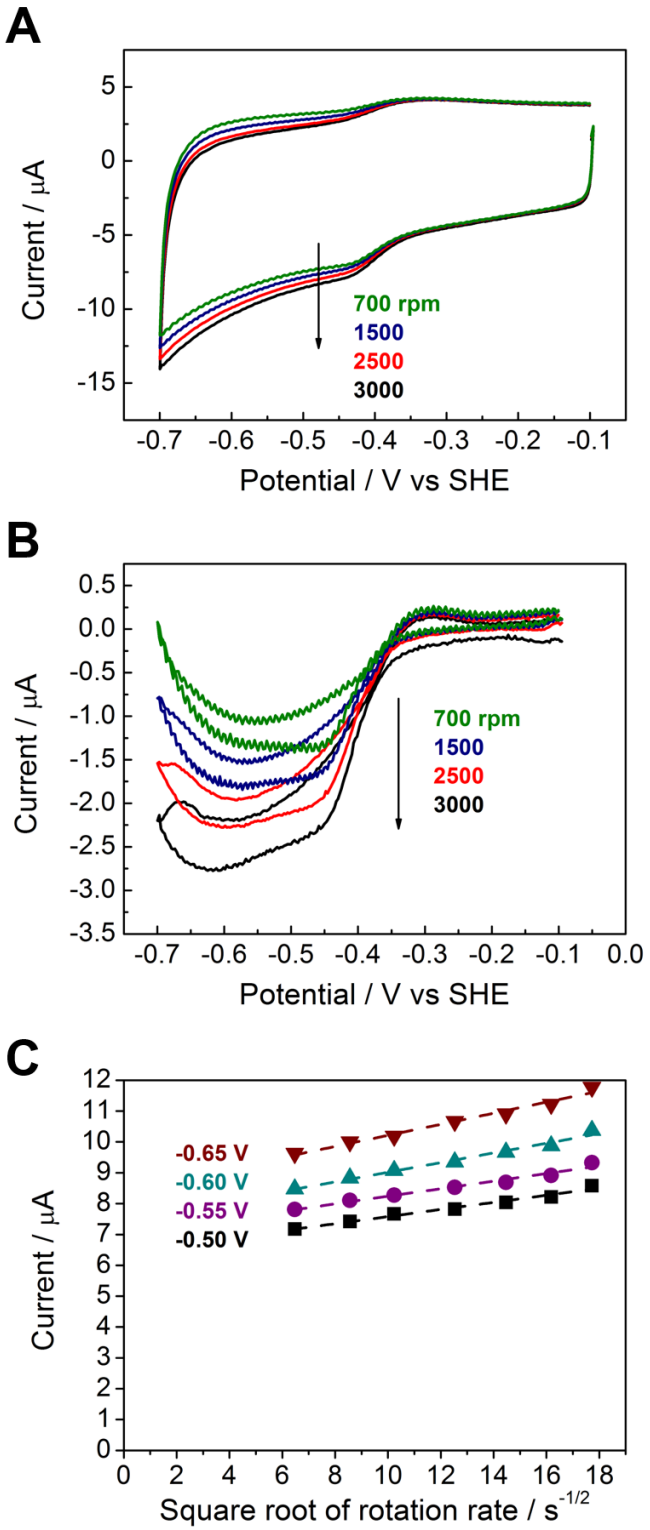

Figure 3.18 Rotation rate dependence of $NADP^+$ reduction by FNR@ITO/PGE. **A)** Cyclic voltammograms of FNR@ITO/PGE at various rotation rates. $NADP^+$ 50 μM, scan rate 20mVs^{-1}. **B)** Cyclic voltammograms subtracted by the voltammogram without $NADP^+$ **C)** Plot of uncorrected current against the square root of rotation rate at various potentials. Other conditions: buffer 25 mM MES 25 mM TAPS, pH 8.0, 20 °C, and purged with Ar before measurement.

The ideal limiting current for a rotating disk electrode is given by the Levich equation:

$$I = 0.620nFAD^{2/3}\omega^{1/2}v^{-1/6}C$$

where n is the number of electrons, F is the Faraday constant, A is the electrode area, D is the diffusion coefficient, ω is the rotation rate, v is the kinematic viscosity (0.01 cm^2s^{-1} at 20 °C for an aqueous solution), and C is the bulk concentration of the redox species. Figure 3.17C shows the plot of the uncorrected current at various potentials versus the square root of rotation rate. The linear relationship indicated that $NADP^+$ reduction at the FNR@ITO/PGE electrode was diffusion-limited. Although the measured current does not reach a true limiting value, the Levich equation could be used to give an estimate of the diffusion coefficient of $NADP^+$, using the slope of the plots in Figure 3.18C. The obtained diffusion coefficients are given below in Table 3.4, as well as the value from stationary measurements (using the Randles-Sevcik equation) and the range of literature values. At more negative potentials, the values from rotation measurements seem to approach that from the stationary measurement.

Table 3.4 Comparison of the diffusion coefficient of $NADP^+$ obtained from stationary measurments, rotating measurements, and literature values.

Method	Diffusion coefficient (cm^2s^{-1})
Rotation, -0.50 V *vs* SHE	9.9×10^{-7}
Rotation, -0.55 V	1.1×10^{-6}
Rotation, -0.60 V	1.6×10^{-6}
Rotation, -0.65 V	1.9×10^{-6}
Stationary (Randles-Sevcik eq.)	6.2×10^{-6}
Literature[39-42]	$2.0 – 6.7 \times 10^{-6}$

3.3 Conclusions and perspectives

Guided by the electrostatic nature of FNR binding to ferredoxin, I constructed a porous ITO electrode that made possible direct electrochemical measurements of FNR. Firstly, the non-turnover peaks of FNR are a measure of the amount of electroactive FNR molecules on the electrode. Due to the porous nature of the ITO electrode, typical FNR loading was more than hundreds of monolayer equivalents. Not all of the FNR molecules were equally participating in catalysis, indicated by the following observations: a) $NADP^+$/NADPH interconversion was diffusion-controlled, with the diffusion coefficient similar to that of NADPH in aqueous solution, suggesting that only FNR molecules near the solution interface were active, b) TOF values calculated from total FNR coverage were orders of magnitude below values from solution assays, and with the FNR molecules intact on the ITO electrode (as evident from a stable reduction potential for FNR) and with fast electron transfer to and from the electrode, the TOF is not expected to be drastically different from the natural case, and c) peak-like features assigned to the FNR non-turnover peaks could be observed in catalytic voltammograms in the presence of $NADP^+$. Therefore, the total FNR coverage as calculated from non-turnover peaks must be an over-estimation of the actively participating FNR molecules.

To the best of my knowledge, this work is the first demonstration of the direct electrochemistry of FNR. All previous electrochemical studies used an electron mediator, such as ferrocenemethanol or the whole electron transport chain (cytochrome c_6, PSI, ferredoxin).[19,22] In the case of direct electrochemistry, only a small amount of enzyme sample is needed, and once the enzyme is loaded onto an electrode, its environment (e.g. pH, buffer, substrate concentration) can be changed with ease. The system is simplified because there is no need for mediators that are possibly toxic or which may convolute results.

Because of the porous nature of the ITO electrode which allowed adsorption of FNR in large amounts (100 monolayer equivalents or more), the non-turnover signals of FNR could be observed clearly, which allowed a facile determination of its two-electron reduction potential, and the width of the non-turnover peaks can be correlated to the difference in reduction potential of the two one-electron steps. These results demonstrate an alternative method for measuring the reduction potential of FNR, and the resulting values are comparable to those in literature.

Experiments with enzymes on oxide materials in this group were previously limited either to stationary conditions, or with gas bubbled into the solution, a condition for which electrochemical behaviour is not well defined. This was because such oxide electrodes had been constructed on ITO glass plates by the doctor's blade method and these plate electrodes were unable to be rotated. With the electrophoretic deposition method, the loading of oxide particles is no longer limited to a flat glass plate, and any conductive support can be loaded onto with ease. One example of singular importance is the pyrolytic graphite edge (PGE) electrode, used in this group as rotatable electrodes, which can now act as a conductive support for an ITO layer (with the innovation attributed to Thomas Roberts), thus making possible experiments with FNR@ITO under rotation. The electrophoretic deposition method can also be used to create electrodes with a higher surface area to volume ratio, such as on Ti foil (both sides being conductive) or Ti wire (coiled up), which could be valuable where high currents or FNR loadings are required.

The activity of FNR on ITO can be considered a transfer of cofactor regeneration capability from a chloroplast to an inorganic electrode, thus creating a new hybrid material with potential applications in biotechnology, as will be described in the next chapter (Chapter 4). The FNR@ITO electrode can be coupled to $NADP^+$/NADPH dependent

enzymes, thus providing continuous cofactor recycling for enzyme-catalyzed organic reactions under electrochemical control.

3.4 References

(1) Carrillo, N.; Ceccarelli, E. A. *European Journal of Biochemistry* **2003**, *270*, 1900.

(2) Musumeci, M. A.; Ceccarelli, E. A.; Catalano-Dupuy, D. L. In *Advances in Photosynthesis - Fundamental Aspects*; Najafpour, M., Ed.; InTech: 2012.

(3) Arakaki, A. K.; Ceccarelli, E. A.; Carrillo, N. *The FASEB Journal* **1997**, *11*, 133.

(4) Ceccarelli, E. A.; Arakaki, A. K.; Cortez, N.; Carrillo, N. *Biochimica et Biophysica Acta (BBA) - Proteins and Proteomics* **2004**, *1698*, 155.

(5) Zhang, L.; Happe, T.; Melis, A. *Planta* **2002**, *214*, 552.

(6) Hemschemeier, A.; Fouchard, S.; Cournac, L.; Peltier, G.; Happe, T. *Planta* **2008**, *227*, 397.

(7) Hemschemeier, A.; Happe, T. *Biochimica et Biophysica Acta (BBA) - Bioenergetics* **2011**, *1807*, 919.

(8) Melis, A.; Happe, T. *Plant Physiology* **2001**, *127*, 740.

(9) Beer, L. L.; Boyd, E. S.; Peters, J. W.; Posewitz, M. C. *Current Opinion in Biotechnology* **2009**, *20*, 264.

(10) Hermoso, J. A.; Mayoral, T.; Faro, M.; Gómez-Moreno, C.; Sanz-Aparicio, J.; Medina, M. *Journal of Molecular Biology* **2002**, *319*, 1133.

(11) Piubelli, L.; Aliverti, A.; Arakaki, A. K.; Carrillo, N.; Ceccarelli, E. A.; Karplus, P. A.; Zanetti, G. *Journal of Biological Chemistry* **2000**, *275*, 10472.

(12) Deng, Z.; Aliverti, A.; Zanetti, G.; Arakaki, A. K.; Ottado, J.; Orellano, E. G.; Calcaterra, N. B.; Ceccarelli, E. A.; Carrillo, N.; Karplus, P. A. *Nat Struct Mol Biol* **1999**, *6*, 847.

(13) Batie, C. J.; Kamin, H. *Journal of Biological Chemistry* **1984**, *259*, 1976.

(14) Hurley, J. K.; Morales, R.; Martínez-Júlvez, M.; Brodie, T. B.; Medina, M.; Gómez-Moreno, C.; Tollin, G. *Biochimica et Biophysica Acta (BBA) - Bioenergetics* **2002**, *1554*, 5.

(15) Kurisu, G.; Kusunoki, M.; Katoh, E.; Yamazaki, T.; Teshima, K.; Onda, Y.; Kimata-Ariga, Y.; Hase, T. *Nature Structural Biology* **2001**, *8*, 117.

(16) Batie, C. J.; Kamin, H. *Journal of Biological Chemistry* **1981**, *256*, 7756.

(17) Batie, C. J.; Kamin, H. *Journal of Biological Chemistry* **1984**, *259*, 8832.

(18) Batie, C. J.; Kamin, H. *Journal of Biological Chemistry* **1986**, *261*, 11214.

(19) Madoz, J.; Fernández-Recio, J.; Gómez-Moreno, C.; Fernández, V. c. M. *Bioelectrochemistry and Bioenergetics* **1998**, *47*, 179.

(20) de Lacey, A. L.; Bes, M. T.; Gómez-Moreno, C.; Fernández, V. M. *Journal of Electroanalytical Chemistry* **1995**, *390*, 69.

(21) Madoz-Gúrpide, J.; Abad, J. M.; Fernández-Recio, J.; Vélez, M.; Vázquez, L.; Gómez-Moreno, C.; Fernández, V. M. *Journal of the American Chemical Society* **2000**, *122*, 9808.

(22) Fourmond, V.; Lagoutte, B.; Sétif, P.; Leibl, W.; Demaille, C. *Journal of the American Chemical Society* **2007**, *129*, 9201.

(23) Shipovskov, S.; Bonamore, A.; Boffi, A.; Ferapontova, E. E. *Chemical Communications* **2015**, *51*, 16096.

(24) Daido, T.; Akaike, T. *Journal of Electroanalytical Chemistry* **1993**, *344*, 91.

(25) Léger, C.; Elliott, S. J.; Hoke, K. R.; Jeuken, L. J. C.; Jones, A. K.; Armstrong, F. A. *Biochemistry* **2003**, *42*, 8653.

(26) Hirst, J. *Biochimica et Biophysica Acta (BBA) - Bioenergetics* **2006**, *1757*, 225.

(27) Heering, H. A.; Weiner, J. H.; Armstrong, F. A. *Journal of the American Chemical Society* **1997**, *119*, 11628.

(28) Keirns, J. J.; Wang, J. H. *Journal of Biological Chemistry* **1972**, *247*, 7374.

(29) Smith, J. M.; Smith, W. H.; Knaff, D. B. *Biochimica et Biophysica Acta (BBA) - Bioenergetics* **1981**, *635*, 405.

(30) Pueyo, J. J.; Gomez-Moreno, C.; Mayhew, S. G. *European Journal of Biochemistry* **1991**, *202*, 1065.

(31) Corrado, M. E.; Aliverti, A.; Zanetti, G.; Mayhew, S. G. *European Journal of Biochemistry* **1996**, *239*, 662.

(32) Faro, M.; Gómez-Moreno, C.; Stankovich, M.; Medina, M. *European Journal of Biochemistry* **2002**, *269*, 2656.

(33) Anusevičius, Ž.; Misevičienė, L.; Medina, M.; Martinez-Julvez, M.; Gomez-Moreno, C.; Čėnas, N. *Archives of Biochemistry and Biophysics* **2005**, *437*, 144.

(34) Sánchez-Azqueta, A.; Musumeci, M. A.; Martínez-Júlvez, M.; Ceccarelli, E. A.; Medina, M. *Biochimica et Biophysica Acta (BBA) - Bioenergetics* **2012**, *1817*, 1063.

(35) Sánchez-Azqueta, A.; Catalano-Dupuy, D. L.; López-Rivero, A.; Tondo, M. L.; Orellano, E. G.; Ceccarelli, E. A.; Medina, M. *Biochimica et Biophysica Acta (BBA) - Bioenergetics* **2014**, *1837*, 1730.

(36) Rodkey, F. L.; Donovan, J. A. *Journal of Biological Chemistry* **1959**, *234*, 677.

(37) Berg, J. M.; Tymoczko, J. L.; Stryer, L. *Biochemistry. 5th edition*; W. H. Freeman: New York, 2002.

(38) Bard, A. J.; Faulkner, L. R. *Electrochemical Methods*; 2nd ed.; Wiley, 2001.

(39) Moiroux, J.; Elving, P. J. *Journal of the American Chemical Society* **1980**, *102*, 6533.

(40) Domenech, A.; Garcia-Espana, E.; A. Ramirez, J.; Celda, B.; Carmen Martinez, M.; Monleon, D.; Tejero, R.; Bencini, A.; Bianchi, A. *Journal of the Chemical Society, Perkin Transactions 2* **1999**, 23.

(41) Wu, Z.; Jing, W.; Wang, E. *Electrochemistry Communications* **1999**, *1*, 545.

(42) Banks, C. E.; Compton, R. G. *Analyst* **2005**, *130*, 1232.

(43) Bugg, T. *Introduction to Enzyme and Coenzyme Chemistry* 2nd ed.; Blackwell, 2004.

(44) J. Timson, D. *Current Enzyme Inhibition* **2015**, *11*, 12.

Chapter 4

The electrochemical leaf: an $NADP^+$/NADPH regeneration system for enzyme-catalysed organic synthesis

Chapter 4

The electrochemical leaf: an $NADP^+$/NADPH regeneration system for enzyme-catalysed organic synthesis

Abstract

In the previous chapter (Chapter 3), ferredoxin-$NADP^+$ reductase (FNR) was shown to be active when adsorbed onto an ITO electrode, and this resulting FNR@ITO electrode is potentially applicable as a cofactor regeneration system. In this chapter, I demonstrate coupling of FNR@ITO to 3 different $NADP^+$/NADPH dependent enzymes: glutamate dehydrogenase (GLDH), isocitrate dehydrogenase (ICDH), and ketoreductase. In the case of GLDH, the coupled reaction was fast and observable as a current enhancement in both directions, *i.e.* amination of 2-oxoglutarate and deamination of L-glutamate. A bulk conversion experiment was also conducted for L-glutamate synthesis with product detection by NMR analysis. For ICDH, the decarboxylation of isocitrate was successfully coupled, and coupling to ketoreductase was confirmed by product analysis using GC-MS since the reaction was so slow that direct observation of the coupling by voltammetry was not possible. With a view towards a cofactor regeneration system for industrial use, the stability of FNR on ITO under various conditions, as well as its activity on different electrode materials, was investigated. The stability of FNR on ITO was measured from changes in its electroactive coverage, and more than 50% of the initial loading remained after 24 h at 20 °C. Decreased stability was observed with higher ionic strength of the buffer, higher temperature, and more negative applied potential. In addition to ITO, FNR was also active on another conducting oxide, fluorine-doped tin oxide (FTO), as well as some semiconducting materials ($SrTiO_3$ and ZrO_2).

4.1 Introduction

4.1.1 Cofactor regeneration systems in biocatalysis

In organic synthesis on the industrial scale, enzymes are valuable because of their high efficiency and specificity.[1] The enzyme class, oxidoreductases, require a cofactor in stoichiometric amounts to supply redox equivalents in order to catalyse reactions. For example, D-lactate dehydrogenase consumes NADH to convert pyruvate to lactate. Since nicotinamide cofactors (NAD(P)H) are too expensive to use in stoichiometric amounts, a regeneration system is required for a large-scale system.

A number of different approaches have been studied for a cofactor regeneration system.[2-5] The cofactor can be regenerated by a second enzyme, which has to be supplied with its own substrate. For the example of D-lactate dehydrogenase mentioned above, Whitesides used formate dehydrogenase to regenerate NADH, as shown in scheme 4.1.[6]

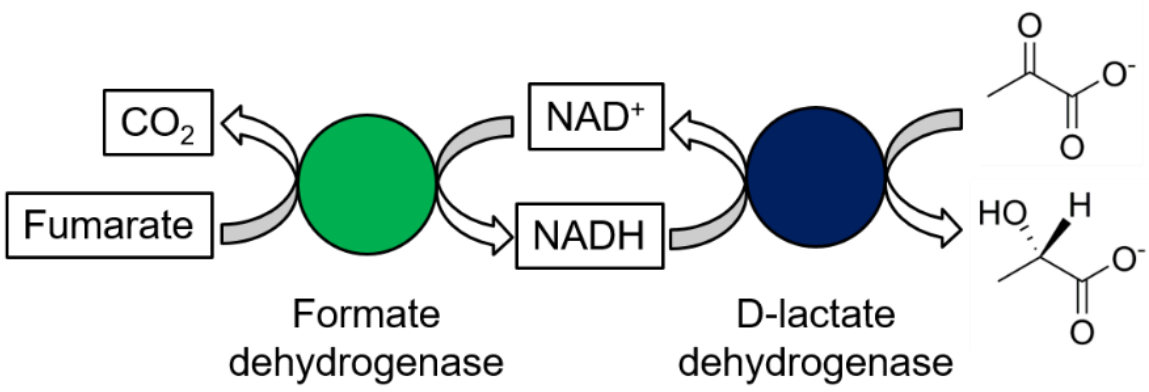

Scheme 4.1 NADH regeneration by formate dehydrogenase, coupled to D-lactate dehydrogenase

This method requires fumarate as a second substrate within the same solution. Although fumarate does not interfere with D-lactate production, and CO_2 can be purged out of the reaction solution to drive the equilibrium towards NADH production, the presence of a second enzyme and substrate in solution necessitates a further separation step downstream.

A similar system was also developed, based on glucose-6-phosphate dehydrogenase as the NAD(P)H regeneration catalyst.[7]

Molecular hydrogen can also be used to drive cofactor regeneration,[8] provided that there is a suitable enzyme that possesses both hydrogenase and diaphorase activities. Liese and coworkers used hydrogenase I from *Pyrococcus furiosus* (an anaerobic and hyperthemophilic species of Archaea), which can consume H_2 to drive $NADP^+$ reduction, as shown in Scheme 4.2.[9,10] They coupled this hydrogenase to an alcohol dehydrogenase which converts acetophenone to (S)-phenyl ethanol. The hydrogenase was still active when adsorbed onto beads made of graphite or glass, which could then be incorporated into a continuously-operated fluidized bed reactor. Since *Pyrococcus furiosus* is a thermophilic organism, the hydrogenase remains active up to 80 °C, but at such higher temperature ranges NADPH stability becomes an issue.[11]

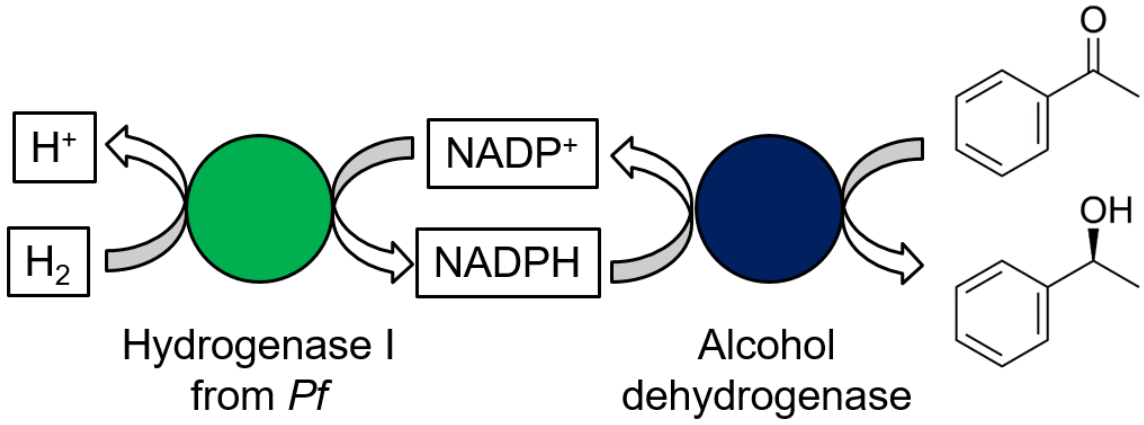

Scheme 4.2 NADPH regeneration by hydrogenase I from *Pyrococcus furiosus*, coupled to an alcohol dehydrogenase.

More recently, Reeve and Vincent have developed a modular, H_2-driven NADH regeneration system as shown in Scheme 4.3,[12-14] where hydrogenase 2 from *Escherichia coli* and a fragment of the soluble hydrogenase from *Ralstonia eutropha*, which respectively act as separate H_2 oxidation and NAD^+ reduction units, were connected electrically by being

co-adsorbed onto carbon particles. Using H_2 as the substrate for the driving cofactor regeneration simplifies the system in terms of product separation, but hydrogenases typically require an anaerobic environment. Adsorbing the regeneration enzymes onto particles allowed ease of collection and reuse.

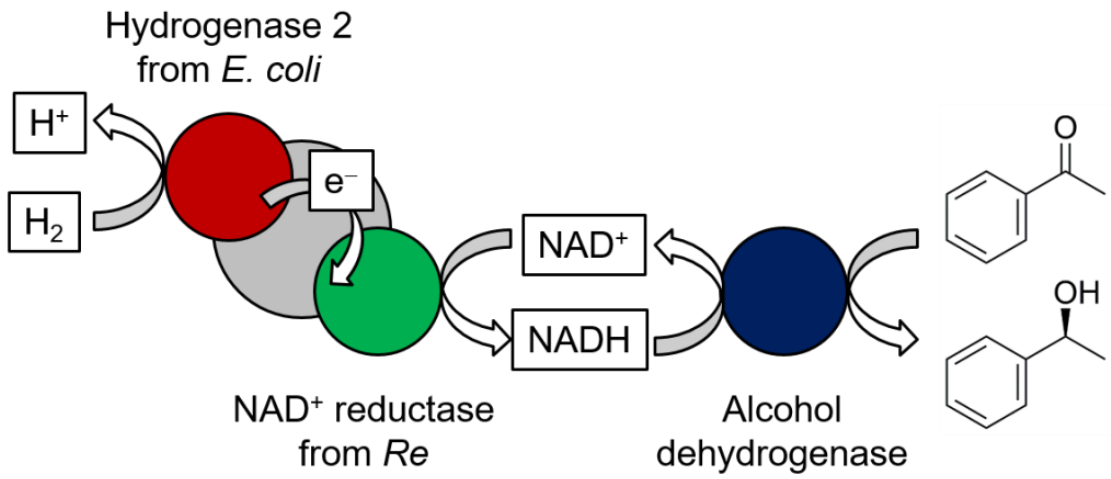

Scheme 4.3 NADH regeneration by two enzymes co-adsorbed onto conducting particles.

Another approach involves the use of whole cells for cofactor regeneration.[15] For example, whole cells of *Lactobacillus kefir* were used to convert (2,5)-hexanedione to (2R,5R)-hexanediol.[16,17] The driving force was supplied by adding glucose, which can supply 12 NADPH equivalents per molecule. However, not all of the driving force went towards substrate conversion, since some was required to provide energy for maintenance of general cellular function. Glucose metabolism then drives NADPH regeneration, which in turn drives the two reduction steps in the conversion of (2,5)-hexanedione to (2R,5R)-hexanediol. The use of whole cells can simplify the regeneration process as the active enzymes do not need to be purified, but it can also make optimization of the system difficult due to the large variety of components involved.

Non-enzymatic and non-biological systems have also been investigated.[3,18] A Rh-containing complex $[Cp^*Rh(bpy)(H_2O)]^{2+}$ (with $Cp^* = C_5Me_5$, byp = 2,2'-bipyridine) was

found to be active for reduction of $NAD(P)^+$ to the biologically active form of NAD(P)H (*i.e.* with hydrogen atoms in the (1, 4) positions, in contrast to the inactive form with (1, 6) positions).[19-24] Its catalytic cycle is shown in Scheme 4.4. The active (reduced) form of the complex can be generated by either a chemical reductant such as formate, or by an electrode. Although such chemical catalysts may be simpler to prepare compared to enzymes, a noble-metal complex is uneconomical unless the value of the product is relatively high (see also discussion in Section 4.3). In addition, the turnover frequencies of chemical catalysts are at least an order of magnitude lower than that of enzymes.

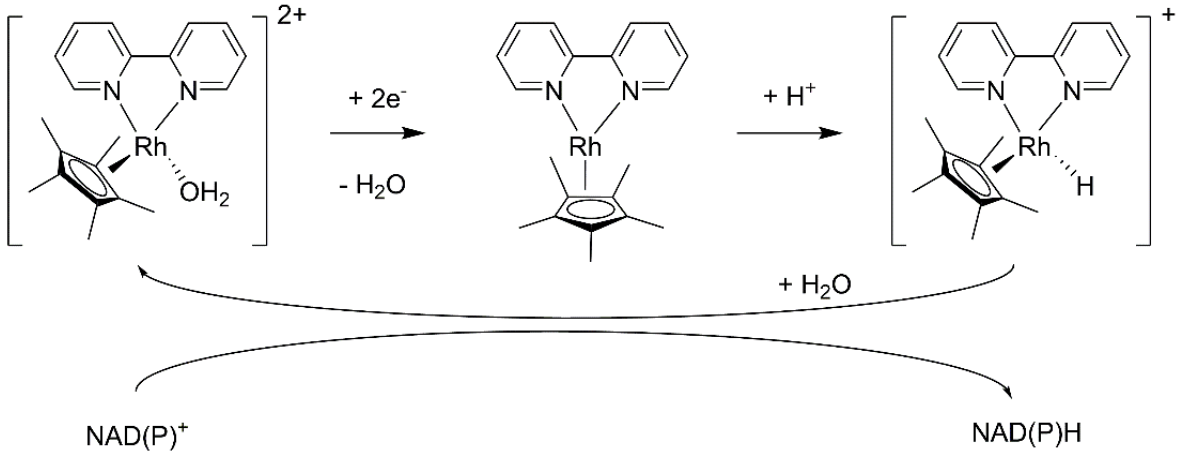

Scheme 4.4 A Rh complex for NAD(P)H regeneration.

As the reducing force, electrons could be considered the simplest and most convenient source, and various electrochemical methods for NAD(P)H regeneration have been studied, with various approaches shown in Scheme 4.5. The simplest case is the direct reduction of $NAD(P)^+$ at an electrode,[25-27] for example at a hanging mercury drop electrode,[28,29] glassy carbon,[30] or other metal electrodes.[31,32] Usually direct electrochemistry of NAD(P)H is irreversible, *i.e.* with very large separation of reduction and oxidation peaks, and the overpotential requirements are high (ca. -1.2 V *vs* SCE for NAD^+ reduction and 0.5 V *vs* SCE for NADH oxidation). The reaction proceeds by two steps of one-electron reductions, in which the first step is the formation of the NAD(P) radical. In the second step,

protonation can occur at two different sites, leading to either the biologically active 1,4 NAD(P)H or the inactive 1,6 NAD(P)H. Additionally, the NAD(P) radical can also dimerize to form $NAD(P)_2$, which is another loss pathway. The proportion of active NAD(P)H formed depends on many factors such as electrode material and overpotential, and in some cases the proportion can be as low as 10%.[31] Lower overpotential can lead to lower levels of dimerization as the population of NAD(P) radicals is smaller, but it also leads to slower overall rates. Clearly, anything less than 100% conversion to the active form is unacceptable for use in a practical NAD(P)H regeneration system, since in a system that generates 99% active form, the usable proportion of NAD(P)H would drop to 37% after 100 cycles and 0.0043% after 1000 cycles (see also Section 4.3 Figure 4.14).

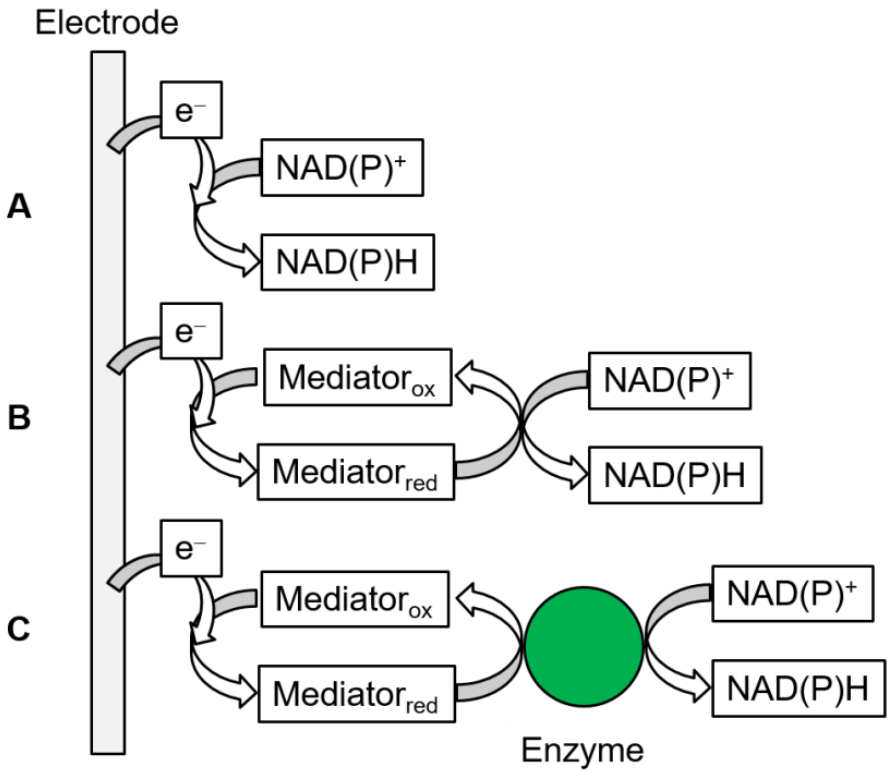

Scheme 4.5 Electrochemical methods for NAD(P)H regeneration. **A)** Direct **B)** via electron mediator **C)** via electron mediator and enzyme

Electron mediators can be used to transfer electrons from the electrode to $NAD(P)^+$, such as methyl viologen (MV), neutral red,[33] or the Rh complex mentioned previously.[22] Electron mediators can also be used to deliver electrons to enzymes which then catalyze the reduction of $NAD(P)^+$. For example, a tungsten wire was used as the working electrode to reduce FNR via MV as an electron mediator.[34] There are also examples in literature of direct electron transfer from an electrode to an enzyme with diaphorase activity: the aforementioned soluble dehydrogenase,[12] a hydrogenase from *Alcaligenes eutrophus* in solution with a Pt electrode,[35,36] and a subunit of mitochondrial Complex I.[37]

The various types of cofactor regeneration systems are summarised in the table below.

Table 4.1 Various approaches to cofactor regeneration

Type	Driving force	Advantages	Disadvantages
Enzymatic	Substrate for regeneration enzyme	NAD(P)H specificity High rates	Product separation Enzyme stability and cost
Whole-cell	Substrate for cell metabolism	Enzyme purification not required	Product separation High biomass waste Possible product degradation
Chemical	Chemical reductant	Relatively simple components	May not be NAD(P)H-specific Lower rates Noble-metal complex
Electrochemical	Electrode potential	Cheap electrical supply	Involves mediators Low specificity

4.1.2 The Electrochemical Leaf

As described in the previous section, each type of cofactor regeneration system has advantages and disadvantages. An ideal regeneration system should have the following qualities:

1. High specificity and rate – The system should only produce the biologically useful form of NAD(P)H with high turnover.

2. Electron driven – Electrons are a cheap and convenient source of reduction equivalent.

3. Mediator-free – Electron mediators can complicate the system, and some are toxic.

4. Air-stable – The system needs to be able to function in air for ease of use.

Chapter 3 described the basic electrochemistry and activity of ferredoxin-$NADP^+$ reductase (FNR), which is a natural candidate for an $NADP^+$/NADPH regeneration system. I draw a parallel between the activity of FNR in the biological leaf and FNR on an ITO electrode, as shown in Scheme 4.6 below.

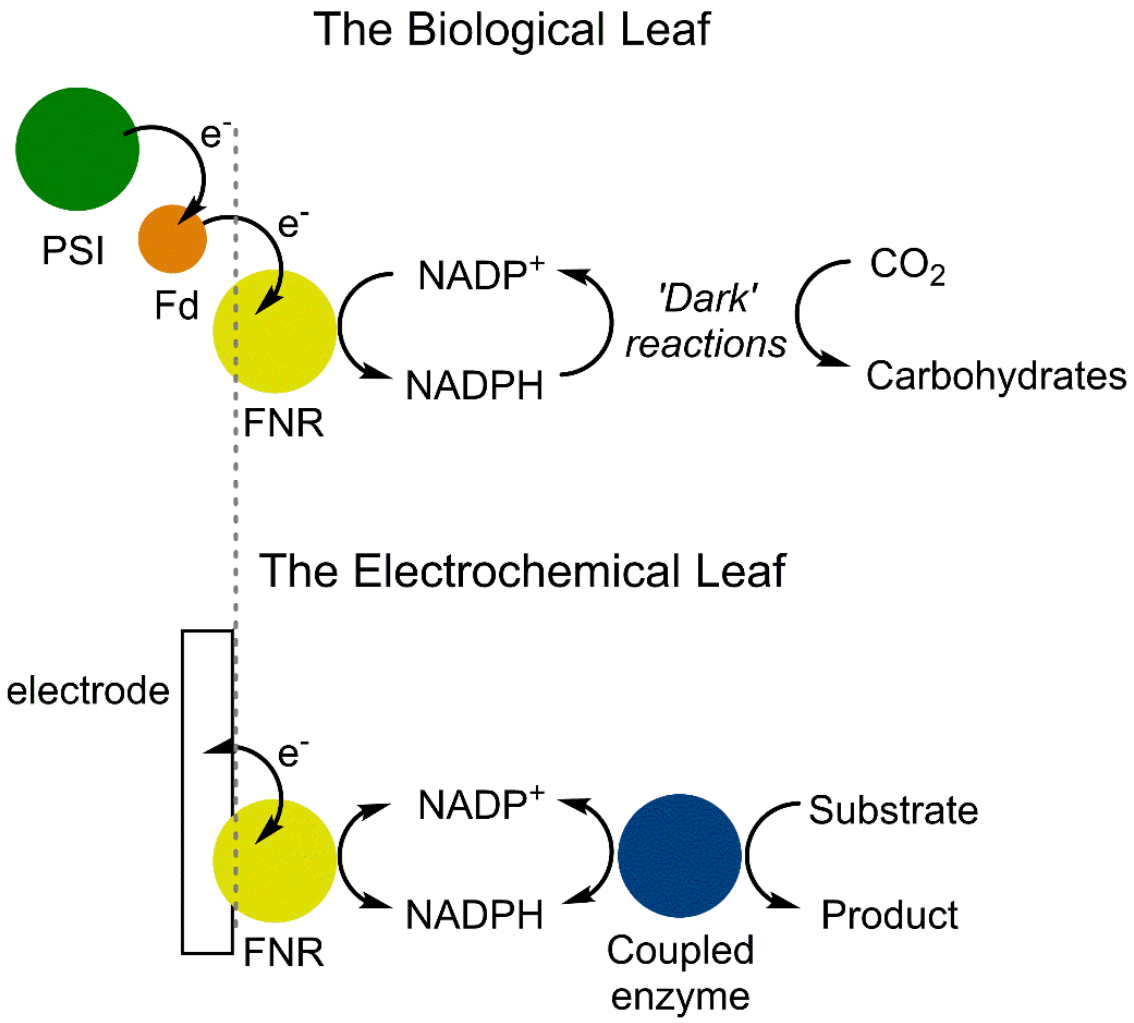

Scheme 4.6 Comparison of the biological leaf and the $NADP^+$/NADPH regeneration system, which we term the "electrochemical leaf".

In the biological leaf, the role of FNR is to receive electrons from Photosystem I *via* ferredoxin, and use those electrons to reduce $NADP^+$. The NADPH produced is then used in the downstream Calvin cycle, also known as 'Dark' reactions, which involve CO_2 assimilation. In the 'Electrochemical Leaf', the electron supply to FNR instead comes from an electrode, and the FNR@ITO electrode can then be coupled to an NADPH-dependent enzyme of choice. The system can also be driven in reverse, *i.e.* $NADP^+$ regeneration, by changing the applied voltage, which is not the usual function of FNR *in vivo*.

4.1.3 Aims of this chapter

In this chapter, I demonstrate that the FNR@ITO electrode can be coupled to various downstream enzymes for organic synthesis, using both $NADP^+$ and NADPH regeneration. The coupling can be directly observed by voltammetry in the case of fast downstream reactions, and direct product detection by other methods (e.g. NMR, GC-MS) is required for slower reactions. With a view towards a practical regeneration system, the stability of FNR on ITO was also investigated, and other electrode materials were examined for FNR adsorption and activity.

4.2 Results and discussion

4.2.1 Coupling to a secondary enzyme for organic synthesis

4.2.1.1 Glutamate dehydrogenase (GLDH)

To demonstrate the ability of the FNR@ITO electrode to act as an $NADP^+$/NADPH regeneration system, it was coupled to glutamate dehydrogenase, which catalyzes the conversion of 2-oxoglutarate (α-ketoglutarate) to L-glutamate in the presence of NH_4^+ and NADPH, as shown in the equation below.

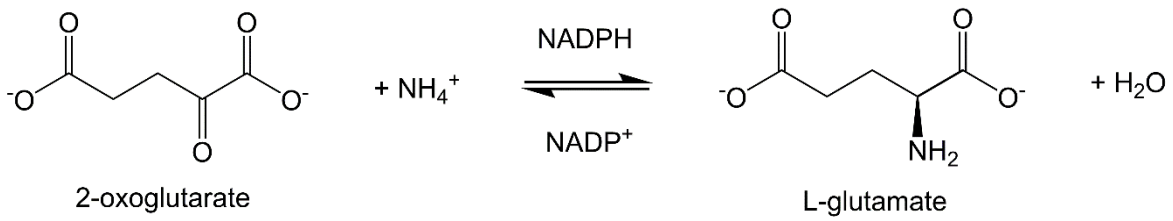

The effect of coupling was clearly observable as shown in Figure 4.1. An FNR@ITO/PGE electrode was constructed, then a cyclic voltammogram with $NADP^+$ (50 µM) was measured, and the expected $NADP^+$ reduction and NADPH oxidation peak-like currents were observed (black line). At a stationary electrode, catalytic currents behave as a peak due to depletion of the substrate near the electrode surface, *i.e.* diffusion-controlled. The substrates for GLDH (2-oxoglutarate 5 mM, $(NH_4)_2SO_4$ 10 mM) were already present in the cell solution, and they did not interfere with the electrochemistry of FNR, as the $NADP^+$ reduction and NADPH oxidation currents were unchanged.

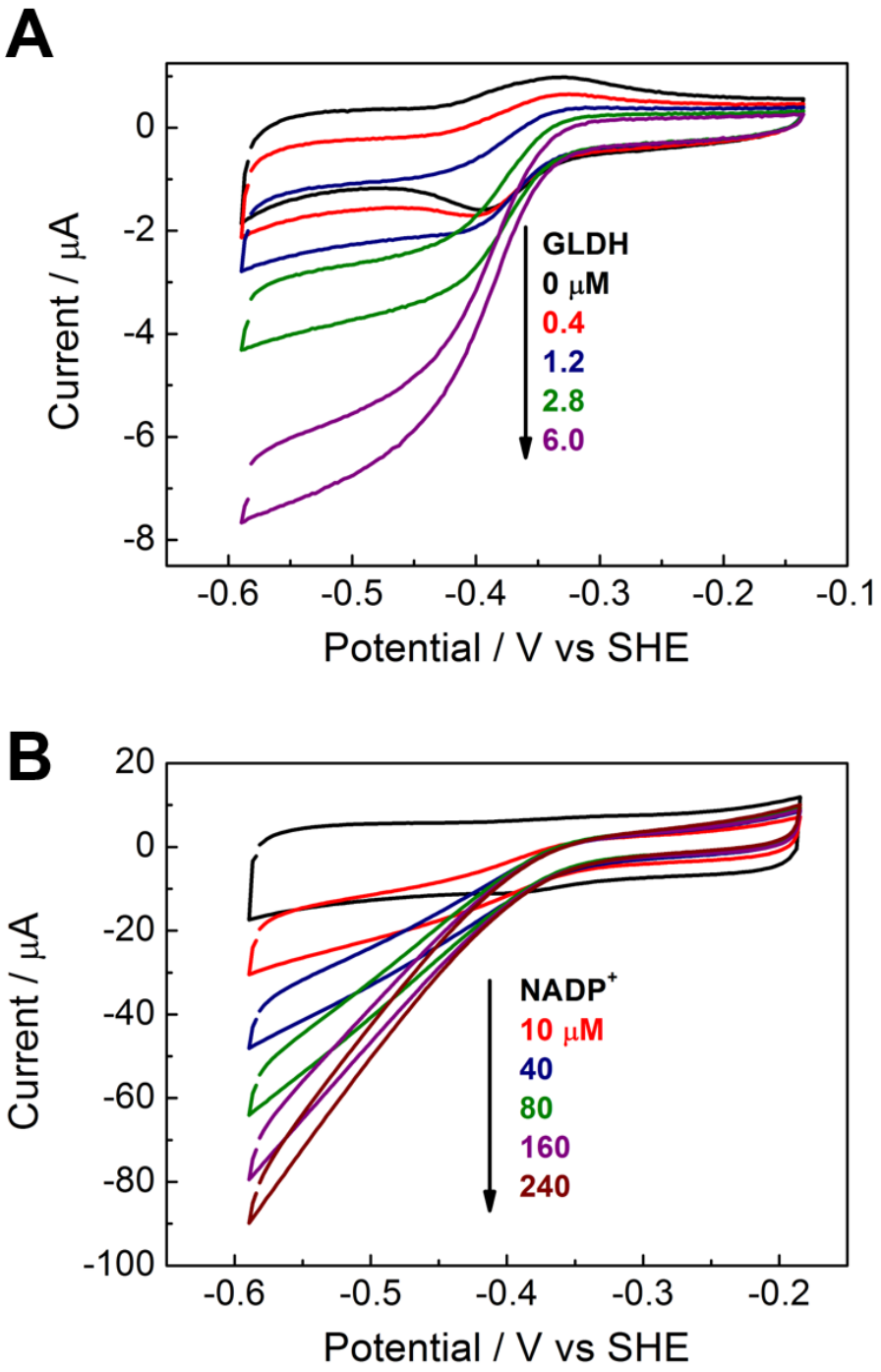

Figure 4.1 Reductive amination of 2-oxoglutarate by glutamate dehydrogenase contained in the cell solution, coupled to NADPH regeneration by FNR@ITO. **A)** FNR@ITO/PGE electrode, area 0.09 cm^2. NH_4^+ 20 mM, 2-oxoglutarate 10 mM, $NADP^+$ 50 µM initially (black) GLDH was added to the solution to final concentrations of 0.4, 1.2, 2.8, and 6.0 µM as indicated in graph. **B)** FNR@ITO/ITO glass electrode, area 1.5 cm^2. NH_4 20 mM, 2-oxoglutarate 20 mM, $NADP^+$ 10 µM at start (black). GLDH 2.0 µM was injected (red), then $NADP^+$ was increased to 40, 80, 160, and 240 µM as indicated in graph. Other conditions: MES 25 mM, TAPS 25 mM buffer solution pH 8, 20 °C, stationary electrode, scan rate 5 mV s^{-1}, solution purged with Ar before measurement.

On addition of GLDH to the solution (0.4 – 6.0 μM), the peaks converted to a catalytic reduction wave, the intensity of which increased with amount of GLDH. This indicates that the GLDH in solution is consuming the NADPH produced by FNR@ITO to produce L-glutamate, returning $NADP^+$ to the solution in the process. Even though the $NADP^+$ concentration at any point cannot be higher than the initial concentration, the flux of $NADP^+$ to the electrode surface is increased compared to the case without GLDH, which results in a reduction wave. In this way, the effect of coupling FNR@ITO to a downstream enzyme can be directly observed in a voltammogram. For Figure 4.1B, a similar experiment was conducted using an FNR@ITO/ITO glass electrode, and in this case the initial $NADP^+$ concentration was 10 μM (black trace). Again, NH_4^+ and 2-oxoglutarate were present in the solution from the start of the experiment. After GLDH was injected (red trace) a reduction wave was observed, the magnitude of which increased with $NADP^+$ concentration. These experiments, together with the diffusion-controlled nature of the voltammograms explained in the previous chapter (Chapter 3 Section 3.2.4), indicate that the limiting component is not the reaction catalysed by FNR but the amination reaction by GLDH, and that any sufficiently fast coupled reaction should be observable in a voltammogram.

The reverse reaction, i.e. the conversion of L-glutamate to 2-oxoglutarate, should also be possible, given the appropriate substrates and electrode potential. The FNR@ITO electrode serves as an $NADP^+$ regeneration system in this case. This proved to be challenging, as the rate for the reverse direction (0.59 s^{-1}) is much slower than that for the forward reaction (32 s^{-1}) as measured by solution assays.[38] Experiments were conducted in a manner similar to those in Figure 4.1, but with NADPH and L-glutamate instead of $NADP^+$, NH_4^+, and 2-oxoglutarate, and no oxidation current enhancement was observed (data not shown) under various substrate concentrations and buffer pH values. Therefore, optimisation of reaction conditions was required to facilitate this slower reverse downstream

reaction. GLDH was co-loaded with the FNR onto the ITO electrode, and the ITO electrode area was increased by changing the conductive support from PGE to ITO glass (Figure 4.2). By ensuring GLDH was in close proximity to FNR instead of in solution, the $NADP^+$ generated did not need to diffuse a large distance. In addition, using a slower scan rate (1 mVs^{-1}) allowed more time for the coupled reaction to occur .

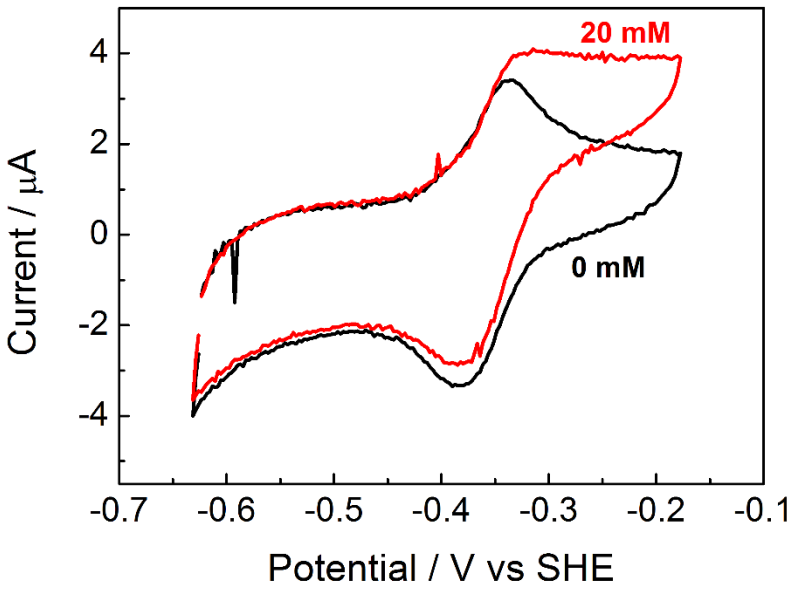

Figure 4.2 The oxidative deamination of L-glutamate by glutamate dehydrogenase coupled to $NADP^+$ regeneration by FNR@ITO; both enzymes were co-adsorbed onto the working electrode. NADPH 50 µM initially (black); L-glutamate injected to a final concentration of 20 mM (red). Other conditions: MES 25 mM, TAPS 25 mM buffer solution pH 8, 20 °C, stationary electrode, scan rate 1 mV s^{-1}, solution purged with Ar before measurement.

For the black trace in Figure 4.2, FNR (6 µL of 200 µM) and GLDH (8 µL of 200 µM) were loaded at the same time onto the electrode and incubated for 10 minutes at room temperature before recording the voltammetric response to NADPH (50 µM). The GLDH was not electroactive on the ITO electrode, and therefore was difficult to quantify, but the coloading of GLDH did not alter the signals of FNR (both non-turnover and turnover signals). The coupled reaction was initiated by injection of substrate for the GLDH reverse reaction, L-glutamate (20 mM), and enhancement of the oxidation current was observed (red

trace). This indicated a successful coupling, *i.e.* GLDH converted $NADP^+$ to NADPH, and $NADP^+$ was regenerated by the FNR@ITO electrode. The reduction peak was only slightly decreased, in contrast to the forward direction (see Figure 4.1), which is indicative of the slow reaction in the reverse direction.

Glutamate dehydrogenase serves as a tool to demonstrate coupling of organic synthesis to the FNR@ITO electrode, and its ability to act as both an NADPH and $NADP^+$ regeneration system as required. To confirm that L-glutamate was produced in these coupled reactions, a bulk conversion experiment was conducted by chronoamperometry at a reducing potential, and at the end of the experiment the cell solution was analyzed by NMR. The reverse direction (2-oxoglutarate production) was too slow to be monitored in this way. In all cases, the Pt counter electrode was located in a side arm linked to the main compartment by a glass frit in order to minimize oxidation of the product of the coupled reaction at the counter electrode. For these long chronoamperometry experiments with product detection at the end, the buffer system was changed to borate to avoid conflicting peaks in product analysis by NMR. Since a stationary electrode is not required for these experiments, the cell solution was continuously stirred by Ar bubbling to increase mass transport of the coupled enzyme and substrates. A FNR@ITO/Ti foil electrode was held at -0.46 V vs SHE (*i.e.* 110 mV of overpotential for $NADP^+$ reduction at pH 8.0) and glutamate dehydrogenase was present in solution (4 μM final concentration), and the current over time is shown in Figure 4.3. The ratio of the electrode area (double-sided Ti support, total area 2.6 cm^2) to cell volume (2 mL) was increased to improve performance by increasing product concentration and mass transport efficiency.

Before starting the chronoamperometry, $NADP^+$ (20 μM), NH_4^+ (20 mM) and 2-oxoglutarate (5 mM) were present in the solution, and a cyclic voltammogram was recorded to confirm the coupling with GLDH as in a similar manner to Figure 4.1. After

16 h, the current had dropped to a low background value, indicating that the substrate (2-oxoglutarate, 5 mM) had been exhausted (Figure 4.3). After 20 h, an aliquot of the cell solution was taken for NMR analysis, which showed the L-glutamate concentration to be 4.74 mM, and that no 2-oxoglutarate was detected. The 2-oxoglutarate to L-glutamate conversion was 95%, calculated from the starting 2-oxoglutarate concentration at 5 mM. An important metric for evaluating an NADPH regeneration system is the total turnover number (TTN), defined as the number of moles of product of the coupled reaction per mole of starting $NADP^+$, *i.e.* the average number of times $NADP^+$ has been recycled in the system. Note that TTN, a measure of turnover per cofactor, is different from the TON (turnover number) which is a measure of turnover per catalytic unit (FNR molecules in this case). For Figure 4.3, starting with 20 µM $NADP^+$, I obtained 4.74 mM L-glutamate (by NMR analysis), yielding a TTN of 237.

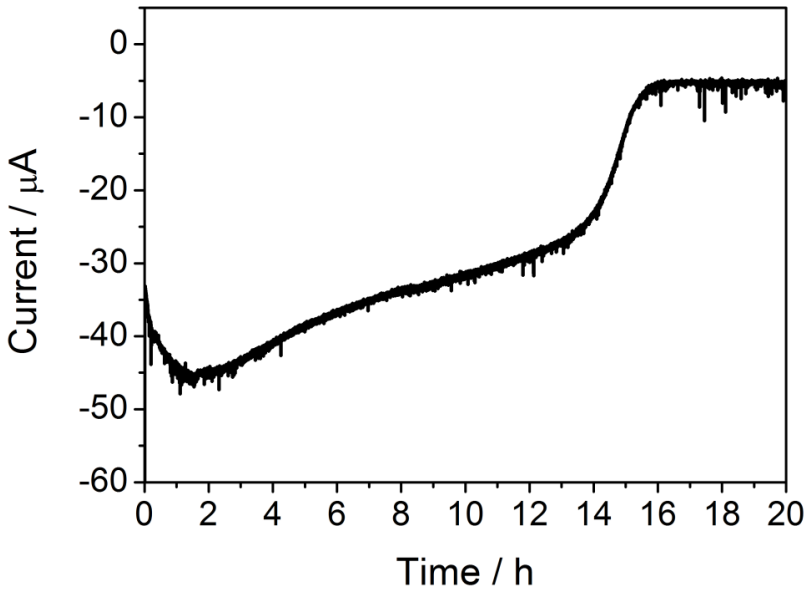

Figure 4.3 Chronoamperometry of L-glutamate synthesis coupled to FNR@ITO. Electrode: FNR@ITO/Ti foil (double-sided, 2.6 cm^2) Conditions: electrode potential -0.46 V vs SHE, 50 mM borate (pH 8.0), cell volume 2 mL, $NADP^+$ 20 µM, NH_4^+ 20 mM, 2-oxoglutarate 5 mM, glutamate dehydrogenase 4 µM, room temperature, constant Ar bubbling.

A further bulk conversion experiment was conducted in a slightly different manner to improve the measurement of the total charge passed to better correlate to the detected final product, and also to demonstrate the longer life-time of the system (Figure 4.4). The ITO electrode was constructed on ITO glass (area 3 cm^2) and FNR was loaded as described previously, and the current measurement was started with GLDH (4 µM) and NH_4^+ (20 mM) already in solution. Upon injection of $NADP^+$ (20 µM) a small reduction current was observed which decreased after 2 h when all of the $NADP^+$ was consumed (shown in the inset of Figure 4.4A). At this point, 2-oxoglutarate was injected to a final concentration of 5 mM, and a large increase in reduction current was observed, corresponding to the increased $NADP^+$ flux to the electrode due to GLDH consuming 2-oxoglutarate and converting NADPH to $NADP^+$, and the experiment continued until the current had once again dropped to the low background level. The charge passed at this point was consistent with total consumption of reactants. After 20 h, an aliquot of the cell solution was removed for NMR analysis.

The charge passed was also determined (Figure 4.4B) taking into account the small residual background current observed in all chronoamperometric experiments. Although the source of this background current is not clear, at least a part of it is attributable to traces of dissolved O_2 entering the cell from the atmosphere or through the glass frit, despite continuous bubbling with Ar. This can be taken as support for the system working in the presence of O_2, which would be typical in an industrial-scale setting. All experiments, including the purification of FNR, were conducted in a normal aerobic atmosphere on the bench, thus demonstrating the air-stability of the system and purging with Ar was conducted before electrochemical measurements only to eliminate O_2 reduction signals which would convolute the electrochemical results.

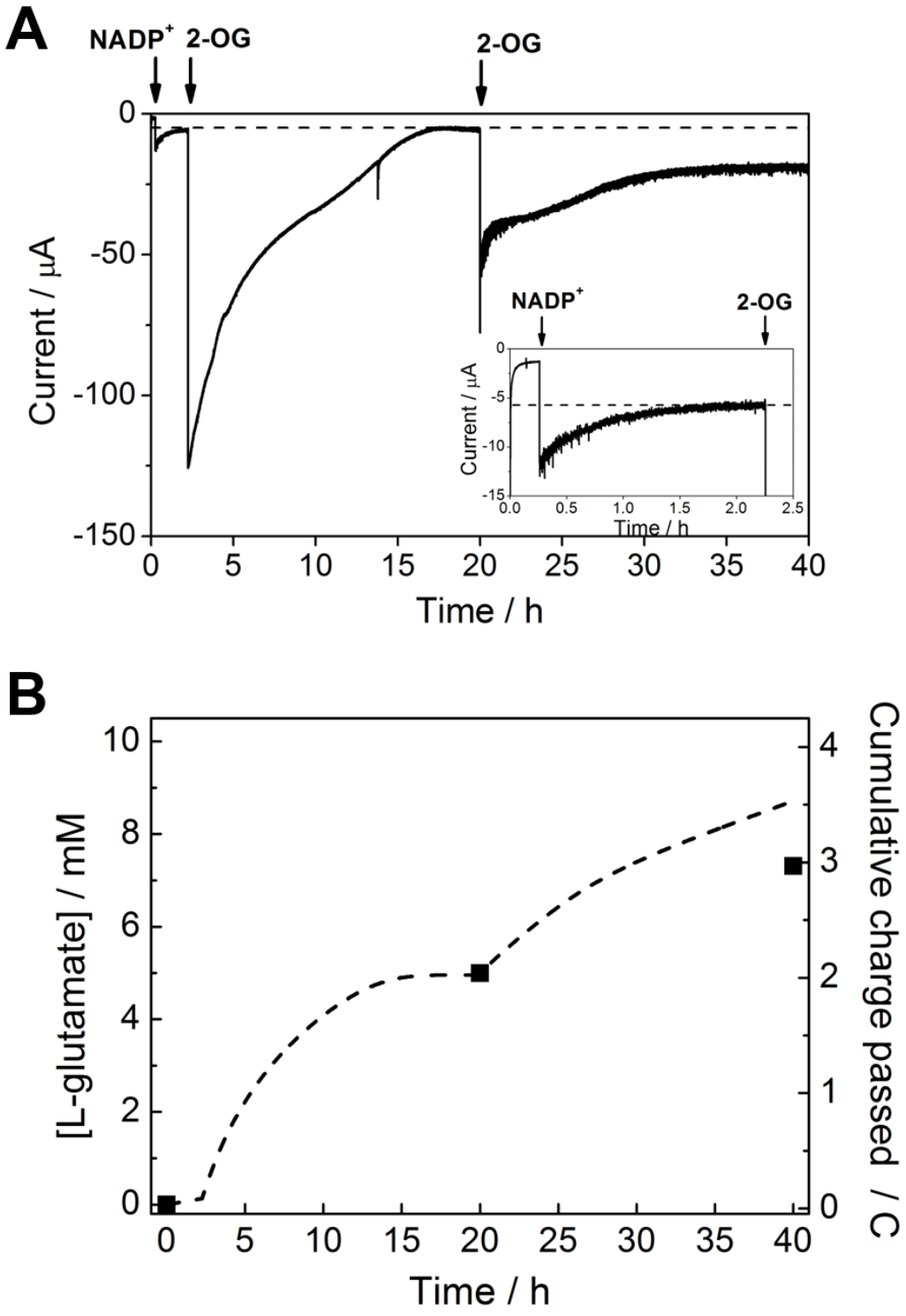

Figure 4.4 Electrochemical monitoring of L-glutamate synthesis coupled to FNR@ITO. **A)** Electrode: FNR@ITO/ITO glass (3 cm^2) Conditions: electrode potential -0.46 V vs SHE, 50 mM borate (pH 8.0), cell volume 2.1 mL, NH_4^+ 20 mM, glutamate dehydrogenase 4 μM, room temperature, constant Ar bubbling. Injections of $NADP^+$ 20 μM and 2-oxoglutarate 5 mM (twice) indicated by arrows. Inset shows magnification of the initial 0.6 h and $NADP^+$ injection. **B)** Background-subtracted cumulative charge passed (dashed line) from Figure 4.4A. The dots are direct measurement of L-glutamate by NMR analysis of cell solution.

As shown in Figure 4.4B, the amount of charge passed before addition of 2-oxoglutarate was 8.9 mC, equivalent to 4.6 x 10^{-8} moles of NADPH (concentration 22 μM, in 2.1 mL of solution). The charge passed after adding 2-oxoglutarate, corrected for background, was 2.01 C, equivalent to 1.04 x 10^{-5} moles of L-glutamate, giving a concentration of 4.97 mM in 2.1 mL of solution. From NMR, the L-glutamate concentration after 20 h was 5.2 mM, the increase in concentration from that expected (5.0 mM), indicating that some concentration had occurred, possibly due to evaporation of the cell solution from Ar bubbling. Based on the coulometric data, the TTN is 226: this compares with 261 using the quantity of $NADP^+$ and the NMR-derived L-glutamate concentration. Errors in coulometric calculations arise from the difficulty in subtracting background current, whereas errors in chemical quantities arise from the difficulty in accurately weighing small amounts of nicotinamide cofactor and reduction of solution volume over the course of the experiment. Care was taken to moisturize the Ar used to bubble the solution by running it through a water bubbler first, but a small evaporation of cell solution was unavoidable.

At 20 h, a further addition of 2-oxoglutarate was made, sufficient to give approximately 5 mM final concentration, then the experiment was continued for another 20 h. The immediate recovery of at least 50% of the expected reduction current showed that the FNR@ITO electrode was still active. From NMR, the L-glutamate concentration after 40 h was 7.31 mM, amounting to 73 % conversion (of 10 mM 2-oxoglutarate) and a TTN of 366.

NMR analysis was used for direct production detection and quantification. A sample of the cell solution was taken and mixed with D_2O in a 9:1 (cell solution:D_2O) ratio. Measurements of pure 2-oxoglutarate and L-glutamate at known concentrations were taken to establish the chemical shifts and obtain a calibration curve for peak area *vs* concentration. In general, the substrate and product concentrations had to be in the order of 1 mM or greater

to obtain a clear NMR spectrum. For 2-oxoglutarate, triplets at 2.34 and 2.91 ppm were observed, corresponding to the protons at positions 4 and 3 respectively. The peak areas were 1:1 as expected for 2 protons at each position. For L-glutamate, multiplet peaks at 1.99 and 2.25, and a quadruplet at 3.65 ppm were observed. The peak area ratios were close to 2:2:1, corresponding to the protons at the 3, 4, and 2 positions respectively.

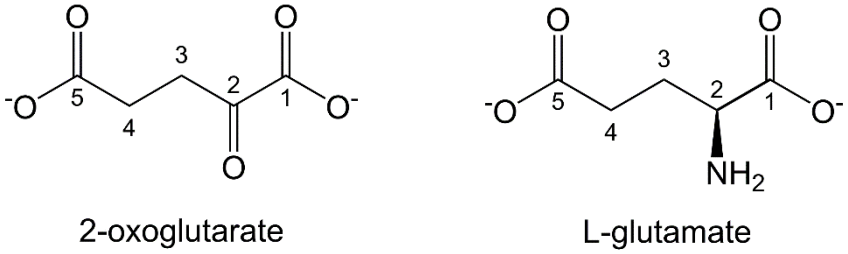

Figure 4.5A shows the NMR spectrum of the initial cell solution containing 5 mM 2-oxoglutarate. After chronoamperometry for 20 h a sample of the cell solution was taken for analysis, the NMR signals from 2-oxoglutarate had totally disappeared, and peaks corresponding to L-glutamate appeared (Figure 4.5B). This indicated the complete conversion of 2-oxoglutarate to L-glutamate within that period of time. For the sample taken after reinjecting 2-oxoglutarate and continuing the reaction for another 20 h, the signal from the cumulative L-glutamate produced, as well as the 2-oxoglutarate remaining in the cell solution, can be observed (Figure 4.5C).

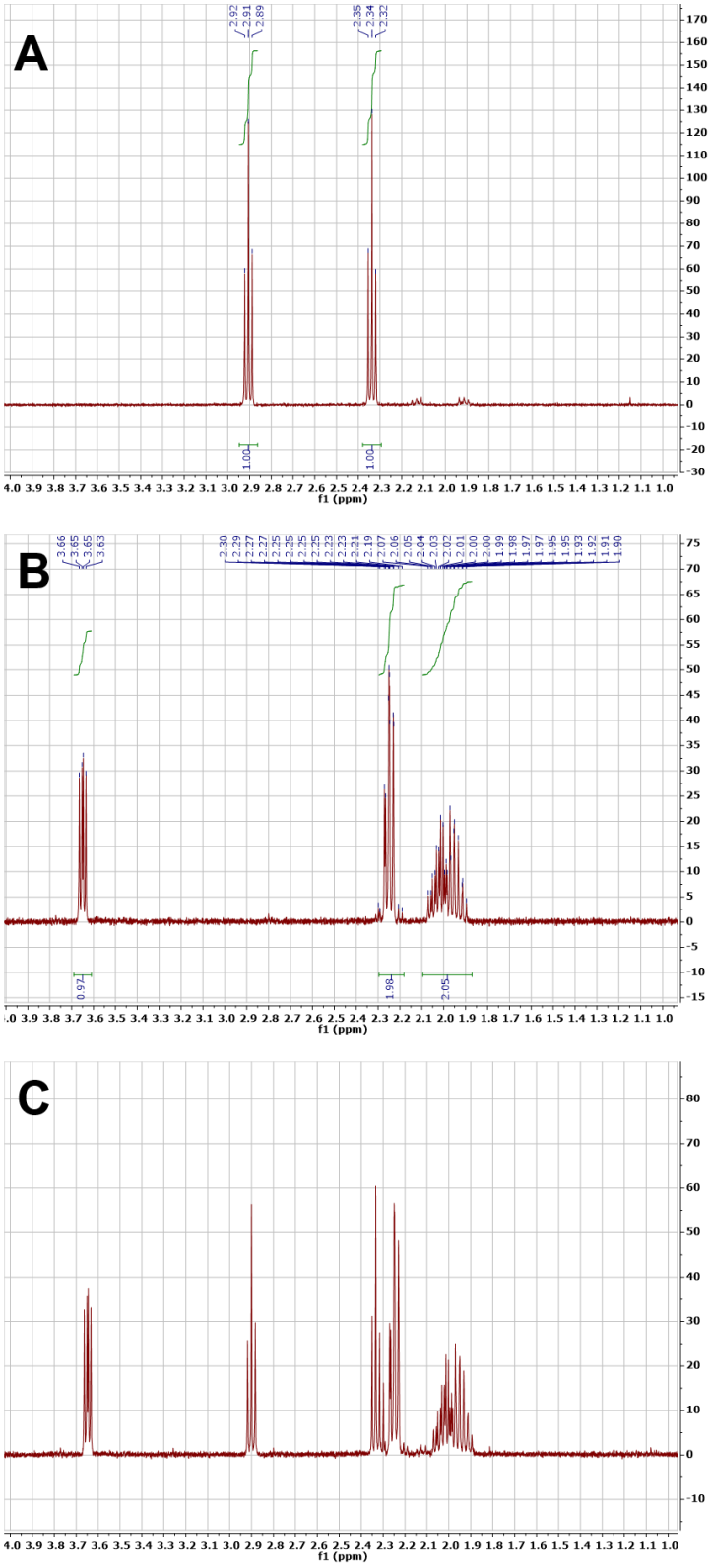

Figure 4.5 NMR spectra of cell solutions for the experiment shown in Figure 4.4 **A)** Initial cell solution, showing integrals for 2-oxoglutarate. **B)** After chronoamperometry for 20 h, showing integrals for L-glutamate. **C)** After chronoamperometry for 40 h. The peaks for 2-oxoglutarate can be observed, because 2-oxoglutarate was replenished at 20 h and was not exhausted. The L-glutamate peaks correspond to the cumulative amount produced over 40 h.

4.2.1.2 Isocitrate dehydrogenase (ICDH)

As another demonstration of coupling FNR@ITO to organic synthesis, I used isocitrate dehydrogenase (ICDH), which catalyses the conversion of 2-oxoglutarate and CO_2 to isocitrate in the presence of NADPH, as shown in the equation below.

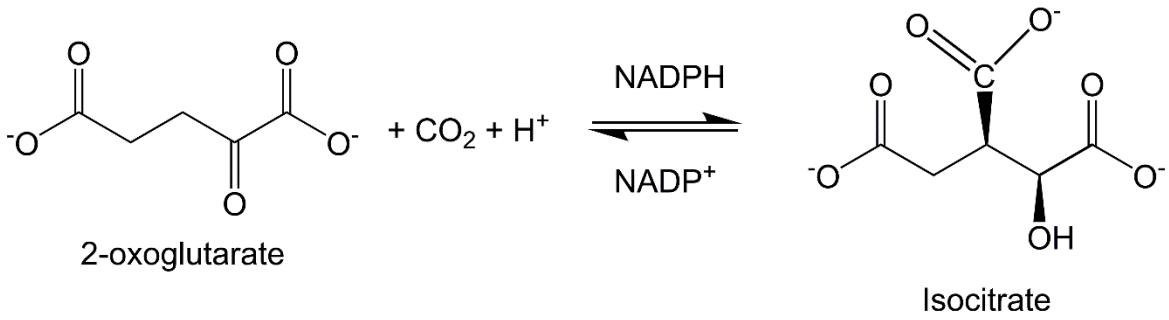

However, coupling in this NADPH-consuming direction, *i.e.* CO_2 assimilation, was not successful (data not shown). As the source of CO_2, I tried both CO_2 bubbled into the cell solution, as well as dissolving $NaHCO_3$ into the solution. The ICDH concentration was also increased, but still no current enhancement was observed. As the reaction in this direction is unfavourable *in vivo*,[39] it may not be possible to drive isocitrate production by this enzyme.

In Figure 4.6, the coupling of ICDH in the reverse direction (2-oxoglutamate production in the presence of $NADP^+$) to FNR@ITO was demonstrated in a similar manner to that of GLDH (Figure 4.2). Coupling could not be observed when the ICDH was in solution, but it was successful when proximity between ICDH and FNR was improved by coloading each enzyme on the electrode. Again, ICDH (24 µL of 310 µM) was co-immobilized onto the ITO electrode along with FNR at the start of the experiment, and the coupled reaction was initiated by injecting isocitrate (1 mM), resulting in enhancement of the oxidation current. In this case, a lower starting NADPH concentration allowed for the detection of a subtler current enhancement, which is typical for the slower coupled reactions

(unlike the fast GLDH-catalysed reaction). This demonstrates that the FNR@ITO electrode can be coupled to a variety of $NADP^+$/NADPH dependent enzymes, and the $NADP^+$/NADPH recycling by FNR is sufficiently fast so that the limiting component is the coupled enzyme.

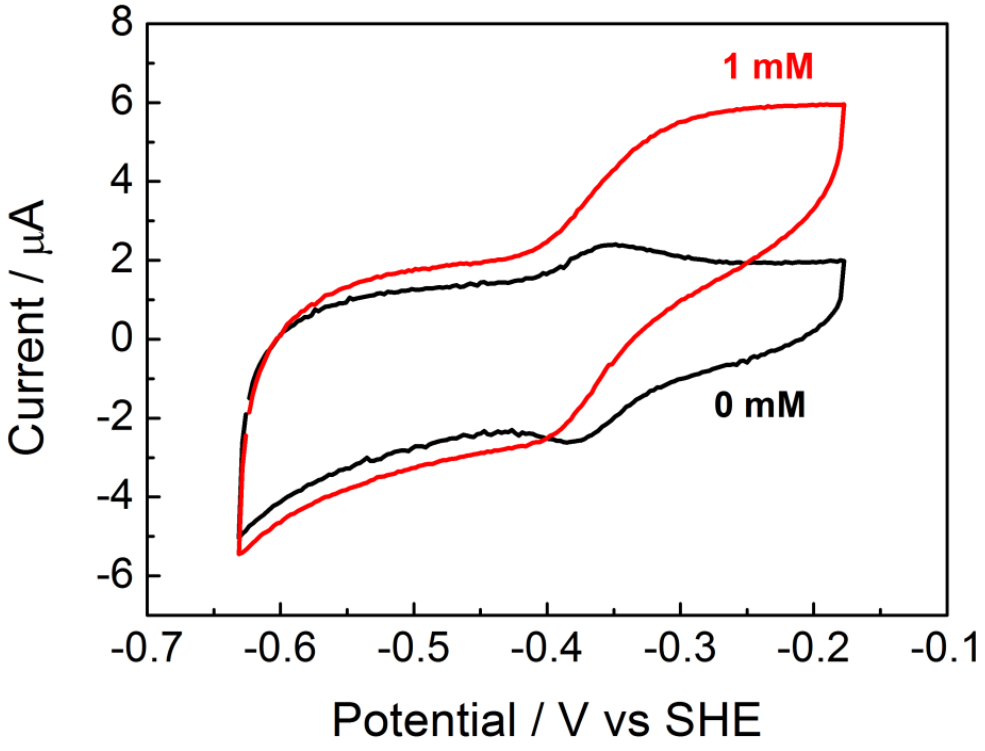

Figure 4.6 Oxidative decarboxylation of L-isocitrate by isocitrate dehydrogenase coloaded on FNR@ITO electrode, isocitrate 1 mM, NADPH 5 µM, Mg^{2+} 2 mM, scan rate 1 mV s^{-1}. Other conditions: MES 25 mM, TAPS 25 mM buffer solution pH 8.0, 20 °C, stationary electrode, solution purged with Ar before measurement.

4.2.1.3 Ketoreductase

As another demonstration of coupling, ketoreductase, which catalyses the conversion of ethyl-4-chloroacetoacetate (ECAA) and ethyl-(S)-4-chloro-3-hydroxybutyrate (ECHB), as shown in the equation below, was chosen.

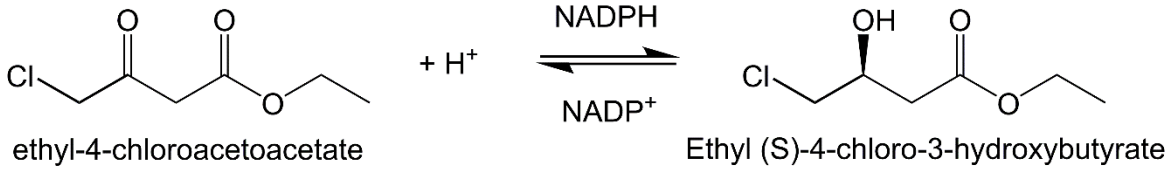

ethyl-4-chloroacetoacetate Ethyl (S)-4-chloro-3-hydroxybutyrate

This ketoreductase has a much slower rate than glutamate dehydrogenase which made the reaction more challenging; consequently, coupling was not observable in cyclic voltammograms under similar conditions as in the case of GLDH or ICDH, even with coloading of the ketoreductase onto the same electrode as FNR. Therefore, the coupling had to be observed by direct product detection after chronoamperometry for a long period. In a typical experiment, an FNR@ITO/Ti foil electrode (area 2.5 cm^2) was set up in a cell of volume 2 mL containing ECAA (10 mM). The electrode was held at -0.46 V vs SHE for 20 h, then the product was extracted from the cell solution into chloroform for analysis by GC-MS (the resulting product concentrations were too low for reliable NMR analysis).

Table 4.2 Reaction conditions and detected product concentrations for coupling reactions with ketoreductase

pH	Initial $NADP^+$ concentration	ECHB concentration after 20 h (μM)	Total Turnover number, TTN
7	5	97.0	19.4
8	5	11.1	2.2
6	10	214.3	21.4
7	10	303.5	30.3
8	10	452.0	45.2
8	1	6.1	6.1

Table 4.2 shows the buffer pH, initial $NADP^+$ concentrations, product (ECHB) concentration after 20 h and TTN. The largest TTN was obtained by starting with 10 μM $NADP^+$, in which the final amount of product obtained was 450 μM in 2.5 mL of cell solution, corresponding to a TTN of 45. The variation in data was large as reproducibility was low, owing to the slow rate of the ketoreductase. Some of the experiments were conducted with lower initial $NADP^+$ concentrations, in order to increase the TTN, but this resulted in lower TTNs, probably due to the lower rate for the ketoreductase when the NADPH present was too low.

4.2.2 Stability of FNR@ITO

Results from Section 4.2.1 showed that the FNR@ITO electrode was still active after operating continuously for 20 – 40 h, but stability was difficult to quantify since the concentration of the substrate for the coupled enzyme decreased over time. In this section, I aim to quantify the stability of FNR on ITO without other convoluting factors, and this was accomplished by tracking the change in FNR coverage over time under various conditions.

4.2.2.1 Buffer ionic strength

The interaction between FNR and the ITO electrode is expected to be electrostatic, based on the similarities to the interaction with its biological redox partner, ferredoxin.[40] Therefore, a buffer with a higher ionic strength should result in weaker binding between FNR and the electrode. As shown in Figure 4.7, first an FNR@ITO/PGE electrode was made, then cyclic voltammograms were recorded in the usual working buffer (MES 25 mM, TAPS 25 mM, pH 8.0) and FNR coverage determined from the area of the non-turnover peaks. The electrode was then left in the same buffer solution for a period of time, before recording voltammograms again (black trace). A fresh FNR@ITO/PGE electrode was then

made and FNR coverage measured in a similar manner, then the electrode was placed in a buffer containing additional NaCl 1 M for a period of time, before returning it to the original buffer to measure the FNR coverage (red trace). In the low ionic strength buffer (*i.e.* no additional NaCl), FNR coverage was stable over the course of the 1 h experiment, However, at an extremely high ionic strength, FNR coverage decreased to less than 50 % of the initial value after 1 h. If the interaction between FNR and ITO is mainly electrostatic, then an increase in buffer ionic strength would lead to screening of the electrostatic force, leading to weaker binding. These results indicate that the working buffer for FNR should have as low an ionic strength as possible while still retaining buffer capacity and conductivity. In addition, experiments conducted in phosphate buffer (data not shown) usually led to very small or non-existent FNR non-turnover signals, and consequently no $NADP^+$ reduction activity and as such phosphate ions should be avoided. This is due to the strong affinity of phosphate ions for metal oxide surfaces[41] which can cause FNR to be displaced from the ITO electrode.

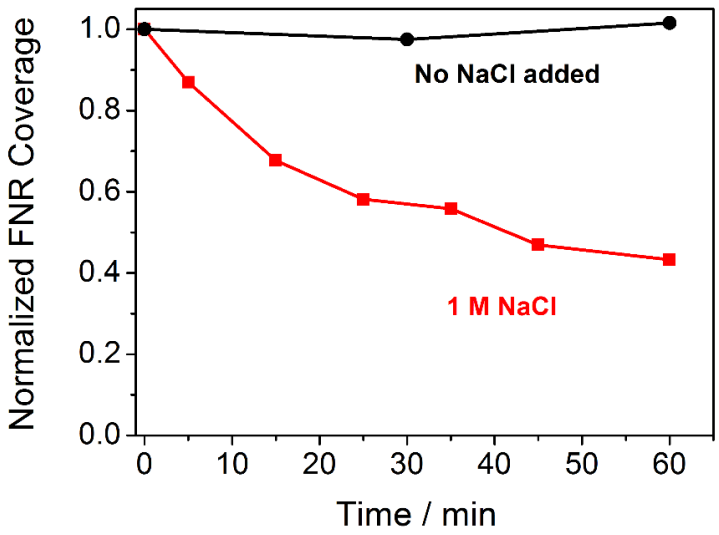

Figure 4.7 Time course of FNR coverage of FNR@ITO/ITO glass electrodes in buffers with different salt concentrations. Black: MES 25 mM, TAPS 25 mM, pH 8.0 buffer. Red: the same buffer with additional NaCl 1 M. Other conditions: 20 °C, no applied potential (cell off or disconnected) between cyclic voltammogram measurements.

4.2.2.2 Applied potential

The results from the Chapter 3 indicated that the potential applied to FNR can affect the stability of its FAD group. More specifically, the reduced form of FAD is much more likely to dissociate from FNR than the oxidized form, based on the differences in reduction potential of free FAD (-0.25 V vs SHE at pH 8.0) and FNR-bound FAD (-0.38 V). This is confirmed by monitoring changes in FNR coverage similar to the previous section, with a cyclic voltammogram taken every 30 min and holding the FNR@ITO electrode at a certain potential in between cyclic voltammogram measurements (Figure 4.8).

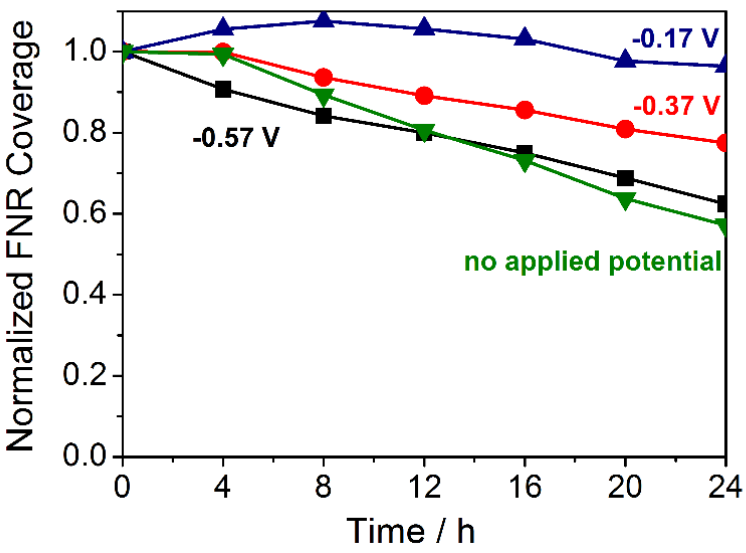

Figure 4.8 Time course of FNR coverage of FNR@ITO/ITO glass electrodes under different applied potentials. Black: -0.57 V *vs* SHE, Red: -0.37 V, Blue: -0.17 V, Green: no applied potential (cell off). Other conditions: MES 25 mM, TAPS 25 mM, pH 8.0 buffer. 20 °C

4.2.2.3 Temperature

The effect of temperature on the stability of FNR@ITO was also investigated (Figure 4.9A). Using a fresh FNR@ITO/ITO glass electrode for each experiment, the cell was held at different temperatures (30 °C, 20 °C, and 10 °C) while cyclic voltammograms were

measured every 30 min with the cell off in between, and FNR coverage was determined from the non-turnover peaks. At 10 °C, the coverage of FNR did not significantly change after 24 h, while at 20 °C and 30 °C the coverages decreased to less than 60 % and 15 % of the initial values, respectively. Longer-term storage of FNR@ITO was also investigated (Figure 4.9B) by making an FNR@ITO/ITO glass electrode, measuring FNR coverage by cyclic voltammograms, then storing the electrode in buffer in a cold room at 4°C for approximately 24 h before taking another measurement. After 1 week of this process, almost 40% of the initial FNR coverage remained, and FNR was confirmed to still be active by adding $NADP^+$ and observing a reduction current (data not shown). Temperature can affect the stability of FNR@ITO electrodes in mainly two ways: the FNR-ITO interaction and the FAD-FNR interaction, but it was difficult to distinguish between the two cases from this experiment.

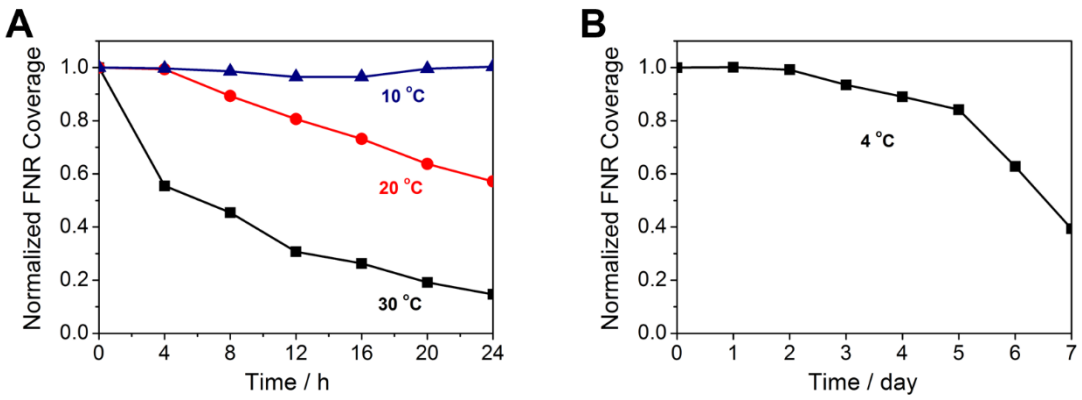

Figure 4.9 Time course of FNR coverage of FNR@ITO/ITO glass electrodes at various temperatures. **A)** Cell was held constantly at 30 °C (black), 20°C (red), and 10 °C (blue). **B)** The FNR coverage was measured at 20°C, then the FNR@ITO/ITO glass electrode was stored in buffer at 4 °C between measurements. Other conditions: MES 25 mM, TAPS 25 mM, pH 8.0 buffer, no applied potential (cell off or disconnected) between cyclic voltammogram measurements.

4.2.3 FNR on other electrode materials

Experiments up to this point have been based on the strong interaction between FNR and ITO, and it was of interest to investigate whether FNR could display similar behaviour on other electrode materials. First, I investigated fluorine-doped tin oxide (FTO), another commonly used conducting oxide material. The FTO electrode was constructed by electrophoretic deposition onto ITO glass and pyrolytic graphite edge (PGE) electrodes, similar to the construction of ITO electrodes. The results are shown in Figure 4.10 and Table 4.3.

Table 4.3 The potential, peak width at half maximum height, and coverage of FNR on an FTO electrode in the pH range 5.0 – 9.0. The average values from 3 repeats is shown, ± 1 standard deviation.

pH	FNR potential (mV vs SHE)	Half-height peak width (mV)		Coverage (pmol cm^{-2})
		Anodic	Cathodic	
5.0	-270 ± 3	58 ± 2	64 ± 4	90 ± 10
6.0	-320 ± 2	64 ± 5	75 ± 4	80 ± 20
7.0	-356 ± 3	67 ± 4	62 ± 7	80 ± 30
8.0	-387 ± 6	66 ± 12	65 ± 8	100 ± 50
9.0	-418 ± 2	50 ± 1	52 ± 1	100 ± 30

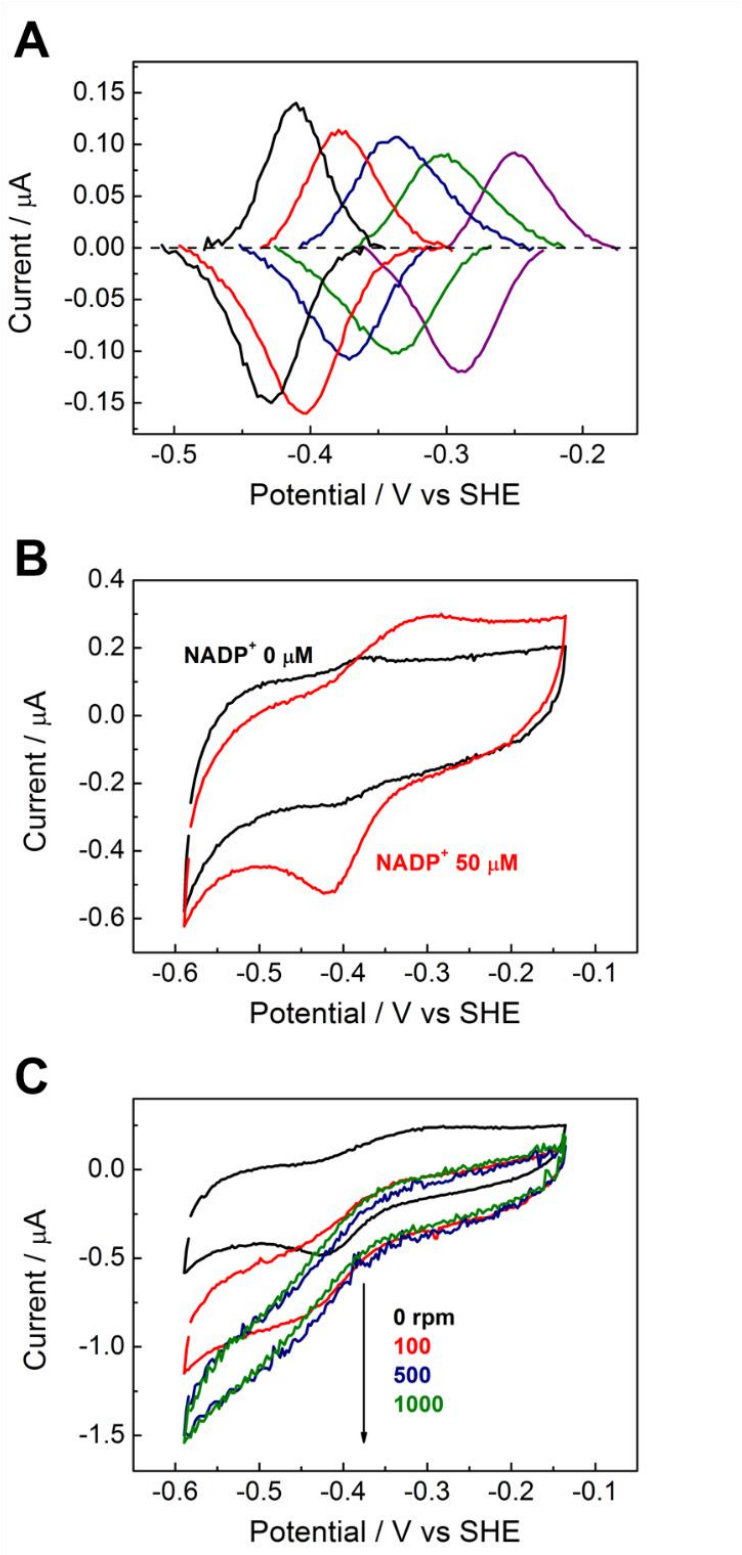

Figure 4.10 Electrochemistry of FNR on FTO electrodes. **A)** Background-subtracted currents showing non-turnover peaks of FNR, from pH 9.0 (right) to pH 5.0 (left). **B)** Cyclic voltammograms of FNR at a stationary FTO electrode with $NADP^+$ 0 µM (black) and 50 µM (red). **C)** Cyclic voltammograms under rotation with $NADP^+$ 50 µM. Other conditions: buffer solution containing MES 25 mM, TAPS 25 mM, pH 8.0, 20 °C, and purged with Ar before measurement.

The reduction potential of FNR on FTO and its degree of change in the pH range 5.0 – 9.0, as measured from the non-turnover signal (Figure 4.10A), were not significantly different from the case on ITO (see details of FNR@ITO in Chapter 3 Section 3.2.3). The peak width at half-maximum of the non-turnover peaks, which reveals information on the degree of cooperativity between the two one-electron transfer steps, were also relatively unchanged, although the spread of the values was larger. The most noticeable difference was in the coverage, in which the overall FNR coverage on FTO was smaller than on ITO, and the trend with pH was not as large. The lower overall coverage compared to ITO is partly due to the difference in particle size (FTO *ca.* 200 µm, ITO *ca.* 50 µm), leading to lower available surface for FNR adsorption for the same geometric area. Another possible reason is the difference in surface chemistry – ITO is composed of 90 % indium and 10 % tin, whereas FTO is mainly tin oxide with fluorine present at a much lower doping level.

The activity of FNR was also tested on ZrO_2 and $SrTiO_3$ (Figure 4.11), both of which are n-type semiconductors with large band gaps (5.0 eV and 3.25 eV, respectively). Within the potential range of interest for $NADP^+$/NADPH interconversion (-0.6 – 0.0 V vs SHE), both materials should not be very conductive, as is typical for n-type semiconductors.

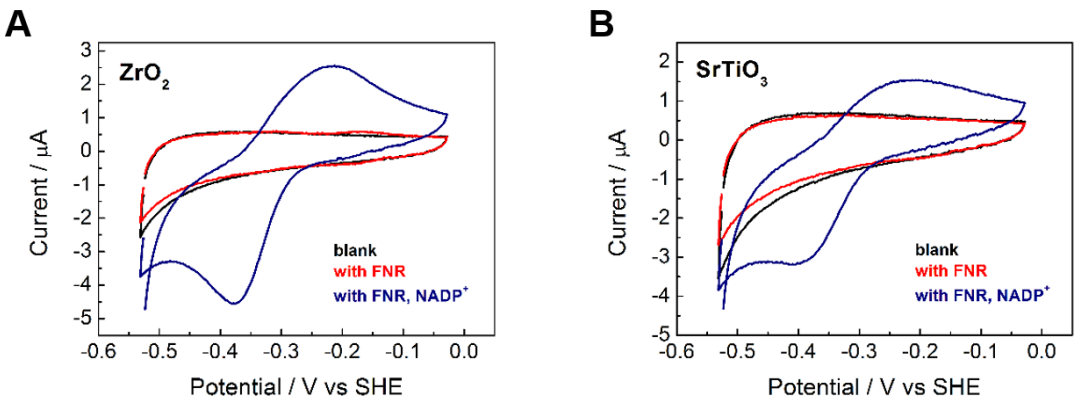

Figure 4.11 Electrochemistry of FNR on ZrO_2 (A) and $SrTiO_3$ (B), in both cases showing the blank (black), after FNR loading (red) and after injection of $NADP^+$ 50 µM (blue). Other conditions: MES 25 mM and TAPS 25 mM buffer pH 7.0, 20 °C, scan rate 5 mV/s, stationary electrode.

Previous work by Bachmeier[42] showed that catalytic activity by enzymes (hydrogenase and carbon monoxide dehydrogenase) adsorbed on TiO_2 electrodes was biased towards reduction, even though the enzymes themselves are bidirectional. This is because the flat band potential of TiO_2 is near the reduction potential for H^+ and CO_2 reduction, thus the TiO_2 electrode has a high carrier density in the reducing region but low carrier density in the oxidizing region.

The ZrO_2 and $SrTiO_3$ electrodes were made by the doctor's blade method on ITO glass. No non-turnover peaks were observed after dropping FNR onto the electrodes (red trace in Figure 4.11A and B). Even though the layer thickness and surface character of ZrO_2 and $SrTiO_3$ are not expected to be very different from ITO, *i.e.* the electrode layer should be porous and possessing a large surface area for FNR adsorption, the FNR adsorbed throughout the layer would not be electroactive since the material has low conductivity in this potential range. It was surprising that catalytic currents were recorded on addition of $NADP^+$ (50 μM, blue trace), indicating that electroactive FNR molecules must be present. The likely adsorption site for FNR molecules is on the ITO glass (which acts as a conductive support) at the junction with the oxide material; the oxide particles may help to anchor the FNR molecules in contact with the back conductive support.

On ZrO_2, a pair of small redox peaks were observed at approximately -0.20 V vs SHE after loading FNR, which corresponds to the potential of free FAD. This suggests that some FNR molecules have released their FAD group and therefore have become inactive, although the reason this occurs on ZrO_2 is unclear. It is possible that the FNR solution also contained some free FAD, which is a byproduct during the enzyme purification process. Another feature common to results on both ZrO_2 and $SrTiO_3$ is the decrease in oxidation current compared to the case of ITO. This is due to the nature of n-type semiconductors; the hole concentration is lower, thus limiting the rate of electron transfer in the anodic direction.

4.2.4 FNR on templated ITO

Modification of the method for constructing the ITO layer could potentially change the coverage of FNR and the access of $NADP^+$. One method is to use a template, around which, the ITO layer could be formed, followed by removal of the template. Polystyrene (PS) beads can be used as templates, as they are easily removed by heat treatment or reaction with base or organic solvent and they can be obtained with uniform size, and have been previously used to construct a templated ITO layer.[43,44] The PS beads (1 μm diameter) were loaded onto ITO glass by suspending a piece of ITO glass vertically in a suspension of PS beads, then leaving the suspension to evaporate either at room temperature or heating at 40-50 °C. In this way, the PS beads self-assemble as ordered layers at the liquid-solid interface which gradually moves downwards as the suspension evaporates (Figure 4.12A, B). In the next step, the PS bead layer is infiltrated with a suspension of ITO particles in ethanol (Figure 4.12 B, C). Since the ITO particles (approximately 50 nm diameter) are smaller than the spaces between PS beads, they were able to infiltrate through. Finally, the electrode was heated at 450 °C for 1 h, to remove the PS beads, leaving behind the templated ITO layer (Figure 4.12 E, F).

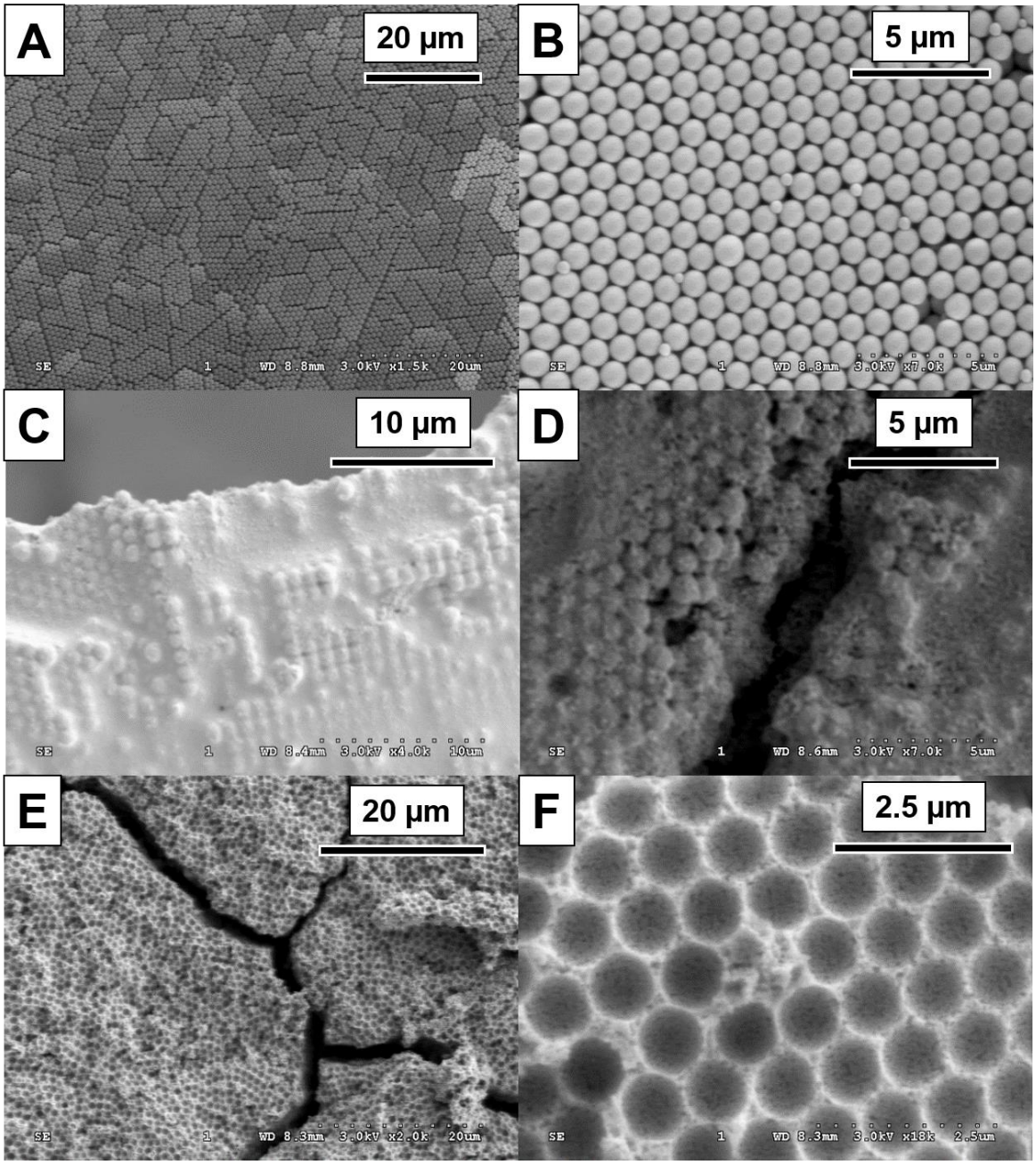

Figure 4.12 SEM images of PS-templated ITO electrodes. **A, B)** PS beads assembled onto ITO glass. **C, D)** PS bead layer after dropping ITO suspension. **E, F)** Templated ITO layer after heating to remove PS beads.

Alternatively, templated ITO electrodes were constructed by pre-mixing ITO and PS beads in a suspension, then using that suspension in the doctor's blade method on ITO glass, then heating under the same conditions (450 °C for 1 h) to remove the PS beads (Figure 4.13). Pores made by PS beads can be observed, but these were more disordered than

compared to Figure 4.12 where the PS beads were loaded on first before infiltrating with ITO particles.

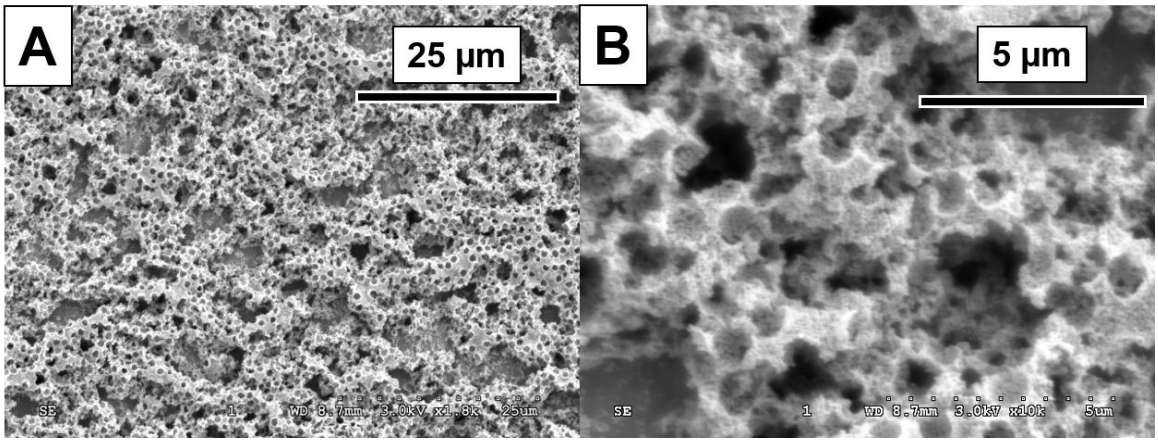

Figure4.13 SEM images of a templated ITO electrode, made by pre-mixing ITO particles and PS beads, then heated to remove the beads.

Figure 4.14 shows the cyclic voltammograms of these templated ITO electrodes (A: ordered PS layer, B: pre-mixed PS and ITO) after loading with FNR as described previously, and injection of $NADP^+$.

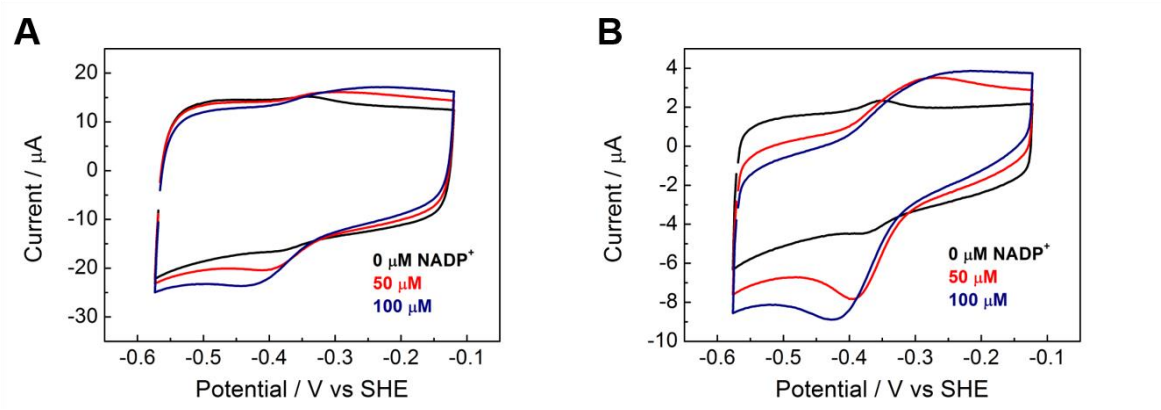

Figure 4.14 Cyclic voltammograms of FNR loaded onto templated ITO electrodes constructed by **A)** sequentially self-assemble PS beads then infiltrate with ITO particles and **B)** pre-mixing PS and ITO then constructing the ITO layer. Non-turnover peaks (black) and after addition of $NADP^+$ to 50 µM (red) and 100 µM (blue). Other conditions: MES 25 mM and TAPS 25 mM buffer pH 8, 20 °C, scan rate 5 mV/s, stationary electrode.

In both cases, the FNR coverage as calculated from its non-turnover peak area (ordered PS layer 56 pmol cm^{-2}, pre-mixed PS and ITO 32 pmol cm^{-2}) were much smaller than that of FNR on untemplated ITO electrodes constructed by electrophoretic deposition (typically >200 pmol cm^{-2}, see Chapter 3 Section 3.2.3). However, a clear comparison cannot be made, because of the variation in the overall ITO layer thickness, which in turn determines the available area for FNR to adsorb. The turnover frequency (TOF), calculated from the $NADP^+$ reduction current and FNR coverage, was not significantly different from the untemplated electrodes (ordered PS layer 0.3 s^{-1}, pre-mixed PS and ITO 0.5 s^{-1}, untemplated typically 0.4 s^{-1}). It was noted in Chapter 3 Section 3.2.4 that TOF calculation in this way gives an underestimate, as there are always redundant (*i.e.* not participating in catalysis) FNR molecules. Since the untemplated ITO electrodes constructed by electrophoretic deposition were already porous (see Chapter 3 Section 3.2.2), the additional porosity from PS bead templating did not seem to create a significant difference in $NADP^+$/NADPH catalysis by FNR.

4.3 Conclusions and perspectives

Building on the new hybrid FNR@ITO electrode material explained in the previous chapter, this chapter investigated its potential application as a cofactor regeneration system coupled to enzyme-catalyzed organic reactions. First, glutamate dehydrogenase (GLDH) provided a fast system to demonstrate coupling, in which a stereospecific reaction was continuously driven by NADPH recycling. Although the product (L-glutamate) is not particularly valuable, it serves to show how a coupled organic reaction can be observable by voltammetry. The reverse direction, 2-oxoglutarate production driven by $NADP^+$ recycling

at FNR@ITO, was also achieved by providing the appropriate substrates and electrode potentials.

In this chapter I also investigated the activity of FNR on other electrode materials. Fluorine-doped tin oxide (FTO), another commonly used conducting oxide material with similar properties to ITO, was shown to also be compatible with FNR, although the coverage of FNR was smaller. The properties of FNR itself was not affected by the electrode material. Semiconductor materials ($SrTiO_3$, ZrO_2) were also able to interact with FNR, although in a different manner from ITO and FTO.

The stability of FNR on ITO electrodes was investigated by measuring the changes in FNR coverage over time under different conditions, and it was found that stability increased with lower buffer ionic strength, more positive applied potential, and lower temperature. The FNR@ITO electrode can be stored at 4 °C, at least on the scale of one week, while retaining a significant portion of adsorbed and intact FNR, which is desirable for ease of storage in a commercial application. The trends for potential and temperature are in opposition to that for a high catalytic rate of $NADP^+$ reduction (more negative potential, higher temperature), meaning that there is a trade-off between stability and rate.

Throughout the coupled reaction experiments in this chapter, it was evident that the limiting component is not the FNR@ITO electrode, as $NADP^+$/NADPH interconversion by FNR is fast. The overall rate is governed by either the rate of the coupled enzyme or the diffusion of $NADP^+$/NADPH from FNR@ITO to the coupled enzyme. For the former, the only way is to increase the amount of the coupled enzyme. A higher temperature would increase the rate, but also may complicate matters as it may cause degradation of the FNR@ITO electrode as well as NADP(H). For the latter case, cell design and electrode design are key in improving performance. A clear example is the reverse reaction of GLDH

(L-glutamate to 2-oxoglutarate), in which GLDH had to be coloaded with FNR on to the same ITO electrode for successful coupling. By coloading, the distance through which $NADP^+$ has to diffuse is significantly smaller. Looking at the *in vivo* situation, the environment of FNR in the chloroplast is perfectly adapted for maximal diffusion efficiency. Various enzymes and redox molecules of the are either embedded in membranes or otherwise confined to small volumes. Future optimisation of the electrochemical leaf both in terms of electrochemical cell and electrode design will take inspiration from nature and mimic the aspects of the chloroplast.

At which point can a cofactor regeneration system be considered economically viable? This relies on many factors: the cost of the cofactor, the cost of the system, its efficiency (in terms of Total Turnover Number, TTN, *i.e.* how many times it can recycle the cofactor), its specificity in regenerating the biologically useful form of the cofactor (*e.g.* 1,4-NADPH over 1,6-NADPH, which can be quantified by the percentage of usable cofactor remaining after 1 regeneration cycle), and the value of the product of the coupled reaction.

Assuming all of the regenerated cofactor reacts to produce the product and 1 mole of cofactor is required per 1 mole of product, the total amount of product after N number of regeneration cycles is

$$P = \int_0^N s^x \, C_0 \, dx$$

where P is the total number of moles of product, s is the specificity of the cofactor regeneration system, and C_0 is the initial number of moles of the cofactor. The amount of product made after certain numbers of cycles is shown in Figure 4.14 for various values of s.

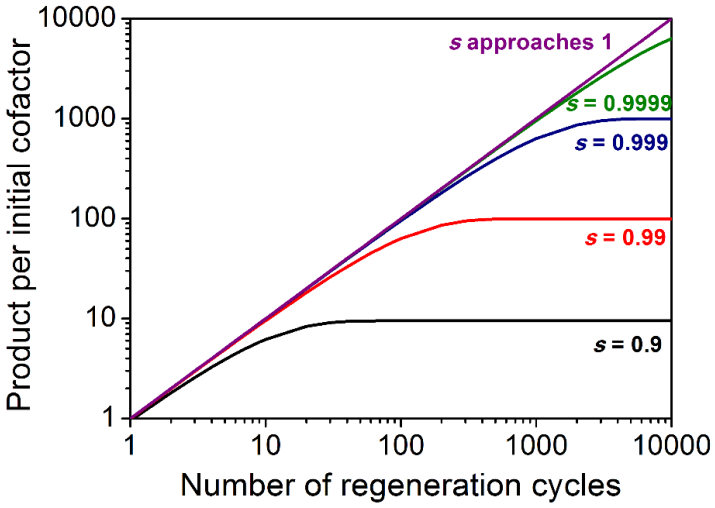

Figure 4.14 Relationship between total moles of product per mole of initial cofactor (P/C_0) and number of regeneration cycles, for various values of specificity (s, the percentage of usable cofactor remaining after 1 regeneration cycle)

Even with a specificity of 0.999 (*i.e.* 99.9 % of the cofactor remains usable after 1 regeneration cycle), the amount of product reaches a limiting value after approximately 1000 regeneration cycles. For an enzymatic regeneration system such as FNR@ITO, the specificity approaches 1, and the amount of product made is equal to the number of regeneration cycles completed, *i.e.* the TTN. This underscores the importance of specificity in a regeneration system, and indicates that only enzymatic systems are viable for usage in very high number of regeneration cycles (upwards of 10,000).

In simplified terms, the total cost to produce 1 mole of product can be written as

$$Cost_{total} = \frac{1}{P} Cost_{Fixed} + \frac{1}{TTN} Cost_{Cofactor} + Cost_{Variable}$$

where P is the total amount of product in moles, $Cost_{Fixed}$ is the fixed cost (sum of costs that are independent of the amount of product made, such as equipment or components of the regeneration system), TTN is the Total Turnover Number, $Cost_{Cofactor}$ is the cost of 1 mole of cofactor, and $Cost_{Variable}$ is the variable cost (sum of costs that scale per mole of product,

such as secondary substrate, electricity, or manpower). In the electrochemical leaf, the fixed costs would include the potentiostat, electrode materials, and costs involved in FNR purification. The variable costs would be minimal, as only electricity is required, and no post-separation step is necessary. Note that there is no magic number for TTN in order to become economically viable, as many factors are involved. Clearly, for lowering the cost, the improvement in TTN is more effective if the cofactor is more expensive. If the product is valuable, the requirement for TTN is less demanding. With increased scale of production, the fixed costs should become relatively small. If the total cost is lower than the value of the product, then the regeneration system can be considered economically viable.

4.4 References

(1) Schmid, A.; Dordick, J. S.; Hauer, B.; Kiener, A.; Wubbolts, M.; Witholt, B. *Nature* **2001**, *409*, 258.

(2) Wu, H.; Tian, C.; Song, X.; Liu, C.; Yang, D.; Jiang, Z. *Green Chemistry* **2013**, *15*, 1773.

(3) Hollmann, F.; Arends, I. W. C. E.; Buehler, K. *ChemCatChem* **2010**, *2*, 762.

(4) Wichmann, R.; Vasic-Racki, D. In *Technology Transfer in Biotechnology: From lab to Industry to Production*; Kragl, U., Ed.; Springer Berlin Heidelberg: Berlin, Heidelberg, 2005, p 225.

(5) van der Donk, W. A.; Zhao, H. *Current Opinion in Biotechnology* **2003**, *14*, 421.

(6) Shaked, Z. e.; Whitesides, G. M. *Journal of the American Chemical Society* **1980**, *102*, 7104.

(7) Wong, C.-H.; Whitesides, G. M. *Journal of the American Chemical Society* **1981**, *103*, 4890.

(8) Lauterbach, L.; Lenz, O.; Vincent, K. A. *FEBS Journal* **2013**, *280*, 3058.

(9) Greiner, L.; Schroder, I.; Muller, D. H.; Liese, A. *Green Chemistry* **2003**, *5*, 697.

(10) Mertens, R.; Greiner, L.; van den Ban, E. C. D.; Haaker, H. B. C. M.; Liese, A. *Journal of Molecular Catalysis B: Enzymatic* **2003**, *24–25*, 39.

(11) Wu, J. T.; Wu, L. H.; Knight, J. A. *Clinical Chemistry* **1986**, *32*, 314.

(12) Lauterbach, L.; Idris, Z.; Vincent, K. A.; Lenz, O. *PLOS ONE* **2011**, *6*, e25939.

(13) Reeve, H. A.; Lauterbach, L.; Ash, P. A.; Lenz, O.; Vincent, K. A. *Chem. Commun.* **2012**, *48*, 1589.

(14) Reeve, H. A.; Lauterbach, L.; Lenz, O.; Vincent, K. A. *ChemCatChem* **2015**, *7*, 3480.

(15) Schrewe, M.; Julsing, M. K.; Buhler, B.; Schmid, A. *Chemical Society Reviews* **2013**, *42*, 6346.

(16) Haberland, J.; Hummel, W.; Daussmann, T.; Liese, A. *Organic Process Research & Development* **2002**, *6*, 458.

(17) Haberland, J.; Kriegesmann, A.; Wolfram, E.; Hummel, W.; Liese, A. *Applied Microbiology and Biotechnology* **2002**, *58*, 595.

(18) Hollmann, F.; Hofstetter, K.; Schmid, A. *Trends in Biotechnology* **2006**, *24*, 163.

(19) Ruppert, R.; Herrmann, S.; Steckhan, E. *Tetrahedron Letters* **1987**, *28*, 6583.

(20) Ruppert, R.; Herrmann, S.; Steckhan, E. *Journal of the Chemical Society, Chemical Communications* **1988**, 1150.

(21) Steckhan, E.; Herrmann, S.; Ruppert, R.; Dietz, E.; Frede, M.; Spika, E. *Organometallics* **1991**, *10*, 1568.

(22) Hollmann, F.; Schmid, A.; Steckhan, E. *Angewandte Chemie International Edition* **2001**, *40*, 169.

(23) van Esch, J. H.; Hoffmann, M. A. M.; Nolte, R. J. M. *The Journal of Organic Chemistry* **1995**, *60*, 1599.

(24) Hollmann, F.; Witholt, B.; Schmid, A. *Journal of Molecular Catalysis B: Enzymatic* **2002**, *19–20*, 167.

(25) Janik, B.; Elving, P. J. *Chemical Reviews* **1968**, *68*, 295.

(26) Elving, P. J.; Schmakel, C. O.; Santhanam, K. S. V.; Zuman, P. *C R C Critical Reviews in Analytical Chemistry* **1976**, *6*, 1.

(27) Gorton, L.; Domínguez, E. In *Encyclopedia of Electrochemistry*; Wiley-VCH Verlag GmbH & Co. KGaA: 2007.

(28) Schmakel, C. O.; Santhanam, K. S. V.; Elving, P. J. *Journal of The Electrochemical Society* **1974**, *121*, 345.

(29) Schmakel, C. O.; Santhanam, K. S. V.; Elving, P. J. *Journal of the American Chemical Society* **1975**, *97*, 5083.

(30) Man, F.; Omanovic, S. *Journal of Electroanalytical Chemistry* **2004**, *568*, 301.

(31) Damian, A.; Omanovic, S. *Journal of Molecular Catalysis A: Chemical* **2006**, *253*, 222.

(32) Ali, I.; Khan, T.; Omanovic, S. *Journal of Molecular Catalysis A: Chemical* **2014**, *387*, 86.

(33) Karyakin, A. A.; Bobrova, O. A.; Karyakina, E. E. *Journal of Electroanalytical Chemistry* **1995**, *399*, 179.

(34) DiCosimo, R.; Wong, C.-H.; Daniels, L.; Whitesides, G. M. *The Journal of Organic Chemistry* **1981**, *46*, 4622.

(35) Cantet, J.; Bergel, A.; Comtat, M. *Journal of Electroanalytical Chemistry* **1992**, *342*, 475.

(36) Cantet, J.; Bergel, A.; Comtat, M. *Enzyme and Microbial Technology* **1996**, *18*, 72.

(37) Zu, Y.; Shannon, R. J.; Hirst, J. *Journal of the American Chemical Society* **2003**, *125*, 6020.

(38) Rife, J. E.; Cleland, W. W. *Biochemistry* **1980**, *19*, 2321.

(39) Barnes, L. D.; McGuire, J. J.; Atkinson, D. E. *Biochemistry* **1972**, *11*, 4322.

(40) Batie, C. J.; Kamin, H. *Journal of Biological Chemistry* **1981**, *256*, 7756.

(41) Antelo, J.; Avena, M.; Fiol, S.; López, R.; Arce, F. *Journal of Colloid and Interface Science* **2005**, *285*, 476.

(42) Bachmeier, A.; Wang, V. C. C.; Woolerton, T. W.; Bell, S.; Fontecilla-Camps, J. C.; Can, M.; Ragsdale, S. W.; Chaudhary, Y. S.; Armstrong, F. A. *Journal of the American Chemical Society* **2013**, *135*, 15026.

(43) Mersch, D.; Lee, C.-Y.; Zhang, J. Z.; Brinkert, K.; Fontecilla-Camps, J. C.; Rutherford, A. W.; Reisner, E. *Journal of the American Chemical Society* **2015**, *137*, 8541.

(44) Sokol, K. P.; Mersch, D.; Hartmann, V.; Zhang, J. Z.; Nowaczyk, M. M.; Rogner, M.; Ruff, A.; Schuhmann, W.; Plumere, N.; Reisner, E. *Energy & Environmental Science* **2016**, *9*, 3698.

Chapter 5

Solar-driven NADPH production

Chapter 5

Solar-driven NADPH production

Abstract

Solar energy can be harnessed to drive NADPH production in a photoelectrochemical cell, where FNR@ITO is used as the cathode, and a light-absorbing semiconductor is used as the photoanode. As a first demonstration, a dye-sensitized TiO_2 electrode was used as the photoanode, and light-driven $NADP^+$ reduction was achieved under no applied bias. However, the overall cycle was not complete, as the dye required a sacrificial electron donor because it cannot oxidize water. To achieve simultaneous $NADP^+$ reduction and water oxidation under visible light, WO_3 or $BiVO_4$, with band gaps of 2.8 and 2.4 eV respectively, were used as the photoanode materials, and NADPH production was confirmed under visible light irradiation with an applied bias. This work serves as a proof-of-principle system for the first step of a 'solar-to-chemicals' process, and with further improvement could be coupled to downstream enzymes to synthesize valuable, complex compounds.

5.1 Introduction

5.1.1 Solar-to-chemicals using the 'photoelectrochemical leaf'

Research on conversion of solar energy into chemical energy has focused on water splitting to produce H_2 as a fuel (see further details in Chapter 1 Section 1.1.2).[1] More complex fuels, such as methanol or formate can also be produced, but this requires an additional step of CO_2 assimilation. The light-absorbing components have similar requirements, but coupling that to catalysts for synthesizing complex chemicals can be more difficult than for H_2 production.

We can envision solar NADPH production as the first step in a 'solar-to-chemicals' process, mimicking the division of labour in natural photosynthesis. In the chloroplast, the 'Light' processes consist of light absorption to generate NADPH and ATP as energy carriers, which are then used in the 'Dark' processes to drive CO_2 assimilation and synthesis of carbohydrates. The previous two chapters (Chapters 3 and 4) extensively described the 'electrochemical leaf', in which ferredoxin-$NADP^+$ reductase (FNR) was adsorbed onto an indium tin oxide (ITO) electrode to create an electrochemical $NADP^+$/NADPH recycling system, where the reducing power was the potential applied by a potentiostat. Importantly, this can be replaced by a light-absorbing electrode to create a photoelectrochemical system.

A diagram of the proposed photoelectrochemical NADPH generation cell is shown in Figure 5.1. When a photoanode is irradiated with light that has sufficient energy to excite electrons across its band gap, an electron-hole pair is created. The electron can be transported to the back contact of the photoanode (the conductive support which is ITO glass in this case), then transferred to the cathode, which is the FNR@ITO electrode from previous chapters (see Chapters 3 and 4). The holes in the photoanode then can carry out water oxidation. The conduction band of the photoanode determines whether the overall reaction

can proceed under light without an applied bias. If the conduction band is not sufficiently negative, a voltage can be applied to the system to satisfy this thermodynamic requirement. The relevant reactions are listed as follows:

Light absorption: $h\nu \rightarrow e^- + h^+$

Reduction half-reaction: $NADP^+ + 2e^- + H^+ \rightarrow NADPH$ $E^0 = -0.32$ V vs SHE at pH 7

Oxidation half-reaction: $2H_2O + 4h^+ \rightarrow O_2 + 4H^+$ $E^0 = 0.82$ V

Overall reaction: $2\ NADP^+ + 2H_2O \rightarrow 2NADPH + O_2 + 2H^+$

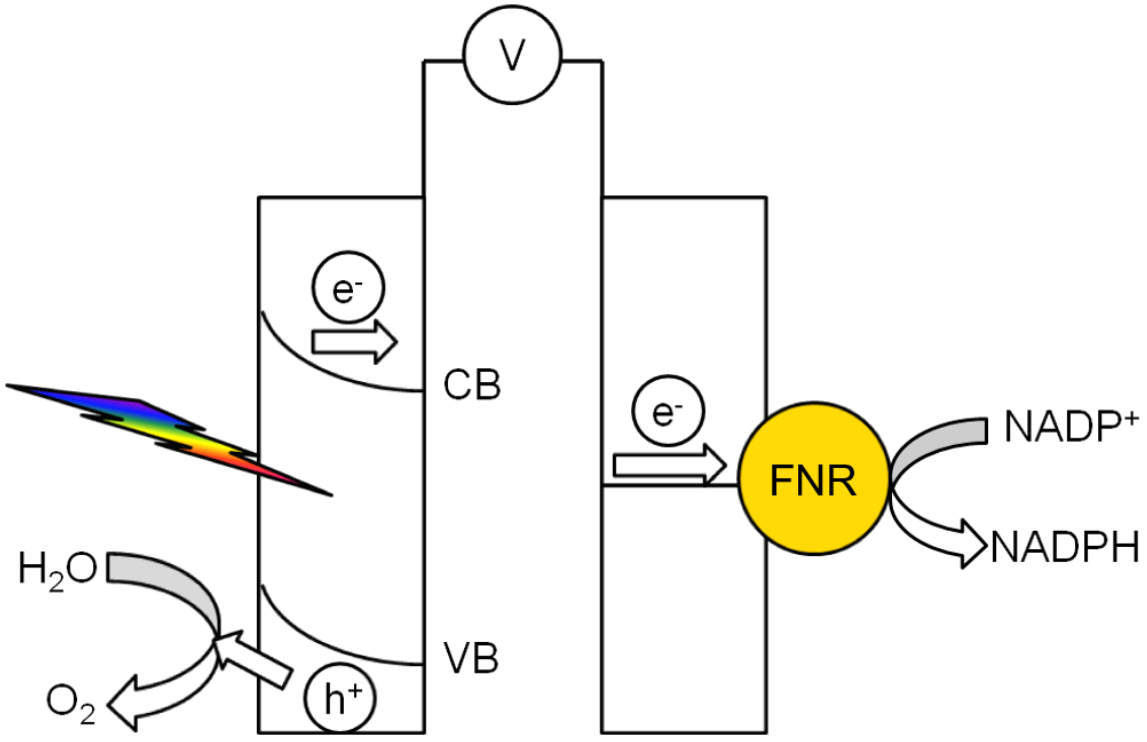

Figure 5.1 Diagram of a photoelectrochemical cell, with a FNR@ITO cathode for $NADP^+$ reduction and a photoanode for light absorption and water oxidation. CB: conduction band, VB: valence band.

5.1.2 Previous solar-driven NADPH production systems

There have been some reports in the literature with the goal of solar-driven NAD(P)H production as well as a coupled downstream process that consumes NAD(P)H. Nam *et al.* used a Fe_2O_3 photoanode modified with FeOOH as the water oxidation catalyst, combined with a black Si cathode and a Rh complex in solution for NAD^+ reduction.[2] This Rh complex catalyst has been previously used in electrochemical and chemical cofactor regeneration systems (see Chapter 4 Section 4.1 for details). The system was further coupled to an NADH-dependent glutamate dehydrogenase, and light-driven L-glutamate synthesis was demonstrated, although the applied potential requirement was high (at least 1.1 V). The limiting component of this system was the Fe_2O_3 photoanode, which typically has good light absorption properties (absorbs up to 600 nm) but inferior carrier transport and conduction band level. Similar work of the same group[3,4] used Eosin Y or other xanthene-based dyes as the light absorber, with direct electron transfer to the Rh complex and using triethanolamine as a sacrificial electron donor.

Brown *et al.* used a particulate system, composed of CdSe quantum dots and FNR.[5] Although CdSe is a narrow band gap semiconductor (*i.e.* band gap <3.0 eV, capable of absorbing visible light) with a favourable conduction band position, it undergoes self-decomposition under light irradiation, therefore a sacrificial electron donor (ascorbic acid in this case) is required. The production of NADPH was measured using a fluorescence-based detection kit, and the TOF was 0.4 s^{-1} under 405 nm light irradiation, probably due to slow electron transfer from CdSe to FNR. The system was coupled to an NADPH-dependent alcohol dehydrogenase and NADPH recycling was confirmed from detection of the product of the coupled enzyme, although the total turnover number (TTN, moles of product of the coupled enzyme per mole of initial $NADP^+$) was low (around 3) and the final product concentration was small (less than 1 μM). It was found that Cd^{2+} inhibited the catalytic

activity of FNR,[6] and the low activity may have been the result of Cd^{2+} leeching from CdSe into the solution. Similar work involved covalently binding FNR to CdSe/ZnS quantum dots,[7] but only FNR activity with a redox mediator (either ferredoxin, ferricyanide, or dibromothymoquinone) was shown, and light-driven reaction was not demonstrated.

The ideal system for light-driven NAD(P)H production should use an enzyme for generation of NAD(P)H, to provide high turnover rates and specificity for NAD(P)H, and on the light absorption side, the material should work under visible light, be capable of water oxidation, and operate without an applied bias.

5.1.3 Aims of this chapter

Building on the FNR@ITO electrode from Chapter 3, the feasibility of using solar energy to drive $NADP^+$ reduction was investigated. First, a dye-sensitized TiO_2 electrode was used as the photoanode, which could carry out light-driven NADPH production when connected to an FNR@ITO cathode without an applied bias. However, due to slow water oxidation kinetics of the dye, a sacrificial electron donor was necessary. Next, narrow band gap oxide semiconductors (WO_3 and $BiVO_4$) were investigated as photoanodes. Additionally, light-driven NADPH production was also investigated in a particulate system, where FNR was adsorbed onto semiconductor particles in suspension.

5.2 Results and discussion

5.2.1 Dye-sensitized TiO_2 as a photoanode

As a demonstration of light-driven NADPH production, a dye-modified TiO_2 electrode was chosen as the photoanode, and its photocurrent is shown in Figure 5.2. TiO_2 is a wide band gap semiconductor (*i.e.* band gap > 3.0 eV) that can only absorb light in the UV region, so modification with a dye extends light absorption into the visible region. The dye used herein was a Ru-based dye, $[(Ru(bpy)_2(4,4\text{-}(PO_3H_2)_2bpy))Br_2$ (bpy = 2,2-bipyridine)], also known as RuP, previously used in light-driven H_2 production by Reisner *et al*. and CO_2 reduction by Woolerton *et al*..[8,9] However, the use of a dye sensitizer means that water oxidation cannot be achieved, due to slow water oxidation kinetics of the dye. In this experiment, MES buffer acted as a sacrificial electron donor because it is more easily oxidized than water.

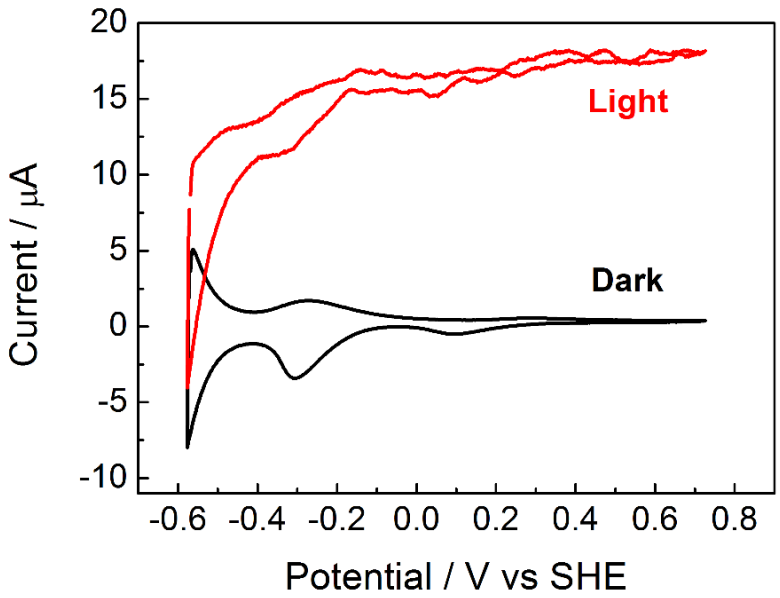

Figure 5.2 Cyclic voltammograms of TiO_2 modified with RuP under dark conditions (black line) and visible light illumination (red line) in a three-electrode setup, with a Pt wire as the counter electrode and Ag/AgCl as the reference electrode. Electrode area 1.5 cm^2, Other conditions: Scan rate 20 mV s^{-1}, 0.2 M MES buffer pH 7.0, 20 ^oC, N_2 bubbling. Projector lamp, λ >420 nm.

In Figure 5.2, the current of an RuP/TiO_2 electrode is shown for dark and light (λ > 420 nm) conditions. The TiO_2 electrode was constructed by the doctor's blade method on ITO glass (see Chapter 6 Section 6.2.3 for details) using P25 TiO_2 (a mixture of anatase and rutile phase TiO_2), and the RuP dye was loaded by submerging the TiO_2 electrode in dye solution and stirring overnight at room temperature. There was a noticeable color change (white to light yellow/orange) of the TiO_2 electrode, indicating that the RuP dye had been adsorbed. In the dark, the TiO_2 showed the expected 'trumpet' shape, and under visible light illumination an oxidation current could be clearly observed. This is typical of an n-type semiconductor, as photocurrents are caused by the minority carrier (holes for n-type, electrons for p-type), and the photocurrent onset potential was more negative than the potential window of the experiment (-0.6 V *vs* SHE at pH 7.0).

To create a photoelectrochemical NADPH generation cell, the RuP/TiO_2 electrode was connected to a FNR@ITO electrode (prepared as described in Chapter 3 Section 3.2.3 and 3.2.4) in a two-electrode setup, as shown in Figure 5.3A. Visible light irradiation generates excited electrons in the RuP dye, which are then transferred to the conduction band of TiO_2 then across the circuit to the FNR@ITO electrode for $NADP^+$ reduction. The electrons were replenished by the MES buffer which acted as a sacrificial electron donor.

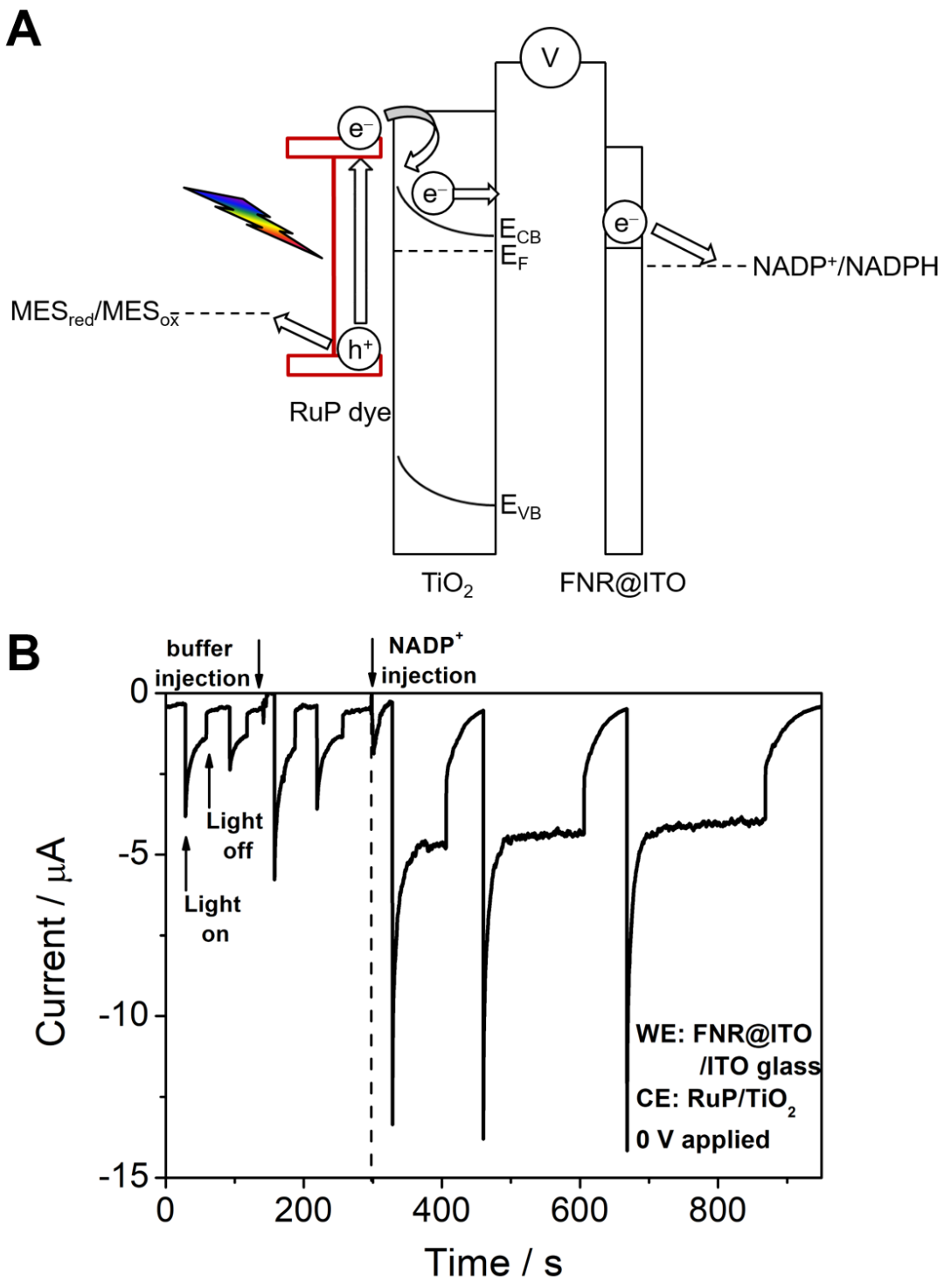

Figure 5.3 A) Diagram of photoelectrochemical NADPH production cell with working electrode: FNR@ITO/ITO glass, and counter electrode (photoelectrode): RuP-sensitized TiO_2 in a two-electrode setup. E_{CB}: conduction band level, E_F: Fermi level, E_{VB}: valence band level. The relative reduction potentials of $NADP^+$ and MES are indicated. **B)** Chronoamperometry of the photoelectrochemical cell with 0 V applied bias under intermittent visible light irradiation (Projector lamp, $\lambda > 420$ nm). 0.2 M MES buffer pH 7, 20 ^oC, N_2 bubbling. At 295 s, $NADP^+$ was injected to 0.38 mM final concentration.

Figure 5.3B shows the photocurrent of the photoelectrochemical cell where the cathode is FNR@ITO/ITO glass and the anode is RuP/TiO_2 in a two-electrode setup, with zero applied bias. At the start, with no $NADP^+$ present, the photocurrent is small. After injection of $NADP^+$ into the system (at 295 s, 0.38 mM final concentration), the photocurrent is significantly increased. In control runs with buffer injections (at 135 s in Figure 5.3B), or $NADP^+$ injection into a setup with no FNR (data not shown), no significant photocurrent increase was observed. The slight photocurrent increase after buffer injection may be due to the dissolved O_2 in the injected volume, and as N_2 was continuously bubbled into the cell, this O_2 was gradually purged out, and the photocurrent returned to the same magnitude as before injection. This shows that the greatly enhanced photocurrent after $NADP^+$ injection is indeed from $NADP^+$ reduction by photogenerated electrons being supplied to the FNR@ITO electrode. The signal spikes at the start of light illumination are due to recombination of the photogenerated electrons and holes, at surface trap states of TiO_2 for example.[10,11] The photocurrent that contributed to $NADP^+$ reduction is the current that reaches a plateau under light, minus that of the photocurrent with no $NADP^+$. Note that the total charge passed calculated from the photocurrent was small compared to the total amount of $NADP^+$ present, therefore the $NADP^+$ concentration was not significantly changed and the photocurrent was steady.

Even though this setup (RuP/TiO_2 anode and FNR@ITO cathode) was not a complete cycle due to the need for sacrificial reagents (which was the MES buffer), it still demonstrates that $NADP^+$ reduction can be driven by light illumination on a photoelectrode, as long as the conditions for band positions and photoelectron generation are met. In this case, since the conduction band level of TiO_2 is more negative than $NADP^+$ reduction potential, the reaction proceeded under light without an applied bias.

5.2.2 Narrow band gap materials as photoanodes

To create a photoelectrochemical system that is capable of both $NADP^+$ reduction and water oxidation, there are constraints for the light-absorbing material as follows (see also Figure 5.4A, B):

1. Using the FNR@ITO as the cathode, the photoanode must be an n-type semiconductor material, because the photocurrent is generated by the minority carrier (holes in the case of n-type semiconductors, see also Chapter 6 Section 6.1.5).

2. The conduction band maximum must be more negative than the $NADP^+$ reduction potential, otherwise an applied bias will be needed.

3. The valence band minimum must be more positive than the water oxidation potential. Most oxide materials satisfy this condition.

4. The material must be stable under water-oxidizing conditions, ruling out chalcogenides (*e.g.* CdS, CdSe) as they tend to self-decompose under light irradiation.[12]

5. The band gap must be smaller than 3.0 eV to be able to absorb visible light.

Based on these requirements, as well as the need for a relatively simple synthesis route, $BiVO_4$ and WO_3 were chosen as candidates for the photoanode material. Their band gaps are narrow (WO_3 2.8 eV, $BiVO_4$ 2.4 eV), thus they can absorb visible light (Figure 5.4A). Particulate WO_3 is commercially available, while $BiVO_4$ can be produced from simple routes.[13-15] The only disadvantage is that their conduction band levels are not sufficiently negative for $NADP^+$ reduction, therefore an applied bias is required.

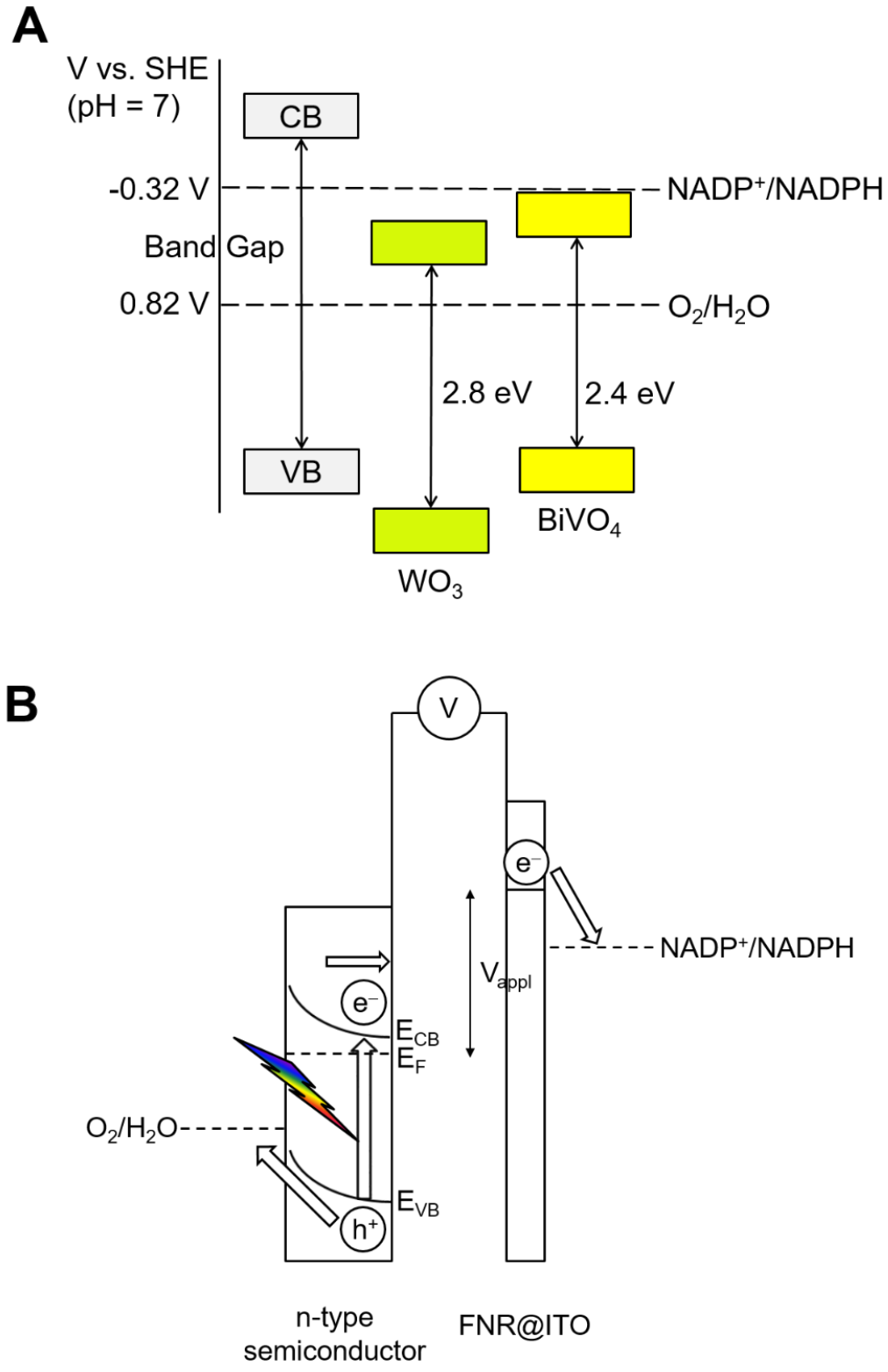

Figure 5.4 A) Band diagrams of an ideal photoelectrode material (gray), WO_3 (green) and $BiVO_4$ (yellow). CB: Conduction band, VB: Valence band. **B)** Diagram of a photoelectrochemical cell for light-driven $NADP^+$ reduction. E_f: Fermi level, V_{appl}: Applied voltage.

Figure 5.4B shows a diagram of a photoelectrochemical cell where a n-type semiconductor is used as the photoanode. Under light irradiation with sufficient energy, an electron is excited from the valence band into the conduction band, leaving a hole in the valence band. The holes are transported to the photoanode surface and then used in water oxidation. The electrons are transported to the back contact (ITO glass) of the photoanode then across the circuit to the cathode, and the potential of the cathode (FNR@ITO in this case) is equal to the Fermi level of the photoanode (see Chapter 6 Section 6.1.5 for more details on semiconductor photoelectrochemistry).[16] If this potential is not sufficiently negative for $NADP^+$ reduction, then a potential must be applied (V_{appl}) by the potentiostat until $NADP^+$ reduction can be achieved. A larger applied potential leads to a smaller solar energy conversion efficiency, defined as follows:[17]

$$\eta = \frac{J\left(V_{reaction} - V_{appl}\right)}{P} \qquad Eq.1$$

where η is the solar energy conversion efficiency, J is the photocurrent density, $V_{reaction}$ is the overall cell potential of the reaction (the difference in reduction potentials of $NADP^+$ reduction and water oxidation, 1.1 V in this case), V_{appl} is the applied potential, and P is the power density of the light illumination.

The WO_3 electrode was constructed by loading WO_3 particles onto ITO glass using the doctor's blade method, in which WO_3 particles were sonicated in dilute HNO_3 solution, then pasted onto cleaned ITO glass slides and calcined at 450 °C for 30 min (see Chapter 6 Section 6.2.3 for more details). Figure 5.5 shows the photocurrent of the WO_3 electrode under visible light irradiation (a Xe lamp at 300 W with a cutoff filter, $\lambda > 420$ nm).

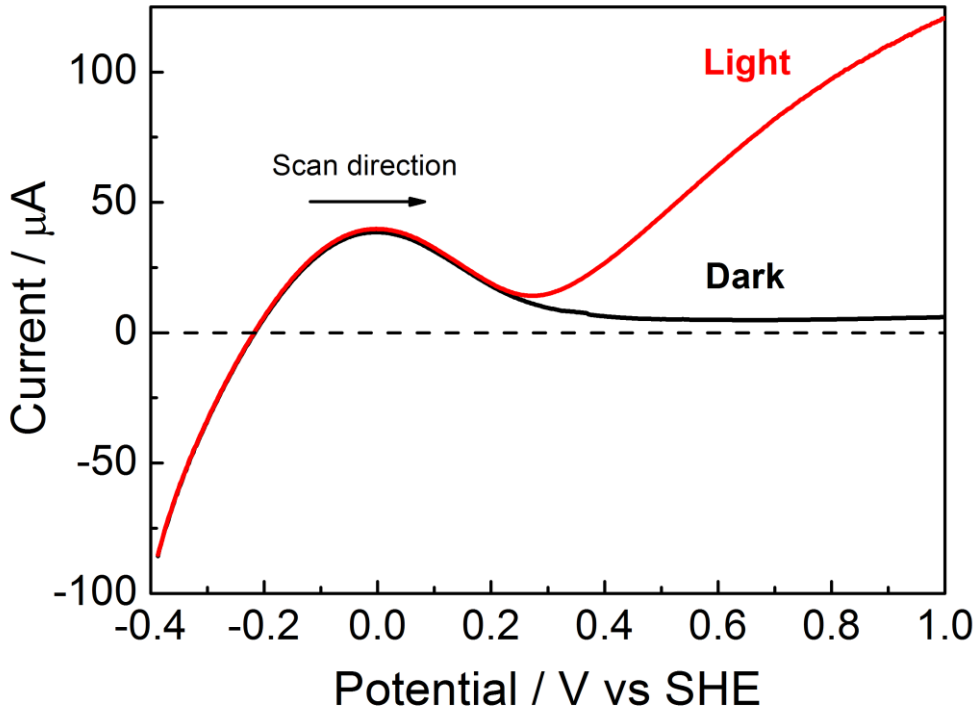

Figure 5.5 Photocurrent of a WO_3 electrode. Linear sweep voltammetry of the WO_3 electrode, showing the dark current (black) and photocurrent (red). Electrode area (1.5 cm^2) Visible light irradiation (λ > 420 nm, 300 W Xe lamp). Scan rate 20 mV s^{-1} from negative to positive potential.

Under irradiation, there was a photo-oxidation current, as expected for an n-type semiconductor, with an onset potential of approximately 0.25 V *vs* SHE. At pH 8.0, the reduction potential of FNR is at -0.38 V, indicating that at least 0.63 V of applied voltage is required to drive $NADP^+$ reduction by using this WO_3 photoanode. In practice, the needed applied voltage is likely to be greater due to overpotential requirements in both half-reactions, as well as the iR drop in a two-electrode setup. Although the FNR@ITO electrode behaves as a reversible $NADP^+$/NADPH interconversion electrode, some degree of overpotential is required for a significant catalytic current.

Light-driven NADPH production was demonstrated in a two-electrode setup, with WO_3 as the photoanode and FNR@ITO/Ti foil as the cathode, as shown in Figure 5.6A.

Before starting chronoamperometry, the coverage of FNR on ITO was determined from non-turnover peaks during cyclic voltammentry (as explained in Chapter 3 Section 3.2.3), and the FNR coverage was 47 pmol cm^{-2} (1.4×10^{-10} mol of FNR on 1.5 cm^2 double sided ITO on Ti foil). The applied voltage was set at 1.1 V, to increase the driving force as much as possible. As the difference in reduction potentials of $NADP^+$ reduction and water oxidation at pH 8.0 is 1.1 V, if the applied potential was any greater, it would not demonstrate the light-driven nature of the system, as the applied potential would in theory be sufficient to drive the reaction.

At the start, in the dark and without $NADP^+$, there was a small residual current (less than 1 μA), then as the light was turned on, a current spike that rapidly decayed was observed. The nature of this background current is unclear, but it cannot be $NADP^+$ reduction as there is still no $NADP^+$ in the cell. This current is therefore possibly due to H^+ reduction by the exposed surface of the Ti electrode. At 250 s, $NADP^+$ was injected into the cell to 200 μM final concentration, and an increase in reduction current was observed (approximately 9 μA), indicating that $NADP^+$ reduction was occurring. The current after this point is then a contribution of both the background current and $NADP^+$ reduction.

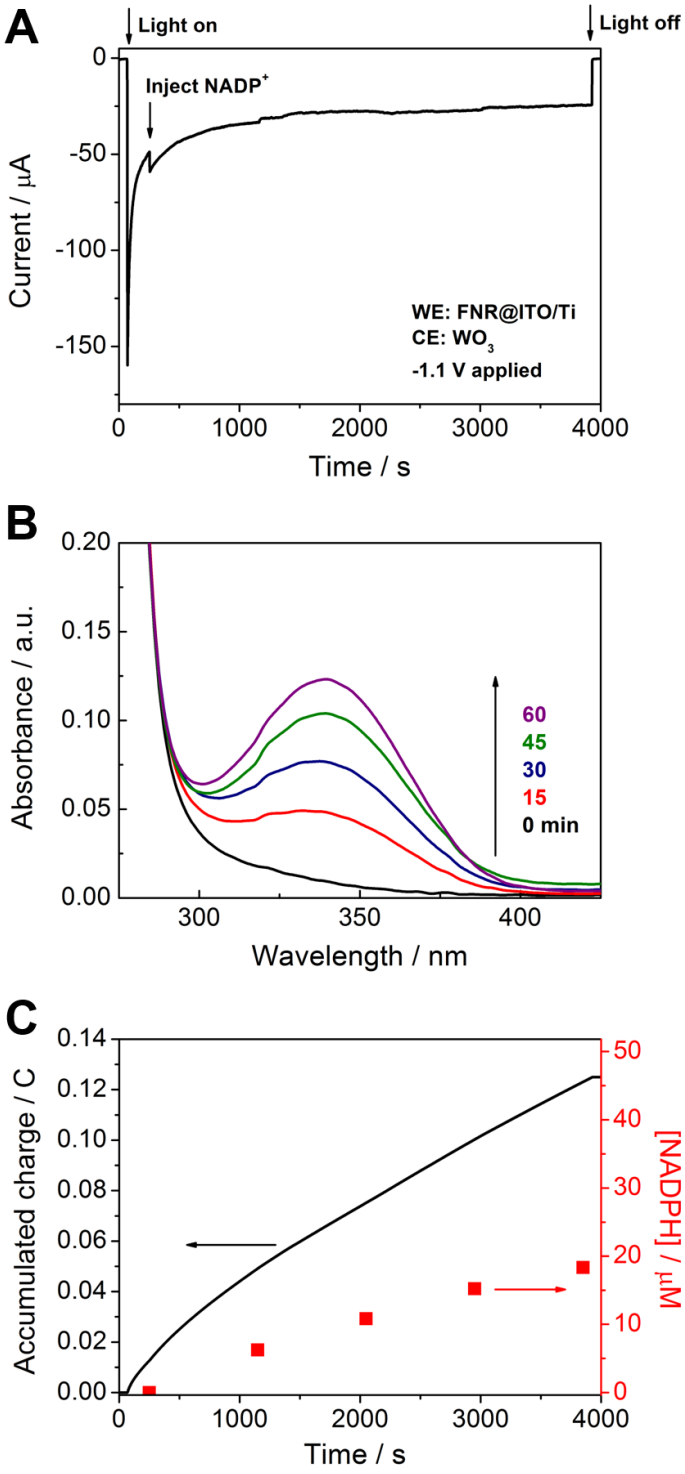

Figure 5.6 Performance of a phototoelectrochemical NADPH generation cell consisting of a WO_3 photoanode and FNR@ITO/Ti foil cathode. **A)** Chronoamperometry of WO_3 and FNR@ITO in a two-electrode setup with an applied voltage of 1.1 V. At 250 s, $NADP^+$ was injected to 200 µM final concentration. **B)** UV-vis absorbance of cell solution at regular intervals, showing increasing NADPH absorption peaks at 340 nm. **C)** The accumulated charge passed during chronoamperometry from graph A (black, left axis) and the NADPH concentration in the cell as determined by UV-vis from graph B (red, right axis). Other conditions: 50 mM borate buffer pH 8.0, 20 °C, Ar bubbling.

Every 15 minutes, a small aliquot (0.5 mL) was taken from the cell (initial volume 14 mL) and UV-vis absorbance was measured to determine NADPH concentration from its distinctive peak at 340 nm, as shown in Figure 5.6B. The NADPH concentration in the cell increased with light irradiation time. The NADPH concentration was calculated from the absorbance at 340 nm, using the extinction coefficient of 6220 M^{-1} cm^{-1}.[18] Figure 5.6C shows a comparison of the accumulated charge passed (black line, left axis) and the NADPH concentration in the cell (red dots, right axis). The scales in both axes are the same, *i.e.* the accumulated charge passed on the left axis is equivalent to the NADPH concentration on the right axis with a cell volume of 14 mL. The discrepancy between the total charge passed and the detected NADPH indicates that a significant background current contributed to the overall charge passed. The Faradaic efficiency for NADPH production was 34 % after 15 min and 40 % after 1 hour, as calculated from the charge involved in NADPH production and the total charge passed. Using the amount of FNR on the electrode, the turnover number (TON, moles of NADPH produced per mole of FNR) was calculated as 1800, and the turnover frequency (TOF, moles of NADPH produced per mole of FNR per time) was 0.5 s^{-1}.

Control experiments (not shown) were conducted in two ways: (a) using an ITO/Ti foil cathode with no FNR loaded, but with the same $NADP^+$ concentration and light irradiation, and (b) using the same FNR@ITO/Ti foil and WO_3 electrodes, with the same applied potential but no light irradiation. No NADPH was detected in either case, demonstrating that the NADPH generated in Figure 5.6 was indeed from light excitation of WO_3 and $NADP^+$ reduction by FNR.

A similar experiment to that shown in Figure 5.6 (two-electrode setup of FNR@ITO/Ti foil and WO_3) was also carried out with a smaller applied bias (0.8 V, which is 0.3 V smaller). As shown in Figure 5.7, with an applied potential of 0.8 V, a current

increase was still observed with $NADP^+$ injection, and production of NADPH was confirmed by UV-vis absorbance. The decrease in NADPH production rate after 1 h is due to deactivation of FNR (possibly from light deactivation or from a reactive species generated at the photoanode). In this case, since the applied bias (0.8 V) is smaller than the theoretical voltage required for the overall reaction (1.1 V, from the difference in reduction potentials of $NADP^+$ reduction and water oxidation), a solar-to-NADPH conversion efficiency (η) can be calculated using Eq.1 mentioned above. Using the amount of NADPH detected after 7200 s to obtain the average photocurrent density, and estimating the power output of the lamp from a spectrum of a 300 W Xe lamp[19] held at a distance of 3 cm (0.1 W cm^{-2}), η is approximately 0.001%. A smaller applied bias (0.7 V) was also examined (data not shown), but no significant photocurrent increase was observed with $NADP^+$ injection. This is in line with the expectation that the necessary bias must be more than 0.63 V (calculated from the difference between photocurrent onset potential of WO_3 in Figure 5.5, and the reduction potential of FNR at -0.38V).

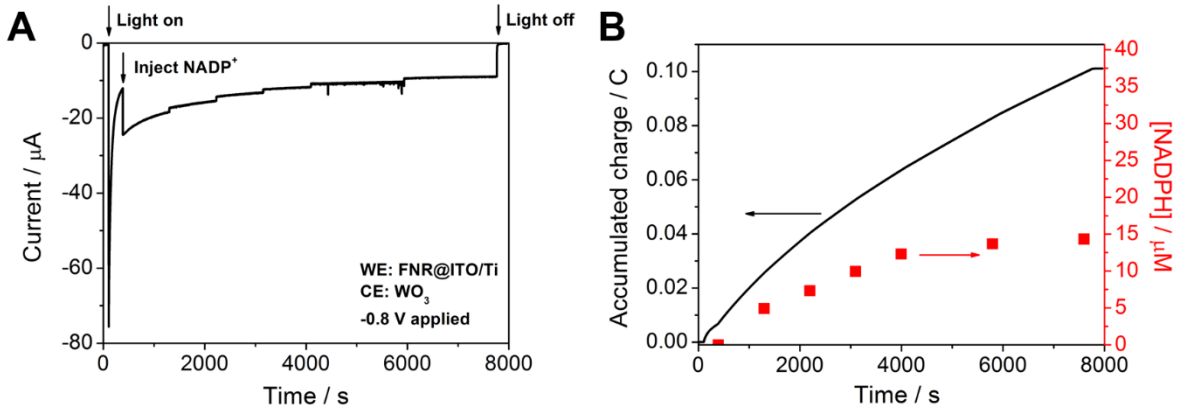

Figure 5.7 A phototoelectrochemical NADPH generation cell consisting of a WO_3 photoanode and FNR@ITO/Ti foil cathode. **A)** Chronoamperometry of WO_3 and FNR@ITO in a two-electrode setup with an applied voltage of 0.8 V. At 395 s, $NADP^+$ was injected to 200 μM final concentration. Visible light irradiation (λ >420 nm, 300 W Xe lamp). **B)** The accumulated charge passed during chronoamperometry in B) (black, left axis) and the NADPH concentration in the cell as determined by UV-vis (red, right axis). Other conditions: 50 mM borate buffer pH 8.0, 20 °C, Ar bubbling.

Another semiconductor material ($BiVO_4$) was investigated as the photoanode. Particulate $BiVO_4$ was synthesized in a method similar to a published procedure,[13] then loaded onto ITO glass by the doctor's blade method similar to WO_3. The photocurrent onset of $BiVO_4$ (Figure 5.8) was at -0.20 V *vs* SHE, which is considerably more negative than that of WO_3 (0.25 V, also at pH 8.0). This is due to the conduction band of $BiVO_4$ being at a more negative level than that of WO_3 (Figure 5.4A), which indicates that the overall reaction should proceed with less applied bias. In a two-electrode setup, with $BiVO_4$ as the photoanode and FNR@ITO as the cathode (Figure 5.9A), with an applied bias of 0.7 V, there was an increase in photocurrent after injection of $NADP^+$, and the produced NADPH was measured by UV-vis absorbance (Figure 5.9B, C). A smaller applied potential (0.4 V) was attempted (data not shown), and although a photocurrent increase was observed, the amount of produced NADPH was too low to observe by UV-vis spectroscopy.

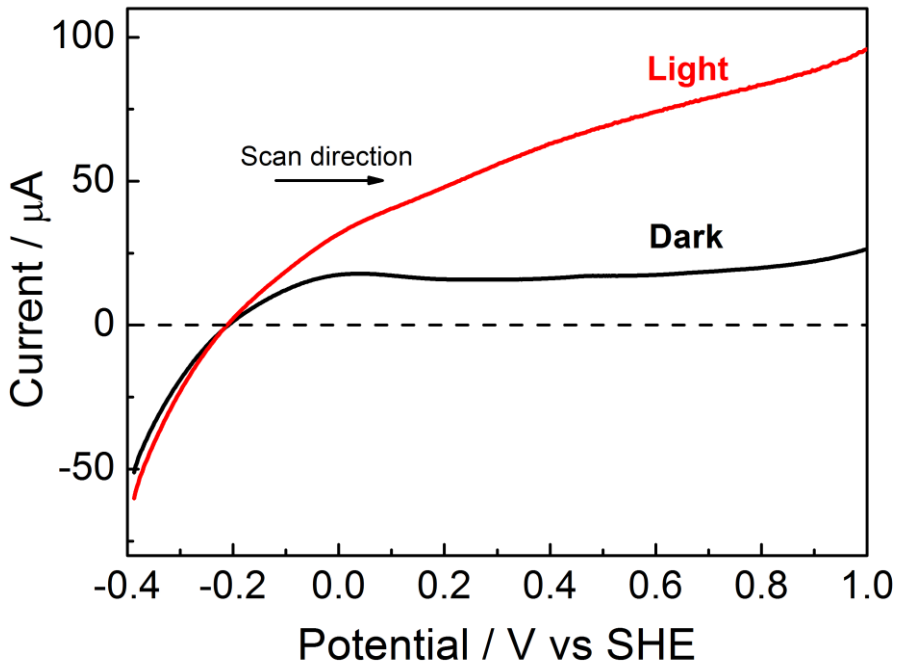

Figure 5.8 Photocurrent of a $BiVO_3$ electrode. Linear sweep voltammetry of the $BiVO_4$ electrode, showing the dark current (black) and photocurrent (red). Electrode area (1.5 cm^2) Visible light irradiation ($\lambda > 420$ nm, 300 W Xe lamp).

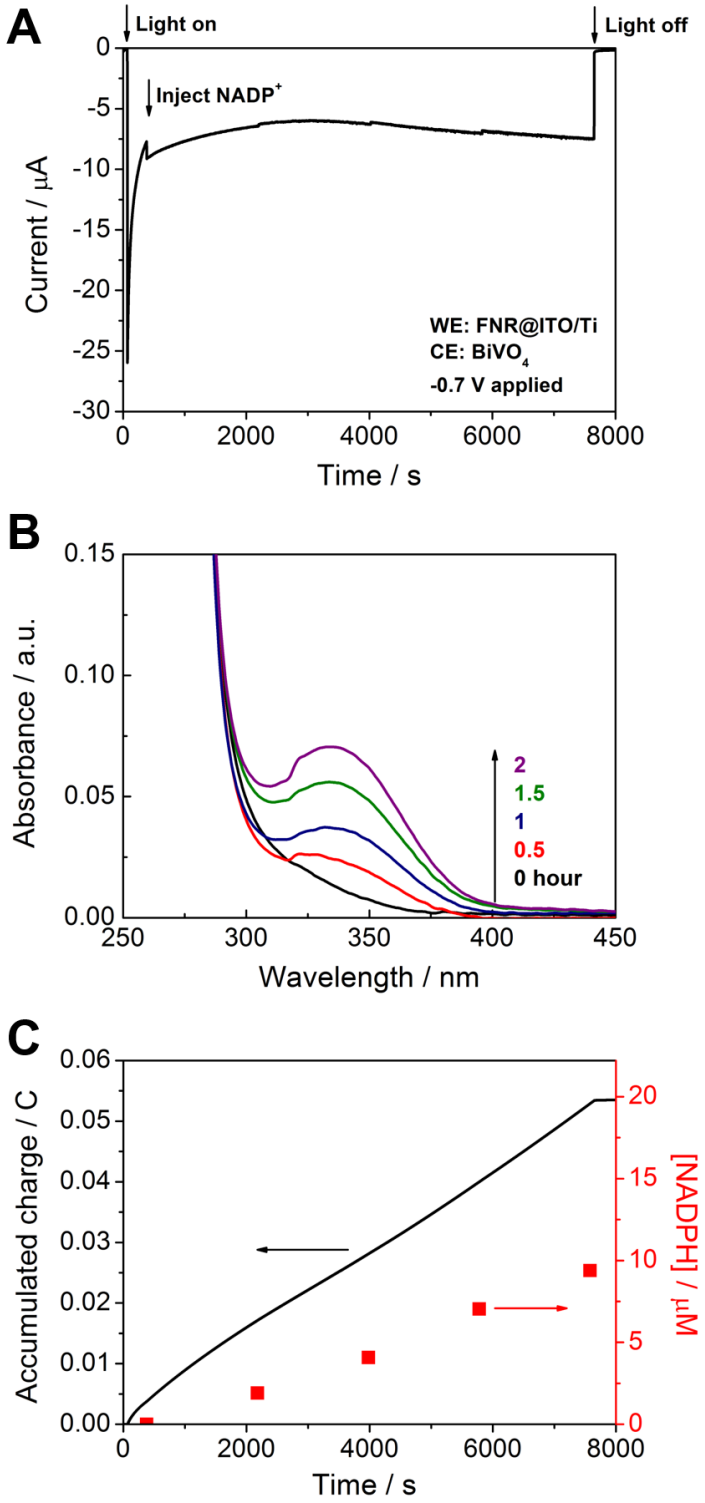

Figure 5.9 Performance of a phototoelectrochemical NADPH generation cell consisting of a $BiVO_4$ photoanode and FNR@ITO/Ti foil cathode. **A)** Chronoamperometry of $BiVO_4$ and FNR@ITO in a 2-electrode setup with an applied voltage of 0.7 V. At 380 s, $NADP^+$ was injected to 200 µM final concentration. **B)** UV-vis absorbance of cell solution at regular intervals. **C)** The accumulated charge passed during chronoamperometry in B) (black, left axis) and the NADPH concentration in the cell as determined by UV-vis (red, right axis). Other conditions: borate buffer pH 8.0, 20 °C, Ar bubbling

The performance of the photoelectrochemical NADPH production cell was limited by two factors: the required applied bias and the FNR loading on the cathode. The magnitude of the required applied bias to achieve $NADP^+$ reduction depends on the conduction band level of the photoanode. This could be lessened by using materials with more negative conduction band levels (such as C_3N_4, TaON or Ta_3N_5), or loading water oxidation catalysts onto the photoanode surface to lessen the overpotential for water splitting. The FNR loading on the cathode is the limiting component for the current in the overall cell at a given applied potential, as seen when comparing the magnitude of the currents of the photoanode and the FNR@ITO cathode separately. The amount of FNR loading was improved by using Ti foil to increase the electrode area of the FNR@ITO cathode, but this could be improved further by using a combination of Ti foil and Ti wire, or multiple electrodes.

5.2.3 A particulate semiconductor system

A particulate system can also be used in light-driven NADPH production (Figure 5.10). For example, FNR can be adsorbed onto the surface of TiO_2 particles, which can generate excited electrons and holes under irradiation. Since the conduction band of TiO_2 is more negative than the reduction potential of $NADP^+$, these photogenerated electrons can drive $NADP^+$ reduction. In this particulate system, WO_3 and $BiVO_4$ cannot be used because their conduction band levels are not sufficiently negative, and additional potential cannot be applied unlike the case of a photoelectrochemical system described above.

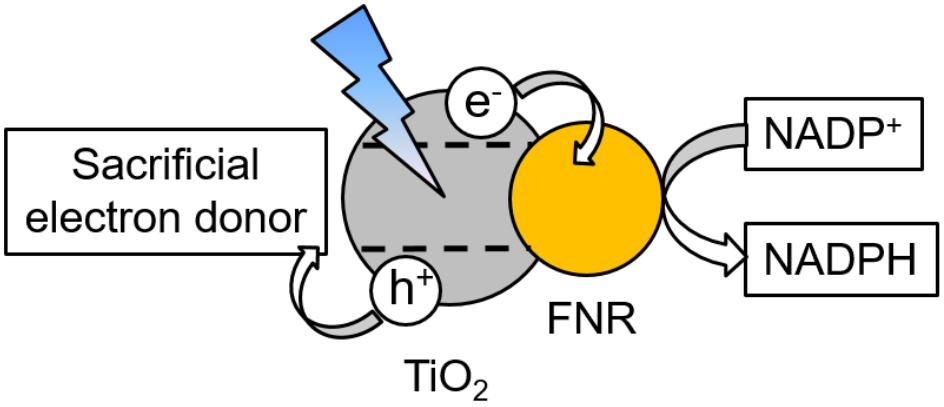

Figure 5.10 Diagram of a particulate semiconductor (TiO_2) light-driven system for NADPH production.

First, TiO_2 (P25, 5 mg) was sonicated in buffer solution (25 mM MES, 25 mM TAPS, pH 8.0, 5 mL) for 20 min in the reaction vial to disperse the particles. Then FNR (4.5 µL at 589 µM) was added to the vial and stirred in the dark for 20 min to allow for adsorption of FNR on the TiO_2 particles. The vial was then purged with Ar for 10 min to remove O_2, then UV irradiation (λ = 365 nm) was commenced. After certain amounts of time, a small aliquot (0.5 mL) of the reaction solution was taken from the vial, and centrifuged to remove TiO_2 particles, then the UV-vis absorbance (Figure 5.11A) was measured to quantify the production of NADPH. The absorbance of NADPH at 340 nm was converted to NADPH concentration (Figure 5.11B) by the extinction coefficient of NADPH.

The NADPH concentration increased with UV irradiation up to 30 min, after which it decreased, and the sharp peak in UV absorbance at 340 nm turned into a broad slope. This is possibly due to dimerization of NADPH to $(NADP)_2$, where NADPH undergoes a one-electron oxidation from photogenerated holes on the bare TiO_2 surface to produce $NADP^{\bullet}$ which can dimerize.[20] Control experiments in the absence of TiO_2, FNR or UV irradiation did not result in NADPH production, which demonstrated that the NADPH production observed with all 3 components present was indeed due to the photogenerated electrons in

TiO_2 being transferred to FNR to carry out $NADP^+$ reduction. The amount of FNR adsorbed onto TiO_2 particles was not quantified, but in principle this could be carried out in a similar manner to Chapter 2 Section 2.2.2, using the strong absorbance peak of the FAD group.

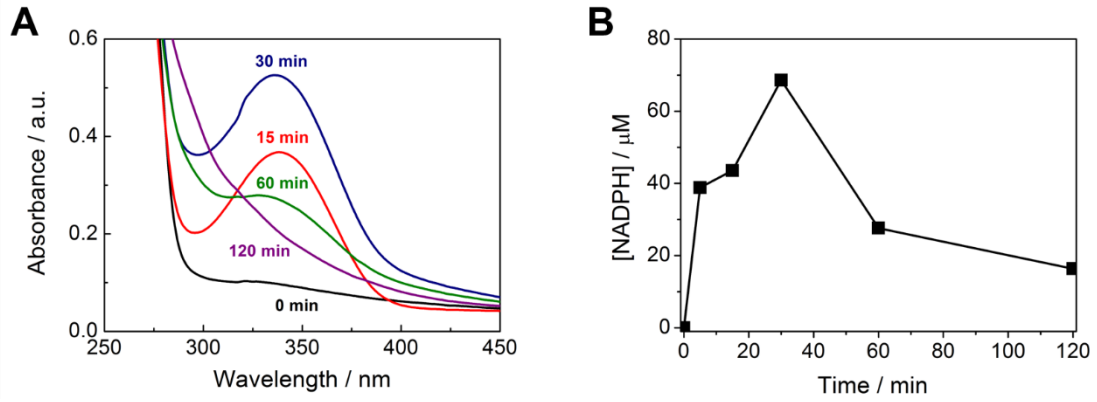

Figure 5.11 Solar-driven NADPH production by a particulate FNR-TiO_2 system. **A)** UV-vis absorbance of the reaction solution after centrifugation to remove TiO_2 particles. **B)** Time course of NADPH production. Reaction conditions: TiO_2 5 mg, buffer solution (25 mM MES, 25 mM TAPS, pH 8.0) 5 mL, FNR 0.53 μM, initial $NADP^+$ 200 μM. UV lamp (365 nm), room temperature.

Further experiments were conducted to investigate the decrease in NADPH production rates. A particulate TiO_2-FNR was prepared similarly to the previous experiment and irradiated with UV light, and NADPH concentration reached a maximum around 20-30 min, after which it decreased. After 60 min of irradiation, either additional $NADP^+$ (Figure 5.12A) or FNR (Figure 5.10B) was injected into the reaction vial, and irradiation was continued. Addition of $NADP^+$ did not lead to more NADPH production, which means the lack of $NADP^+$ (due to degradation) was not the cause for decrease in NADPH production rate. However, addition of FNR led to restoration of activity, indicating that the initial amount of FNR was deactivated after UV irradiation.

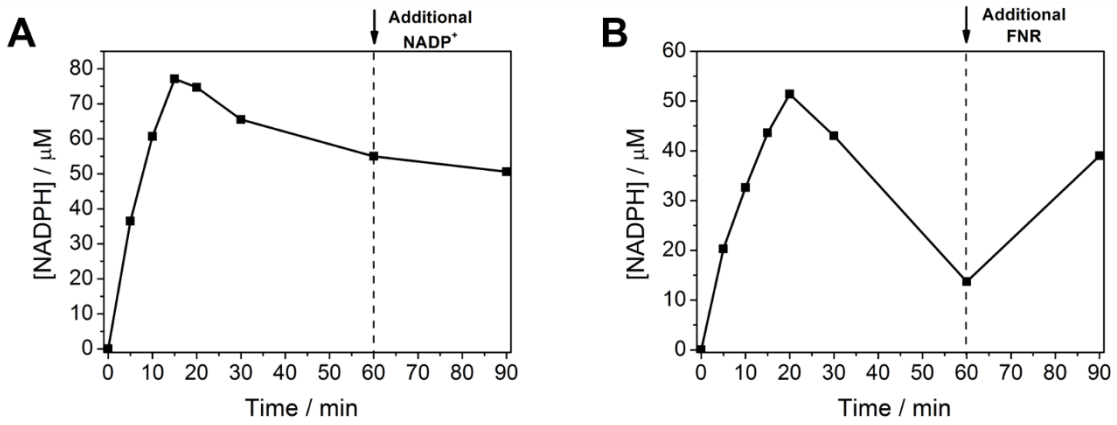

Figure 5.12 Re-addition of $NADP^+$ or FNR to a particulate TiO_2-FNR system under UV irradiation (365 nm) **A)** Reaction conditions: TiO_2 10 mg, buffer solution (25 mM MES, 25 mM TAPS, pH 8.0) 10 mL, FNR 0.35 μM, initial $NADP^+$ 200 μM. After 60 min, additional $NADP^+$ 200 μM **(**final concentration) was injected. **B)** Reaction conditions: TiO_2 3 mg, buffer solution (25 mM MES, 25 mM TAPS, pH 8.0) 10 mL, FNR 0.09 μM, initial $NADP^+$ 200 μM. After 60 min, additional FNR 0.18 μM **(**final concentration) was injected.

5.3 Conclusions and perspectives

As a continuation of the previous chapters on the FNR@ITO electrode (the electrochemical leaf in Chapters 3 and 4), here the FNR electrode was combined with a light-absorbing electrode to create a light-driven NADPH production system, or what we might call the 'photoelectrochemical leaf'. In this way, the functions of the leaf are mimicked even more closely: light absorption, leading to $NADP^+$ reduction and water oxidation.

The feasibility of the system was demonstrated by using a dye-sensitized TiO_2 electrode as the photoanode, in which $NADP^+$ reduction was observed under visible light without an applied bias. However, the requirement for a sacrificial electron donor makes this system unattractive for further investigation. By changing the photoanode materials to narrow band gap semiconductors (WO_3, $BiVO_4$), simultaneous water oxidation and $NADP^+$ reduction was achieved. However, this comes at the cost of an applied bias (0.7 – 1.1 V), as

the conduction band levels of these materials are not more negative than the $NADP^+$ reduction potential.

A particulate system was also examined, using TiO_2 particles to absorb UV light and generate excited electrons that could drive $NADP^+$ reduction by FNR. Under UV irradiation, FNR was deactivated, and some of the produced NADPH was degraded. In future systems, this could be circumvented by using visible-light active materials, such as a dye or a narrow band gap material with suitable band positions.

In principle, the 'photoelectrochemical leaf' described in this chapter could also be coupled to a downstream enzyme such as L-glutamate dehydrogenase demonstrated in Chapter 4 - a true solar-to-chemicals process. However, the rate of $NADP^+$ reduction in the current system is too slow to generate sufficient amounts of the downstream product for detection. A downstream NADPH-dependent enzyme for CO_2 assimilation using this system would be a true recreation of the biological leaf.

5.4 References

(1) Lewis, N. S.; Nocera, D. G. *Proceedings of the National Academy of Sciences* **2006**, *103*, 15729.

(2) Nam, D. H.; Ryu, G. M.; Kuk, S. K.; Choi, D. S.; Son, E. J.; Park, C. B. *Applied Catalysis B: Environmental* **2016**, *198*, 311.

(3) Lee, S. H.; Nam, D. H.; Kim, J. H.; Baeg, J.-O.; Park, C. B. *ChemBioChem* **2009**, *10*, 1621.

(4) Lee, S. H.; Nam, D. H.; Park, C. B. *Advanced Synthesis & Catalysis* **2009**, *351*, 2589.

(5) Brown, K. A.; Wilker, M. B.; Boehm, M.; Hamby, H.; Dukovic, G.; King, P. W. *ACS Catalysis* **2016**, *6*, 2201.

(6) Grzyb, J.; Waloszek, A.; Latowski, D.; Więckowski, S. *Journal of Inorganic Biochemistry* **2004**, *98*, 1338.

(7) Szczepaniak, K.; Worch, R.; Grzyb, J. *Journal of Physics: Condensed Matter* **2013**, *25*, 194102.

(8) Reisner, E.; Powell, D. J.; Cavazza, C.; Fontecilla-Camps, J. C.; Armstrong, F. A. *Journal of the American Chemical Society* **2009**, *131*, 18457.

(9) Woolerton, T. W.; Sheard, S.; Reisner, E.; Pierce, E.; Ragsdale, S. W.; Armstrong, F. A. *Journal of the American Chemical Society* **2010**, *132*, 2132.

(10) Hagfeldt, A.; Lindström, H.; Södergren, S.; Lindquist, S.-E. *Journal of Electroanalytical Chemistry* **1995**, *381*, 39.

(11) Tafalla, D.; Salvador, P.; Benito, R. M. *Journal of The Electrochemical Society* **1990**, *137*, 1810.

(12) Kudo, A.; Miseki, Y. *Chemical Society Reviews* **2009**, *38*, 253.

(13) Ye, H.; Park, H. S.; Bard, A. J. *The Journal of Physical Chemistry C* **2011**, *115*, 12464.

(14) Yu, J.; Zhang, Y.; Kudo, A. *Journal of Solid State Chemistry* **2009**, *182*, 223.

(15) Kang, D.; Kim, T. W.; Kubota, S. R.; Cardiel, A. C.; Cha, H. G.; Choi, K.-S. *Chemical Reviews* **2015**, *115*, 12839.

(16) Hisatomi, T.; Kubota, J.; Domen, K. *Chemical Society Reviews* **2014**, *43*, 7520.

(17) Walter, M. G.; Warren, E. L.; McKone, J. R.; Boettcher, S. W.; Mi, Q.; Santori, E. A.; Lewis, N. S. *Chemical Reviews* **2010**, *110*, 6446.

(18) Horecker, B. L.; Kornberg, A. *Journal of Biological Chemistry* **1948**, *175*, 385.

(19) Spectral irradiance from Newport, lamp model 6258, http://assets.newport.com/webdocuments-en/images/light_sources.pdf

(20) Gorton, L.; Domínguez, E. In *Encyclopedia of Electrochemistry*; Wiley-VCH Verlag GmbH & Co. KGaA: 2007.

Chapter 6

Electrochemical theory and experimental methods

6.1 Electrochemical theory

6.1.1 Protein film electrochemistry

Protein film electrochemistry (PFE),[1-3] involves investigation of redox-active enzymes directly adsorbed (or 'wired') onto the surface of an electrode (Figure 6.1). In the presence of substrate for the enzyme, the electrode acts as an electron source or sink to regenerate the active redox state of the enzyme, and the current flowing through the electrode is proportional to the turnover rate of the enzyme.

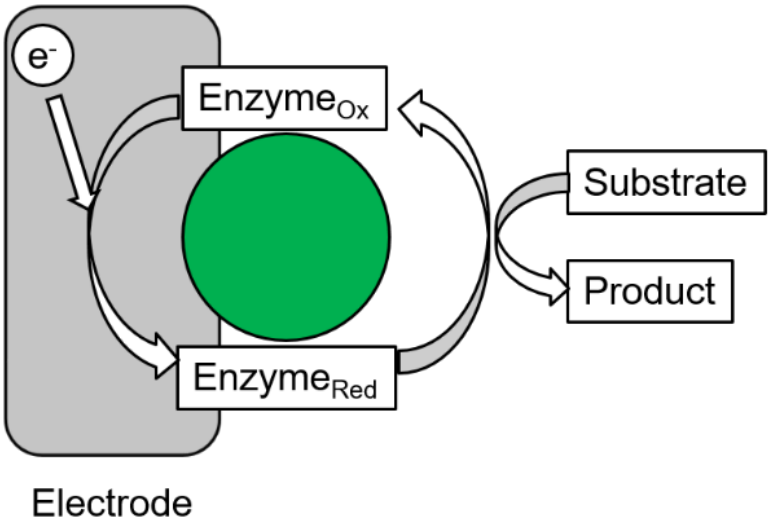

Figure 6.1 Diagram of an enzyme adsorbed onto an electrode, using reduction as an example. At a sufficiently negative potential, the electrode provides electrons to convert the oxidized form of the enzyme (Enzyme$_{Ox}$) to the reduced form (Enzyme$_{Red}$). The Enzyme$_{Red}$ then catalyses the reduction of substrate to product, returning to Enzyme$_{Ox}$ in the process.

The overall process can be broken down into the following components:

(1) Interfacial electron transfer between the electrode and the enzyme.

(2) Intramolecular electron transfer within the enzyme

(3) The kinetics of the enzyme

(4) Mass transport of the substrate to the electrode.

Any of these processes can be the current-limiting process. For enzymes without an internal

electron transfer chain such as Fe-S clusters, process (2) can be excluded. In this thesis, most voltammetry experiments are conducted at a sufficiently slow scan rate such that a steady-state is reached at each potential. The rate of interfacial electron transfer is fast, and the current should be controlled only by the kinetics of the enzyme and mass transport of the substrate.

Protein film electrochemistry presents several unique advantages in the study of enzymes. First, the required amount of enzyme sample is small, as it only needs to cover a small electrode area. Assuming that interfacial electron transfer is fast, the adsorbed enzyme will be at equilibrium with the electrode, *i.e.* potential control over the enzyme shall be established. Having immobilized enzyme on an electrode allows the environment of the enzyme (such as the concentration of substrates or inhibitors, or buffer composition) to be changed easily and repeatedly with the same film of enzyme, while maintaining potential control throughout. Achieving direct electron transfer between the electrode and enzyme circumvents possible convolutions from mediator diffusion and an additional electron transfer step.

6.1.2 Electrochemical setup

An electrochemical cell consists of two half-cells that are connected electrically through an electrolyte. The half-reaction of interest occurs at the working electrode (WE) and the circuit is completed by another half-reaction at the counter electrode (CE). In a three-electrode configuration, a third electrode (the reference electrode, RE) is used as a reference for the applied potential at the working electrode. The applied potential at the working electrode is written as

$$E = E_{WE} - E_{RE} - iR$$

where E_{WE} is the potential across the WE/solution interface, E_{RE} is the potential across the

RE/solution interface, R is the resistance of the electrolyte solution between the surfaces of WE and RE, and *i* is the current which should be minimal because the reference electrode is connected through a large resistance in the circuit. In this way, almost all of the current passes through the counter electrode, and the potential of the reference electrode remains unchanged throughout the experiment. A two-electrode configuration, *i.e.* without a reference electrode, can also be set up by referencing the potential of the WE to the CE. This is used in experiments where it is desirable to pass current through the same electrode that also acts as a potential reference, for example in Chapter 5 where the CE was a photoanode. In that case, both the reactions at the WE and CE are of interest, and the voltage of the overall cell is an important parameter.

6.1.3 Electrochemical techniques

Cyclic voltammetry

In cyclic voltammetry experiments, the electrode potential is swept between two set values at a constant rate (Figure 6.2), and the current is recorded. The resulting current-potential curve is called a voltammogram.

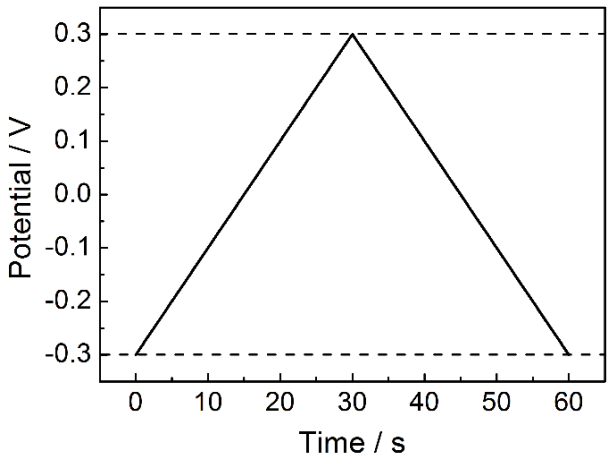

Figure 6.2 The potential sweep in a cyclic voltammogram

Chronoamperometry

Chronoamperometry involves holding the electrode potential at a constant value while measuring current over time. In stationary systems with planar diffusion of a redox couple in solution, the ideal current varies with the inverse of the square root of time, as described by the Cottrell equation.[4] However, in this thesis, chronoamperometry is used as a method for bulk electrolysis, and the cell solution is stirred by either a stirrer bar or by gas bubbling, to facilitate mass transport. Although this means that the nature of the mixing is not precisely describable, a compromise was necessary since this is a practical constraint due to the characteristics of the large working electrode which could not be rotated at high rates in a controlled manner.

Excluding the charging current (which decays exponentially with time), the charge passed during chronoamperometry corresponds to the charge used to convert substrate to product. The total charge passed q can be obtained by integrating the current obtained from chronoamperometry over the period of interest,

$$q = \int I \, dt$$

The charge passed can then be converted to the amount of product by using Faraday's constant, which is 96485 C mol^{-1} (*i.e.* the charge contained in 1 mol of electrons),

$$q = nFX$$

where X is the amount of product in moles and n is the number of electrons per reaction.

6.1.4 Types of currents

Non-faradaic current

Current that does not involve electron transfer to or from an electroactive species, *i.e.* charge does not cross the electrode/solution interface, is termed non-faradaic current (or charging current). This is due to the creation of an 'electrical double layer', in which charge

accumulates on the electrode as the potential is applied, and a corresponding charge of opposite sign accumulates in the solution near the electrode surface. This is equivalent to a capacitor, and the capacitance C is defined as

$$C = \frac{q}{E}$$

where q is the charge on the capacitor and E is the potential across the capacitor.

The current is charge passed over time,

$$I = \frac{dq}{dt} = C\frac{dE}{dt} = Cv$$

where ν is the scan rate. The charging current varies linearly with the capacitance C and the scan rate ν.

Faradaic current

Current that involves oxidation or reduction of an electroactive species is termed Faradaic current. In this thesis, two cases of Faradaic current are distinguished: in absence and presence of the substrate for the enzyme. In the absence of substrate (also called the non-catalytic or non-turnover case), the current represents the conversion of the adsorbed enzyme layer from one redox state to another. In the presence of substrate, the current represents the rate of consumption of the substrate.

Characteristics of a non-catalytic (non-turnover) signal

For a redox species adsorbed onto the surface of an electrode (also known as a thin layer), corresponding to the non-turnover signals of an adsorbed enzyme species (also covered in Chapter 3), a mathematical description of its voltammogram can be derived as follows.[5] The redox reaction is

$$Ox + ne^- \leftrightarrow Red$$

where Ox is the oxidized form, Red is the reduced form, and the reaction involves n electrons.

Assuming that the interfacial electron transfer between the electrode and the enzyme is fast, and therefore the coverages of Ox and Red reach an equilibrium at each applied potential, the equilibrium is described by the Nernst equation

$$E = E^0 - \frac{RT}{nF} ln \frac{\Gamma_{Red}}{\Gamma_{Ox}}$$

where E is the potential, E^0 is the formal reduction potential of the redox couple, R is the gas constant, T is the temperature, F is the Faraday constant, and Γ is the coverage (mol cm^{-2}) of each species.

If the total amount of adsorbed species is constant,

$$\Gamma_{total} = \Gamma_{Red} + \Gamma_{Ox}$$

combining this with the Nernst equation yields the coverage of the reduced species as a function of the electrode potential:

$$\Gamma_{red} = \frac{\Gamma_{total}}{1 + \exp[\frac{nF}{RT}(E - E^0)]}$$

Consider that the current is rate of reaction (or equivalently, the change in coverage of either species over time),

$$I = -nFA \frac{d\Gamma_{Red}}{dt}$$

where I is the current, and A is the electrode area.

Combining this with the previous equation gives the current as a function of the potential, *i.e.* a voltammogram,

$$I = \frac{n^2F^2A\Gamma_{total}}{RT} \frac{\exp\left[\frac{nF}{RT}(E - E^0)\right]}{\left\{1 + \exp\left[\frac{nF}{RT}(E - E^0)\right]\right\}^2} \frac{dE}{dt} \qquad Eq.1$$

where $\frac{dE}{dt}$ is the rate of change of potential, *i.e.* the scan rate, also written as ν. The function is shown in Figure 6.3 below. For simplicity, only the oxidative peak is treated here, but in

a full cyclic voltammogram there should be an equal and symmetrical reductive peak on the reverse scan.

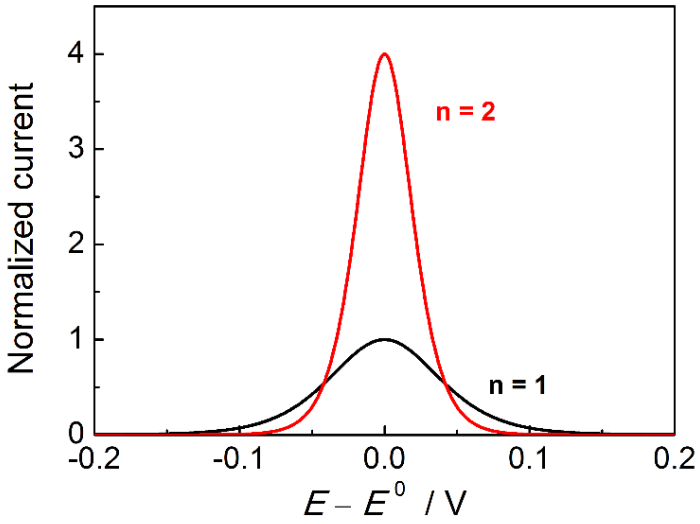

Figure 6.3 Ideal voltammograms of an adsorbed redox species at 20 °C, with n = 1 (black) and n = 2 (red). Curve obtained from plotting Eq.1 in Excel with $E - E^0$ intervals of 0.001 V, then normalizing to peak current for the n = 1 case.

The peak of the voltammogram can be found at the point where the derivative of the current against potential ($\frac{dI}{dE}$) is zero, yielding

$$E_{peak} = E^0 \text{ and}$$

$$I_{peak} = \frac{n^2F^2A\Gamma_{total}\nu}{4RT}$$

The peak current varies with the square of the number of electrons involved, explaining why non-turnover signals are sharper for the case of n = 2 compared to n = 1. Also note that the peak current varies linearly with the scan rate, as this can be used as a diagnostic to distinguish whether a redox species is adsorbed onto the electrode.

The peak width at half maximum height, δ, can be calculated by using $I_{peak}/2$ and solving for E in Eq. 1, yielding

$$\delta = 2\frac{RT}{nF}\ln\left(3 + 2\sqrt{2}\right) = 3.53\frac{RT}{nF}$$

$$\delta = \frac{89}{n} \text{ mV at 20 °C}$$

Remarkably, the ideal δ only depends on the number of electrons and the temperature, providing a convenient description of a redox system. In practical terms, a true n = 2 signal is rarely observed,[2,6] partly due to possible thermodynamic dispersion of the adsorbed species (*i.e.* variation in reduction potential across the ensemble of adsorbed species), or kinetic dispersion (*i.e.* variation in electron transfer rates), leading to broadening of the peak.

Another reason for peak broadening is the degree of cooperativity. An ideal n = 2 reaction means that the reaction is fully cooperative, *i.e.* the intermediate one-electron reduced species is instantly converted fully to the two-electron reduced state. However, in practice the semi-reduced state always has some level of stability. We can treat a n = 2 reaction as a sequence of two n = 1 reactions as follows:

$$\text{Ox} \underset{E_1}{\overset{+e^-}{\rightleftharpoons}} \text{Semi} \underset{E_2}{\overset{+e^-}{\rightleftharpoons}} \text{Red}$$

where Semi is the semi-reduced (one-electron reduced) species and Red is the fully reduced (two-electron reduced) species.

The current as a function of potential can be derived in a similar manner to the one-step case.[5,7] The total coverage now becomes

$$\Gamma_{total} = \Gamma_{Red} + \Gamma_{Semi} + \Gamma_{Ox}$$

and the Nernst equation can be written as

$$E = E_1 - \frac{RT}{F}\ln\left(\frac{\Gamma_{Semi}}{\Gamma_{Ox}}\right) = E_2 - \frac{RT}{F}\ln\left(\frac{\Gamma_{Red}}{\Gamma_{Semi}}\right)$$

As in the one-step case, we want to rearrange the Nernst equations so that the coverage of a species can be written as a function of potential, and this can be done by introducing the coproportionation constant (*K*)

$$K = \frac{(\Gamma_{Semi})^2}{\Gamma_{Ox}\Gamma_{Red}} = \exp[\frac{F}{RT}(E_1 - E_2)]$$

and a potential function

$$\xi = \frac{\Gamma_{Ox}}{\Gamma_{Red}} = \exp[\frac{2F}{RT}(E - E^0)]$$

where, in this case, E^0 is the reduction potential of the two-electron reaction, defined as the average of E_1 and E_2. The current, equal to the rate of consumption of Γ_{Red} or production of Γ_{Ox} in the one-step case, is now equal to the consumption of Γ_{Red} and $\Gamma_{Semi,}$ or the production of Γ_{Semi} and Γ_{Ox}. Considering that it takes 2 electrons to consume one molecule of Red and 1 electron to consume one molecule of Semi, the current function can be written in terms of K and ξ as follows:

$$I = -FA\frac{d(2\Gamma_{Red} + \Gamma_{Semi})}{dt} = \frac{F^2 A\Gamma_{total}\nu}{RT}\frac{\left(4 + \sqrt{K\xi} + \sqrt{\frac{K}{\xi}}\right)}{\left(\sqrt{\xi} + \sqrt{K} + \frac{1}{\sqrt{\xi}}\right)^2} \qquad Eq.2$$

The function is plotted out in Figure 6.4 below for a range of differences between the reduction potentials of each of the one-electron steps ($E_1 - E_2$), and the peak widths at half maximum (δ) were calculated for a range of $E_1 - E_2$ (shown in Table 6.1). As E_2 becomes more negative than E_1, the peak shape converges to the shape of an ideal n = 2 case (*i.e.* the fully cooperative case), and when E_2 becomes more positive than E_1, the peak broadens and eventually splits into two separate peaks when the difference is large (200 mV or more).[2]

As the total charge passed during one sweep is equal to the charge used to fully convert all of the adsorbed species from one form to the other, assuming no other processes are occurring, the total coverage of the adsorbed species Γ_{total} (mol cm^{-2}) can be determined (provided that the electrode area and scan rate are known) by integrating the current,

$$\int I\,dE = \int I\,dt(\frac{dE}{dt}) = nFA\Gamma_{total}\cdot\nu$$

where n is the number of electrons per reaction, F is Faraday's constant, A is the electrode

area, Γ_{total} is the coverage of the redox species, and ν is the scan rate.

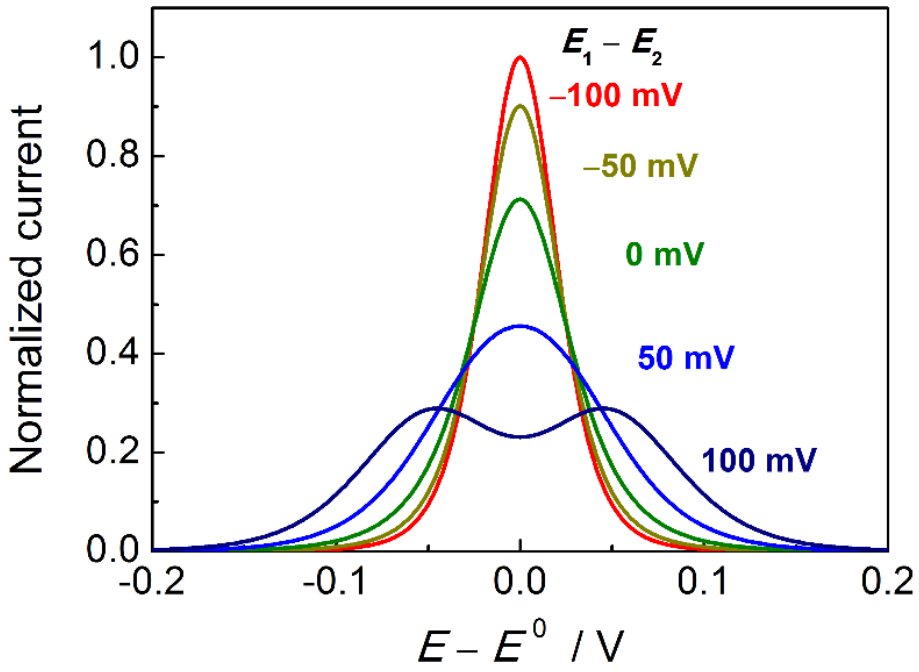

Figure 6.4 Ideal voltammograms of a two-electron reaction for an adsorbed species at 20 °C, for a range of $E_1 - E_2$. Curve obtained by plotting Eq.2 in Excel with $E - E^0$ intervals of 0.001 V, then normalizing to the $E_1 - E_2$ = -100 mV case.

Table 6.1 The ideal peak width at half maximum (δ) for a range of $E_1 - E_2$

$E_1 - E_2$ (mV)	peak width δ (mV)
50	107.9
40	94.6
30	84.0
20	75.7
10	69.3
0	64.3
-10	60.4
-20	57.3
-30	54.9
-40	52.9
-50	51.4

Characteristics of a catalytic current

When the substrate of a redox enzyme (which is adsorbed on an electrode surface) is present in solution, the current is the rate of enzyme catalysis. If the enzyme operates reversibly and the kinetics are sufficiently fast, the current characteristics approach that of a redox couple in solution at a stationary electrode (Figure 6.5). For example, starting with the oxidized form of the substrate in solution, when the potential is too positive, no reduction occurs. As the potential is swept towards more negative values, more driving force is given to the enzyme for reduction and therefore the reduction current increases. As the reaction continues, the substrate near the electrode surface becomes depleted, and at some point the reduction current decreases due to mass transport limitation. For a stationary reversible system, the peak current[4] is given as:

$$I_{peak} = 0.4463(\frac{F^3}{RT})^{1/2} n^{3/2} A D^{1/2} C v^{1/2}$$

where D is the diffusion coefficient and C is the bulk concentration of the redox species. This equation is also known as the Randles-Sevcik equation, named after the initial formulations. The peak current can be determined by measuring from an extrapolated linear baseline from the part of the voltammogram before onset of the current peak. The peak current varies with the bulk concentration, as well as with the square root of the scan rate. The latter is useful as a diagnostic, to determine whether a redox species is in solution. The diffusion coefficient can be obtained from the slope of a plot between peak current and square root of scan rate.

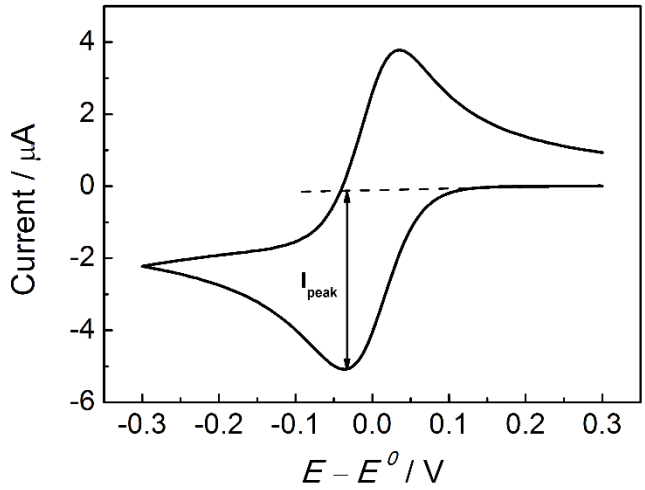

Figure 6.5 Simulated cyclic voltammogram showing peak current. Simulation was written in Excel using the finite difference method, following the procedure in ref[8]. Parameters: diffusion coefficient 1 $\times 10^{-5}$ cm^2 s^{-1}, scan rate 0.02 V s^{-1}, initial bulk concentration of oxidized species 50 μM.

Redox reactions at the electrode coupled to a homogeneous reaction

The products of redox reactions at the electrode can be coupled to homogeneous reactions in solution. One case of interest for this thesis is the catalytic regeneration mechanism (also referred to as EC', denoting an electron transfer step followed by a chemical step) in which the first step is the redox reaction at the electrode (taking reduction as an example),

$$Ox + ne^- \leftrightarrow Red$$

and the reduced product further reacts with a species (X) in solution

$$Red + X \rightarrow Ox + Y$$

regenerating the oxidized species, assuming that X and Y are not electroactive. Figure 6.6 shows simulated cyclic voltammograms of this reaction mechanism. As the coupled reaction rate increases (Figure 6.6A), the reduced species is consumed and therefore the oxidative peak decreases. At the same time, the oxidized species is replenished and no longer depleting near the electrode surface, resulting in enhancement of the reductive current and loss of its

peak-like character. The shape of the CV also depends on the scan rate (Figure 6.6B), as faster scan rates mean there is less time for the coupled reaction to occur. In the extreme case, this causes the voltammogram to revert to the original uncoupled, reversible shape, *i.e.* the scan has 'outrun' the coupled reaction. Therefore, slow coupled reactions may not be observable if the scan rate is not sufficiently slow.

In this thesis, this reaction mechanism corresponds to reversible $NADP^+$/NADPH at the FNR@ITO electrode, with a coupled downstream enzyme (glutamate dehydrogenase, for example) and its substrates (NH_4^+, 2-oxoglutarate) present in solution, ready to consume NADPH and regenerate $NADP^+$ (see also Chapter 4):

At the electrode: $NADP^+ + H^+ + 2e^- \leftrightarrow NADPH$

In solution: $NADPH + NH_4^+ + \text{2-oxoglutarate} \rightarrow NADP^+ + \text{L-glutamate}$

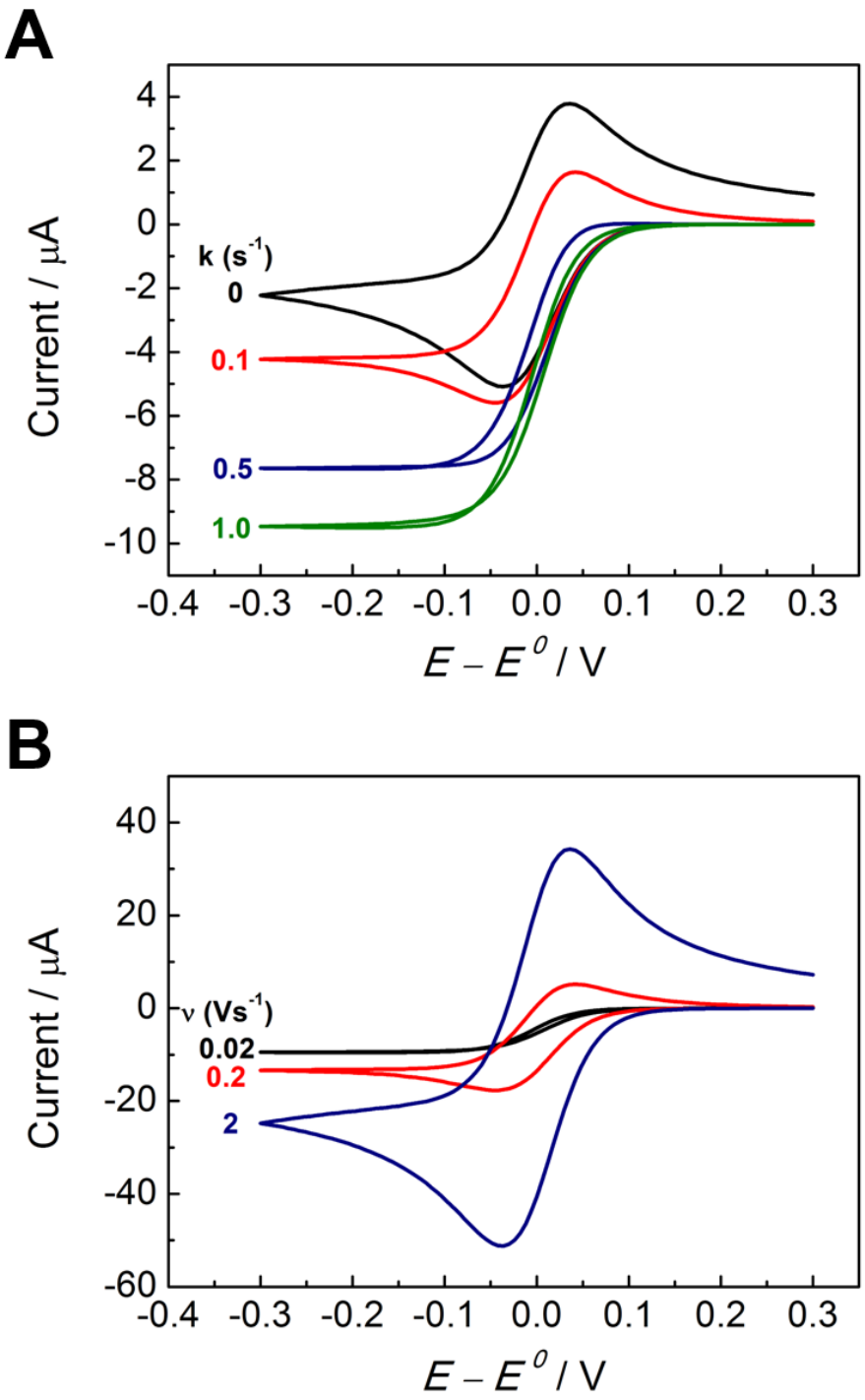

Figure 6.6 Simulated cyclic voltammograms with a coupled catalytic reaction. **A)** Effect of the rate (k) for the coupled reaction on the cyclic voltammogram for the redox reaction at the electrode. **B)** Effect of scan rate (ν) on the cyclic voltammogram for the redox reaction at an electrode when coupled to a downstream reaction. Simulation was written in Excel using the finite difference method, following the procedure in ref[8]. Parameters: diffusion coefficient 1×10^{-5} cm^2 s^{-1}, scan rate 0.02 V s^{-1} unless indicated, initial bulk concentration of oxidized species 50 μM.

6.1.5 Semiconductor materials and their photoelectrochemistry

The (photo)electrochemistry of semiconductors is covered in many excellent reviews.[9-13] Semiconductors can be described using the energy band model, with the highest energy filled electronic band (called the valence band, VB) and an empty band (the conduction band, CB) lying higher in energy, separated by a band gap (Figure 6.7). If the semiconductor is irradiated with photons with energy at least equal to the band gap energy, electrons from the VB can be excited into the CB, creating free (mobile) electrons in the CB and leaving a positively charged hole in the VB.

For undoped (also known as intrinsic) semiconductors, the concentration of electrons and holes are equal. Semiconductors can be doped to increase the concentration of one of the charged species. For an n-type semiconductor, the concentration of electrons is significantly higher than holes, thus electrons and holes are called the majority and minority carriers, respectively. The reverse is true for a p-type semiconductor. Doping in semiconductors can be caused by addition of impurities to an intrinsic semiconductor, such as adding P (a group V element) to intrinsic Si (group IV) causes it to become n-type, due to excess electrons provided by the P atoms. Alternatively, doping can also be caused by nonstoichiometry of the semiconductor, such as interstitial atoms or crystal defects. For many oxide materials, oxygen vacancies can lead to excess electrons which can cause n-type doping.

The Fermi level (E_F) of a semiconductor is defined as the energy level in which the probability of finding an electron is 0.5, and this is equivalent to the electrochemical potential of electrons in that semiconductor. The Fermi level lies midway between the conduction band and valence band in intrinsic semiconductors, closer to the conduction band for n-type, and closer to the valence band for p-type semiconductors.

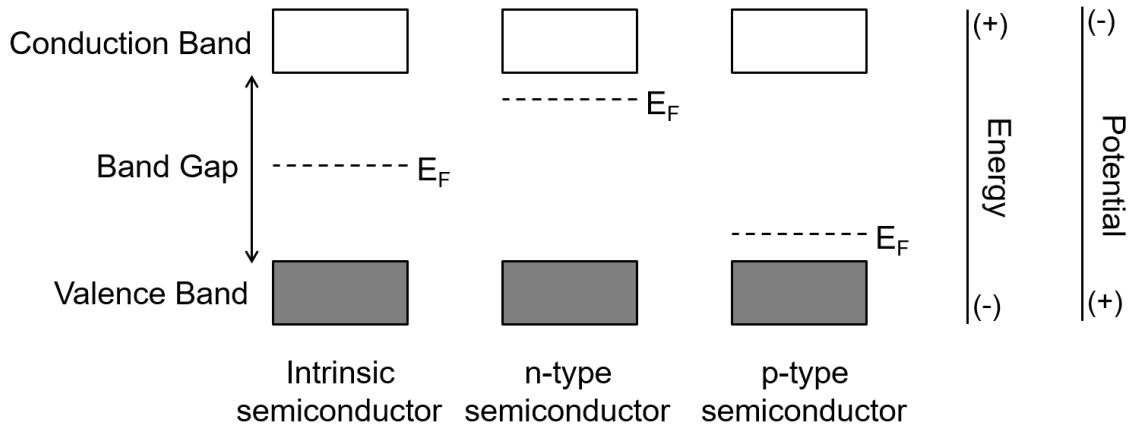

Figure 6.7 Band diagrams of semiconductors and their Fermi levels (E_F).

When a semiconductor electrode comes into contact with an electrolyte solution containing a redox couple (A/A^-), the energy level of its electrons will equilibrate with that of the electrolyte. Using an n-type semiconductor as an example (Figure 6.8), the Fermi level is higher in energy than that of the redox couple, and therefore electrons flow out from the semiconductor into the solution, creating a depletion layer or space charge region in the semiconductor near the interface. This charge transfer continues until the electrochemical potentials of both the semiconductor and solution are equal, and since the levels of the conduction and valence bands are 'pinned' at the surface, this causes band bending (*i.e.* a potential gradient).

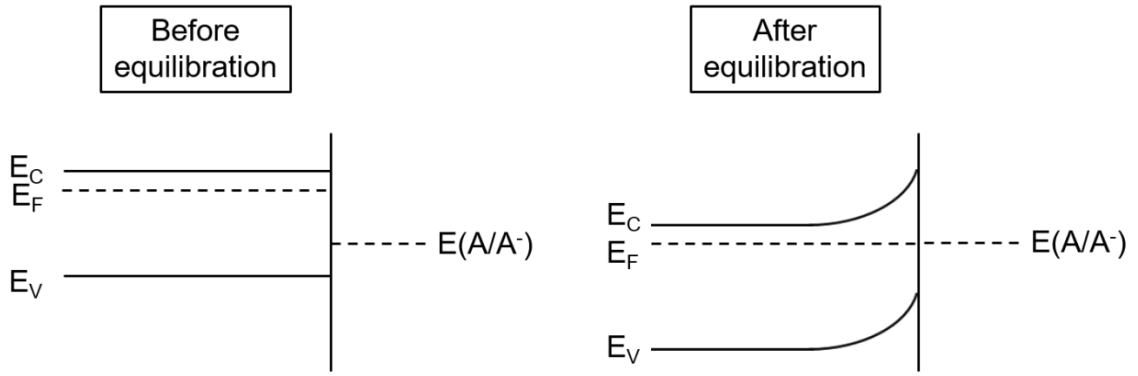

Figure 6.8 Energy diagram of a semiconductor-electrolyte interface, before and after equilibration, using an n-type semiconductor as an example. E_C: Conduction band energy, E_V: Valence band energy, E_F: Fermi level, A/A^-: redox couple in solution.

Applying a potential to a semiconductor electrode is equivalent to shifting its Fermi level (E_F). As the magnitude of the band gap and the relation between the conduction band energy (E_C), valence band energy (E_V) and E_F do not change with applied potential, the nature of the band bending depends on the applied potential (Figure 6.9). The flat band potential (E_{fb}) is the applied potential where the bands become flat. When the potential is more positive than E_{fb}, a potential gradient is created such that electrons are moved to the back contact, and holes move to the semiconductor surface. Note that for an n-type semiconductor, the hole concentration in the dark is small, and a current is observed only upon band gap excitation, which generates electron-hole pairs. When the potential is more negative than E_{fb}, a potential gradient is created in the opposite direction, and electrons move towards the semiconductor surface.

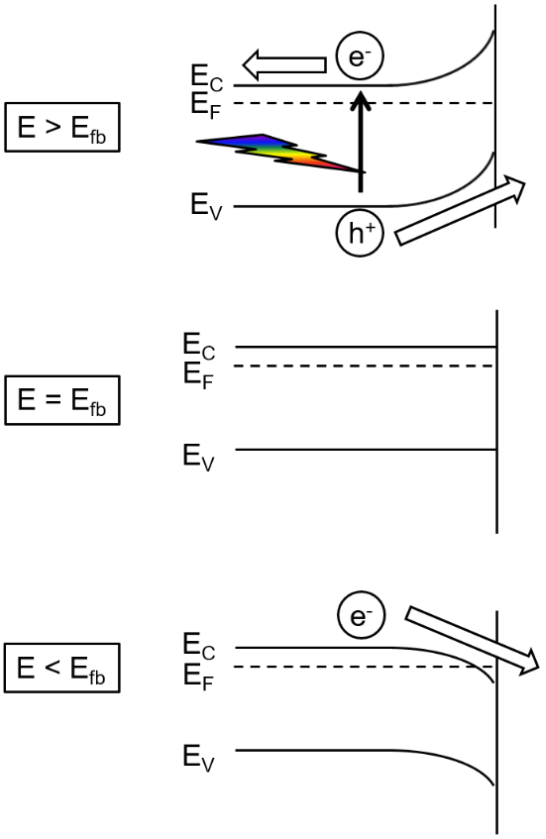

Figure 6.9 Energy diagram of an n-type semiconductor electrode at various potentials relative to its flat-band potential (E_{fb}).

Figure 6.10 shows the current-potential characteristics of an ideal n-type semiconductor. In the dark, the semiconductor behaves like a diode, allowing current to pass only when the potential becomes sufficiently negative. Under light irradiation with enough energy to excite electrons across the band gap, minority carriers are generated which contributes to the photocurrent. The contribution of the photocurrent at more negative potentials is insignificant since the electron concentration is already high in an n-type semiconductor. This leads to the general rule that photocurrent is generated by the minority carrier, and thus an n-type semiconductor is expected to be a photoanode, and a p-type semiconductor to be a photocathode.

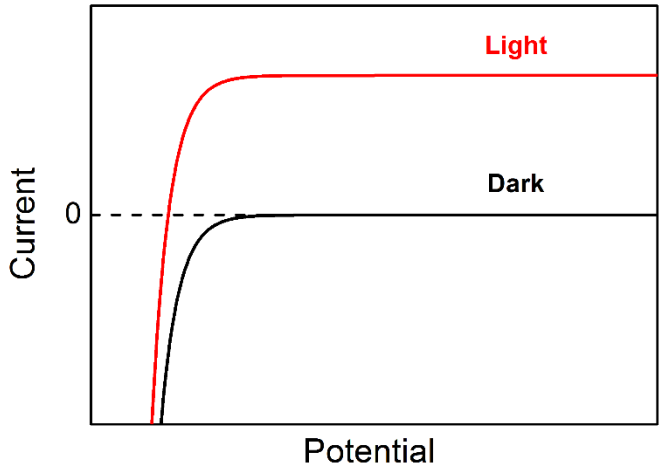

Figure 6.10 Ideal photocurrent of an n-type semiconductor electrode in the dark (black) and under light irradiation (red). Curves obtained from assuming the total current has contributions from minority and majority carriers. The current from minority carriers depends on light intensity, and is assumed to be constant at each intensity, while the current from majority carriers behaves like a diode.[12]

6.2 Experimental methods

6.2.1 Purification of tetrachloroethene reductive dehalogenase (PceA) from *Sulfurospirillum multivorans*

The enzyme tetrachloroethene reductive dehalogenase (PceA) was provided by Cindy Kunze from the group of Gabriele Diekert at Institut für Mikrobiologie, Friedrich-Schiller-Universität Jena, Lehrstuhl für Angewandte und Ökologische Mikrobiologie, Jena, Germany.

PceA was purified from a *Sulfurospirillum multivorans* mutant strain producing PceA with a C-terminal Strep-Tag. The strain was cultivated in 12 L pyruvate/fumarate-containing medium[14] in the presence of 0.72 mM $FeSO_4$ and kanamycin. The cells were harvested under oxic conditions before disruption via French Press under anaerobic conditions. $PceA_{strep}$ was purified under anoxic conditions via gravity flow using Strep-Tactin (IBA, Göttingen, Germany) as described previously.[15,16] A total of 2.3 mg of PceA-Strep were obtained from 1.9 g cell protein. The enzyme was stored at -80 °C. The concentration of enzyme solution was 1.187 mg/mL.

6.2.2 Purification of ferredoxin-$NADP^+$ reductase (FNR) from C*hlamydomonas reinhardtii*

The plasmid for FNR as well as initial batches of FNR were provided by Martin Winkler from the group of Professor Thomas Happe at AG Photobiotechnologie Ruhr-Universität Bochum, Bochum, Germany. Later, FNR was produced and purified under guidance from Dr. Clare F. Megarity.

Competent *Escherichia coli* BL21-DE3 cells were transformed with a pASK-IBA7 plasmid containing the gene encoding C*hlamydomonas reinhardtii* FNR with a Strep-Tag and also the genes which confer ampicillin resistance. A single colony resulting from this

transformation was selected, grown overnight and scaled up, using ampicillin throughout to ensure the selection of only those cells containing the genes which confer ampicillin resistance and therefore also the gene encoding FNR. The over-expression of FNR was induced by the addition of anhydrotetracycline. Cells were disrupted by French press and insoluble material removed by centrifugation. The resulting supernatant was purified using a strep-tactin chromatography column; FNR was eluted from the column using desthiobiotin and the fractions were pooled, concentrated and stored at -80 °C. A His-tagged analogue was also expressed and its activity was comparable to the strep-tagged version. The coding sequence for FNR (present in the pASK-IBA7 vector) was amplified by PCR and cloned into a pLATE5 N-terminal Histag/EK vector by ligation-independent cloning. The His-tagged enzyme was expressed in *E. coli* BL21-DE3 cells (induced by addition of Isopropyl β-D-1-thiogalactopyranoside (IPTG)) and purified using nickel-affinity chromatography.

6.2.3 Electrode fabrication

6.2.3.1 Pyrolytic graphite edge (PGE) electrode

Pyrolytic graphite edge (PGE) electrodes were fabricated in-house; a small piece of pyrolytic graphite was fixed by silver glue to a metal contact rod in a Teflon casing, then the exposed sides of the graphite piece was covered in epoxy resin. The graphite was oriented so that the basal planes were perpendicular to the surface (approximately 0.03 – 0.3 cm^2).

6.2.3.2 Metal oxide electrodes

Metal oxide electrodes: TiO_2 in Chapter 2, ITO in Chapters 3 and 4, and WO_3 in Chapter 5, were fabricated by loading the oxide particles onto a conductive support. (Note that the *support* in this case is typically called the *substrate* in the materials field, but this is avoided here since it may be confused for the substrate of an enzyme.) When using glass

plates with a thin layer of ITO (also called ITO glass) as the support, the plates were cut into pieces of typically 2.5 × 1.0 cm^2, then cleaned by sonicating in acetone, ethanol, then water for 15 min each, then allowed to dry in an oven at approximately 80 °C. The metal oxide particles were loaded onto the conductive side of the ITO glass by either of two methods described below.

Doctor's blade method

Metal oxide particles were added to either 0.1 M HNO_3 or acetic acid/ethanol solution, and sonicated for 30 min. Clean ITO glass slides were fixed onto a flat surface using scotch tape, with the conductive side upwards, and the tape marked out the area to be loaded with metal oxides. An aliquot of the metal oxide suspension (approximately 20 μL per 1 cm^2 of exposed glass) was dropped onto the ITO glass, a glass slide was used to scrape off the excess to leave a flat layer behind. After leaving to dry at room temperature, the loaded ITO glass slides were calcined at 450 °C for 30 min with a 5 °C/min ramp rate.

Electrophoretic deposition method

Indium tin oxide (ITO) electrodes were made by electrophoretic deposition[17,18] of ITO powder (Sigma) onto a conductive support, either ITO-glass slides (SPI Supplies), a pyrolytic graphite edge (PGE) electrode, or Ti foil (Sigma). A suspension of ITO (0.02 g) and I_2 (0.005 g) was prepared in acetone (20 mL) and sonicated for 30 mins. Two conductive supports were held in parallel orientation in the ITO suspension with a separation of 1 – 2 cm, and a voltage of 10 V applied for 3 – 6 mins. The electrode was then left to dry in air before use. Fluorine-doped tin oxide (FTO) electrodes were also made in a similar manner.

6.2.4 Electrochemical measurements

Glovebox and equipment

Experiments with the oxygen-sensitive tetrachloroethene reductive dehalogenase (PceA, Chapter 2) were conducted inside an anaerobic glovebox with a N_2 atmosphere (Belle Technologies, O_2 < 5 ppm).

Experiments with ferredoxin-$NADP^+$ reductase (FNR, Chapters 3 – 5) were conducted on the bench. Electrochemical measurements were taken after purging the cell with Ar to remove dissolved O_2 which could give rise to reduction currents.

A potentiostat (either PGSTAT10 or PGSTAT101) was used for electrochemical measurements, with the software NOVA1.10.

Reference electrodes

The reference electrodes used in this thesis were either SCE (saturated calomel electrode) or Ag/AgCl (kept in 3 M KCl). The reference electrodes were calibrated by measuring their potential against a Pt wire in a saturated quinhydrone solution at pH 4.0 and pH 7.0 The potential was converted to standard hydrogen electrode (SHE) using the following equations:

$$E_{SHE} = E_{SCE} + 0.244 \text{ at 20 °C with saturated KCl}$$

$$E_{SHE} = E_{Ag/AgCl} + 0.211 \text{ at 20 °C with 3 M KCl}$$

6.2.5 Light driven reactions

Light-driven dehalogenation by PceA adsorbed onto TiO_2 particles

TiO_2 particles (P25, Degussa, 7 mg) were sonicated in Tris buffer (pH 7, 7 mL) for 15 min, then 7 µL of PceA solution (1.19 mg/mL) was added to the suspension which was stirred for a further 20 min. The substrate solution, either PCE or TCE in EtOH, was added

and the reaction vessel was sealed with a Teflon cap. Note that TCE is known to dissolve rubber, therefore rubber stoppers should be avoided for prolonged reactions. A UV lamp (UVL-28 EL series, 365 nm, 8 W, held at 1.5 cm distance) was used to illuminate the vessel under continuous stirring. Periodically, a 0.5 mL sample of the liquid phase was taken for product detection by GC-MS headspace analysis. The cell was not thermostatted: during irradiation, the temperature of the solution increased from 24 ^{o}C to 30 ^{o}C over the course of 4 h.

Light-driven NADPH production by FNR on ITO electrodes

A photoanode (either WO_3 or $BiVO_4$) was connected to an FNR@ITO electrode in a one-compartment cell in a two-electrode configuration. The cell was immersed in a water jacket kept at 20 °C. A Xe lamp at 300 W was used, held at a distance 3 cm from the photoanode, and a cutoff filter (λ >420 nm) to ensure that only visible light was irradiated.

6.2.6 UV-vis spectroscopy

Absorbance spectra were recorded with a Perkin-Elmer Lambda 19 UV-vis spectrometer using quartz cuvettes. To determine the amount of PceA adsorbed onto TiO_2 particles (Chapter 2), the spectrum of the PceA solution (5.95 μg/mL in Tris buffer pH 7) was measured before and after stirring (following centrifugation) with TiO_2 particles (1 mg/mL) for 20 min. The concentration of NADPH (Chapter 5) was also determined by UV-vis absorbance at 340 nm.

6.2.7 Gas chromatography – Mass spectrometry (GC-MS)

For analysis of PCE, TCE and cDCE, GC-MS headspace analysis was used, where

the sample vial was heated to increase the partial pressure of the analyte in the vial headspace. (Agilent 7890B, HP5 column, He carrier gas). The GC sampling vial was incubated at 60 °C for 5 min before a sample of the headspace was taken. The GC oven was held at 40 °C for 5 min after injection, then ramped up to 290 °C at a rate of 50 °C/min. Calibration was established with standard solutions of PCE, TCE, and *c*DCE

For analysis of the product of ketoreductase catalysis (ECHB), the product was extracted into chloroform by agitating 1 mL of cell solution with 1.5 mL of chloroform for 10 minutes; the chloroform phase was then placed in a GC sampling vial for direct injection.

6.2.8 NMR spectroscopy

A sample of the cell solution was mixed with D_2O to make a 90:10 (H_2O:D_2O) mixture, and the ^1H spectra were recorded on a Bruker AVIIIHD 400 instrument using a setting for the suppression of water signals. The results were analyzed in the program MestreNova. The peak area corresponding to the product was compared to a calibration curve obtained from standard solutions of known concentration.

6.2.9 Scanning electron microscopy (SEM)

SEM images were acquired by Thomas O. M. Samuels (from the group of Professor Jamie Warner, Materials Department, Oxford) using a Hitachi S-4300 with a field-emission electron source at an accelerating voltage of 3 kV.

6.2.10 Buffer solutions

Tris-NH_4 (Chapter 2)

A solution of Tris-HCl 100 mM and $(NH_4)_2SO_4$ 4 mM was prepared in ultrapure

water (Millipore, 18 MΩ cm), the pH was adjusted by adding concentrated NaOH or HCl.

MES-TAPS (Chapter 3, 4)

A mixture of MES and TAPS buffer was chosen due to the wide pH range used in the experiments. MES-TAPS buffer was prepared by first making a solution of 25 mM MES and 25 mM TAPS in ultrapure water (Millipore, 18 MΩ cm), then adjusting the pH to the desired value by adding concentrated NaOH.

Borate buffer (Chapter 4, 5)

Separately, solutions of H_3BO_3 50 mM and $Na_2B_4O_7$ 12.5 mM were prepared in ultrapure water (Millipore, 18 MΩ cm), then the $Na_2B_4O_7$ solution was titrated into the H_3BO_3 solution until the desired pH (8.0) was attained.

6.3 References

(1) Léger, C.; Elliott, S. J.; Hoke, K. R.; Jeuken, L. J. C.; Jones, A. K.; Armstrong, F. A. *Biochemistry* **2003**, *42*, 8653.

(2) Hirst, J. *Biochimica et Biophysica Acta (BBA) - Bioenergetics* **2006**, *1757*, 225.

(3) Léger, C.; Bertrand, P. *Chemical Reviews* **2008**, *108*, 2379.

(4) Bard, A. J.; Faulkner, L. R. *Electrochemical Methods*; 2nd ed.; Wiley, 2001.

(5) Heering, H. A.; Weiner, J. H.; Armstrong, F. A. *Journal of the American Chemical Society* **1997**, *119*, 11628.

(6) Armstrong, F. A.; Camba, R.; Heering, H. A.; Hirst, J.; Jeuken, L. J. C.; Jones, A. K.; Le′ ger, C.; McEvoy, J. P. *Faraday Discussions* **2000**, *116*, 191.

(7) Plichon, V.; Laviron, E. *Journal of Electroanalytical Chemistry and Interfacial Electrochemistry* **1976**, *71*, 143.

(8) Brown, J. H. *Journal of Chemical Education* **2015**, *92*, 1490.

(9) Nozik, A. J.; Memming, R. *The Journal of Physical Chemistry* **1996**, *100*, 13061.

(10) Tan, M. X.; Laibinis, P. E.; Nguyen, S. T.; Kesselman, J. M.; Stanton, C. E.; Lewis, N. S. In *Progress in Inorganic Chemistry*; John Wiley & Sons, Inc.: 2007, p 21.

(11) Walter, M. G.; Warren, E. L.; McKone, J. R.; Boettcher, S. W.; Mi, Q.; Santori, E. A.; Lewis, N. S. *Chemical Reviews* **2010**, *110*, 6446.

(12) Krishnan, R. In *Encyclopedia of Electrochemistry*; Wiley-VCH Verlag GmbH & Co. KGaA: 2007.

(13) Gratzel, M. *Nature* **2001**, *414*, 338.

(14) Scholz-Muramatsu, H.; Neumann, A.; Meßmer, M.; Moore, E.; Diekert, G. *Archives of Microbiology* **1995**, *163*, 48.

(15) Bommer, M.; Kunze, C.; Fesseler, J.; Schubert, T.; Diekert, G.; Dobbek, H. *Science* **2014**.

(16) Neumann, A.; Wohlfarth, G.; Diekert, G. *Journal of Biological Chemistry* **1996**, *271*, 16515.

(17) Besra, L.; Liu, M. *Progress in Materials Science* **2007**, *52*, 1.

(18) Krüger, H. G.; Knote, A.; Schindler, U.; Kern, H.; Boccaccini, A. R. *Journal of Materials Science* **2004**, *39*, 839.

Chapter 7

Conclusions

7.1 Conclusions

7.1.1 Direct electron transfer from inorganic materials to enzymes (Chapter 2, 3)

Throughout this thesis, I have exploited the usefulness of inorganic materials as 'unnatural' electron donors to enzymes, for both studying the intrinsic properties of enzymes as well as creating hybrid systems to produce specific chemicals. First, in Chapter 2, direct electron transfer was observed from TiO_2 to tetrachloroethene reductive dehalogenase PceA. This is possible because the conduction band level of TiO_2 was more negative than that of the electron entry points (Fe-S clusters in PceA), which is a necessary condition for electron transfer from a semiconductor material to an enzyme.

The ITO electrodes used in Chapters 3 to 5 allowed facile investigation of the properties of FNR, which was not possible with conventional graphite electrodes. Based on similarities of ITO to the biological redox partner of FNR, ferredoxin, FNR could be adsorbed onto ITO electrodes in an electroactive configuration. In this case, ITO behaves as a metallic material, but with the added benefit of having surface hydroxyl groups which makes the surface negatively charged at a sufficiently high pH. The porous nature of the ITO layer allowed FNR to be adsorbed in up to hundreds of monolayer equivalents, leading to strong non-turnover signals.

7.1.2 'The electrochemical leaf': A new cofactor regeneration system (Chapter 3, 4)

The discovery of the activity of FNR on ITO led to the creation of an $NADP^+$/NADPH regeneration system that is potentially scalable to industrial application, and a patent application[1] has been filed based on this work. Investigation of the electrochemical leaf proceeded rationally step-by-step, with the first step being the interaction between FNR and the ITO electrode. Analysis of these non-turnover signals

yielded information on the reduction potential of FNR and the level of cooperativity in the two electron transfer steps to its FAD group. After confirming the FNR-ITO interaction, $NADP^+$ was added to the system to observe the catalytic activity of FNR. Production of NADPH was observable in the return oxidative scan of stationary cyclic voltammetry, as well as UV-vis absorbance of the cell solution at 340 nm. Finally, the $NADP^+$/NADPH recycling by the FNR@ITO electrode was coupled to downstream enzymes, and the downstream products were confirmed by NMR which matched well with the charge passed monitored during chronoamperometry.

The electrochemical leaf was successfully coupled to three downstream enzymes (glutamate dehydrogenase, isocitrate dehydrogenase, and ketoreductase), and in one case it was able to work in both directions, for either $NADP^+$ regeneration or NADPH regeneration. The limitation is not at the FNR@ITO electrode, as FNR catalyses the interconversion of $NADP^+$/NADPH rapidly and reversibly, but at the coupled enzyme. The 'leaf' can also be constructed on different oxide materials, and FNR was stable on an ITO electrode with 40% of the initial FNR coverage remaining after storage at 4 °C for one week.

Cofactor regeneration has been extensively studied by a large variety of approaches, but the electrochemical leaf, *i.e.* direct electrochemical control of $NADP^+$/NADPH recycling by FNR, possesses some distinct advantages. The 'leaf' retains the high selectivity of an enzyme-based system, while also possessing the benefits of an electrochemical system. The reducing power is supplied by electrons which are inexpensive, and the reaction can be monitored easily from the current. In addition, the leaf can be inserted into a reactor, then easily removed afterwards because the system does not use additional substrates or generate any by-products. Finally, the leaf is air-stable and easily scalable, which makes the system potentially useful at an industrial scale.

7.1.3 Solar-to-chemicals processes by enzyme-material composites (Chapter 2, 5)

This thesis also explored the possibilities of using enzyme-materials hybrids for 'solar-to-chemicals' conversion. In Chapter 2, TiO_2 was used as the light absorber, and PceA was used as the surface catalyst for the conversion of tetrachloroethene (PCE) to trichloroethene (TCE) and then selectively *cis*-dichloroethene (*c*DCE). Without the enzyme PceA as a catalyst, PCE and TCE decompose on bare TiO_2 to give a mixture of products. In Chapter 5, light-driven NADPH production was achieved by connecting the FNR@ITO electrochemical leaf to a light-absorbing photoanode, as well as by FNR adsorbed onto TiO_2 particles.

Solar-to-chemical processes were achieved in this thesis using both particulate and photoelectrochemical configurations. Photoelectrochemical systems possess the distinct advantages of better charge separation at the light absorber (due to the potential gradient) and the separation of products at each electrode. In addition, each electrode can be developed and optimized separately. However, the electrode area scales in two dimensions while the reaction cell scales in three dimensions, and in this regard the particulate system is more scalable.

The results of this thesis have shown the importance of choosing the right combinations of light absorbers and catalysts to construct a solar-to-chemicals system. Semiconductors are well suited as light absorbers, and the range of light utilization can be tuned by changing the composition or dye sensitization. Enzymes are excellent catalysts for a specific reaction, but they are more fragile (in terms of synthesis and operating conditions) than inorganic catalysts such as metals or metal oxides. Therefore, it would be difficult for enzymes to compete with inorganic materials for large-scale bulk production of fuels such

as H_2. Instead, enzymes excel in cases where the specificity is of the utmost importance, such as in cofactor regeneration, and also where the value of the products is high.

7.2 Future work

The two enzyme-material composites presented in this thesis (PceA-TiO_2 and FNR-ITO) were able to perform the desired catalytic reactions, but further improvements to the systems are possible. In addition, the usage of TiO_2 and ITO electrodes could be extended to study other enzymes.

7.2.1 Electrode design

Results from Chapter 4 on the electrochemical leaf indicates that, at the present stage, the efficiency of the system (as measured by the Total Turnover Number (TTN) of $NADP^+$) is still too low for practical use. The electrode area could be increased, on a macro scale, by using flexible conductive supports such as Ti foil or wire which could be shaped to maximally fill a given electrochemical cell. However, there is a limit to this approach, and this should be possible to overcome by increasing the electrode area on a micro scale by using porous materials such as Ni foam as the conductive support. If the pores are not too small, electrodeposition of ITO should proceed in the same manner as onto a flat surface.

The enzyme-materials composites in the thesis relied entirely on electrostatic interactions between the two. This was sufficient for experiments over the course of days, at room temperature and a relatively low ionic strength, but harsher conditions would cause detachment of enzyme from the electrode. Covalent linkage between the enzyme and electrode is one possible method to overcome this limitation. The covalent linkage can be nonspecific, such as by functionalization of the electrode surface with -COOH, then forming peptide bonds with exposed -NH_2 groups on the enzyme.[2] More specific bonding is also

possible, but this would involve engineering FNR to have surface groups such as -S from cysteines.

7.2.2 The ITO electrode

In Chapter 3, while the porous ITO layer allowed adsorption of very large amounts of FNR and facile investigation of its non-turnover peaks, the fact that some FNR molecules participated unequally in the catalytic reaction meant that measuring the turnover frequency (TOF) of FNR was not straightforward. While the thickness of the ITO layer by electrophoretic deposition could be controlled to some extent, there was still variation with each preparation (and this is already much improved from the doctor's blade method which was less controllable). A more systematic investigation of ITO electrode preparation methods as well as other FNR loading methods (such as stirring in dilute solution) can make possible FNR coverages that are nearer to the ideal monolayer. In addition to measuring the TOF more accurately, it can also lead to less redundant enzyme molecules in a practical system.

The ease of fabrication of metal oxide electrodes by electrophoretic deposition, especially onto a PGE electrode, means that this system can be used to investigate enzyme-materials composites under hydrodynamic control, which was not possible before. The porous ITO electrode can also be used to investigate non-turnover signals of other enzymes that may be difficult to observe due to their low coverage.

7.2.3 Extending the scope of the electrochemical leaf

Wild type FNR can only utilize NADP(H) as its substrate, but it can be engineered to increase its specificity towards NAD(H).[3,4] This can increase the scope of the 'electrochemical leaf' to include coupling to NADH-dependent enzymes. The power source for the 'leaf' was changed to light by using a photoanode as shown in Chapter 5, and this can also be switched to a H_2-consuming anode, such as Pt, resulting in a H_2-driven system similar to that of Vincent *et al*.[5] It should also be possible to coload Pt and FNR onto ITO particles to create a particulate version of the same system.

7.2.4 The photoelectrochemical leaf

Results in Chapter 5 showed that light-driven NADPH production was achieved in both photoelectrochemical and particulate systems. However, the photoelectrochemical system still required an applied bias to function. Different semiconductor materials, such as C_3N_4 or TaON,[6,7] can lead to simultaneous $NADP^+$ reduction and water oxidation with no applied bias. Another possibility is to use a p-type semiconductor as a photocathode (with FNR adsorbed) and an n-type semiconductor as a photoanode in a dual light absorber system which can potentially overcome the requirements for an applied bias. Finally, the system can be coupled to a downstream CO_2-reducing enzyme, creating a true 'photoelectrochemical leaf' that can simultaneously carry out CO_2 reduction and water oxidation.

7.3 References

(1) Armstrong, F. A.; Siritanaratkul, B.; Megarity, C. F.; Roberts, T. G.; Happe, T.; Office, I. P., Ed. United Kingdom, 2016.

(2) Krishnan, S.; Armstrong, F. A. *Chemical Science* **2012**, *3*, 1015.

(3) Deng, Z.; Aliverti, A.; Zanetti, G.; Arakaki, A. K.; Ottado, J.; Orellano, E. G.; Calcaterra, N. B.; Ceccarelli, E. A.; Carrillo, N.; Karplus, P. A. *Nat Struct Mol Biol* **1999**, *6*, 847.

(4) Piubelli, L.; Aliverti, A.; Arakaki, A. K.; Carrillo, N.; Ceccarelli, E. A.; Karplus, P. A.; Zanetti, G. *Journal of Biological Chemistry* **2000**, *275*, 10472.

(5) Reeve, H. A.; Lauterbach, L.; Lenz, O.; Vincent, K. A. *ChemCatChem* **2015**, *7*, 3480.

(6) Kuriki, R.; Maeda, K. *Physical Chemistry Chemical Physics* **2017**.

(7) Maeda, K.; Domen, K. *The Journal of Physical Chemistry C* **2007**, *111*, 7851.

Appendix 1

Gas chromatography and mass spectrometry (GC-MS) of chlorinated ethenes

1. A typical headspace GC-MS chromatogram from solution containing tetrachloroethene (PCE), trichloroethene (TCE), and *cis*-dichloroethene (*c*DCE)

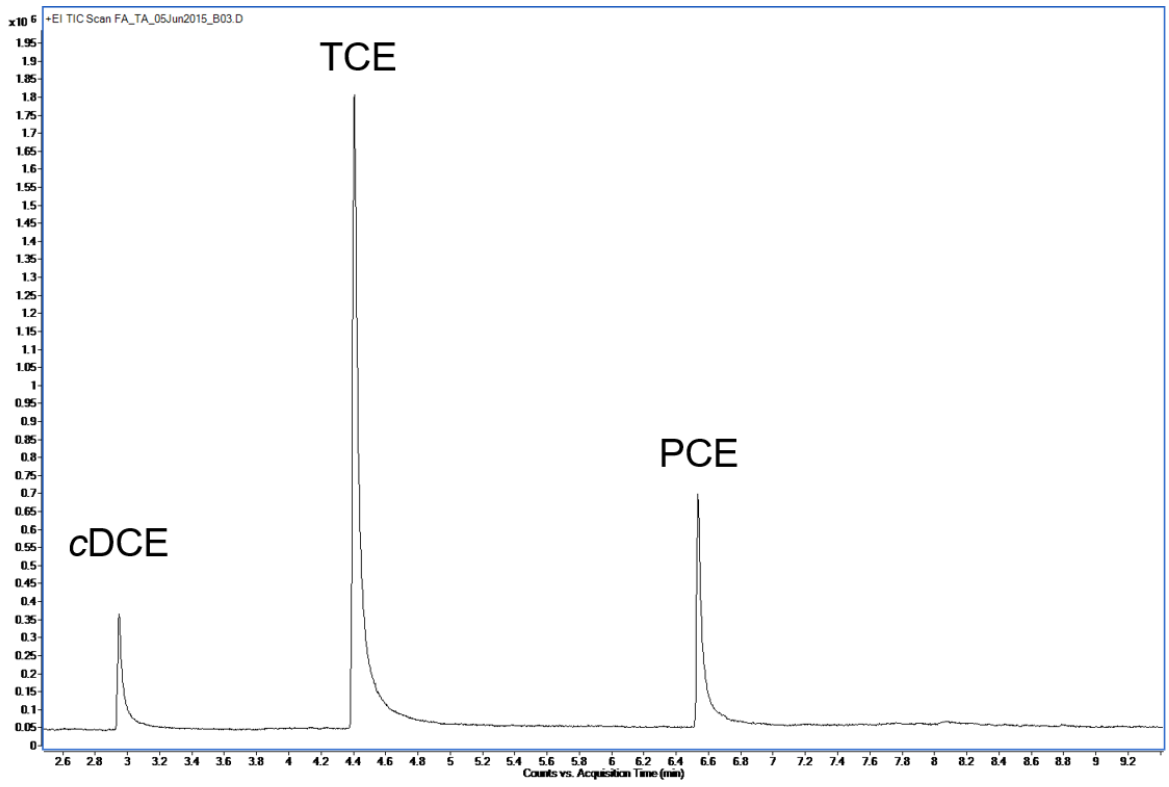

2. Mass spectrum of tetrachloroethene (PCE)

PCE (experiment)

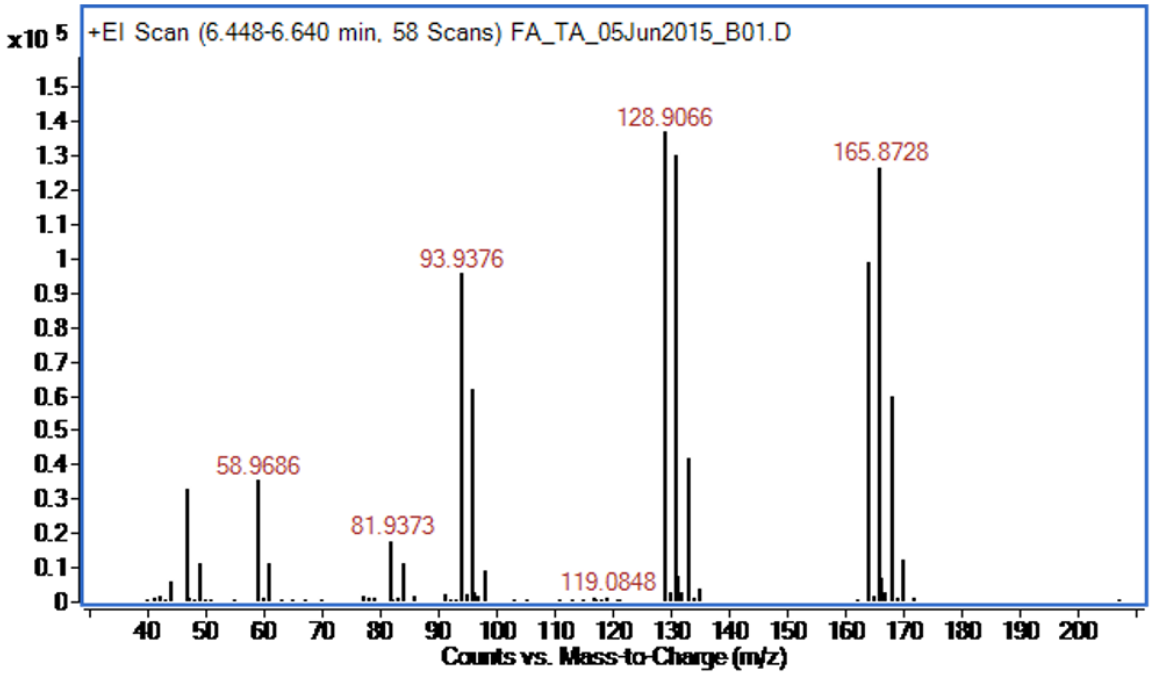

PCE (database)

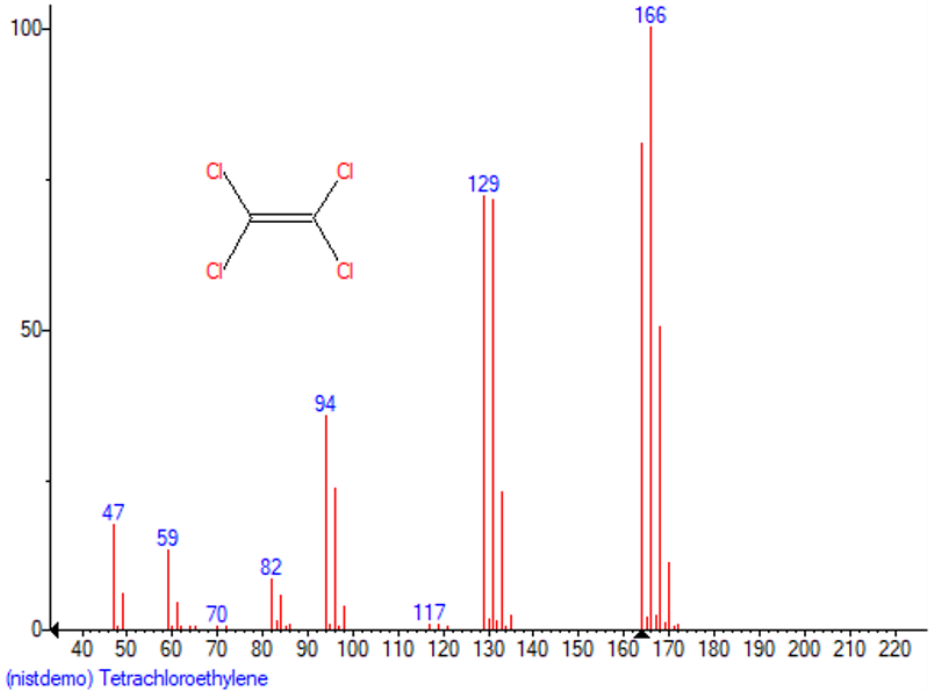

3. Mass spectrum of trichloroethene (TCE)

TCE (experiment)

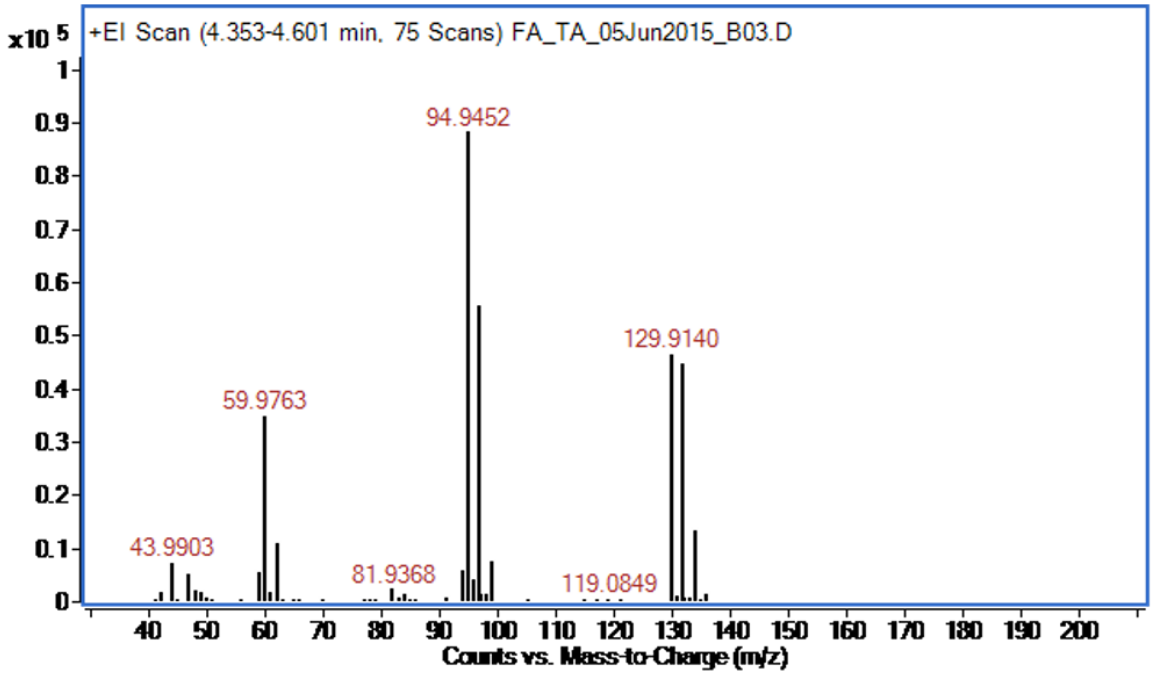

TCE (database)

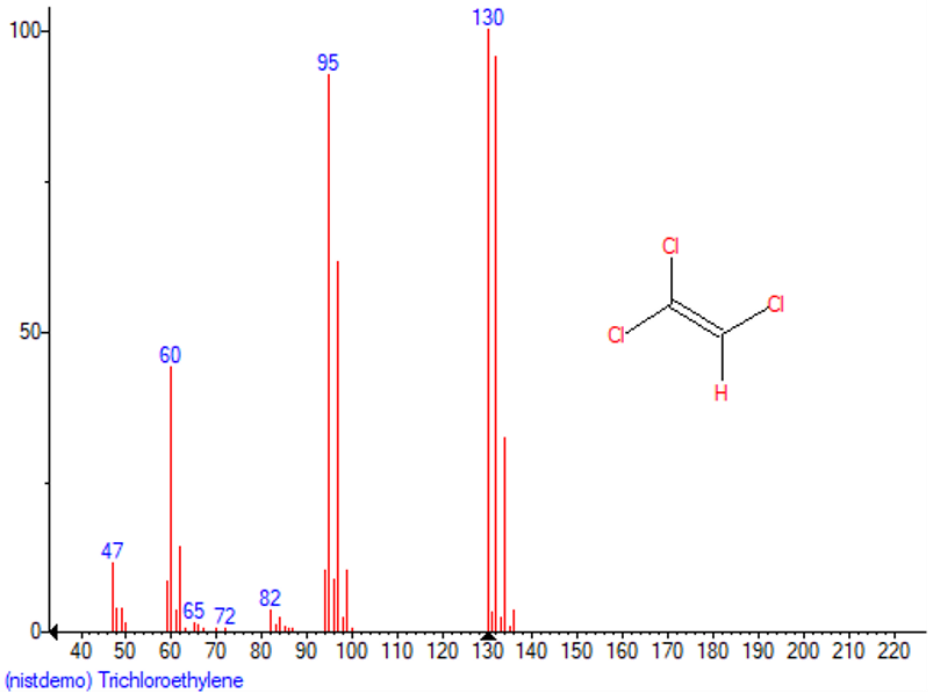

4. Mass spectrum of *cis*-dichloroethene (*c*DCE)

*c*DCE (experiment)

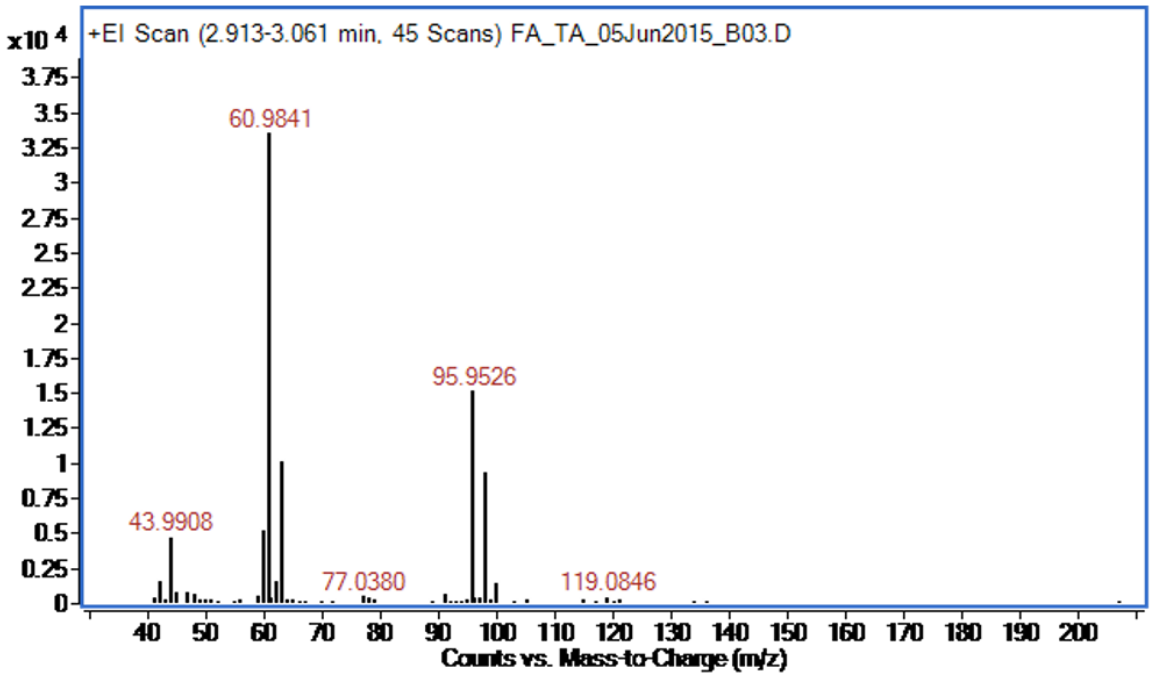

*c*DCE (database)

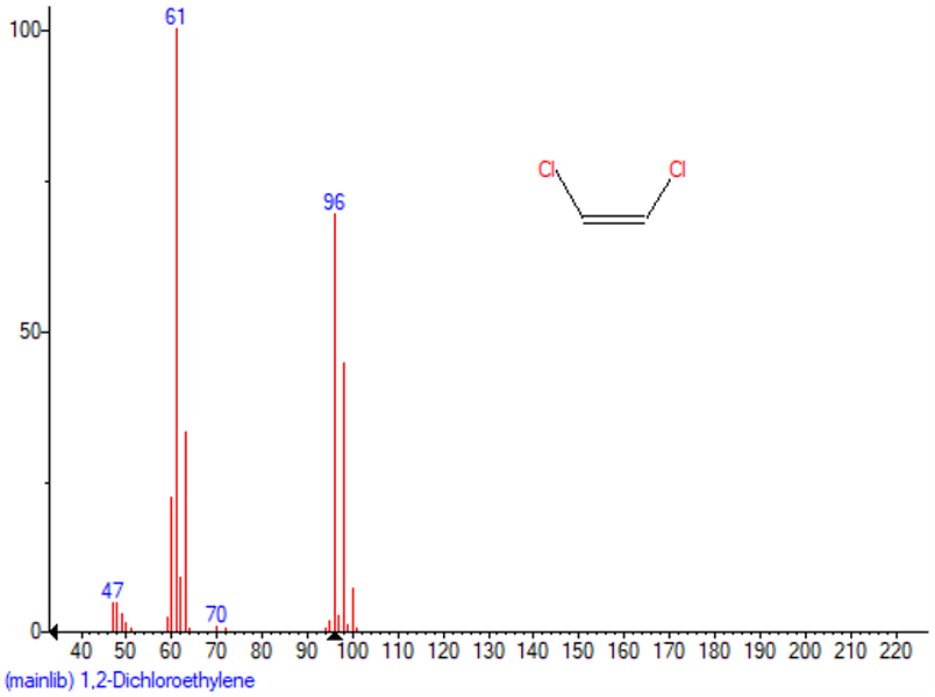

Symbols and Abbreviations

2-OG	2-oxoglutarate
A	Ampere
A	Area
Å	Angstrom
AdoCbl	Adenosylcobalamin
Arg	Arginine
ATP	Adenosine triphosphate
bpy	2,2'-bipyridine
BV	Benzyl viologen
°C	Celcius
C	Concentration, Capacitance
C	Coulomb
CB	Conduction band
Cc	Cobaltocene
*c*DCE	*cis*-dichloroethene
CE	Counter electrode
CODH	Carbonmonoxide dehydrogenase
Cp	Cyclopentadienyl
D	Diffusion coefficient
E	Potential
E coli	*Escherichia coli*
EC	Enzyme commission number
ECAA	ethyl-4-chloroacetoacetate
ECHB	ethyl-(S)-4-chloro-3-hydroxybutyrate
E_F	Fermi level
EtOH	Ethanol
eV	Electron volt
F	Faraday constant
FAD	Flavin adenine dinucleotide
fcc_3	flavocytochrome c_3
Fd	Ferredoxin
FMN	Flavin mononucleotide
FNR	Ferredoxin-$NADP^+$ reductase
FTO	Fluorine-doped tin oxide
GC-MS	Gas chromatography-Mass spectrometry
GLDH	L-glutamate dehydrogenase
Gly	Glycine
Gox	Glucose oxidase
HOMO	Highest occupied molecular orbital
I	Current
ICDH	Isocitrate dehydrogenase
ITO	Indium tin oxide
J	Current density
J	Joule

k_b	Backward rate constant
k_{cat}	Catalytic rate constant
K_d	Dissociation constant
kDa	kilodalton
kf	Forward rate constant
K_M	Michaelis-Menten constant
LUMO	Lowest unoccupied molecular orbital
Lys	Lysine
MES	2-(N-morpholino)ethanesulfonic acid
mg	milligram
mL	millilitre
mM	millimolar
M	Molar
MQ	MilliQ water
MV	Methyl viologen
mV	millivolt
n	number of electrons
NAD(H)	Nicotinamide adenine dinucleotide
NADP(H)	Nicotinamide adenine dinucleotide phosphate
NMR	Nuclear magnetic resonance
OEC	Oxygen evolving complex
P	Power density
PCE	Tetrachloroethene (or perchloroethene)
PceA	Tetrachloroethene reductive dehalogenase
PDB	Protein data bank
Pf	*Pyrococcus furiosus*
PFE	Protein film electrochemistry
PGE	Pyrolytic graphite edge
Phe	Phenylalanine
PS	Polystyrene
PSI	Photosystem I
PSII	Photosystem II
q	Charge
R	Gas constant
Rdase	Reductive dehalogenase
RE	Reference electrode
RHE	Reversible hydrogen electrode
RuP	$Ru(bpy)_2(4,4\text{-}(PO_3H_2)_2bpy)Br_2$
s	Second
SAM	Self-assembled monolayer
SCE	Saturated calomel electrode
SEM	Scanning electron microscopy
Ser	Serine
SHE	Standard hydrogen electrode
T	Temperature
TAPS	N-Tris(hydroxymethyl)methyl-3-aminopropanesulfonic acid

TCE	Trichloroethene
TEOA	Triethanolamine
TOF	Turnover frequency
TON	Turnover number
Tris	Tris(hydroxymethyl)aminomethane
Trp	Tryptophan
TTN	Total turnover number
Tyr	Tyrosine
ν	Kinematic velocity
V_{appl}	Applied potential
VB	Valence band
V_{max}	Maximum rate
W	Watt
WE	Working electrode
Γ	Coverage
δ	Peak width at half maximum height
η	Efficiency
λ	Wavelength
ν	Scan rate
μ	Micro